

Pickering emulsions, colloidosomes & micro-encapsulation

PROEFSCHRIFT

ter verkrijging van de graad van doctor aan de
Technische Universiteit Eindhoven, op gezag van de
rector magnificus, prof.dr.ir. C.J. van Duijn, voor een
commissie aangewezen door het College voor
Promoties in het openbaar te verdedigen
op donderdag 12 mei 2011 om 16.00 uur

door

Johannes Wilhelmus Otto Salari

geboren te Alkmaar

Dit proefschrift is goedgekeurd door de promotoren:

prof.dr.ir. L. Klumperman
en
prof.dr. J. Meuldijk

Copromotor:
dr. H.M. Wyss

Salari, Joris W.O.

The research described in this thesis was supported by Capzo International BV.

A catalogue record is available from the Eindhoven University of Technology Library.

ISBN: 978-90-8891-267-2

Copyright © 2011 by Joris W.O. Salari

Printed by: Boxpress BV || Proefschriftmaken.nl

Contents

Summary	6
Samenvatting	8
List of symbols	11
1 Introduction	15
1.1 Phase change materials	17
1.1.1 Salt hydrates	18
1.1.2 Encapsulation	19
1.2 Pickering emulsions	21
1.2.1 The stability of Pickering emulsions	23
- Coalescence	26
- Colloidal stability	32
- Sedimentation/creaming	36
- Ostwald ripening	37
1.2.2 Conclusion	37
1.3 Outline thesis	38
2 Structural characterization of Pickering emulsions & colloidosomes	43
2.1 Introduction	45
2.2 Structural characterization	47
2.2.1 Three-phase contact angle, θ	47
2.2.2 Droplet diameter, D	48
2.2.3 Structural organization of particles	50
2.3 Conclusion	65

3 Colloidal cages: colloidosomes with tunable particle packing	67
3.1 Introduction	69
3.2 Experimental	70
3.3 Results	75
3.3.1 Particle synthesis	75
3.3.2 Colloidal cage formation	78
3.3.3 Theoretical modeling particle packing	89
3.4 Discussion	93
3.5 Conclusion	95
4 Steric stabilization of Pickering emulsions	97
4.1 Introduction	101
4.2 Experimental	102
4.3 Results	105
4.3.1 Particle synthesis: Soap-free emulsion polymerization	105
4.3.2 Pickering emulsion formation	106
4.3.3 Adsorption of pS-b-EP	109
4.3.4 Microcapsule formation: sintering	114
4.4 Discussion	115
4.5 Conclusion	117
5 Wetting and colloidal stability of hairy particles: a SCF theory	119
5.1 Introduction	121
5.2 Self Consistent Field Theory	123
5.2.1 The model	124
5.2.2 Parameters	126
5.3 Results	126
5.3.1 oil/water (o/w)	127
5.3.2 surface/o/w (s/o/w)	127
5.3.3 s/poly(isobutylene)/o/w	132
5.3.4 Conversion to colloidal system	135
5.3.5 Colloidal stability	138
5.4 Discussion	139
5.5 Conclusion	143

6 Drainage during the interfacial adsorption of hairy particles	147
6.1 Introduction	149
6.2 Experimental	151
6.3 Results	153
6.3.1 Particle synthesis: dispersion polymerization	153
6.3.2 Pickering emulsions: rate of particle adsorption	157
6.4 Discussion	162
6.5 Conclusion	169
7 Salt hydrate Pickering emulsions and micro-encapsulation	171
7.1 Introduction	173
7.2 Experimental	177
7.3 Results	180
7.3.1 Seeded dispersion polymerization	180
7.3.2 $\text{CaCl}_2 \cdot 6\text{H}_2\text{O}$ /pMMA Pickering emulsions	182
7.3.3 Microcapsules	183
7.3.4 Thermal properties	189
7.3.5 Deliquescence	193
7.4 Discussion	194
7.5 Conclusion	195
Epilogue	197
Acknowledgements	203
Curriculum Vitae, list of publications and presentations	206

Summary

The research that is presented in this thesis was originally motivated by the development of a micro-encapsulation method for salt hydrates. For a long time, salt hydrates have been suggested as suitable materials for thermal energy storage applications, due to their high latent heat of fusion and crystallization. Therefore, salt hydrates are often referred to as phase change materials (PCMs). However, in retrospect, this thesis can better be seen as an investigation towards the efficient micro-encapsulation of aqueous liquids in general. Particle-stabilized emulsion droplets (Pickering emulsions) are used as scaffolds for the formation of polymer microcapsules.

Chapter 1 gives a short historical background of the application of salt hydrates as PCMs and explains common methods for micro-encapsulation. Chapter 1 continues with a general description of Pickering emulsions and, finally, discusses the stability and stabilization mechanisms of Pickering emulsions, because these aspects determine the success and efficiency of microcapsule formation.

Chapter 2 demonstrates how structural information of Pickering emulsions can be derived from light microscopy and scanning electron microscopy images, because the described methods are used extensively throughout the thesis. The relevant parameters for the structure and stability of Pickering emulsions are the three-phase contact angle of the particle with the oil-water interface, the droplet diameter, as well as the structural organization of particles on the droplet surface.

Chapter 3 describes the formation, characterization and modeling of permeable capsules composed of colloidal particles (colloidosomes) with a tunable particle density and a well-defined porosity. The particle density is controlled by the particle size, of which the colloidosomes are composed. The ‘large’ particles (5.0 μm) densely pack and show an almost crystalline particle configuration. Smaller particles show incomplete surface coverages, which scales with the particle size. The attractive nature of the particles proved to be the most important factor for the formation of these structures for which we coined the name *colloidal cages*. In the first place, the attraction resulted in the formation of irregular-shaped aggregates that prevent the formation of a dense packing. Secondly, the attractive

particle potential allowed the formation of jammed particle networks on the droplet surface, which are capable of resisting droplet coalescence even at low particle densities.

In chapter 4 it is demonstrated that additional steric stabilization is provided to Pickering emulsion droplets by the adsorption of poly(styrene-*block*-(ethylene-*co*-propylene)) (pS-*b*-EP) and that it is a requirement for the efficient synthesis of polymeric microcapsules. Otherwise, if no pS-*b*-EP is used, significant aggregation is observed. Size exclusion chromatography is used to prove and quantify the adsorption of pS-*b*-EP onto the Pickering emulsion droplets. Microcapsules are formed by heating the Pickering emulsion above the glass-transition temperature of the particles.

In chapter 5, the assembly of sterically-stabilized colloids at liquid-liquid interfaces is investigated with the Self Consistent Field (SCF) theory using the discretization scheme that was developed by Scheutjens, Fler and co-workers. The model is based on a poly(methyl methacrylate) (PMMA) particle with poly(isobutylene) (PIB) grafted to the surface. The stabilizing groups on the particle surface have a significant effect on the interfacial assembly and, therefore, also on the formation and properties of Pickering emulsions. The effect of the steric stabilizer on the wetting behavior, the activation barrier for particle adsorption and colloidal stability are numerically solved with the SCF theory. This chapter demonstrates the fundamental relationship and provides a quantitative comparison between the wetting behavior and the colloidal stability and it gives a better understanding of the particle adsorption at soft interfaces.

The assembly of sterically-stabilized colloids at oil-water interfaces is studied experimentally by the formation of Pickering emulsions. The results are described in chapter 6. Especially, the effect of the steric stabilizer with respect to the kinetics of particle adsorption is investigated. The rate of particle adsorption is measured by the evolution of the droplet diameter during emulsification. A strong dependence of the steric stabilizer concentration on the kinetics of particle adsorption has been found, which is due to the repulsive barrier before interfacial adsorption. The activation barrier E_A for particle adsorption is derived from this measurement and is, interestingly, several orders of magnitude higher than the corresponding colloidal stability. A possible mechanism that can lead to such a repulsive force is the inhibited drainage of solvent from the layer of steric

stabilizer upon interfacial assembly. Deformation of the o/w interface occurs, when the solvent does not have time to drain, which results in a dramatic increase of the interfacial energy. This chapter identified the relevance of drainage in the formation of Pickering emulsions.

In the final chapter we report, for the first time, the micro-encapsulation of calciumchloride hexahydrate ($\text{CaCl}_2 \cdot 6\text{H}_2\text{O}$). The procedure consists of two steps. First, the salt hydrate is emulsified in an oil with the aid of poly(methyl methacrylate) (pMMA) microparticles. The second step is the addition and *in situ* polymerization of MMA, which ultimately results in pMMA microcapsules. The microcapsule size and shell thickness is controlled during the synthesis. The thermal properties are characterized by differential scanning calorimetry (DSC) and X-ray diffraction (XRD), which shows a clear effect of compartmentalization of $\text{CaCl}_2 \cdot 6\text{H}_2\text{O}$ on the crystallization behavior. Nucleation and crystallization are clearly restricted to the microcapsules, where otherwise a single nucleation results in the crystallization of the entire sample.

Samenvatting

De inkapseling van zouthydraten vormde de motivatie voor het onderzoek dat is beschreven in dit proefschrift. Vanwege hun hoge latente smelt- en kristallisatie warmte zijn zouthydraten uitermate geschikte materialen voor thermische energie opslag en worden daarom vaak aangeduid als fase-overgangs materialen (PCMs). Terug kijkend kan dit proefschrift echter beter worden gezien als een onderzoek naar de efficiënte micro-encapsulatie van hydrofiele vloeistoffen, waarbij emulsies gestabiliseerd door vaste deeltjes (Pickering emulsies) de basis vormen voor de polymere microcapsules.

Hoofdstuk 1 geeft een korte achtergrond over de toepassing van zouthydraten als PCM en een overzicht van de gebruikelijke inkapselingsmethoden. Het hoofdstuk gaat verder met een algemene beschrijving van Pickering emulsies en bespreekt de stabiliteit en stabilisatiemechanismen van Pickering emulsies. Dit aspect bepaalt uiteindelijk het succes en de efficiëntie waarmee de microcapsules gevormd worden.

Hoofdstuk 2 beschrijft hoe de structurele informatie van een Pickering emulsie kan worden afgeleid uit licht- en elektronenmicroscopie-beelden. De beschreven methoden zijn uitvoerig gebruikt bij het onderzoek dat leidde tot dit proefschrift. De relevante parameters voor de structuur en stabiliteit van Pickering emulsies zijn de drie-fasen contact hoek van het deeltje met het water-olie grensvlak, de druppelgrootte en de ordening van de deeltjes op het oppervlak van de emulsie druppel.

Hoofdstuk 3 beschrijft de vorming, karakterisatie en modellering van permeabele capsules, die zijn samengesteld uit colloïdale polymeerdeeltjes (colloidosen), met een gecontroleerde deeltjesdichtheid en porositeit. De deeltjesdichtheid wordt beïnvloed door de grootte van de deeltjes waaruit de colloidosen zijn samengesteld. Een hoge dichtheid wordt behaald met ‘grote’ deeltjes (5,0 μm) die een bijna-kristallijne ordening laten zien. Kleinere deeltjes laten een onvolledige bedekking van de colloidosen zien. De bedekkingsgraad van de colloidosen schaaft met de deeltjesgrootte. De aantrekking tussen de deeltjes is de belangrijkste factor bij de vorming van de gevormde structuren, waarvoor wij de naam *colloïdale kooien* opperen. In de eerste plaats zorgt de aantrekking tussen de deeltjes voor de vorming van onregelmatige aggregaten, die voorkomen dat hoge dichtheden worden behaald. In de tweede plaats zorgt de aantrekking tussen de deeltjes voor stabiele emulsiedruppels bij een onvolledige bedekking.

Hoofdstuk 4 beschrijft de sterische stabilisatie van poly(styreen) Pickering emulsie druppels, door de adsorptie van poly(styreen-*blok*-(ethyleen-*co*-propyleen)) (pS-b-EP). Dit is een vereiste voor de efficiënte productie van polymere microcapsules. Als er geen pS-b-EP wordt gebruikt neemt de aggregatie aanzienlijk toe en neemt derhalve de efficiëntie af. Gel-permeatie chromatografie is gebruikt om aan te tonen hoeveel pS-b-EP adsorbeert op de Pickering emulsie druppels. De microcapsules worden gevormd door het verwarmen van de Pickering emulsie boven de glasovergangstemperatuur van de polystyreen deeltjes.

Hoofdstuk 5 beschrijft de adsorptie van sterisch gestabiliseerde polymeer deeltjes op een water-olie grensvlak middels de ‘Self Consistent Field’ theorie met behulp van het diskretisatie schema van Scheutjens, Fler en medewerkers. Het model is gebaseerd op een polymethylmethacrylaat (pMMA) deeltje waaraan polyisobutyleen (pIB) is bevestigd op het oppervlak. Het effect van deze pIB sterische stabilisator op de bevochtiging, de activerings barrière en de colloïdale stabiliteit zijn numeriek opgelost met de SCF theorie.

Dit hoofdstuk toont de fundamentele relatie tussen de bevochtiging en de colloïdale stabiliteit en geeft op deze manier een beter inzicht in de vorming Pickering emulsies.

In hoofdstuk 6 is de adsorptie van sterisch gestabiliseerde pMMA deeltjes op water-olie grensvlakken experimenteel bestudeerd door de vorming Pickering emulsies. Het effect van de sterische stabilisator op de kinetiek van de deeltjes adsorptie is voornamelijk onderzocht. De snelheid van deeltjesadsorptie wordt gemeten door de evolutie van de druppelgrootte tijdens het emulgeren. Als gevolg van de activeringsenergie, door de sterische stabilisator, wordt een sterke afhankelijkheid op de kinetiek van de deeltjesadsorptie waargenomen. De activeringsenergie is afgeleid uit deze meting en blijkt meerdere ordes groter te zijn dan de colloïdale stabiliteit. Een mogelijk mechanisme dat kan leiden tot een dergelijk afstoting is de vertraagde drainage van oplosmiddel uit de laag van de sterische stabilisator tijdens de adsorptie. Vervorming van het water-olie grensvlak kan gebeuren, wanneer het oplosmiddel geen tijd heeft om weg te vloeien. Dit resulteert in een significante toename van de vrije grensvlak energie.

In hoofdstuk 7 wordt de inkapseling op micro-schaal van calciumchloride-hexahydrate ($\text{CaCl}_2 \cdot 6\text{H}_2\text{O}$) beschreven. De procedure bestaat uit grofweg twee stappen. Als eerste stap wordt $\text{CaCl}_2 \cdot 6\text{H}_2\text{O}$ geëmulgeerd in een olie met behulp van pMMA deeltjes. De tweede stap is de toevoeging en *in situ* polymerisatie van MMA, wat uiteindelijk resulteert in pMMA microcapsules. De grootte van de microcapsules en de schil dikte wordt ingesteld tijdens de synthese. De thermische eigenschappen van $\text{CaCl}_2 \cdot 6\text{H}_2\text{O}$ zijn gemeten met ‘differential scanning calorimetry’ en röntgendiffractie en laten een duidelijk effect zien van de segregatie van het geëncapsuleerde $\text{CaCl}_2 \cdot 6\text{H}_2\text{O}$. Nucleatie en kristallisatie zijn duidelijk beperkt tot de microcapsules, waar anders nucleatie zou leiden tot kristallisatie van het gehele monster.

List of symbols

α	inclination angle of a particle with central axis of the colloidosome
a	dimension of a lattice site (SCF-theory)
A	surface area
A_H	Hamaker constant
A_{wo}	surface area of the water-oil interface
A_{pw}	surface area of the particle-water interface
A_{po}	surface area of the particle-oil interface
β	angular displacement
c	packing factor
C	pre-exponential factor
d_n	number-average particle diameter
d_v	volume-average particle diameter
Δ	polydispersity index
D	droplet diameter
ϵ	dielectric constant
E	constant
E_A	activation energy for particle adsorption
E_B	binding energy of a particle with the water-oil interface
E_{col}	energy required for the coalescence of two Pickering emulsion droplets
E_{def}	interfacial free energy of deformation of the water-oil interface

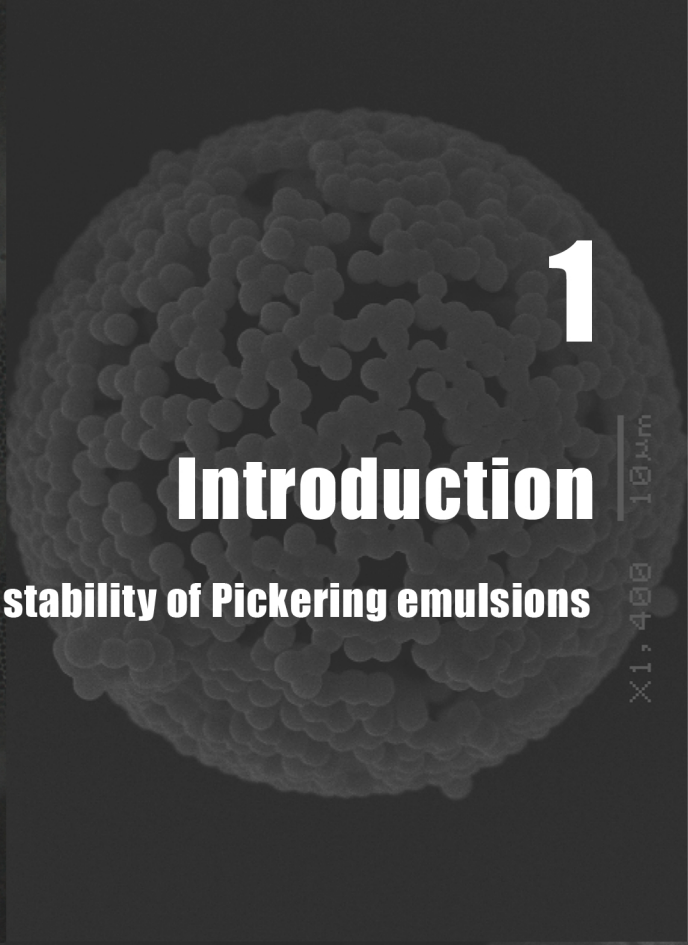
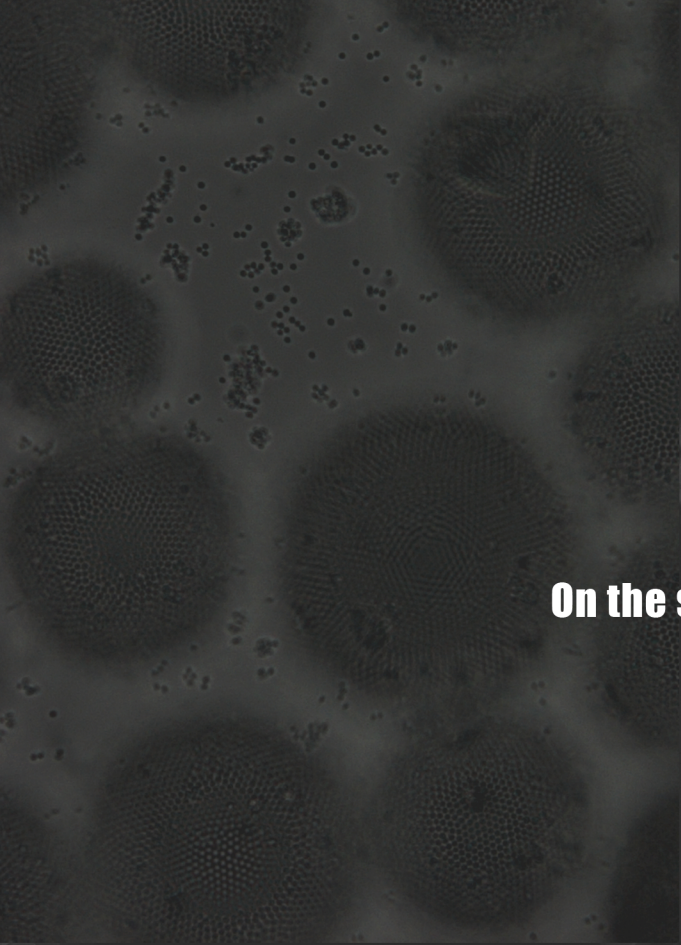
List of symbols

E_k	kinetic energy of a particle colliding with a droplet
ΔE_{PP}	net particle-particle potential
ΔE_{PI}	net particle-interface potential
f	mean-field free energy density
F	mean free energy
ΔF	excess mean free energy
γ	interfacial free energy
γ_{wo}	interfacial tension oil-water
γ_{pw}	interfacial tension particle-water
γ_{po}	interfacial tension particle-oil
g	gravitational constant
$g(r)$	radial pair-correlation function
Γ	amount
$\Gamma^\#$	excess amount
Γ_{PIB}	surface concentration poly(isobutylene)
ΔG	Gibbs free energy of emulsification
h	film thickness
h_{CR}	critical film thickness
h_{MIN}	minimum film thickness
h_{FLOC}	film thickness of the secondary minimum
J	particle flux
J_0	initial particle flux

k	rate constant for particle adsorption
k_B	Boltzmann constant
l	lattice layer
L	dimension-less volume of a lattice layer
m_P	mass particle
M_w	molecular weight
Δn	number of particles desorbed from the water-oil interface
N	number of particles
N_A	number of particles adsorbed to the water-oil interface
N_B	number of particles in the continuous phase
N_{agg}	aggregate size
N_{col}	number of particles on colloidosome surface
p	planar distance of the particle center to the central axis of the colloidosome
Π	disjoining pressure
P_{ADS}	probability for particle adsorption
P_C	capillary pressure
$P_{C,max}$	maximum capillary pressure
ΔP	La Place pressure
Q	partition function
ρ	particle surface density
ρ_{max}	maximum particle surface density
$\Delta\rho$	density difference between the dispersed- and continuous phase
r	center-center interparticle distance

List of symbols

R	particle radius
τ	shear rate
T	temperature
T_{PC}	phase change temperature
u	potential
φ	volume fraction
v	fluid velocity
v_{rotor}	rotational velocity of rotor
$\langle \Delta v \rangle$	average velocity difference between droplet and particle
ϕ_{HS}	hard-sphere potential
ϕ_{PHS}	polarizable hard-sphere potential
V_A	attractive particle potential
V_D	volume of the dispersed phase
V_R	repulsive particle potential
x_c	x-coordinate of the colloidosome
x_p	x-coordinate of a particle on the colloidosome surface
χ	Flory-Huggins interaction parameter
y_c	y-coordinate of the colloidosome
y_p	y-coordinate of a particle on the colloidosome surface
z	height of the particle's center to the water-oil interface
z_p	z-coordinate of a particle on the colloidosome surface
θ	three-phase contact angle



1

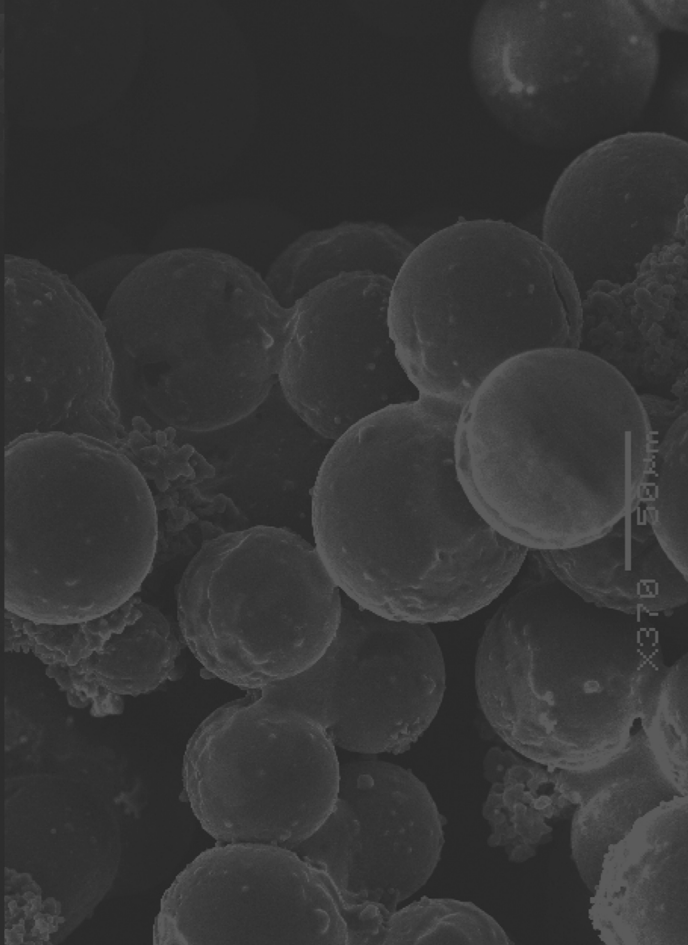
Introduction

On the stability of Pickering emulsions

X1,400 10 μm



X950 20 μm



X370 50 μm

Abstract: For a long time, salt hydrates have been suggested as suitable materials for thermal energy storage applications, due to their high latent heat of fusion and crystallization.¹⁻⁵ Therefore, salt hydrates are often referred to as phase change materials (PCMs). The application of salt hydrates as PCMs has been hampered by an efficient encapsulation technique, which would allow the incorporation of salt hydrates in existing materials and processes. The renewed interest and further development of solid particle-stabilized emulsions (Pickering emulsions) in the last two decades has paved the way for the micro-encapsulation of salt hydrates. The introductory chapter shortly explains the working principle of PCMs and salt hydrates in particular. The introduction then continues with the current state of the art in micro-encapsulation and the potential of Pickering emulsions for this purpose. Finally, the introduction elaborates on the different parameters that determine the stability of Pickering emulsions, because it is this aspect that ultimately determines the success and efficiency of micro-encapsulation.

The research that is presented in this thesis is originally motivated by the development of a micro-encapsulation method for salt hydrates, in particular, which are suitable PCMs, due to their high latent heat of fusion and crystallization.¹⁻⁵ However, in retrospect, this thesis can better be seen as an investigation towards the efficient micro-encapsulation of aqueous liquids, in general, from Pickering emulsions.

1.1 Phase change materials

The most common example of PCMs in our daily life is probably ice. ‘Cold’ is stored at 0 °C by freezing the water into small ice cubes. The heat of melting is taken from the beverage and hereby cools your drink. Heat packs or hand-warmers are another common example of PCMs, but work in an opposite manner. In fact, the material in the hand warmers is based on a salt hydrate and releases heat by triggering crystallization. The hand-warmers can be re-used by putting them in boiling water to melt the crystallized material again. Although the first example is used for cooling and the second for warming, both examples release and take up heat by crystallization and melting, respectively.

Thermal energy storage is not only beneficial to reduce the mismatch between energy supply and demand, but it also improves the performance of energy systems and conserves energy.¹⁻⁵ The great advantage of PCMs for thermal energy storage, is their high heat storage capacity in combination with a narrow temperature range in which the energy is stored. In principle, the phase change temperature (T_{PC}) is discrete, which means that energy is stored at exactly T_{PC} . In contrast to sensible thermal energy storage, which requires a wide temperature range to store an equivalent amount of heat. Besides the existing daily life examples, more advanced applications for PCMs can be envisioned, such as its integration in buildings⁶⁻⁸ and for efficient heat transportation.⁹⁻¹¹ For example, PCMs can be incorporated in buildings as a heat buffer to reduce daily temperature fluctuations, which leads to a more comfortable indoor climate and energy/costs savings for heating as well as air conditioning. Moreover, PCMs can be dispersed in heat transfer fluids to efficiently transport heat from one location to another, which is particularly interesting for industrial settings or in combination with solar energy for domestic applications. In this case, the use of PCMs leads to a reduced equipment size and/or heat losses during transportation of an equal amount of thermal energy.

1.1.1 Salt hydrates

The existing PCMs can roughly be divided into 2 classes; the *inorganic* PCMs, which comprises mostly salt hydrates (table 1.1), and *organic* PCMs which constitute paraffin or waxes and fatty acids. Other PCMs do exist, but the majority of research is performed on these materials. Excellent review articles are available that describe the field of research and applications more thoroughly.¹⁻⁴ Moreover, a book on “Heat and cold storage with PCMs” is published recently. For more detailed information the author refers to this book and the review articles.^{1-4, 12} The advantages and disadvantages of the two major PCMs will briefly be discussed. The two most important advantages of salt hydrates are their low cost of production and their high thermal energy storage capacity. Due to the high density ($\gg 1.0 \cdot 10^3 \text{ kg/m}^3$) of salt hydrates, the heat capacity per unit volume is superior to that of organic PCMs. The major disadvantage of organic PCMs is, however, their flammability, which has especially limited their application in buildings. Salt hydrates, on the other hand, have flame retardant properties and are therefore more suitable for that particular application. Moreover, salt hydrates have a relatively high thermal conductivity and a small volume change upon melting and crystallization, which is also beneficial for the final application. Organic PCMs are by far superior in terms of their thermal properties. Paraffins and fatty acids melt and crystallize at practically the same temperature, *i.e.* the equilibrium phase transition temperature. Salt hydrates exhibit serious undercooling and melt incongruently. This drawback of salt hydrates can be overcome by the addition of nucleating agents and optimization of the salt composition. Therefore, we believe that salt hydrates are the most promising class of materials for the application of PCMs.

Table 1.1 Various common salt hydrates that are suitable for thermal energy storage and water.¹⁻⁴

Material	Phase change temperature, T_{PC} [°C]	Latent heat [J/g]
H ₂ O	0	334
CaCl ₂ ·6H ₂ O	29	191
Na ₂ SO ₄ ·10H ₂ O	32	251
Na(CH ₃ COO)·3H ₂ O	58	226
Mg(NO ₃) ₂ ·6H ₂ O	89	163
MgCl ₂ ·6H ₂ O	117	169

1.1.2 Encapsulation

Due to the solid-liquid phase transition, encapsulation is required for the application of any PCM. Moreover, PCMs need to be protected from the surroundings and vice versa. Salt hydrates, for example, are corrosive and sensitive towards water. Either water is attracted (deliquescence) or hydrate water can evaporate depending on the type of salt hydrate. This leads to a different molar ratio of the pure salt and water, which has a negative effect on the thermal properties. Through encapsulation, the desired composition of the PCM is maintained. The majority of commercially available PCMs are macro-encapsulated, *i.e.* salt hydrates have been packaged in aluminium pods,¹³ polyolefin panels have been impregnated with paraffin¹⁴ and fatty acids have been encapsulated in a material resembling bubble-wrap.¹⁵ Micro-encapsulated paraffin is produced and commercialized under the name Micronal®.¹⁶ A poly(methyl methacrylate) shell encapsulates the paraffin, which is inert and therefore allows the incorporation in existing building materials, such as plaster, concrete or insulation foams. A similar approach is envisioned with the micro-encapsulation of salt hydrates. To the best of the authors knowledge, the encapsulation of salt hydrates has only been reported once by Capzo Int.¹⁷ The encapsulation method developed by Capzo starts from a polymer/salt hydrate composite, which is ground to form solid particles. The salt hydrate particles are subsequently encapsulated by deposition of styrene-maleic anhydride copolymers, which can be cross-linked to yield stable polymer shells. The grinding process limits the particle size and yields a broad particle size distribution (0.25 – 10 mm). Moreover, the present method requires modification of the core salt hydrate material.

One can only speculate about the reasons for the large contrast between salt hydrates and organic PCMs, in terms of micro-encapsulation.¹⁶ A possible reason could be that salt hydrates are not compatible with the traditional micro-encapsulation technologies. Standard micro-encapsulation methods include interfacial polymerization or (mini-) emulsion polymerization.¹⁸⁻²⁰ These methods emulsify an organic liquid in water and subsequent polymerization leads to the formation of microcapsules (fig. 1). Such methods are not possible with salt hydrates. In the first place, salt hydrates are obviously water-soluble and need to be emulsified in an organic liquid, which poses limitations to the existing polymerization techniques. However, similar methods in inverse (water-in-oil) emulsions are available.²¹⁻²³ Encapsulation by interfacial polymerization requires the mixing of two different monomers in the continuous- and dispersed phase. Polymerization occurs at the oil/water interface, hereby creating a polymer shell around the emulsion droplets. The

monomers generally used for this process are di-amines, acid chlorides and/or isocyanates. The high salt content in the essentially aqueous solution negatively affects the solubility, reactivity and compatibility of the available monomers. If the monomer is soluble in the salt hydrate at all, which is rarely the case, degradation occurs upon contact with the salt hydrates. Another method, similar to the fabrication of Micronal®, is (mini) emulsion polymerization. This method requires the mixing of (vinyl)monomers with the dispersed phase. Polymerization leads to phase separation with the oil and the polymer consequently forms a shell around the droplet, when the interfacial tensions are optimized. A similar approach is not possible with salt hydrates, because the solubility and compatibility of such monomers is limited.

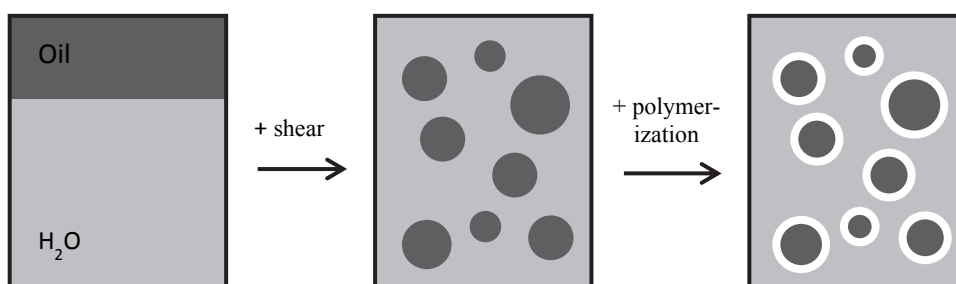


Figure 1.1 General micro-encapsulation procedure. *Left:* Oil and water are added to the reactor. *Middle:* The oil is emulsified in water to form small droplets. *Right:* Polymerization leads to shell formation at the oil-water interface and finally results in microcapsules.

Ideally, the pure salt hydrate is emulsified and the shell forming material is applied from the continuous phase, as is the case for micro-encapsulation by *in situ* polymerization or (complex) coacervation.^{20, 24} These techniques encapsulate emulsion droplets by deposition of polymer purely from the continuous phase and require no mixing with dispersed phase. A common example of *in situ* polymerization is the polymerization of melamine and formaldehyde in the aqueous phase. The formed polymer is insoluble in water and deposits onto the emulsion droplets leading to strong and impermeable capsules. (Complex) coacervation requires the phase separation and deposition of polymer onto the droplets. Phase separation can be achieved by a change in solubility due to, for example, solvent evaporation or the complexation with another polymer. One of the very first applications of microcapsules, namely carbonless copy paper, uses the complex coacervation of gelatin and arabic gum.²⁵ Also for these techniques, there is a large contrast in the number of publication

reporting the encapsulation of aqueous or oily liquids. To the author's knowledge, only one study reports the encapsulation of hydrophilic liquids using one of these methods.²⁴ Landfester and coworkers precipitated poly(methyl methacrylate) (pMMA) onto aqueous mini emulsion droplets by solvent evaporation. A mixture of a good and poor solvent is used, in which pMMA is dissolved. The good solvent is evaporated and pMMA precipitates to yield the microcapsules. The advantage of this method is that the pure salt hydrate is emulsified and is not modified. In the course of this thesis a similar micro-encapsulation approach has been developed, namely the *in situ* polymerization in the presence of Pickering emulsion droplets.

1.2 Pickering emulsions

The renewed interest and further development of Pickering emulsions in the last two decades has paved the way for the micro-encapsulation of salt hydrates. Emulsions can be solely stabilized by solid particles, in contrast to conventional molecular surfactants, to form so-called Pickering or solids-stabilized emulsions. In 1903 Ramsden had reported the stabilization of emulsions with solid particles for the first time.²⁶ However, Pickering stabilization derived its name from a paper by Pickering in 1907.²⁷ Since then, occasionally articles have been published in this field,²⁸⁻³⁰ but in general there has been no significant interest in this field until 1990. Since then, Pickering stabilization regained new interest promoted by the work of Velev,³¹⁻³³ who demonstrated its potential for micro-encapsulation and the development of advanced materials in general. However, it was Weitz³⁴⁻³⁷ and Bon³⁸⁻⁴¹ and their coworkers in the last decade who realized the synthesis of capsules from Pickering emulsions with a precise control of size, permeability and mechanical properties. The assembly of colloidal particles at liquid-liquid interfaces is governed by the interfacial free energies γ of the particle and the two liquid phases, respectively.⁴² Young's equation (eq. 1.1), relates the interfacial tensions to the equilibrium position of the particle at the interface, through the 3-phase contact angle (θ , see also fig. 1.2a).⁴³

$$\cos \theta = \frac{\gamma_{po} - \gamma_{pw}}{\gamma_{ow}} \quad 1.1$$

γ_{PO} , γ_{PW} and γ_{OW} are the interfacial tensions of the particle/oil, particle/water and oil/water interface, respectively. By definition, a particle adsorbs to the o/w interface when it is partially wetted by the two liquid phases, or in other words when $0^\circ < \theta < 180^\circ$ (fig. 1.2). Although, experimental studies report that an intermediate θ values ($60^\circ < \theta < 120^\circ$) yield the most stable Pickering emulsions.^{28, 30} Moreover, θ determines the type of emulsion that is preferred.^{44, 45} Hydrophilic particles ($\theta < 90^\circ$) protrude more into the aqueous phase and prefer the formation of oil-in-water (o/w) emulsion. Vice versa, hydrophobic particles ($\theta > 90^\circ$) stabilize water-in-oil (w/o) emulsions. The fundamental difference between Pickering stabilization and molecular surfactants is the relatively large size of the stabilizing entities, resulting in strong binding energies of the particles with the interface (eq. 1.2).⁴⁶

$$E_B = \pi R^2 \gamma_{OW} (1 - |\cos \theta|)^2 \quad 1.2$$

E_B is the desorption energy of a particle from the liquid interface into the continuous phase of the emulsion. This means that colloidal particles with a radius R : (0.01 - 10) μm and intermediate θ are practically irreversibly attached to the interface (E_B : (10^2 - 10^6) $k_B T$), leading to the formation of highly stable emulsion droplets. A detailed discussion of the stability of Pickering emulsions is given in section 1.2.1b. Pickering emulsions have found their way in various applications and industrial processes, such as crude-oil processing³⁷, food^{47, 48}, mineral flotation⁴⁹ and cosmetics,⁵⁰ due to the strong adsorption of particles to liquid interfaces. Moreover, Pickering emulsion droplets have recently been extensively used as scaffolds for the synthesis of advanced supracolloidal materials, such as colloidosomes,³⁴ colloidal nano-composites,³⁹ porous solids and foams.⁵¹ The work reported in this thesis also uses Pickering emulsion droplets as a scaffold to synthesize polymer micro-capsules. Colloidosomes, see figure 2b, c, deserve special attention, because they are particularly close to the structure that is aimed for. Although it was Velev who synthesized similar structures for the first time, Dinsmore³⁴ later defined colloidosomes as: "selectively permeable capsules that are composed of colloidal particles." The assembly of spherical particles onto emulsion droplets results in a solid shell that is inherently porous (fig. 1.2). The size of the interstitial voids is directly related to the particle size and directly controls the permeability, which can be used potentially for the controlled release and selective transport across the particle shell.

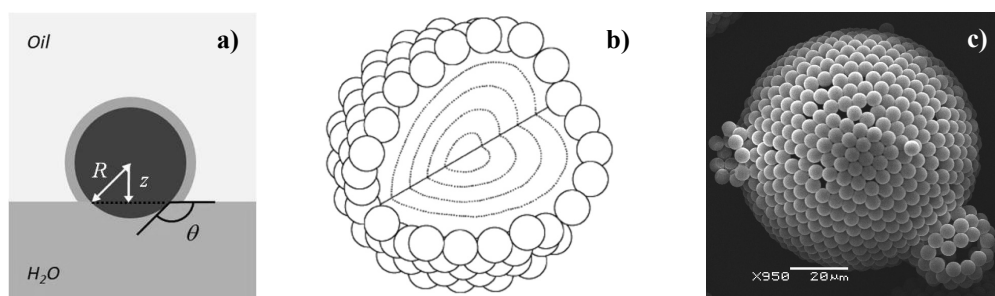


Figure 1.2 Pickering stabilization *a)* A solid particle that is assembled at the water/oil interface. *b)* An emulsion droplet that is surrounded with solid particles. *c)* A permeable microcapsule or colloidosome that is composed of polystyrene particles (chapter 2). R is the radius of the particle. θ is the three-phase contact angle. z is the distance from the center of the particle to the interface. The dark grey circle represents the solid particle. The light gray area that surrounds the particle is the layer with stabilizing groups, which is attached to the particle and is, in this case, soluble in the oil.

In particle-stabilized emulsions the material of interest is, as a matter of fact, already encapsulated. Although reinforcement of the particle layer surrounding the droplets is still required to obtain mechanically stable capsules, which can be achieved in a variety of ways. For example, a polymer can be adsorbed to physically cross-link the particles^{32, 34, 35, 52} or the particle layer can be chemically cross-linked.^{4, 32, 53-56} In the case of polymer particles, heating above the glass-transition temperature (sintering) allows the particles to partially or completely fuse and form a solid polymer shell.^{19, 35, 57-59} A more recent development is the formation of an interpenetrating polymer network throughout the particles that reinforces the particle layer.³⁸ Chapter 7 describes a novel method to reinforce the particle layer and form microcapsules, which is done by *in situ* polymerization.

1.2.1 The stability of Pickering emulsions

The stability of Pickering emulsions is paramount to the *success* and *efficiency* of the synthesis of microcapsules in particular and the formation of advanced materials in general. Coalescence of droplets during the procedure obviously leads to unsuccessful encapsulation. Ideally, each Pickering emulsion droplet remains segregated and ultimately becomes a microcapsule. Flocculation of emulsion droplets also reduces the encapsulation efficiency. For example, the physical or chemical cross-linking may occur between

particles from different emulsion droplets during collision. Similarly, during the fusion of polymer particles to form a uniform shell, sintering can lead to the irreversible aggregation of emulsion droplets. These undesired effects can easily be circumvented in laboratory scale experiments, for example by working with low solid contents, low shear stirring or specialized set-ups. In scientific literature, a proof-of-principle is often demonstrated on single droplets, which do not require the same criteria for stability as for large quantities emulsion with a relatively high volume fraction of dispersed phase. The stability of Pickering emulsions is of utmost importance for large scale, industrial production and this aspect is the connecting thread throughout this thesis. For this reason, the experiments reported in this thesis have all been performed in mechanically stirred batch reactors of 250 mL.

In principle, all emulsions are thermodynamically unstable. The instability is caused by the large interfacial w/o area upon emulsification and the corresponding increase in the interfacial Gibbs free energy. This means that, in principle, all emulsions tend to phase separate.⁶⁰ The change in Gibbs free energy ΔG of emulsification, in the absence of any surface active agents, scales according to

$$\Delta G \sim \gamma_{ow} \Delta A_{wo}$$

1.3

ΔA is the change in the interfacial w/o area, which obviously increases during emulsification. Therefore, ΔG is positive and the emulsion is thermodynamically unstable. There is not only a contribution of the interfacial free energy, but also of the LaPlace pressure. However, this contribution can also be expressed in terms of γ_{ow} and ΔA , as is the case for equation 1.3. It, therefore, does not change the outcome of the argument.

The presence of emulsifiers, such as molecular surfactants or solid particles, affects the change of the Gibbs free energy upon emulsification. Molecular surfactants lower the interfacial tension γ_{ow} of the oil/water interface and hereby reduce ΔG . Solid particles do not alter γ_{ow} , but adsorb at the w/o interface resulting in a reduction of the w/o interfacial area (eq. 1.2). Spontaneous emulsification only occurs under very specific conditions. For example, high concentrations of particular molecular surfactants can sufficiently reduce γ_{ow} and lead to thermodynamically stable emulsions, *i.e.* micro-emulsions.⁶¹ Spontaneous emulsification can also occur in the presence of solid particles and are referred to as

equilibrium Pickering emulsions. Kegel and co-workers recently described this novel class of emulsions.⁶²⁻⁶⁶ The conditions required are low interfacial tensions between oil and water ($\gamma_{ow} < 10$ mN/m), amphiphilic ions that can adsorb at the droplet surface and colloidal particles.

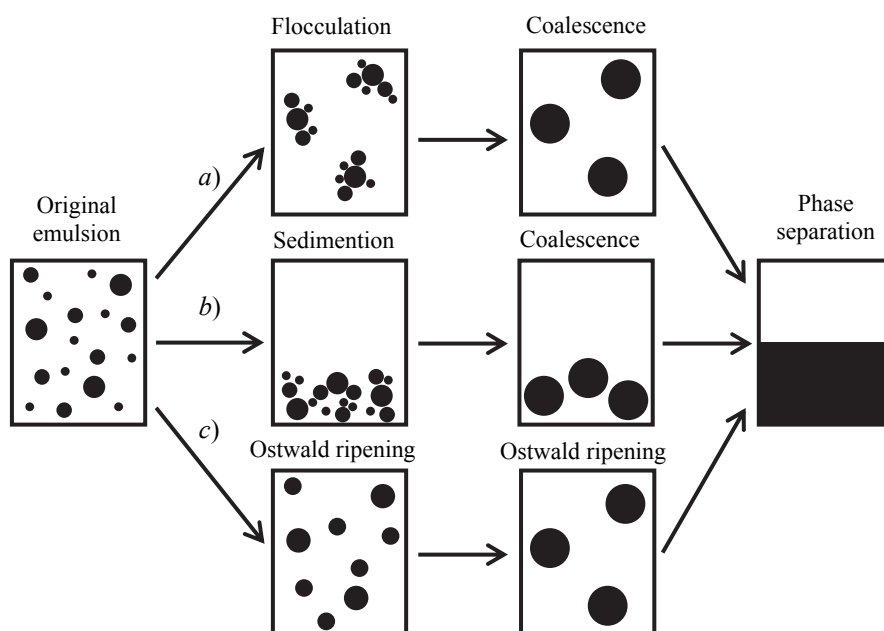


Figure 1.3 Mechanisms that lead to macroscopic phase separation of an emulsion.⁶⁷ *a)* Initially, freely dispersed emulsion droplets can flocculate and subsequently coalesce, which continues until two separate phases are formed. *b)* Emulsions can either sediment or cream, depending on the density difference between the dispersed- and continuous phase, and subsequently coalesce. *c)* Another mechanism that does not require coalescence to phase separate is Ostwald ripening. The dispersed phase has a higher density than the continuous phase.

The various mechanisms that can lead to macroscopic phase separation of an emulsion are illustrated in figure 1.3.⁶⁷ Flocculation occurs when droplets experience an attractive force towards each other and is generally associated with a secondary minimum in the interaction potential.⁶⁸ The origin of attraction is the always present van der Waals interaction. Sedimentation or creaming is caused by a density difference between the dispersed- and continuous phase. Gravity simply pulls the phase with the highest density downwards.

Creaming therefore occurs in o/w emulsions and droplets sediment in w/o emulsions. In figure 1.3 the droplets are denser than the continuous phase. It is the above-described two mechanisms that bring the emulsion droplets together, but it is coalescence that ultimately leads to macroscopic phase separation. Coalescence is the process where two or more droplets merge to form one large droplet. Ostwald ripening is another process that leads to phase separation and does not require coalescence. It occurs when the dispersed phase has a finite solubility in the continuous phase. The larger droplets grow at the expense of the smaller droplets, due to a La Place pressure difference. This process continues until two completely separated phases are formed.

Coalescence stability

Energy of detachment The explanation as to how solid particles impart stability to emulsions is fundamentally different to stabilization by molecular surfactants, due to the relative large size of the stabilizing units and the presence of three-phases, resulting in a three-phase contact angle. The droplet stability of Pickering emulsions is, in the first place, attributed to steric hindrance provided by the particle layer surrounding the droplet and prevents the droplets from coalescing. Binks reported an elegant thermodynamic analysis of the coalescence of two droplets that is based on the energy of desorption of particles from the w/o interface.⁶⁷ Binks demonstrated that although coalescence is thermo-dynamically favorable, the particle layer provides an energy barrier for coalescence. Droplet coalescence leads to a decrease of the droplet surface area per unit volume of the continuous phase. In this calculation it is assumed that the new, larger droplet remains spherical. However, this is not necessarily the case, but nonetheless provides a useful illustration of the coalescence stability. Reduction of the interfacial area ΔA drives this process (eq. 1.3). However, due to a reduced droplet area Δn particles need to be desorbed from the w/o interface. The energy necessary for desorption provides the energetic barrier and is given by

$$E_{COL} = \Delta n \cdot E_B = \Delta n \cdot \pi R^2 \gamma_{OW} (1 - |\cos \theta|)^2 \quad 1.4$$

Equation 1.2 has already demonstrated that for colloids with $R : (0.01 - 10) \mu\text{m}$ and intermediate θ , $E_B : (10^2 - 10^6) k_B T$. E_{COL} is even larger by a factor of Δn , which means that under normal conditions ($k_B T$) the energetic barrier is sufficiently high to prevent coalescence.

Capillary stabilization A different approach considers the capillary pressure in the thin film between two colliding emulsion droplets.⁶⁹⁻⁷² The theoretical approach for stabilization of liquid films by solid particles is based on the shape of the fluid menisci formed between the neighboring particles. This type of stabilization, which is unique for Pickering emulsions, is referred to as capillary stabilization, because it is entirely based on capillary forces. In this approach, the emulsion stability against coalescence is governed by the stability of the thin film between two colliding droplets (fig. 1.4). The particle layers surrounding the droplets trap a film of the continuous phase upon pushing the two droplets together. The film gradually thins until the pressure inside the film exceeds the maximum capillary pressure $P_{C,max}$ (eq. 1.5) and the film ruptures.⁷⁰

$$P_{C,max} = c \frac{\gamma_{ow} \cos \theta}{R} \quad 1.5$$

c is a packing factor that depends on the structural configuration of the particle layer. Equation 1.5 is valid for thin films stabilized by dense particle bilayers. Other types of particle configurations exist, such as monolayer stabilization. Particle bilayer stabilization is the most dominant stabilization mechanism in Pickering emulsions and will be discussed in some detail. $P_{C,max}$ determines the critical film thickness h_{CR} below which the film spontaneously thins due to the Van der Waals attraction between droplets (fig. 1.4). h_{CR} is typically in the order of several nanometers to 30 nm.⁷²

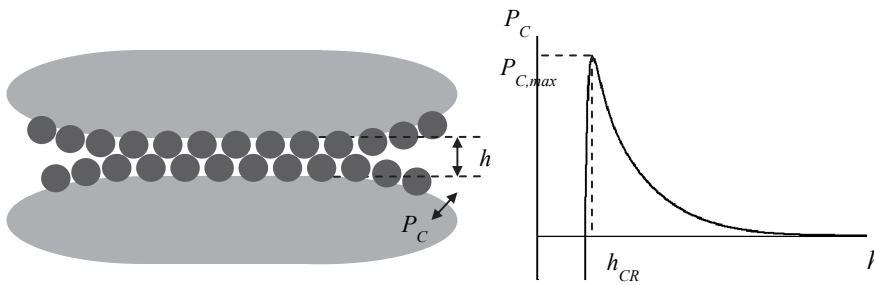


Figure 1.4 Schematic representation of capillary stabilization in Pickering emulsions.⁷² h is the film thickness between two colliding droplets. P_C is the capillary pressure across the film. The graph on the right hand side illustrates the development of P_C with decreasing film thickness.

The capillary pressure that is built up in the film opposes the force by which the droplets collide. The force of two colliding droplets depends on gravity and the position of the droplets in the emulsion (sedimentation/creaming) and/or on the shear rates due to *e.g.* stirring. The balance between these forces operating in opposite direction determines the minimum film thickness h_{MIN} . If h_{MIN} remains larger than h_{CR} , then the film is considered stable and coalescence of the two droplets does not occur.

Drainage contributes to the resistance of emulsion droplets to coalesce. It is well known that drainage plays an important role in the stability of conventional emulsions. Tambe and Sharma specifically discussed the rheological properties of particle stabilized interfaces relate to emulsion stability.⁷³ They predicted an increase of the viscoelastic properties on droplet surfaces for densely packed particle layers. As illustrated in figure 1.4, the particle bilayer traps a thin liquid film. The liquid has to drain to the bulk of the continuous phase when two droplets approach each other. The contribution of particles to the interfacial rheology appears to cause a substantial decrease in the rate of fluid drainage, which results in more stable emulsions as it slows down droplet coalescence.

The three phenomenological models based on the energy of detachment, capillary pressure and drainage, predict an exceptionally high stability of films between densely covered droplets. In fact, most Pickering emulsion droplets should not coalesce under realistic conditions and this is in contradiction to the available experimental studies. Tcholakova *et al* quantitatively compare, in an excellent review, the experimental results from various studies concerning the stability of Pickering emulsions.⁷² The notion that particle-stabilized emulsions are extremely stable is widely-spread, which is supported by the theoretical models. However, Tcholakova concludes that *the available experimental data do not support the hypothesis that particle-stabilized emulsions are exceptionally stable to droplet-droplet coalescence, as compared to the typical surfactant and protein-stabilized emulsions*. The main reason for the discrepancy between theoretical and experimental studies is the assumption made in all models that the particles are homogeneously distributed in the films and are static. Inhomogeneity in the particle layer may cause film rupture at much lower capillary pressures than is predicted by model calculations. Moreover, the deformation of droplets is not accounted for. Coalescence almost always involves deformation of droplets, which increases the droplet surface area and creates sites that are deprived of particles. These weak points also cause rupture of the film at much lower capillary pressures. Moreover, particles can be removed from the contact area between two

droplets due to fluid drainage. It is clear that the actual stability of the droplets is strongly affected by the structural properties of the surrounding particle layer, which will be discussed in the following section.

The 3-phase contact angle θ is by far the most important parameter that characterizes Pickering emulsions. It is a unique feature of particle-stabilized emulsions and results in a completely different type of stabilization. By definition, θ should be between 0° and 180° in order for a particle to adsorb at a particular interface. According to equations 1.2 and 1.4, the most stable emulsions are obtained with $\theta = 90^\circ$. This results in the highest energy of detachment from the interface (eq. 1.2) and the highest kinetic barrier for coalescence (eq. 1.4). On the other hand, the theory of capillary stabilization (eq. 1.5) predicts the most stable emulsions at θ either close to 0° (o/w emulsions) or 180° (w/o emulsions). In fact, the two different mechanisms for stabilization are complementary. Kaptay combined the theory of capillary stabilization with the energy of particle detachment from the interface.⁷⁴ He concluded that the most stable emulsions are obtained for $70^\circ \leq \theta \leq 86^\circ$ for o/w emulsions and $94^\circ \leq \theta \leq 110^\circ$ for w/o emulsions. These theoretical approaches are consistent with the results of many experimental studies that conclude that intermediate contact angles yield the most stable emulsions.^{28, 30, 75}

The packing density and structure of the particle layer is of crucial importance for the stability of Pickering emulsions. The most commonly reported particle configurations are dense, hexagonally close-packed particles (fig. 1.6a).³⁴ It is worth mentioning that, in contrast to planar surfaces, the packing of uniform particles on spherical surfaces leads to the introduction of obligatory defects.^{76, 77} According to Eulers theorem, the total disclination charge, which is the departure of the coordination number on a planar surface of 6, of any triangulation on a sphere must be 12. Soccer balls and C₆₀ fullerenes are typical examples of this phenomenon.⁷⁸ They have 12 pentagonal patches and 20 hexagonal patches. As the number of particles on the sphere increases additional dislocations are introduced, which consist of pairs of 5-7 defects. They still obey Euler's theorem because their net disclination charge is zero. Chains of 5 - 7 dislocations, so-called grain-boundary scars (fig. 1.5), are formed when the system size ($D/4R$) exceeds the critical value of 5. D is the diameter of the colloidosome.

Regular hexagonal close-packed particle bilayers are most often assumed in the calculation of the maximum capillary pressure $P_{C,max}$. However, obligatory defects are introduced on

spherical surfaces, as is always the case for spherical emulsion droplets. Such defects are weak spots where the thin film between two droplets ruptures at lower capillary pressures than is expected. This may be a fundamental reason why lower coalescence stability is observed experimentally for Pickering emulsions than is predicted by model calculations. The described equilibrium particle configurations are only achieved with arbitrary repulsive particles. Non-repulsive and attractive particles can be jammed in lower density particle configurations,^{79, 80} which is accompanied by additional defects that could even further lower $P_{C,max}$.

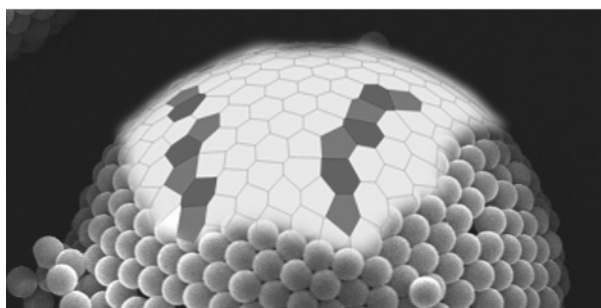


Figure 1.5 Deviation from the hexagonal close-packing on a spherical surface. The light-gray patches denote the pentagonal (5-) coordinated particles and the dark-gray patches denote heptagonal (7-) coordinated particles. Depending on the system size chains of 5- and 7-coordinated particles appear to form so-called grain-boundary scars. A Voronoi-tessellation is overlaid with the SEM image from which it is derived. Details of the characterization of the particle configuration are explained in chapter 2.

Besides dense particle configuration, there are studies reporting incomplete surface coverages that are able to impart coalescence stability to the droplets.⁸¹⁻⁸⁵ Midmore⁸⁴ obtained stable o/w emulsions using colloidal silica particles. Hydroxypropyl cellulose is added to strongly flocculate the particles. Experimentally it is observed that to form stable emulsions coverage of at least 29% of the droplet surface is required. The author proposed that the flocculated particles formed a 2-dimensional gel structure that effectively kept droplets from coalescing (fig. 1.6b). The inter-particle attraction proved to be a key parameter in the formation of stable emulsion droplets. Chapter 3 also describes the formation of Pickering emulsion droplets with incomplete surface coverage. The particles form a surface spanning network, similar to the work of Midmore.⁸⁴ The inter-particle attraction also appears to play an important role in the stability of these emulsion droplets.

The stability against coalescence of Pickering emulsion droplets with such low surface coverages is remarkable, because the three mechanisms of stabilization, *i.e.* based on the energy of detachment, capillary pressure and drainage, hardly contribute in these situations.

Figure 1.6 shows four commonly observed particle configurations in Pickering emulsions. It must be mentioned that this figure shows a highly idealized representation and deviations can easily occur, but it does illustrate clearly the distinct differences among the various structures. Moreover, this illustration is not extensive and other, less common particle configurations have also been reported. It is worth mentioning that highly regular and low density structures are synthesized by Van Blaaderen and co-workers.⁸⁷ The particles are hexagonally close-packed, but the particle separation is several particle diameters. The formation of such a structure requires a long-range repulsive particle-particle interaction, which is possible due to partial immersion of the particles into the oil and the Coulombic repulsion that occurs through the oil instead of the water-phase. Van Blaaderen does not elaborate on the coalescence stability of such droplets, but it is expected that such structures do not impart significant coalescence stability.

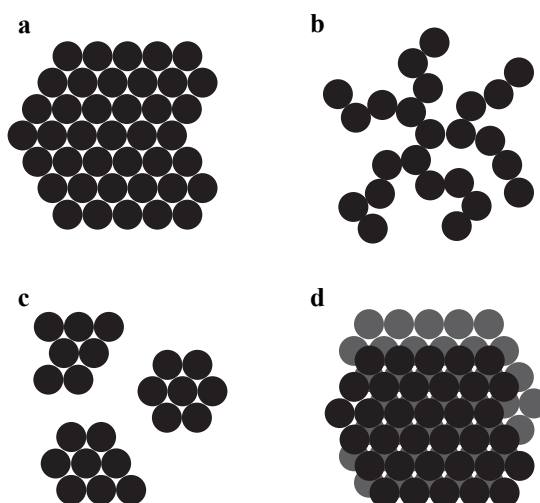


Figure 1.6 Various particle configurations that are observed in Pickering emulsions.⁸⁶ **a)** hexagonally close-packing; **b)** a 2D (colloidal) gel structure; **c)** flocs of densely packed particles that sparsely cover the droplet surface and **d)** particle multilayers.

Three of the four particle configurations are observed throughout the research described in this thesis and demonstrated sufficient coalescence stability. A hexagonally close-packing (fig. 1.6a) is observed in chapters 6 and 7 during the formation of Pickering emulsions with hairy or sterically stabilized particles. Incomplete surface coverages (fig. 1.6b) are observed in the formation of colloidosomes with attractive particles, see chapter 3. Particle multilayers (fig. 1.6d) are reported in chapter 4 that uses initially stable electrostatically charged particles. Salt is added to destabilize the aqueous particle dispersion and promote the formation of Pickering emulsions. The critical concentration of coagulation and interfacial adsorption is practically similar. Therefore, particle aggregation and interfacial adsorption occurs simultaneously, resulting in a particle multilayer on the droplet surface. In summary, the three phenomenological models based on the energy of detachment, capillary pressure and drainage, explain the coalescence stability of particle-stabilized emulsion droplets in a qualitative manner and capture the main trends. However, the agreement between the theoretical predictions and experimental studies is limited. The coalescence stability of Pickering emulsions is overestimated, while at the same time, droplets with incomplete surface coverage exhibit remarkable stability. The systems studied in this thesis all showed sufficient coalescence stability throughout the experiments.

Colloidal stability

Flocculation is the process in which particles or droplets, in the case of Pickering emulsions, aggregate reversibly (fig. 1.3a). While stirring the aggregates continuously form and break up in the flow field. This process is generally associated with a secondary minimum in the inter-particle potential energy.⁶⁸ The colloidal stability or the flocculation stability is of great importance for the synthesis of advanced materials from Pickering emulsion droplets. Reinforcement of the particle layer surrounding the Pickering emulsion droplet is necessary for the synthesis of, for example, stable capsules. During this process, flocculation can lead to the irreversible aggregation of the emulsion droplets and ultimately results in a dramatic loss in the encapsulation efficiency. The stabilization of colloidal dispersions is achieved by surface functional groups that generate a repulsive potential.⁶⁸ These groups can be charged/ionic groups (such as sulfate or carboxylic acid groups), polymers that are attached to the particle surface and extend into the continuous phase or a combination of both. The colloidal stability is described by accounting the attractive van der Waals and repulsive Coulombic interactions. The repulsive interaction by flexible polymers is usually described by the steric interactions, elastic deformation and restricted mobility of the interpenetrating chains. The electrostatic and steric interactions can be

explained in terms of the excess osmotic pressure in the thin film between two colliding particles or droplets. This excess osmotic pressure ‘sucks in’ fluid from the bulk of the continuous phase and hereby creates an effective repulsion.

In contrast to the coalescence stability, the colloidal stability of Pickering emulsions is hardly reported. However, in general, an assessment of the flocculation behavior of Pickering emulsions can be made, because the wetting behavior and the colloidal stability of the stabilizing particles are fundamentally related through their surface functional groups. The colloidal stability of Pickering emulsion droplets is discussed through consideration of the stabilizing particles, because it is the surrounding particles that inevitably determine the interaction with other droplets. The wetting behavior, which is expressed through θ , is determined by the interfacial tensions of the w/o interface γ_{ow} and the respective interfacial tensions of the particle with the oil γ_{po} and water-phase γ_{pw} (eq. 1.1). The interfacial tension of a particle is not only determined by the interfacial tension of the core material, but also by the stabilizing groups. By definition, the stabilizing groups lower the interfacial tension of the particle and the fluid in which it is originally synthesized or dispersed. Vice versa, the stabilizing groups increase the interfacial tension of the particle with the other fluid that constitutes the emulsion. This effect on the wettability is illustrated by the various θ values that are reported in literature of, for instance polystyrene latexes.^{57, 88} Moreover, various values for θ ranging from 90° to 180° have been reported for poly(methyl methacrylate) (pMMA) particles.^{87, 89, 90}

Several authors briefly discuss the colloidal stability of the Pickering particles. The “rule of thumb” for charge-stabilized particles is that ‘flocculating’ conditions enhance the interfacial assembly. There are several reasons for this empirical relation. Firstly, stable charge-stabilized colloids are strongly hydrated due to their double layer,⁶⁸ which affects the surface tensions and renders the particles unsuitable for Pickering stabilization ($\theta < 0^\circ$). Secondly, Coulombic repulsion occurs between the particle and the interface at low ionic strength solutions.⁹¹ Tcholakova extensively describes the role of the electrostatic barrier for particle adsorption during the formation of Pickering emulsions.⁷² The addition of salt effectively screens the electrostatic and hydration repulsion allowing the particles to approach the interface and ultimately adsorb onto the w/o interface. At the same time, the addition of salt screens the repulsion between the particles, resulting in flocculation or aggregate. As a consequence, the resulting Pickering emulsion droplets also flocculate or aggregate. An additional benefit is that the attractive inter-particle potential results in rigid

particle layers surrounding the droplet, which improves the coalescence stability. In normal o/w emulsions, in which water is the continuous phase, the charged surface functional groups can still contribute, although slightly, in a repulsive manner. In some cases, charged particles are suitable to stabilize inverse w/o emulsions. The colloidal stability is worse for such systems, because the low dielectric constant of most common oils ($\epsilon \approx 2$) does not allow the stabilizing groups to dissociate and generate sufficient Coulombic repulsion.⁹² In effect, inverse w/o Pickering emulsions formed with charged particles strongly flocculate. To illustrate this point, some examples from literature are discussed. Bon and co-workers successfully synthesized clay armored polymeric particles.⁹³ Salt is added to drive the clay particles to the o/w interface and stabilize the monomer droplets. The synthesis is successful due to the remarkable stability against coalescence. However, the final latex is unstable and settles in time. Dialysis of the final latex and removal of salt results in a stable latex. Velev extensively reported the synthesis of ‘ordered supra-particles’ or colloidosomes in a series of papers in the 1990s.³¹⁻³³ The different stages of the assembly process are also clearly explained by Binks and Horozov.⁶⁷ First, the electrostatic and hydration repulsion of the particles is decreased to facilitate particle adsorption. Second, casein is added, which adsorbs onto the particle-stabilized droplets. The casein acts as a steric stabilizer to overcome the flocculating nature of the droplets. The colloidal stability of Pickering emulsions is also reported in chapters 4 and 5 of this thesis. Chapter 4 demonstrates that additional steric stabilization is required for the efficient synthesis of microcapsules. Sulfate-stabilized polystyrene (pS) particles were used to form a w/o Pickering emulsion and was heated above the glass-transition temperature to form pS microcapsules. Dramatic aggregation occurred when no additional stabilization was provided. This indicates the unstable nature of the original Pickering emulsion. The efficient synthesis of pS microcapsules was achieved when a block-copolymer was adsorbed, to sterically stabilize the droplets in a similar fashion as Velev and co-workers. Chapter 5 relates the wettability and colloidal stability of sterically stabilized particles in a theoretical framework. Interestingly, it has been demonstrated there is a small window of stabilizer concentrations that exhibit both colloidal stability as well as partial wetting. In the other cases, the particles were either completely wetting, and therefore unsuitable for Pickering stabilization, or were colloiddally unstable.

In consideration of the disjoining pressure Π of interacting Pickering emulsion droplets, the attractive van der Waals interaction of the surrounding particles must be included. This is an extension of the consideration of the capillary pressure in the thin film between two

colliding droplets (fig. 1.3). The relevant distance for flocculation is the film thickness h_{FLOC} between two colliding droplets at which the particles touch. For a dense particle bilayer, h_{FLOC} is given by

$$h_{FLOC} = 2z = 2R|\cos \theta| \quad 1.6$$

z is the equilibrium position of the particle at the interface or in other words the height of the particle center protruding in the continuous phase (fig. 1.2). The interaction of Pickering emulsion droplets at film thicknesses $h > h_{FLOC}$ is determined by the colloidal stability of the particles. As is illustrated in the previous sections, Pickering emulsions tend to flocculate. Therefore, the attractive van der Waals interaction plays a dominant role in this range. For a dense particle bilayer at $h = h_{FLOC}$, the particle layers of two colliding droplets touch exactly. The secondary minimum in the disjoining pressure is located here because from this point capillary pressure starts to play a role (fig. 1.7). Between $h_{CR} > h > h_{FLOC}$ the shape of the fluid menisci between neighboring particles is distorted and a capillary pressure builds up, as explained previously in the section on coalescence stability. Below $h < h_{CR}$ the thin film spontaneously ruptures due to the van der Waals interaction between the droplets and coalesce.

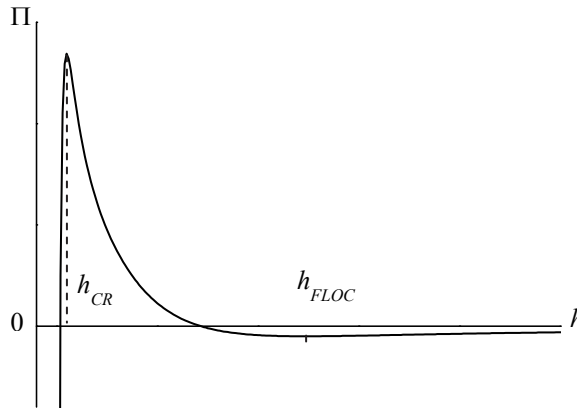


Figure 1.7 Schematic representation of the disjoining pressure Π of Pickering emulsion droplets as a function of the film thickness h . h_{CR} is the critical film thickness below which coalescence occurs. h_{FLOC} is the position of the secondary minimum due to the attractive van der Waals interaction of the stabilizing particles.

Based on the available literature, it is difficult to conclude that all Pickering emulsions are in fact colloidally unstable. In general, it can be concluded that particle-stabilized emulsions tend to flocculate. The reason for this behavior is the fundamental relation between the wettability and the colloidal stability through the stabilizing groups of the Pickering particles. Additional stabilization is desirable for the synthesis of advanced materials in general and specifically microcapsules.

Sedimentation/creaming

Sedimentation/creaming is not unique to Pickering emulsions and is mainly determined by the density difference $\Delta\rho$ between the continuous and the dispersed phases, the droplet size D and the viscosity μ . A small $\Delta\rho$ and D enhances the sedimentation or creaming stability. If the droplet size is in the sub-micrometer range, then thermal motion can keep the droplets dispersed. Otherwise emulsions tend to sediment or cream, depending on the type of emulsion. Normal o/w emulsions cream, while inverse w/o emulsions tend to settle. The sedimentation velocity is given by equation 1.7.⁹⁴ g is the gravitational constant.

$$v = \frac{1}{18\mu} D^2 \Delta\rho g \quad 1.7$$

Ostwald ripening

Ostwald ripening is the process where the large droplets grow at the expense of the smaller droplets and is one of the main reasons for emulsion instability. The driving force for Ostwald ripening is the difference in capillary pressure for small and large droplets, as described by the Young-La Place equation (eq. 1.8).⁶⁰

$$\Delta P = \frac{4\gamma_{ow}}{D} \quad 1.8$$

D is the droplet diameter. Ostwald ripening requires a finite solubility of the dispersed phase in the continuous phase, such that diffusion from the small to the larger droplets is possible. This process continues until one large droplet is left, unless this process is arrested. Normally, an additional compound is added to the droplet which is completely

insoluble in the continuous phase. The concentration of this compound in the droplets increases when Ostwald ripening takes place, creating an osmotic pressure that is able to counteract this process. For example, high salt concentrations in aqueous emulsion droplets are capable of doing this. Ostwald ripening increases the salt concentration in the small droplets, with respect to the large droplets, which correspondingly increases the osmotic pressure. Solid particles are also able to arrest Ostwald ripening, although through a different mechanism. The particles are irreversibly attached to the droplet due to the extremely high energy of particle detachment. The particle layer is compressed upon shrinking of the droplet. Continued shrinkage of the droplets deforms the menisci (inward bending of the fluid interface between the particles) and results in an opposed capillary pressure, which is capable of arresting Ostwald ripening. Instabilities due to Ostwald ripening have not been observed throughout this work, although water (dispersed phase) has a noticeable solubility in heptane (continuous phase). Ostwald ripening has not been particularly studied in the work described in this thesis, but is mentioned here nonetheless to provide a complete picture of the stability of Pickering emulsions.

1.2.2 Conclusion

In summary, all emulsions are in principle unstable and tend to macroscopically phase separate, which can occur through different mechanisms. Namely, flocculation, aggregation and/or sedimentation/creaming and followed by coalescence. A different mechanism that leads to phase separation, which does not require coalescence, is Ostwald ripening. The stabilizing particles in Pickering emulsion can arrest these processes and stop phase-separation leading to a meta-stable system. The high energy of detachment, capillary pressure and drainage provide an energy barrier for coalescence. The different models capture the main trends, but significantly overestimate the absolute coalescence stability. The general notion is that Pickering emulsions are extremely stable. However, experimental data does not support this hypothesis, when compared to conventional surfactant stabilized emulsions. In terms of colloidal stability, it can be concluded that particle-stabilized emulsions tend to flocculate. The reason for this behavior is the fundamental relation between wettability and colloidal stability through the stabilizing groups of the Pickering particles. Additional stabilization is desirable for the efficient synthesis of advanced materials in general and more specifically microcapsules. The stability against sedimentation/creaming is not unique to Pickering emulsions and is related to the density differences, droplet size and viscosity of the continuous phase. Pickering emulsions are

remarkably stable against Ostwald ripening, due to the irreversible attachment of particles to the w/o interface.

1.3 Outline of thesis

The stability of Pickering emulsions has been investigated with the ultimate aim of developing a novel and efficient micro-encapsulation technique for salt hydrates. Most systems proved sufficiently stable against coalescence. However, the colloidal stability of Pickering emulsions is limited and proved an important factor in the efficient synthesis of polymeric microcapsules. Chapter 2 deals with the structural characterization of Pickering emulsions in terms of the three-phase contact angle θ , the droplet diameter D and the structural organization of particles on the droplet surface. Chapter 3 describes the synthesis and characterization of colloidosomes with tunable particle packing. Different particle configurations are observed, ranging from incomplete surface coverages to a dense, almost crystalline particle packing. The assembly and organization of particles on the droplet surface is modeled theoretically. Chapter 4 demonstrates the efficient synthesis of polymer microcapsules from Pickering emulsions. Additional steric stabilization of Pickering emulsions is achieved by the adsorption of poly(styrene-*block*-(ethylene-*co*-propylene)). Chapter 5 relates the wettability and colloidal stability of sterically stabilized polymer particles. The presence of the steric stabilizer on the particle surface results in an activation barrier for interfacial adsorption and is also investigated. In chapter 6, the results of investigations upon the effect of the steric stabilizer on the formation of Pickering emulsions are reported. The effect on the rate of particle adsorption is especially studied. Finally, chapter 7 shows a novel method to micro-encapsulate $\text{CaCl}_2 \cdot 6\text{H}_2\text{O}$ and characterizes the thermal properties of the resulting material.

References

1. Farid, M. M.; Khudhair, A. M.; Razack, S. A. K.; Al-Hallaj, S., *Energy Conversion and Management* **2004**, 45, (9-10), 1597-1615.
2. Regin, A. F.; Solanki, S. C.; Saini, J. S., *Renewable & Sustainable Energy Reviews* **2008**, 12, (9), 2438-2458.
3. Sharma, A.; Tyagi, V. V.; Chen, C. R.; Buddhi, D., *Renewable & Sustainable Energy Reviews* **2009**, 13, (2), 318-345.
4. Zalba, B.; Marin, J. M.; Cabeza, L. F.; Mehling, H., *Applied Thermal Engineering* **2003**, 23, (3), 251-283.
5. Abhat, A., *Solar Energy* **1983**, 30, (4), 313-332.
6. Tyagi, V. V.; Buddhi, D., *Renewable & Sustainable Energy Reviews* **2007**, 11, (6), 1146-1166.
7. Zhu, N.; Ma, Z. J.; Wang, S. W., *Energy Conversion and Management* **2009**, 50, (12), 169-3181.
8. Raj, V. A. A.; Velraj, R., *Renewable & Sustainable Energy Reviews* **2010**, 14, (9), 2819-2829.
9. Inaba, H., *International Journal of Thermal Sciences* **2000**, 39, (9-11), 991-1003.
10. Yang, R.; Xu, H.; Zhang, Y. P., *Solar Energy Materials and Solar Cells* **2003**, 80, (4), 405-416.
11. Zhang, P.; Ma, Z. W.; Wang, R. Z., *Renewable & Sustainable Energy Reviews* **2010**, 14, (2), 598-614.
12. Mehling, H.; Cabeza, L. F., *Heat and cold storage with PCM*. Springer: Berlin, 2008.
13. <http://www.salcabv.nl/index.asp?CategorieID=5&Taal=EN>, **January 2011**.
14. http://energain.co.uk/Energain/en_GB/index.html, **January 2011**.
15. <http://www.phasechangepcm.com/>, **January 2011**.
16. <http://www.micronal.de/portal/basf/ide/dt.jsp?setCursor=1> 286688, **January 2011**.
17. Salari, J. W. O.; Reezigt, H.; Rouwers, B. W. M.; Glastra, H. COATED DISCRETE PARTICLE, METHOD FOR PREPARATION THEREOF, AND PRODUCT IN WHICH THIS PARTICLE IS APPLIED WO 2008/153378 A2
18. Jyothi, N. V. N.; Prasanna, P. M.; Sakarkar, S. N.; Prabha, K. S.; Ramaiah, P. S.; Srawan, G. Y., *Journal of Microencapsulation* **2010**, 27, (3), 187-197.
19. Yow, H. N.; Routh, A. F., *Soft Matter* **2006**, 2, (11), 940-949.
20. Ghosh, S. K., *Functional coatings : by polymer microencapsulation* Weinheim, 2006.
21. Chang, T. M. S., *Science* **1964**, 146, (364), 524-&.
22. Crespy, D.; Stark, M.; Hoffmann-Richter, C.; Ziener, U.; Landfester, K., *Macromolecules* **2007**, 40, (9), 3122-3135.
23. McIlroy, D. A.; Blaiszik, B. J.; Caruso, M. M.; White, S. R.; Moore, J. S.; Sottos, N. R., *Macromolecules* **2006**, 39, (4), 1855-1859.
24. Paiphansiri, U.; Tangboriboonrat, P.; Landfester, K., *Macromolecular Bioscience* **2006**, 6, (1), 33-40.
25. <http://www.appletonideas.com/>, **January 2011**.
26. Ramsden, W., *Proc. Roy. Soc.* **1903**, 72, 156.
27. Pickering, S. U., *J. Chem. Soc.* **1907**, 91, 2001-2021.
28. Finkle, P.; Draper, H. D.; Hildebrand, J. H., *Journal of the American Chemical Society* **1923**, 45, (12), 2780-2788.
29. Wiley, R. M., *Journal of Colloid Science* **1954**, 9, (5), 427-437.
30. Schulman, J. H.; Leja, J., *Trans. Far. Soc.* **1954**, 50, 598.
31. Velev, O. D.; Furusawa, K.; Nagayama, K., *Langmuir* **1996**, 12, (10), 2385-2391.
32. Velev, O. D.; Furusawa, K.; Nagayama, K., *Langmuir* **1996**, 12, (10), 2374-2384.
33. Velev, O. D.; Nagayama, K., *Langmuir* **1997**, 13, (6), 1856-1859.
34. Dinsmore, A. D.; Hsu, M. F.; Nikolaidis, M. G.; Marquez, M.; Bausch, A. R.; Weitz, D. A., *Science* **2002**, 298, (5595), 1006-1009.

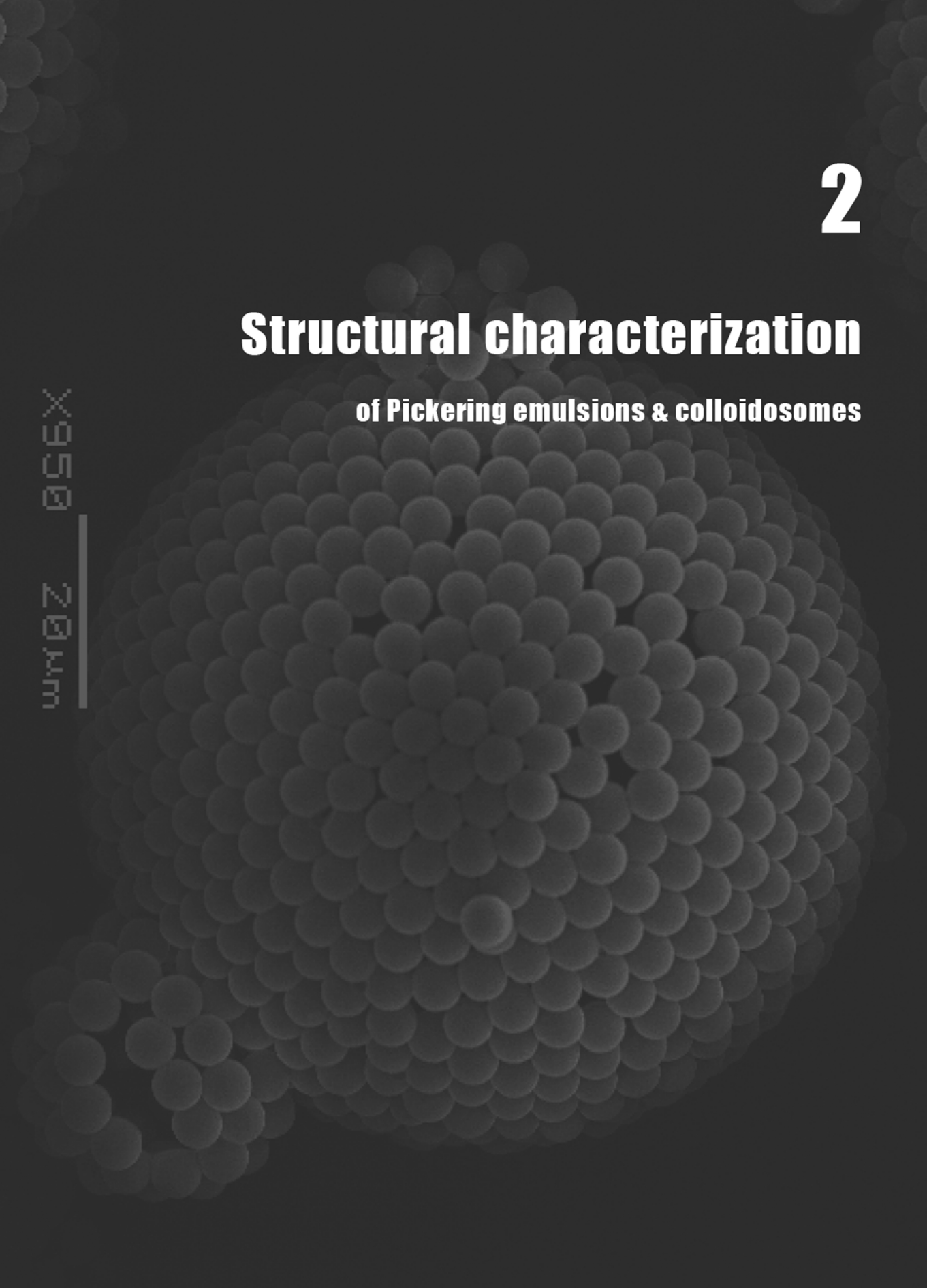
35. Hsu, M. F.; Nikolaidis, M. G.; Dinsmore, A. D.; Bausch, A. R.; Gordon, V. D.; Chen, X.; Hutchinson, J. W.; Weitz, D. A., *Langmuir* **2005**, 21, (7), 2963-2970.
36. Kim, J. W.; Fernandez-Nieves, A.; Dan, N.; Utada, A. S.; Marquez, M.; Weitz, D. A., *Nano Letters* **2007**, 7, (9), 2876-2880.
37. Lee, D.; Weitz, D. A., *Advanced Materials* **2008**, 20, (18), 3498-+.
38. Bon, S. A. F.; Cauvin, S.; Colver, P. J., *Soft Matter* **2007**, 3, (2), 194-199.
39. Bon, S. A. F.; Chen, T., *Langmuir* **2007**, 23, (19), 9527-9530.
40. Chen, T.; Colver, P. J.; Bon, S. A. F., *Advanced Materials* **2007**, 19, (17), 2286-+.
41. Colver, P. J.; Chen, T.; Bon, S. A. F., *Macromolecular symposia* **2006**, 245-246, 34-41.
42. Pieranski, P., *Physical Review Letters* **1980**, 45, (7), 569-572.
43. Young, T., *Phil. Trans.* **1805**, 95, 65-87.
44. Aveyard, R.; Clint, J. H.; Horozov, T. S., *Physical Chemistry Chemical Physics* **2003**, 5, (11), 2398-2409.
45. Kralchevsky, P. A.; Ivanov, I. B.; Ananthapadmanabhan, K. P.; Lips, A., *Langmuir* **2005**, 21, (1), 50-63.
46. Levine, S.; Bowen, B. D.; Partridge, S. J., *Colloids and Surfaces* **1989**, 38, (4), 325-343.
47. Dickinson, E., *Current Opinion in Colloid & Interface Science* **2010**, 15, (1-2), 40-49.
48. Rousseau, D.; Ghosh, S.; Park, H., *Journal of Food Science* **2009**, 74, (1), E1-E7.
49. Philipsen, H. J. A.; Oestreich, M.; Klumperman, B.; German, A. L., *Journal of Chromatography A* **1997**, 775, (1-2), 157-177.
50. Frelichowska, J.; Bolzinger, M. A.; Pelletier, J.; Valour, J. P.; Chevalier, Y., *International Journal of Pharmaceutics* **2009**, 371, (1-2), 56-63.
51. Colver, P. J.; Bon, S. A. F., *Chemistry of Materials* **2007**, 19, (7), 1537-1539.
52. Lawrence, D. B.; Cai, T.; Hu, Z.; Marquez, M.; Dinsmore, A. D., *Langmuir* **2007**, 23, (2), 395-398.
53. Croll, L. M.; Stover, H. D. H., *Langmuir* **2003**, 19, (14), 5918-5922.
54. Skaff, H.; Lin, Y.; Tangirala, R.; Breitenkamp, K.; Boker, A.; Russell, T. P.; Emrick, T., *Advanced Materials* **2005**, 17, (17), 2082-2086.
55. Walsh, A.; Thompson, K. L.; Armes, S. P.; York, D. W., *Langmuir* **2010**, 26, (23), 18039-18048.
56. Thompson, K. L.; Armes, S. P., *Chemical Communications* **2010**, 46, (29), 5274-5276.
57. Arnaudov, L. N.; Cayre, O. J.; Stuart, M. A. C.; Stoyanov, S. D.; Paunov, V. N., *Physical Chemistry Chemical Physics* **2010**, 12, (2), 328-331.
58. Laib, S.; Routh, A. F., *Journal of Colloid and Interface Science* **2008**, 317, (1), 121-129.
59. Nomura, T.; Routh, A. F., *Langmuir* **2010**, 26, (24), 18676-18680.
60. Atkins, P. W., *Physical chemistry*. Oxford University Press: Oxford, 1998.
61. Hunter, R. J., *Foundations of Colloid Science*. Oxford University Press: Oxford, 1989.
62. Kraft, D. J.; de Folter, J. W. J.; Luigjes, B.; Castillo, S. I. R.; Sacanna, S.; Philipse, A. P.; Kegel, W. K., *Journal of Physical Chemistry B* **2010**, 114, (32), 10347-10356.
63. Kraft, D. J.; Luigjes, B.; de Folter, J. W. J.; Philipse, A. P.; Kegel, W. K., *Journal of Physical Chemistry B* **2010**, 114, (38), 12257-12263.
64. Sacanna, S.; Kegel, W. K.; Philipse, A. P., *Physical Review Letters* **2007**, 98, (15).
65. Sacanna, S.; Kegel, W. K.; Philipse, A. P., *Langmuir* **2007**, 23, (21), 10486-10492.
66. Sacanna, S.; Philipse, A. P., *Advanced Materials* **2007**, 19, (22), 3824-+.
67. Binks, B. P.; Horozov, T. S., *Colloidal particles at liquid interfaces*. Cambridge University Press: 2006
68. Herk, A. M. v., *Chemistry and technology of emulsion polymerization*. Wiley-Blackwell: Oxford, 2005.
69. Denkov, N. D.; Ivanov, I. B.; Kralchevsky, P. A.; Wasan, D. T., *Journal of Colloid and Interface Science* **1992**, 150, (2), 589-593.
70. Kruglyakov, P. M.; Nushtayeva, A.; Vilkova, N. G., *Journal of Colloid and Interface Science* **2004**, 276, (2), 465-474.
71. Horozov, T. S.; Aveyard, R.; Clint, J. H.; Neumann, B., *Langmuir* **2005**, 21, (6), 2330-2341.

-
72. Tcholakova, S.; Denkov, N. D.; Lips, A., *Physical Chemistry Chemical Physics* **2008**, 10, (12), 1608-1627.
 73. Tambe, D. E.; Sharma, M. M., *Advances in Colloid and Interface Science* **1994**, 52, 1-63.
 74. Kaptay, G., *Colloids and Surfaces a-Physicochemical and Engineering Aspects* **2006**, 282, 387-401.
 75. Yan, N. X.; Gray, M. R.; Masliyah, J. H., *Colloids and Surfaces a-Physicochemical and Engineering Aspects* **2001**, 193, (1-3), 97-107.
 76. Bowick, M. J.; Nelson, D. R.; Shin, H., *Physical Chemistry Chemical Physics* **2007**, 9, (48), 6304-6312.
 77. Bowick, M. J.; Nelson, D. R.; Travesset, A., *Physical Review B* **2000**, 62, (13), 8738-8751.
 78. Jarrold, M. F., *Nature* **2000**, 407, (6800), 26-27.
 79. Liu, A. J.; Nagel, S. R., *Nature* **1998**, 396, (6706), 21-22.
 80. Trappe, V.; Prasad, V.; Cipelletti, L.; Segre, P. N.; Weitz, D. A., *Nature* **2001**, 411, (6839), 772-775.
 81. Binks, B. P.; Kirkland, M., *Physical Chemistry Chemical Physics* **2002**, 4, (15), 3727-3733.
 82. Gautier, F.; Destribats, M.; Perrier-Cornet, R.; Dechezelles, J. F.; Giernanska, J.; Heroguez, V.; Ravaine, S.; Leal-Calderon, F.; Schmitt, V., *Physical Chemistry Chemical Physics* **2007**, 9, (48), 6455-6462.
 83. Horozov, T. S.; Binks, B. P., *Angewandte Chemie-International Edition* **2006**, 45, (5), 773-776.
 84. Midmore, B. R., *Colloids and Surfaces a-Physicochemical and Engineering Aspects* **1998**, 132, (2-3), 257-265.
 85. Jiang, S.; Granick, S., *Langmuir* **2008**, 24, (6), 2438-2445.
 86. Hunter, T. N.; Pugh, R. J.; Franks, G. V.; Jameson, G. J., *Advances in Colloid and Interface Science* **2008**, 137, (2), 57-81.
 87. Leunissen, M. E.; van Blaaderen, A.; Hollingsworth, A. D.; Sullivan, M. T.; Chaikin, P. M., *Proceedings of the National Academy of Sciences of the United States of America* **2007**, 104, (8), 2585-2590.
 88. Stancik, E. J.; Fuller, G. G., *Langmuir* **2004**, 20, (12), 4805-4808.
 89. Benkoski, J. J.; Hu, H.; Karim, A., *Macromolecular Rapid Communications* **2006**, 27, (15), 1212-1216.
 90. Klein, S. M.; Manoharan, V. N.; Pine, D. J.; Lange, F. F., *Langmuir* **2005**, 21, (15), 6669-6674.
 91. Marinova, K. G.; Alargova, R. G.; Denkov, N. D.; Veleev, O. D.; Petsev, D. N.; Ivanov, I. B.; Borwankar, R. P., *Langmuir* **1996**, 12, (8), 2045-2051.
 92. Hsu, M. F.; Dufresne, E. R.; Weitz, D. A., *Langmuir* **2005**, 21, (11), 4881-4887.
 93. Bon, S. A. F.; Colver, P. J., *Langmuir* **2007**, 23, (16), 8316-8322.
 94. Bird, R. B.; Stewart, W. E., *Transport Phenomena*. John Wiley & Sons: New York, 2007.

Structural characterization

of Pickering emulsions & colloidosomes

X950 20 μm

A scanning electron micrograph (SEM) showing a large, roughly spherical droplet composed of many smaller, uniform spherical particles (nanoparticles) packed together. The droplet is surrounded by a smaller, less dense cluster of similar particles. The background is dark. A scale bar is visible on the left side of the image.

Abstract: In this chapter we demonstrate how structural information of Pickering emulsions and colloidosomes can be derived from light and scanning electron microscopy (SEM) images. The described methods are used extensively throughout this thesis. Important parameters for the structure of colloidosomes are the three-phase contact angle θ , the droplet diameter D , as well as the structural organization of particles on the droplet surface, the main property that constitutes the structure of the colloidosome. In particular, we show how the 3-dimensional structural arrangement of particles in a colloidosome is derived from a single scanning electron microscopy (SEM) image. We exploit the fact that particles are located on the surface of a sphere to directly quantify the 3-dimensional positions of all particles from a single 2-dimensional SEM image. These 3-dimensional particle positions are then used to quantify the structural arrangement of the particles by performing both a Delaunay triangulation (DT) as well as a Voronoi tessellation (VT) of the colloidosome surface, which we use to validate the procedure for determining the 3-dimensional particle positions. In addition to the DT and the VT, we calculate the radial pair correlation function $g(r)$. We explain how the pair correlation function is modified to suit a spherical surface and how the structural order relates to similar data on colloidal films. Our results illustrate that even for a colloidosome in its ground state, the resulting ordering is short-ranged (in our case 4 particle diameters), which is in contrast to densely packed colloidal films.

Part of this chapter is published in: **Soft Matter**, 2011, 7, 2033

2.1 Introduction

Colloidosomes are, as originally defined by Dinsmore *et al.* in 2002,¹ selectively permeable capsules composed of colloidal particles. The intrinsic porosity of colloidosomes can potentially be used for targeted delivery and controlled release of, for example, drugs.² Due to the high energy of desorption of particles from soft interfaces, colloidosomes are surprisingly stable structures. By reinforcing the interactions between particles it is even possible to dry colloidosomes without the collapse or buckling of the structure, which can be exploited for the synthesis of new materials.³⁻⁵ Recently, the particle packing and the defects arising from packing particles on a curved surface have raised significant interest.⁶⁻⁸ On a flat surface, equally sized spherical particles can efficiently pack in a hexagonal lattice, while on a sphere, obligatory defects are introduced.^{7, 9} According to Euler's theorem, the total disclination charge, which is the departure of the coordination number on a planar surface of 6, of any triangulation on a sphere must be 12. Soccer balls and C₆₀ fullerenes are typical examples of this phenomenon.¹⁰ They have 12 pentagonal patches and 20 hexagonal patches. As the number of particles on the sphere increases additional dislocations are introduced, which consist of pairs of 5-7 defects. They still obey Euler's theorem because their net disclination charge is zero. Chains of 5 - 7 dislocations, so-called grain-boundary scars, are formed when the system size ($D/4R$) exceeds approximately the critical value of 5. D is the diameter of the colloidosome and R is the particle radius. Grain-boundary scars, a result of the curvature, are not found in flat colloidal films and/or bulk assemblies and are therefore interesting phenomena by themselves. Moreover, emulsion droplets packed with colloidal particles serve as an experimental model for general theories on particle configurations with arbitrary repulsive interactions on curved surfaces (*e.g.* J.J. Thomson problem⁹ or the generalized form, which is called the Tammes problem¹¹).

Past research has mainly focussed on studying colloidosomes with a high surface coverage of particles, which as a consequence are locally highly ordered. These locally crystalline particle packings only form if the particles can interact repulsively and thus are able to achieve their energetic minimum.⁶ In theory, attractive particles can pack in a similar fashion. However, they generally do not reach their equilibrium configurations. The assembly of attractive colloids is generally kinetically determined and leads to jammed, out-of-equilibrium states. Systematic studies of the type and magnitude of particle interaction on the assembly of particles at a particular interface revealed many other particle configurations; examples of this are colloidal glasses or gels.¹² Occasionally, colloidosomes with a non-crystalline packing are found in the literature,^{8, 13-17} Fortuna *et al*⁸ studied the

assembly of polydisperse particles, which obviously resulted in a non-crystalline packing, and quantified it by the particle coordination numbers and the pair-distribution function. Moreover, the 3D structure of a variety of submicron systems has been reconstructed with Monte Carlo simulations. However, besides the work of Fortuna, systematic studies and a thorough structural characterization have been lacking. S. Jiang for example observed a transition from a low-density, disordered packing to a crystalline packing depending on the contact angle of the particles,¹⁸ but did not quantify this transition. Indeed in most studies the structure of the particles is characterized ‘qualitatively’, by presenting the electron- or light-microscopy images. The principal aim of this paper is, therefore, to demonstrate how those same images can be used to construct a 3D representation of a colloidosome in order to quantitatively characterize the particle configuration.

In the introductory chapter it is explained that the structural properties of the particle layer that surrounds the droplet affects the coalescence stability. Theoretical models that predict the stability, based on the energy of detachment or the capillary pressure, systematically overestimate the stability of Pickering emulsions with respect to coalescence. One of the reasons for this could be the inhomogeneity in the particle layers, which lowers the coalescence stability with respect to theoretically predicted values for regular, dense particle configurations. At the same time, incomplete surface coverages also affect the coalescence stability of Pickering emulsions. Thus, detailed information on the structural properties of the particle layer is highly relevant for more accurate predictions of the stability of Pickering emulsions. The parameters that are measured here are θ , the droplet diameter and the structural organization of particles on the droplet surface.

2.2 Structural characterization

2.2.1 Three-phase contact angle, θ

The three-phase contact angle θ is of obvious relevance for Pickering emulsions. However, it proved difficult to directly measure θ of particles at liquid interfaces. Recent developments report a generic technique to image and study the wettability of spherical particles at liquid interfaces.¹⁹⁻²¹ This technique traps the particles by gelling one of the two liquids. The gel with the trapped particles is subsequently imaged with either SEM or AFM. Here, a different method is used that exploits the deformation of the particles as they are heated to temperatures above their glass-transition. Sintering is required to reinforce the interactions between the particles on the droplet surface and obtain stable capsules. It was

observed that during this process the particles deform, resulting in a reduction of the particle-water contact area, as seen in figure 2.1. This deformation process is driven by surface tension, and we can thus estimate θ .

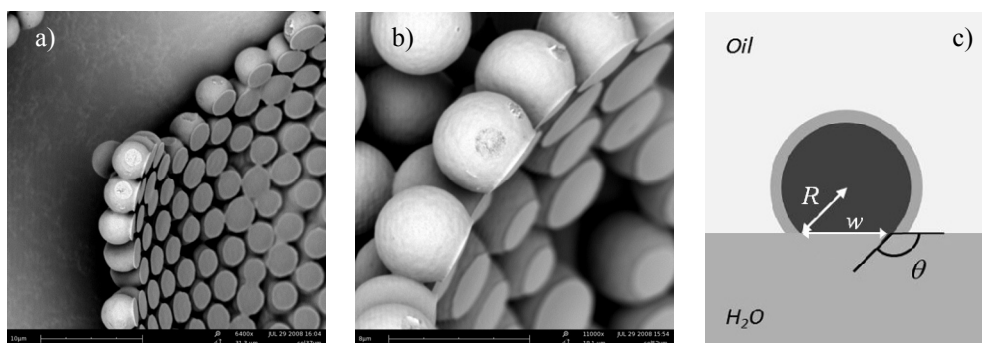


Figure 2.1 Deformation of polymer particles at the droplet surface, due to heating above the glass-transition temperature. *a, b*) SEM images of a side-view of the particle layer that is part of a colloidosome. *c*) Schematic representation of the deformation and the relevant distances (R and w) that are required for the calculation of θ .

The observed deformation allows an estimation of θ . The idealized deformation is schematically represented in figure 2.1. It is assumed that the particle is located at the same position, before and after the deformation. From the SEM image both R and w can be determined, which leads to θ by

$$\sin \theta = \frac{w}{2R} \quad 2.1$$

In this particular case, this leads to a $\theta \approx 130^\circ$. The colloidosome is composed of polystyrene (pS) particles. The synthetic details of the particle synthesis and the colloidosome formation are given in the following chapter 3. A wide range of values for θ for pS particles at alkane/water interfaces have been reported ($90^\circ < \theta < 130^\circ$).¹⁹⁻²² The large difference in wettability of polystyrene particles is caused by the different type and concentrations of stabilizing groups on the particle surface. The experimentally observed θ suggests very hydrophobic particles and a low concentration of stabilizing groups.

It must be mentioned that the observed θ is merely an indication, because of the experimental error in determining w and R from the SEM image. The schematic representation in figure 2.1 does not accurately represent the deformation, which also leads to a widening of the particle body. The time of heating above the glass transition is limited. Prolonged heating can lead to spreading of the particle over the droplet surface, to minimize the oil/water interfacial area. Nevertheless, the measured θ does provide a useful indication of the wettability of the particles.

2.2.2 Droplet diameter, D

Not only Pickering emulsions, but basically any emulsion is characterized by the droplet diameter distribution. This distribution of droplet sizes also provides information on the total available interface between the oil and the water phase, which in turn determines the maximum number of particles that can be located at the surface of the colloidosomes. In practice, the average droplet diameter can often be estimated directly from the assumption that all available particles are densely covering the w/o interface. In this case, the number of particles N_A attached to the w/o interface depends on the droplet diameter D as

$$D = \frac{6V_D}{N_A \cdot 2\sqrt{3} \cdot R^2} \quad 2.2$$

where V_D is the total volume of the dispersed phase.²³ The area A_p that a particle occupies in a hexagonally close-packed structure is $A_p = 2\sqrt{3}R^2$ in which R is the radius of the particle. In this calculation it is assumed that the particles densely pack in a hexagonal close-packing and that curvature effects can be neglected. Throughout this thesis all experiments and Pickering emulsions are designed in such a way that, in the case that all the particles are adsorbed to the w/o interface, 50 μm droplets are obtained. Deviation from this reference value directly identifies differences in the adsorption behavior. For example, an average droplet diameter $D > 50 \mu\text{m}$ indicates that particle adsorption is incomplete. Smaller droplets $D < 50 \mu\text{m}$ demonstrates a difference in the particle packing on the droplet surface, because each particle occupies a larger surface area.

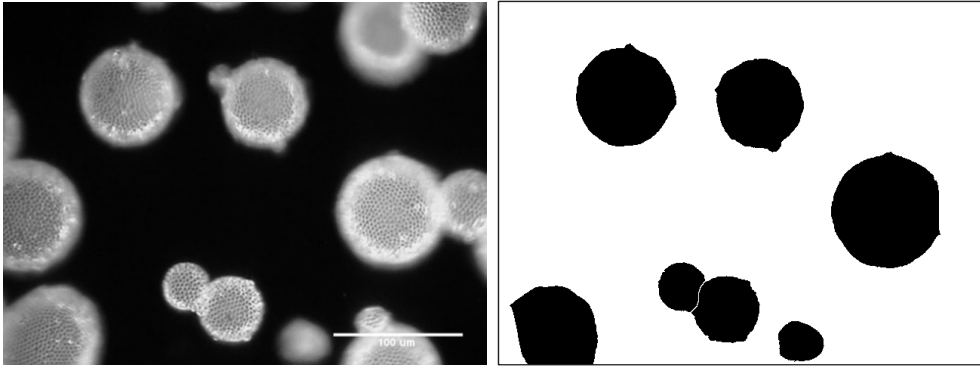


Figure 2.2 Typical light microscopy image (*left*) and mask (*right*) of a Pickering emulsion. The right image is the modified image (mask) from which the droplet diameter is derived.

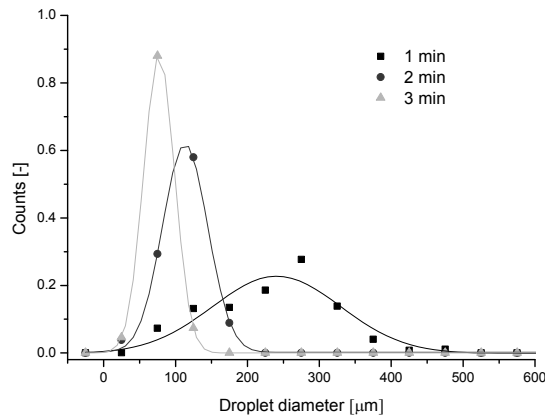


Figure 2.3 Example of the evolution of droplet diameter distributions during emulsification. This example is taken from chapter 6 (fig. 6.8).

The droplet diameter can be derived from light microscopy (LM) and SEM images. A typical LM image is shown in figure 2.2 (left). The image is optimized with the image processing software ImageJ to yield a black and white mask (right). Often the droplets overlap and need to be separated for an accurate analysis of the droplet diameter. A watershed algorithm is used for this purpose. The size-range and circularity are used as criteria to make a representative selection of the droplets. The software ultimately determines the area of each black area, corresponding to a droplet, in the image. Figure 2.3

shows an example from chapter 6 that uses the droplet diameter distributions to determine the rate of particle adsorption during emulsification. It shows a convention emulsification regime, in which the water phase is gradually broken up into smaller droplets. As a matter of fact, the particle diameter is determined in a similar manner as the droplet diameter. The diameter distributions are a histogram of the actual diameters that are counted in the pictures. Moreover, the distributions are often normalized with respect to the peak height or total number of particles. Various averages, such as number or volume average diameter, can be derived from the distributions and are specified where needed.

2.2.3 Structural organization of particles

For the characterization of highly ordered colloidosomes of monodisperse particles, a useful measure of local order is provided by the identification of 5-, 6- and 7-fold coordinated particles by performing a Delaunay triangulation (DT).^{7, 24} However, for non-crystalline systems in a jammed state, alternative ways to structurally characterize particle packings are needed. Therefore, the second aim of this chapter is to provide a short overview of techniques to structurally characterize various particle configurations. The 3D coordinates of the particles have to be known to characterize of any particle configurations, which can be achieved for instance by using laser scanning confocal microscopy (LSCM).⁷ With LSCM the positions of the particles are determined by scanning the colloidosome at different heights and by combining these different images in order to construct a 3D representation.

In this chapter we demonstrate how to construct a 3D representation of a colloidosome based on a single scanning electron microscope (SEM) image. The described procedure is not strictly limited to SEM images. Conventional light microscope images can also be used for this purpose. The first step to obtain the 3D coordinates is to determine the two dimensional (2D) x,y -coordinates of the particles, which is subtracted from the planar SEM image. It is assumed that the colloidosome is perfectly spherical. As a consequence, the corresponding height z of each particle can be directly calculated as follows

$$z_p = \sqrt{D^2 / 4 - p^2}$$

2.3

where p is the planar centre-to-centre distance of the particle to the central axis of the colloidosome and D is the colloidosome diameter, as shown schematically in figure 2.4. p is obtained in a similar manner as z_p . Imagine that x_c, y_c are the planar coordinates of the central axis of the colloidosome and x_p, y_p are the coordinates of a particle, then p is obtained as follows

$$p = \sqrt{(x_p - x_c)^2 + (y_p - y_c)^2} \quad 2.4$$

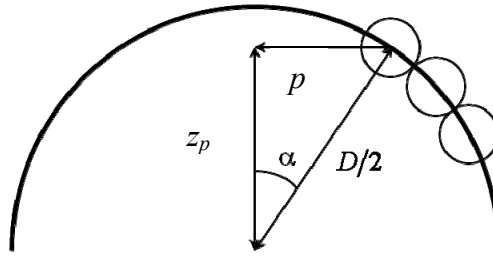


Figure 2.4 Schematic representation how to calculate the height z of each particle on the droplet surface. z is calculated based on the radius ($D/2$) of the colloidosome and the planar distance (p) from the central axis of the colloidosome (eq. 2.3). α is the inclination angle of a particle with respect to the central axis.

For particles close to the edge of the colloidosome the accuracy of the particle positions decreases, because any error in the x - y -position translates to an increasingly larger error in the z -direction. The accuracy of this method is therefore tested by comparing the structural information derived from the DT and the Voronoi tessellation (VT) with the particle diameter. Based on this analysis, a selection of particles is made that accurately represent the particle arrangement of the colloidosome. Various measures for the structural characterization of the particle packing are derived from this selection and subsequently discussed. DT is a method to identify neighboring particles for each particle, which reveals defects (5- & 7-coordinated particles) and the appearance of grain boundary scars. From the triangulation one can also determine the fraction of defects, the interparticle distance and the nearest neighbor angle distribution. A VT also yields information on the neighboring particles, but additionally gives structural information on the area occupied per particle and

the total surface coverage. A combination of the DT and VT has been applied by Sastry to determine the volume, area and connectivity of pores in particle assemblies.²⁵ This method has not been applied to colloidosomes, but is certainly a possibility once the positions of the particles are known. A common technique to characterize structural order is the radial pair correlation function or pair-distribution function $g(r)$, which describes the variation in particle density as a function of the separation distance. Grier and Murray as well as Hansen *et al*, showed how the degree of order in colloidal films can be characterized by the pair-correlation function.^{24, 26} Fortuna *et al*⁸ determined the pair-correlation function from Monte Carlo simulations and compared links between 5-,7-dislocations and 4-, 8-dislocations. Based on the 3D structural information obtained from a single SEM image, in this chapter we will use these different methods to characterize the structure of a colloidosome.

Construction of a 3D image

The SEM image (fig. 2.5) of a highly ordered colloidosome is used to illustrate how to derive the three-dimensional particle coordinates from one single SEM image of a colloidosome. The synthetic details of the colloidosome are discussed in chapter 3 and are only briefly explained here. The particles are synthesized by the dispersion polymerization of styrene in ethanol.²⁷ Secondly, the particles are washed 3 times with clean ethanol to remove excess stabilizer and/or other contaminants, separated from the ethanol and finally re-dispersed in heptane. Water is added to the particle dispersion in heptane while shearing (10.000 rpm) with a rotor-stator mixer, until all the particles are adsorbed to the w/o interface. The Pickering emulsion is then heated above the glass-transition temperature of polystyrene to partly fuse the particles and obtain stable colloidosomes.

The SEM image in figure 2.5 shows that the majority of the particles are packed in a hexagonal close-packing. 5- and 7-coordinated particles are also found, which is expected for colloidosomes with system size, $D/4R$, exceeding the critical value of approximately 5.⁹ In this particular case ($D/4R = 83.3/4 \cdot 2.6 = 7.90$) the theoretical number of excess dislocations per scar is 3.24,⁶ which is consistent with the grain boundary scars found in figure 2.5. Defects are considered to be part of the same scar if they are within 2 separations of the Delaunay triangulated network. This particular SEM image is used to demonstrate the procedure, because the particle configuration is known from the above-mentioned studies and is therefore used for validation.

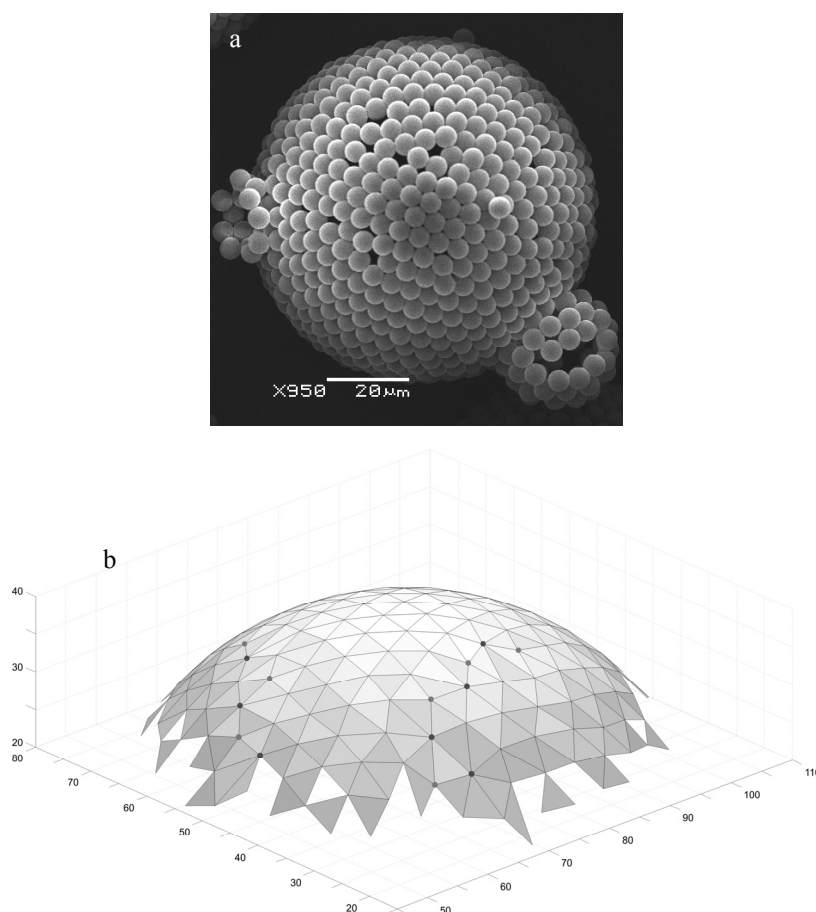


Figure 2.5 3D reconstruction of a colloidosome. **a)** SEM image of colloidosome that is used to construct a 3D representation. **b)** A 3D representation of the Delaunay triangulated network structure of the colloidosome. The 3D reconstruction is a selection of the top half of triangles that accurately represent the structure of the colloidosome. The particles are located on the vertices of this triangulated network. The dots denote pentagonal- (light gray) and heptagonal-coordinated (dark gray) particles, respectively. The x , y and z -axes are scaled in micrometers.

In most cases the images are unevenly lighted or otherwise difficult to process, therefore, to obtain accurate positional data the particles are manually overlaid with a circle. Finally, the centre of each of these circles in the image is determined, which returns the 2D coordinates of all the particles. Some loose particles that are not a part of the main colloidosome, as can be seen in fig. 2.5b, are omitted from the analysis. The second step is to determine the

center and radius of the colloidosome. The same protocol, as described above, is used to determine the center of the colloidosome. A single circle is overlaid with the colloidosome. This yields the apparent radius ($D/2 + R$) of the colloidosome, where R is the radius of the colloidal particles. Now, the planar distance p and the corresponding height $z_p = \sqrt{D^2/4 - p^2}$ is determined for each particle (fig. 2.4). If a particle is located at the center of the colloidosome, the planar distance is 0 and the height equals the radius. On the other hand, if a particle is located at the edge of the colloidosome, the distance equals R and the corresponding height is 0. It is important to note that it is assumed that the colloidosomes are perfectly spherical, which is plausible considering the synthetic procedure and the overview of a large collection of spherical structures in the SEM image (fig 3.5c).

Validation & Characterization

To demonstrate and validate the geometrical procedure to determine 3D particle positions we use the SEM image shown in figure 2.5b as a reference. Any error made in determining the x_p , y_p positions will directly lead to an error in the calculated z -coordinate. As $z_p = \sqrt{D^2/4 - p^2}$, the error made in z_p increases with increasing distance p from the center of the image as

$$\frac{\Delta z_p}{z_p} = \frac{\Delta D \cdot D + \Delta p \cdot p}{D^2 - p^2} \quad 2.5$$

Thus, for particles close to the edge of the colloidosome small errors in the x , y -coordinates that propagate in p result in large errors in the calculated z -coordinate. Additionally, it can be seen in figure 2.5b that it becomes increasingly difficult to determine the position of the particles that are located at the edge of the colloidosome, because they are only partly visible. For these reasons not all the particles that are visible in the SEM image can be located with adequate accuracy. Therefore, an error analysis is performed and the accuracy of the determined positions is tested by directly comparing the structural information derived from the DT and the VT with the particle diameter. The DT allows the calculation of the minimum interparticle distance between neighboring particles, which should reflect the particle diameter. The area occupied per particle and the total surface coverage can be calculated from the VT, which is also related to the particle diameter and should closely resemble that of a hexagonal close-packing.

A *Delaunay triangulation* (DT) is performed to obtain the number of nearest-neighbors of each particle in the colloidosome. The triangulation algorithm is performed on the 2D coordinates and, subsequently, the vertices of the triangulated network are given a certain height in order to construct the 3D triangulated network (fig. 2.5c). The DT data is used to directly test the validity of the 3D particle positions and to decide which part of the 3D image represents the actual structure of the colloidosome. To do so, the interparticle distances are compared with the particle diameter distribution, which is obtained from a separate SEM image of the particles. Moreover, the interparticle distances and their standard deviation are given as a function of the particle position on the surface of the droplet (fig 2.6), which is given the inclination angle α between the particle and the central axis (fig. 2.4). α ranges from 0° to 90° for particles that are, respectively, located at the top or the edge of the hemisphere. The standard deviation is calculated from the distances between the considered particle and its neighbors.

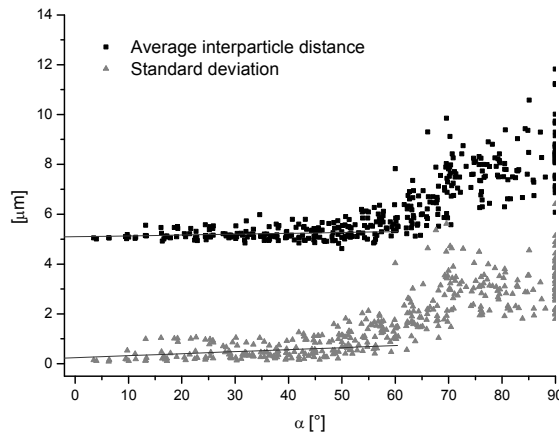


Figure 2.6 The average interparticle distances and standard deviation as a function of position on the colloidosome. The position is represented by the inclination angle α that a particle makes from the central axis.

The graph in figure 2.6 clearly shows two distinct regimes in the particle packing. Near the top of the hemisphere ($0^\circ < \alpha < 45^\circ$) the interparticle distances and standard deviation is rather constant with only minor variation, but particles located at the edge ($45^\circ < \alpha < 90^\circ$) show considerably more variation. The linear fits in figure 2.6 show that on average the

interparticle distance and standard deviation increases slightly with α , while the particle packing should be uniform over the entire colloidosome surface. The reason for this is that the experimental error in the z_p -coordinate of particle position increases with an increasing α , which can be understood by looking at figure 2.4. Any experimental error that is made in determining the x , y - coordinates of each particle propagates in p . Upon mapping the particles onto the sphere, the error in determining the height (Δz_p) propagates with p according to equation 2.4. The error in z can be represented as a function of α (fig 2.7), since α depends on p according to $p = \frac{D}{2} \sin \alpha$. The absolute error in z is unknown. However, the relative error $\Delta z_p / \Delta D$ yields valuable information, because ΔD is the minimal experimental error in determining the particle positions. Figure 2.7 should be considered an illustration and explanation of the observed behavior that is seen in figure 2.6. The increasing error in the particle's position leads to a false representation of the interparticle distances and variation within these values at the edges of the hemisphere ($70^\circ < \alpha < 90^\circ$).

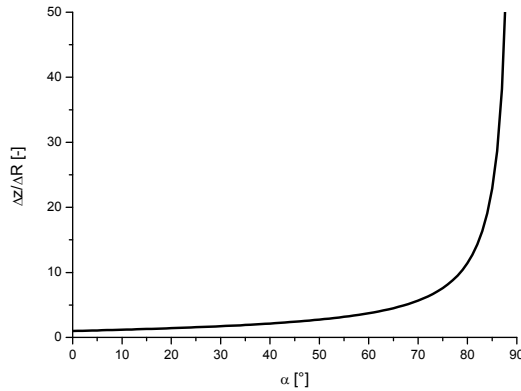


Figure 2.7 The normalized error in the z_p -coordinate, $\Delta z_p / \Delta D$, of the particle's coordinates as a function of the inclination angle α . The actual errors in determining the particle position are unknown. However, the error in z_p scales with d and α according to the graph above.

It can be concluded that the data obtained at the edge of the colloidosome deviates from the data obtained near the top and, therefore, the former does not represent the actual structure of the colloidosome. The reason for the deviation in the second regime is the poor determination of the particle's position. Towards the edges, the particles start to overlap

with each other considerably on the 2D image and are, therefore, only partly visible. Another reason, is that the experimental error in determining x,y -coordinates propagates in z_p according to equation 2.6. The particles at the edge of the image should thus be omitted from the analysis, as their position cannot be determined with sufficient accuracy.⁶

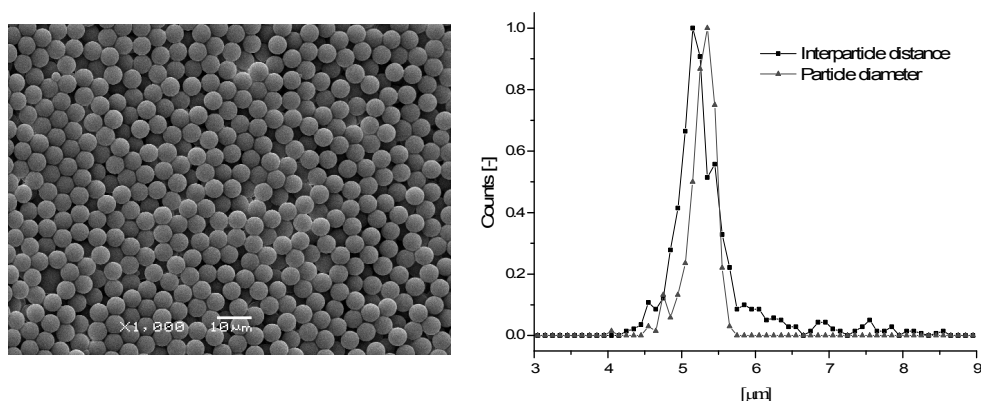


Figure 2.8 The interparticle distances between the nearest-neighbors, as determined from the DT, compared with the particle diameter distribution (graph). SEM image (right) of the polystyrene particles that were used to synthesize the colloidosome.

A comparison of the inter-particle distances and the particle diameter gives more information on the accuracy and validity of the developed method. Both the inter-particle and the particle diameter distribution are shown in figure 2.8. It is expected that a distribution of distances is found, due to the error in determining the particle's position. Furthermore, although the particles are seemingly uniform, a small variation in particle size leads to a distribution in the interparticle distances. It is found that the majority of the distances, however, match the particle diameter, because the particles are in close contact with each other. Additionally, it can be seen that significantly larger interparticle distances are found in comparison with the particle diameter, which can be ascribed to the obligatory coordination defects (5- & 7-coordinated particles). Jammed states will even further increase the interparticle distances, as can be clearly seen in figure 2.5. Surprisingly, it can be seen that the interparticle distance distribution in figure 2.8 is shifted to lower values with respect to the particle diameters. A possible explanation could be that upon heating and fusion (sintering) the polymer particles partly overlap and therefore are closer than expected. Moreover, the particles could be located outside of the adhesion plane, due to

jamming. Nonetheless, it can be concluded that the inter-particle distance is consistent with the particle diameter and that the selection of the data points gives a representative measure of the particle packing within the colloidosome.

Now that the position of all the particles is known and a reliable selection of the data has been made, we can further characterize the particle packing using other structural measures. For illustration, only the data from the SEM image in figure 2.5 is used. As mentioned earlier, the length of the grain boundary scars matches the expectation for this particular system size. In addition, one can also count the total number of 5- and 7-coordinated particles relative to 6-coordinated particles (fig. 2.8). Fortuna *et al* used this method to characterize the packing patterns of armored particles⁸ and found that with increasing polydispersity the fraction of 6-coordinated particles decreased and the number of defects increased. Their simulation of the packing density for an equilibrated armored sphere composed of monodisperse particles is consistent with the values in the histogram in figure 2.9. Another method that can describe the particle packing is the nearest-neighbor angle distribution. Kraft *et al.* already showed the nearest-neighbor angle distribution derived from the 2D projection of a colloidosome.²⁸ It clearly showed 6 peaks with a peak separation of $60 \pm 3.6^\circ$, which indicates a triangular lattice. She based her analysis on the 2D projection and didn't correct for the curvature of the colloidosome. Normally, the angle is measured between the lines connecting two particles in a triangulated network and an arbitrary reference line. However, it is not possible to define a suitable reference line and calculate the angle in a three-dimensional system. Therefore, a different approach has been taken, similar to the work of R.P.A. Dullens.²⁹ He performed a DT on colloidal films, to determine the nearest-neighbors for each particle, and calculated the angles of each triangle in the DT network and plotted the histogram of the angle distribution. He used the full-width-half-maximum (fwhm) to quantify the difference in packing of spherical and polyhedral particles, respectively an ordered and disordered packing. This approach has been used with the 3D triangulated network and the result is shown in figure 2.9. Although the colloidosome is spherical each triangle in the network is planar, which allowed the determination of the angles. The average angle is exactly 60° , which is expected for any set of triangles and the width of the distribution, characterized by the FWHM (full width at half maximum), is approximately 9° . The FWHM found here is higher than by Dullens of a perfect triangular lattice, which could be ascribed to the systematic error in determining the particle position, as described above, which is not present in planar systems. And more importantly, the FWHM is also increased compared to planar packings due to the obligatory

defects that arise by packing particles on a sphere. The fact that these structural parameters are in agreement with previous studies further confirms the validity of constructing the 3D representation from a single microscopy image.

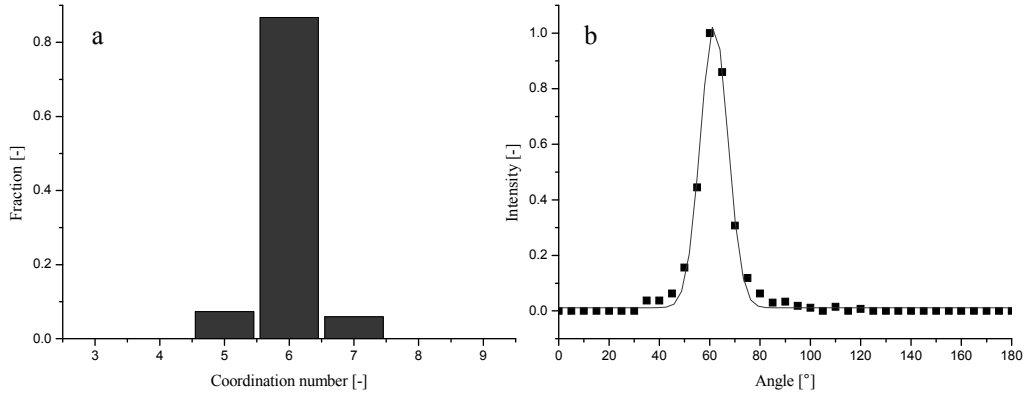


Figure 2.9 Structural information. a) Histogram of the particle coordination number and b) the nearest-neighbor angle distribution of the colloidosome in figure 2.5.

The *Voronoi tessellation* is a complementary technique to the DT that is used to structurally characterize particle configurations.^{28, 30} It is normally used to identify coordination defects, which can also be seen in figure 2.10, but can also be used for other purposes. The VT gives additional information on the area occupied per particle and the total surface coverage, which is related to the particle diameter. The VT can therefore be used to validate the described procedure in a similar manner as is done with the DT. The 3D Voronoi plot (fig. 2.10) is constructed, in the first place, by performing a VT on the 2D (x_p , y_p) coordinates. And secondly, a height is given to the vertices of the VT by $z_p = \sqrt{D^2/4 - p^2}$, wherein p is, in this case, the planar distance of the vertices to the center of the colloidosome. An overlay of the 3D VT and the original SEM image can be seen in figure 1.5.

The area that each particle occupies can be calculated from figure 2.10. The average values and the standard deviation are calculated in a similar manner as was done for the interparticle distances. The average area and standard deviation occupied per particle is calculated from the values of the considered particle and its neighboring particles. The resulting data is given as a function of the particle's position to judge which part of the particle configuration is suitable for further analysis (fig 2.11). Similar to results from the

DT (fig 2.6), two distinct regimes of particle packing are found. At the center of the colloidosome ($0^\circ < \alpha < 45^\circ$), the values for the area per particle remain relatively constant with minor variation, while the values deviate towards the edges ($45^\circ < \alpha < 90^\circ$). Although, it seems that from $0^\circ < \alpha < 45^\circ$ the values are relatively constant, a slight increase in the surface area with an increasing α is observed. The same explanation as for the DT accounts for this behavior, which is the error in determining the particle's position, especially the z_p -coordinate, which increases with an increasing α .

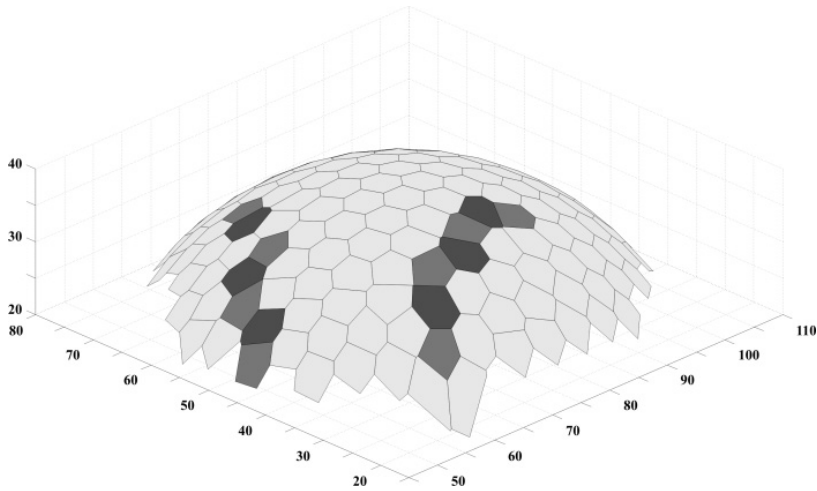


Figure 2.10 3D representation of the Voronoi tessellation of the colloidosome. The particles are located at the centers of the polygons. The light-gray and dark-gray polygons denote pentagonal- and heptagonal-coordinated particles, respectively. The axes are scaled in micrometers.

The same can be concluded from the VT that it becomes increasingly difficult to distinguish each particle towards the edges ($45^\circ < \alpha < 90^\circ$), because the particles start to overlap. At the edge of the colloidosome the VT does not represent the actual structure of the colloidosome. The VT therefore confirms that a selection of approximately half the particles is necessary to accurately characterize the particle packing.

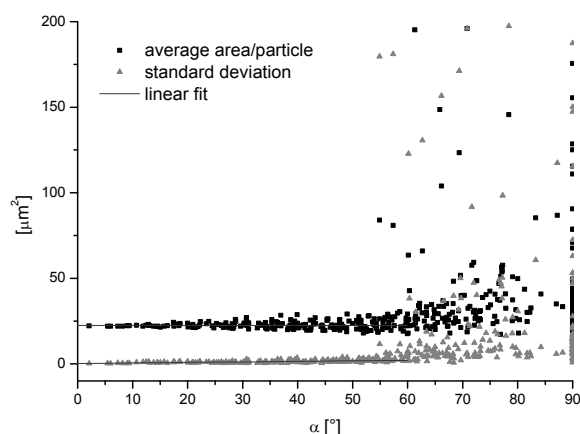


Figure 2.11 The average area per particle and the standard deviation as a function the particle's position, α . Towards the edges of the hemisphere ($45^\circ < \alpha < 90^\circ$) the accuracy in determining the particle position decreases.

The surface areas from the VT can be related to the particle diameter to assess whether reliable data on the particle packing can be obtained. Assuming that the curvature of the colloidosome can be neglected and that one particle occupies an area of πR^2 , yields an average surface coverage of 0.89, which is in reasonable agreement with the maximum surface coverage of 0.907 for hexagonally close-packed particles. The obtained value for the surface coverage is slightly lower, which is probably due to the obligatory defects that occur by packing monodisperse particles on a curved object. Therefore, it can be concluded that the area occupied per particle is consistent with the particle diameter and that a selection of the data points is representative for the actual structure of the colloidosome. Not only the total surface coverage but also the distribution in the area occupied per particle (fig. 2.12) can be used as a measure for the particle packing. The distribution does show a normal distribution. However, higher values are also found, which can be explained by the appearance of 5- and 7-coordinated particles. The main peak position ($23.56 \mu\text{m}^2$) of the graph in figure 2.12 is lower than the average value and yields a surface coverage of 0.92. This surface coverage is determined by dividing the area that a particle occupies (πR^2) by the value of the main peak position. A similar observation was found for the particle size (fig 2.8). Either, due to partly fusing the particles they overlap and occupy less area. Or, due to the curvature the particles can pack denser than initially is expected for hexagonally packed particles in a plane, which is illustrated in figure 2.12.

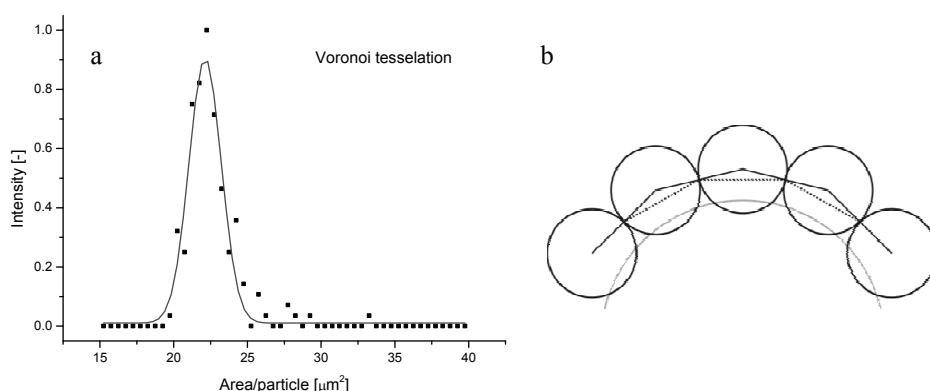


Figure 2.12 Results from the Voronoi tessellation. *a)* Distribution of the area per particle obtained from the VT for the first half of data points ($0^\circ < \alpha < 45^\circ$). *b)* Graphical representation of particles packing on a curved interface.

In conclusion, one can say that the construction of a 3D representation, as described above, is successful. Data obtained from the DT and the VT that is related to the particle diameter allowed a validation of the described procedure and proved that a selection of data points ($0^\circ < \alpha < 45^\circ$) is necessary to accurately represent the structure of the colloidosome. One implicit assumption has to be discussed here. If the particle order at the top of the colloidosome would be significantly different from that found at the edges, then the derived quantitative data would not be representative for the entire colloidosome. However, there is no reason to believe that this is the case, because the size of the defects is small compared to the analyzed area and seems to be distributed evenly over the surface of the colloidosome.

The pair-distribution function $g(r)$ is a universal measure of structure in various systems and it is independent of mathematical transformations, such as the DT and VT. $g(r)$ describes how the particle density varies as a function of the distance from a particle, averaged for all the particles in the system. It has previously been used to study the structural order of colloidal films. Grier and Murray used the pair distribution function as a measure how closely a colloidal film resembles a triangular lattice.²⁶ Hansen *et al.* continued their work and showed how the size of ordered domains is estimated from the same function.²⁴ The pair distribution function as given by the following equation

$$g(r) = \frac{1}{N} \sum_{i=1}^N \frac{n_i(r)}{n_{gas}(r)} \quad 2.6$$

Equation 2.7 had to be modified to suit a spherical surface; here $n_i(r)$ is the number of particle pairs assigned to a bin corresponding to an interparticle distance within the interval $\{r, r + \delta r\}$. This is equivalent to the number of particle centers contained in a ring at a distance, r , and thickness δr over the surface of the sphere from particle i . δr is normally a fraction of r and is set at an arbitrary value of $\delta r = r/20$. The number of particle pairs is normalized with respect to $n_{gas}(r) = \rho(A(r + \delta r) - A(r))$, wherein $A(r + \delta r) - A(r)$ is the area of the ring at a distance r and thickness δr , where ρ is the particle surface density. The positional data allowed the calculation of the particle separations for all visible particle pairs in the colloidosome. However, in this case not the Euclidean distance is used, but the geodesic distance over the surface of the sphere is calculated. To exclude edge effects, a selection of particles that are sufficiently located at the center of the colloidosome are taken into account. The particle positions from 5 different images of similar colloidosomes were used to accurately calculate $g(r)$.

As shown in figure 2.13, the resulting $g(r)$ exhibits 6 distinct peaks, which correspond with those found for monodisperse, hexagonally packed particles with a diameter of $5.01 \pm 0.05 \mu\text{m}$ (table 1). While the size of the particles obtained from $g(r)$ is slightly smaller than that obtained from the previous measurements, it falls within the experimental error. However, no long-range order is observed. $g(r)$ decays within 4 particle diameters, implying a short correlation length. The correlation length is dependent on the system size. For regular packings for large system sizes correspondingly large crystalline domains can form, which result in a longer correlation length. Vice versa, at small system sizes the crystalline domains are also smaller and yield shorter correlation lengths. Here only one particular system is characterized. The variation of system size and the corresponding correlation length could be an interesting topic of further research. Moreover, the length scale of separation that can be accessed is essentially limited by the size of the colloidosome studied. For larger colloidosomes the accessible length scale would thus be larger. In principle the structure of the upper half of the colloidosome can be accessed. Moreover, the accuracy of the determined particle positions decreases towards the edges of the colloidosome. Only particles with sufficient positional accuracy are taken into account.

The length scale over which the correlation function can be accurately determined is thus limited.

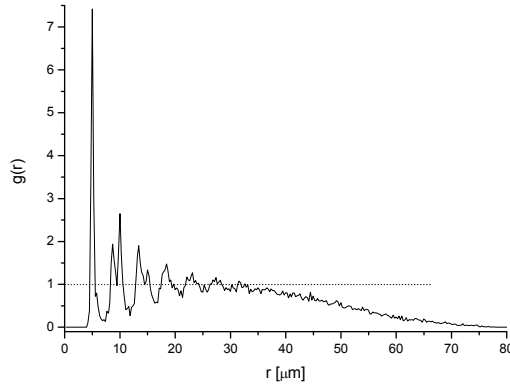


Figure 2.13 The pair distribution function $g(r)$ of the colloidosome in figure 2.5, as a function of the particle separation, r .

Table 2.1 The experimental positions of the peaks in $g(r)$ in figure 2.13 and the normalized theoretical positions of the particles packed in a hexagonal fashion.

Peak	Position $r/2R$	Theoretical position $r/2R$ [-]
1	0.99	1
2	1.74	$\sqrt{3}$
3	2.00	2
4	2.67	$\sqrt{7}$
5	2.97	3

Initially, $g(r)$ asymptotes to 1 before it decays to zero at larger particle separations. The reduction to zero can be explained by the effect that at large particle separations, and for certain particles, the ring $\{r, r + \delta r\}$ is located outside the colloidosome. $g(r)$ is, therefore, only accurate to a particle separation of approximately 30 μm . Given the fact that the particles on the colloidosome are densely packed, it is surprising that $g(r)$ indicates relatively short-ranged order. Especially compared with pair distribution functions obtained from colloidal films.²⁴ However, this could be attributed to the fact that the crystallinity of the colloidosome is disrupted by the grain boundary scars that naturally occur and disrupt the long-range order.

2.3 Conclusion

This chapter demonstrated the structural characterization of Pickering emulsions in terms of the three-phase contact angle θ , the droplet diameter D and the structural organization of particles on the droplet surface, which is used extensively throughout this thesis. In particular, we have shown how a 3D representation of a spherical particle assembly is constructed from a single SEM image and how this can be used to quantitatively characterize the particle packing. A single SEM image yields the two dimensional (x, y) coordinates of the particles and the corresponding height of each particle is calculated by using the boundary condition that all particles are located on a sphere of diameter D . A DT and a VT were performed to extract structural information on the particle packing. The error analysis showed that only the top half ($0^\circ < \alpha < 45^\circ$) of the particles represented the actual structure of the colloidosome. Due to the curvature the particles at the edge of our SEM images are only partly visible; this makes it increasingly difficult to accurately determine their positions. Therefore, a selection of particles had to be made to calculate accurate structural information. The information related to the particle diameter was subsequently used to validate the procedure and it was found that they were in agreement with each other. In addition to the DT and the VT, finally, the pair-distribution was calculated and compared with similar data from colloidal films. It was found that even though the colloidosome is highly regular, the correlation length of the particles remains short-ranged. This effect is caused by the curvature of the colloidosome,⁶ which prevents the long-range crystalline order that is observed in flat, densely packed colloidal films.

References

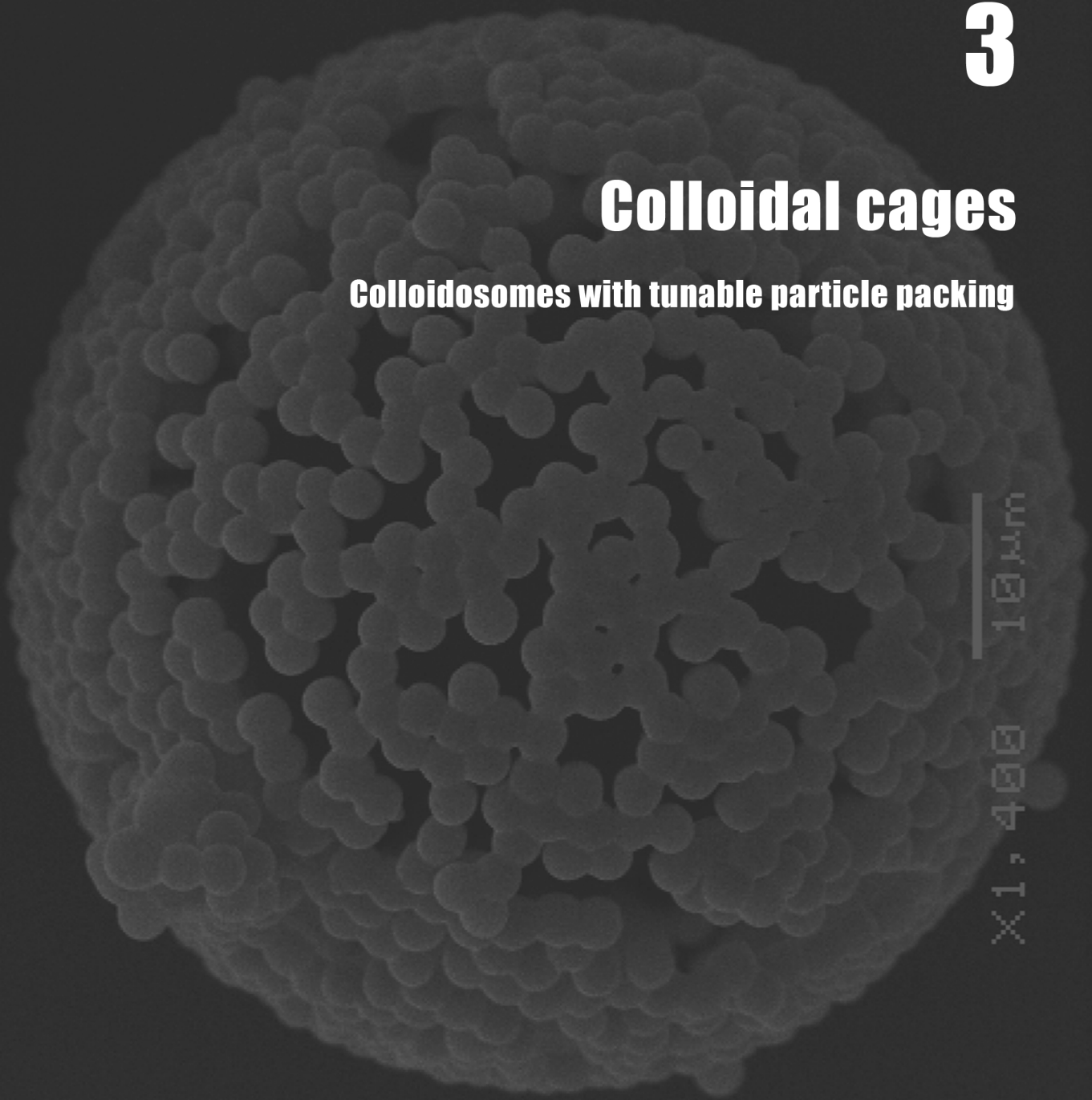
1. A.D. Dinsmore, M. F. H., M.G. Nikolaides, Manuel Marquez, A.R. Bausch, D.A. Weitz, *Science* **2002**, 298, (1), 1006-1009.
2. Rossier-Miranda, F. J.; Schroen, C.; Boom, R. M., *Colloids and Surfaces a-Physicochemical and Engineering Aspects* **2009**, 343, (1-3), 43-49.
3. Arditty, S.; Schmitt, V.; Giernanska-Kahn, J.; Leal-Calderon, F., *Journal of Colloid and Interface Science* **2004**, 275, (2), 659-664.
4. Studart, A. R.; Gonzenbach, U. T.; Akartuna, I.; Tervoort, E.; Gauckler, L. J., *Journal of Materials Chemistry* **2007**, 17, (31), 3283-3289.
5. Tcholakova, S.; Denkov, N. D.; Lips, A., *Physical Chemistry Chemical Physics* **2008**, 10, (12), 1608-1627.
6. Bausch, A. R.; Bowick, M. J.; Cacciuto, A.; Dinsmore, A. D.; Hsu, M. F.; Nelson, D. R.; Nikolaides, M. G.; Travesset, A.; Weitz, D. A., *Science* **2003**, 299, (5613), 1716-1718.
7. Einert, T.; Lipowsky, P.; Schilling, J.; Bowick, M. J.; Bausch, A. R., *Langmuir* **2005**, 21, (26), 12076-12079.
8. Fortuna, S.; Colard, C. A. L.; Troisi, A.; Bon, S. A. F., *Langmuir* **2009**, 25, (21), 12399-12403.
9. Bowick, M. J.; Nelson, D. R.; Travesset, A., *Physical Review B* **2000**, 62, (13), 8738-8751.
10. Jarrold, M. F., *Nature* **2000**, 407, (6800), 26-27.
11. Tammes, P. M. L. On the origin of number and arrangement of the places of exit on pollen grains. Groningen, 1930.
12. Zaccarelli, E., *Journal of Physics-Condensed Matter* **2007**, 19, (32).
13. Binks, B. P.; Kirkland, M., *Physical Chemistry Chemical Physics* **2002**, 4, (15), 3727-3733.
14. Gautier, F.; Destribats, M.; Perrier-Cornet, R.; Dechezelles, J. F.; Giernanska, J.; Heroguez, V.; Ravaine, S.; Leal-Calderon, F.; Schmitt, V., *Physical Chemistry Chemical Physics* **2007**, 9, (48), 6455-6462.
15. Binks, B. P.; Horozov, T. S., *Colloidal particles at liquid interfaces*. Cambridge University Press: 2006
16. Tarimala, S.; Dai, L. L., *Langmuir* **2004**, 20, (9), 3492-3494.
17. Vignati, E.; Piazza, R.; Lockhart, T. P., *Langmuir* **2003**, 19, (17), 6650-6656.
18. Jiang, S.; Granick, S., *Langmuir* **2008**, 24, (6), 2438-2445.
19. Arnaudov, L. N.; Cayre, O. J.; Stuart, M. A. C.; Stoyanov, S. D.; Paunov, V. N., *Physical Chemistry Chemical Physics* **2010**, 12, (2), 328-331.
20. Cayre, O. J.; Noble, P. F.; Paunov, V. N., *Journal of Materials Chemistry* **2004**, 14, (22), 3351-3355.
21. Paunov, V. N., *Langmuir* **2003**, 19, (19), 7970-7976.
22. Stancik, E. J.; Fuller, G. G., *Langmuir* **2004**, 20, (12), 4805-4808.
23. Salari, J. W.; van Heck, J.; Klumperman, B., *Langmuir* **2010**, 26, (18), 14929-14936.
24. Hansen, P. H. F.; Rodner, S.; Bergstrom, L., *Langmuir* **2001**, 17, (16), 4867-4875.
25. Sastry, S.; Corti, D. S.; Debenedetti, P. G.; Stillinger, F. H., *Physical Review E* **1997**, 56, (5), 5524-5532.
26. Grier, D. G.; Murray, C. A., *Direct imaging of the local dynamics of colloidal phase transitions*. VCH Publishers: New York, 1996; pp 69-100; p 69-100.
27. Paine, A. J.; Luymes, W.; McNulty, J., *Macromolecules* **1990**, 23, (12), 3104-3109.
28. Kraft, D. J.; Vlug, W. S.; van Kats, C. M.; van Blaaderen, A.; Imhof, A.; Kegel, W. K., *Journal of the American Chemical Society* **2009**, 131, (3), 1182-1186.
29. Dullens, R. P. A., *Soft Matter* **2006**, 2, (10), 805-810.
30. Wales, D. J.; McKay, H.; Altschuler, E. L., *Physical Review B* **2009**, 79, (22).

3

Colloidal cages

Colloidosomes with tunable particle packing

X1,400 10 μ m



Abstract: This chapter describes in detail the synthesis and characterization of colloidosomes with tunable particle density and well-defined porosity. The permeability could find useful applications for instance for the trapping of living cells in systematic biological studies or for the controlled release/dosage in drug delivery systems. The size of the particles on the surface of the colloidosome controls the particle packing density. ‘Large’ particles (5.0 μm) pack densely and show an almost crystalline particle configuration. However, with decreasing particle size the surface coverage becomes less dense. In analogy with colloidal armors for densely covered colloidosomes, we refer to these structures as *colloidal cages*. The attractive nature of the particle interactions proved to be the most important factor in the formation of colloidal cages. In our picture of the formation of these colloidal cages, attractive forces in the initial particle dispersion already result in the formation of irregular-shaped aggregates, thus preventing the formation of densely packed colloidosomes as the particles are deposited on the surface of the drops. Moreover, the attractive particle potential also enables the formation of jammed particle networks or 2D gels on the droplet surface, which are capable of preventing rearrangements due to Brownian motion or shear forces even at low packing densities. The colloidal cages are characterized using light microscopy (LM) and scanning electron microscopy (SEM). Using these images, the structural organization of the particles on the colloidosome is analyzed particularly in terms of the packing density and the radial-distribution function. The structure of the particles is theoretically modeled with MC-simulations and a simulated diffusion-limited aggregation on the surface of a sphere.

Part of this chapter is in preparation for publication.

3.1 Introduction

Colloidosomes are hollow spherical structures that are formed by the assembly of colloidal particles at the surface of liquid drops¹. As a result, particles are arranged in a solid shell that is inherently porous. The assembly of small solid particles at liquid interfaces is used in various applications, such as crude-oil processing,² food,^{3, 4} mineral flotation⁵ and cosmetics.⁶ Moreover, it is a promising technique for the synthesis of novel materials⁷ and has recently led to the development of selectively permeable capsules, the above-mentioned colloidosomes,¹ nano-composite particles,⁸ porous solids and foams.⁹ The use of uniform spherical particles for the synthesis of colloidosomes has led to a remarkable control in permeability, which arises from the interstitial voids that form among densely packed particles. The size of these voids is directly related to the particle size. This can be exploited for instance in drug delivery applications, as the size of the voids in these densely packed shells directly controls their permeability and thus their release kinetics¹⁰⁻¹².

Here we present an alternative approach to tune the porosity and permeability of colloidosomes by controlling the particle density on the colloidosome surface. At high densities an almost crystalline particle packing is obtained, where the pore size is entirely determined by the particle size. However, at lower densities disordered packings with larger pore sizes can be obtained. In this case the pore sizes are controlled by the packing density as well as by the interaction between the particles, which is a key parameter in the formation of these structures. By using attractive interactions, we ensure the formation of stable droplets and enable the structural arrangement of the particles in a surface spanning network structure. In analogy with the term ‘colloidal armor’ for densely packed colloidosomes, we present here the formation of a new class of material for which we coin the name ‘colloidal cages’.

In most previous studies on colloidosomes colloidal particles with a repulsive inter-particle potential were used. Notably, such a simple repulsive interaction already leads to a rich range of behaviors. Charged, repulsive particles show highly crystalline particle configurations on the droplet surface at both high and low particle densities.¹³ The use of such repulsive particles that are packed on a droplet surface has been used as an experimental model to study the old Johnson Problem, which is the structural arrangement of point-like charges on spherical surfaces.¹⁴ Moreover, this experimental system has revealed new types of defects that only occur on spherical surfaces, so-called grain-boundary scars.^{15, 16} In effect, these systems opened up a new field of research that studies

the effect of curvature and topology on the organization of matter.¹⁷ The interaction of colloidal particles at interfaces is a new and fascinating topic of research. There are different contributions to the particle potential from each phase, which combined can lead to qualitatively new types of assemblies.

Colloids with attractive interactions have so far not been used to study the formation of colloidosomes. However, they are commonly used in the study of colloidal gels and glasses.¹⁸ The most important parameters in colloidal gelation and glass formation are the volume fraction of particles and the inter-particle potential. Both parameters determine the formation and structure of the colloidal gels and glasses and can in principle also be controlled during the formation of colloidosomes. Structuring at the surface of a colloidosome can be viewed as a two-dimensional analogue to aggregation, crystallization, or glass formation in three dimensional systems. Our system of attractive colloids could thus serve as an experimental model to study the assembly of attractive particles into two-dimensional spherical colloidal gels and glasses.

3.2 Experimental

Materials Ethanol (99.9%, Biosolve). Water is double de-ionized with a purification system. Poly(n-vinylpyrrolidone) (pVP) (PVP40, $M_w = 40000$ g/mol, Sigma Aldrich) is used as received. (Styrene (99%, Merck) and divinylbenzene (80% mixture of isomers, Sigma Aldrich) are passed over a column with aluminum-oxide (activated basic, Sigma Aldrich) prior to use to remove inhibitor. The inhibitor-free styrene and divinylbenzene are refrigerated for later use. N,N'-azoisobutyronitrile (AIBN) (98%, Merck) is recrystallized from methanol (99.8%, Biosolve). n-Heptane (>96% Biosolve).

Colloidal particles are synthesized by the dispersion polymerization of styrene, which is performed in a cylindrical 250 mL reactor equipped with four baffles and a four-blade pitched impeller. The exact amounts of ethanol, styrene and water varied for each dispersion polymerization are collected in Table 3.1. The general procedure for the particle synthesis is as follows. The specified amounts of ethanol, water and 3.4 g pVP are charged to the reactor and stirred at 100 rpm until the pVP is completely dissolved. 0.5 g AIBN and 0.2 g divinylbenzene are dissolved in the specified amount of styrene and also added to the reactor. Finally, a thermostatic bath is pre-heated to 70 °C and connected to the reactor, when it reached the specified temperature. The polymerization is performed for at least 12

hours to assure maximum conversion of styrene. Samples are taken during the polymerization from which the conversion is determined gravimetrically. The formed polystyrene (pS) particle dispersion is cooled to room temperature. The excess pVP and residual monomer is removed from the dispersion by performing 3 cycles of centrifugation, decantation of the supernatant solution and re-dispersion in clean ethanol. Subsequently, the particles are isolated and dried to remove residual ethanol.

The pS particles are imaged with scanning electron microscopy (SEM) (Jeol, JSM-500). The sample holder is covered with double-sided conducting carbon tape and a droplet of the pS dispersion is cast on the holder. The sample is dried under air and finally coated with a thin layer of gold. The particle diameter is determined from SEM images. Initially, static light scattering measurements were performed on the dispersion and yielded the same results. Therefore, only the SEM results are shown. The number-, volume average particle diameter and the polydispersity index (Δ) are given by equations 3.1, 3.2 and 3.3. n is the number of particles that is counted.

$$d_n = \frac{\sum_{i=1}^n d_i}{n} \quad 3.1$$

$$d_v = \frac{\sum_{i=1}^n d_i^4}{\sum_{i=1}^n d_i^3} \quad 3.2$$

$$\Delta = \frac{d_v}{d_n} \quad 3.3$$

Formation of colloidal cages

Particle-size dependence The exact amount of pS particles needed to form the colloidosomes can be found in Table 3.1. The specified amount of particles is dispersed in 100 mL heptane. 10 mL of water is added instantly to the particle dispersion in heptane, while the mixture is stirred at 10.000 rpm. The emulsion is additionally stirred for 10 seconds. Both re-dispersion of the particles in heptane and emulsification of water are performed by a standard rotor-stator mixer (IKA Ultra-Turrax T25 basic) at high shear rates (20.000 s⁻¹). Finally, the pS particle-stabilized emulsion is poured in the same reactor as

described above for the dispersion polymerization. An additional 100 mL heptane is added to the reactor to obtain an appropriate volume to fill the reactor. The reactor is heated to 35 °C for 30 minutes, while the mixture is stirred at 400 rpm. The final colloidosome dispersion is imaged with dark-field light microscopy (LM) (Zeiss Axiostar plus) mounted with a standard digital camera and scanning electron microscopy (SEM) (Jeol, JSM-500). The LM images were taken from the actual colloidosome dispersion in heptane. The SEM images are made in a similar manner as is described for the pS particles.

Time-dependence To study the influence of shear during formation of the colloidosomes a set of experiments is performed in which the same particles are used and the shearing time is varied. pS particles with an intermediate particle size ($d_N = 2.7 \mu\text{m}$) are used and the duration of shearing is 2, 5, 10 and 15 s. The rest of the synthetic procedure is as described above. The colloidal cages are characterized by bright-field LM and SEM. The droplet diameters are determined from the LM images and the particle densities are determined from the SEM images.

Table 3.1 Data concerning the particle synthesis, the final particle size and colloidosome formation.

	Styrene ^a [g]	Ethanol ^a [g]	Water ^a [g]	d_n [μm]	$\Delta : d_v/d_n$ [-]	pS particles ^b [g]
I	63.9	126.8	-	5.0	1.01	3.96
II	55.5	134.6	-	3.4	1.02	2.82
III	41.2	146.5	-	2.7	1.01	2.44
IV	27.5	154.5	5.0	1.9	1.02	1.52
V	27.4	150.6	10.0	1.8	1.05	1.45
VI	27.5	142.7	20	1.56	1.04	1.20
VII	27.5	134.8	30	1.30	1.05	1.10
VII	27.5	126.9	40	1.10	1.09	0.99
IX	27.5	119.0	50	1.07	1.22	-
X	27.5	111.1	60	0.95	1.12	-

Column 2 – 4 show the specified amounts required for the dispersion polymerization.^a Column 7 shows the weight of pS particles that is used to form the colloidosomes.^b

3D Structural characterization

The particle configurations of the colloidosomes are characterized by the packing density and the radial distribution function. The particle positions of the colloidosomes are extracted from the SEM images. The x,y -coordinates in plane with the image are directly obtained from the SEM image. A height can then be given to each particle by mapping it on the surface of the sphere, based on the radius of the colloidosome and its curvature. Towards the edges of the colloidosome it becomes increasingly difficult to accurately determine the particle positions, which introduces a systematic error. Therefore, a selection of particles is made that accurately represents the particle configuration of the colloidosome. The exact procedure, the selection of particles and validation of the procedure is described in chapter 2.

Theoretical modeling particle packing

Monte-Carlo simulations A number of particles N_{col} with a particular diameter $2R$, corresponding with the synthetic conditions, are randomly placed on a sphere with diameter $D = 64.8 \mu\text{m}$ and are allowed to equilibrate at temperature T . Two models are used for the particle, respectively the hard sphere (HS) and the polarizable hard sphere (PHS).

$$\phi_{HS}(r) = \begin{cases} +\infty & r < d_n \\ 0 & r > d_n \end{cases} \quad 3.4$$

$$\phi_{PHS}(r) = \begin{cases} +\infty & r < d_n \\ \varepsilon_{PHS} \cdot \left(\frac{2R}{r}\right)^6 & r > d_n \end{cases} \quad 3.5$$

The PHS particles interact purely through a van der Waals-type pair potential, where r is the euclidean distance between two particles and $\varepsilon_{PHS} = A/36$ is a positive energy that is proportional to the Hamaker constant A .^{19, 20} The simulations are performed with a constant N, ρ and T canonical ensemble.^{21, 22} The temperature is irrelevant for the HS model, because the particles are athermal. For the PHS the reduced temperature that is used is $\varepsilon_{PHS}/k_B T = 0.3$. The exact conditions for each density and particle size are collected in table 3.2. A typical run would consist of $5 \cdot 10^5$ single particle moves, keeping the acceptance ratios constant at approximately 0.3. In all the presented plots of the MC radial distribution function, the error bars are not visible on the scales of the graphs. The MC simulations were carried out at the Center for High Performance Computing (CHPC), CSIR Campus, 15 Lower Hope St., Rosebank, Cape Town, South Africa. Manufacturer: IBM e1350 Cluster,

CPU: AMD Opteron, CPU Clock: 2.6 GHz, CPU Cores: 2048, Memory: 16GB, Peak Performance: 3.3 TFlops, Storage: 94 TB (Multicluster), Launch date: 2007.

Table 3.2 Conditions of the MC Simulations.

	N_{col}	D/d_N	ρd_n^2
I	561	13.5	0.98
II	1065	19.5	0.89
III	1498	23.8	0.84

Diffusion-limited aggregation A sphere with an arbitrary number of particles is considered in the aggregation routine. The initial particle positions are arbitrarily chosen from the equilibrated particle configurations of the MC-simulation. The particle diameter and packing density correspond to the experimental conditions (Table 3.3). All the particles are moved simultaneously and randomly over the surface of the sphere. Each movement is performed as follows: First, a random vector is generated and used as a rotation axis. And second, the particle or aggregate of particles is rotated around this rotation axis in a fixed direction and angular displacement β . In order to account for the increased Stokes drag of particle aggregates with increasing size, we choose the angular displacement step to depend on the aggregate size N_{AGG} as:

$$\beta = \left(\frac{\pi}{5 \cdot 10^2} \right) \sqrt{\frac{1}{N_{AGG}}} \quad 3.6$$

N_{AGG} is the number of particles that make up an aggregate. When two particles come in contact, (when the Euclidean distance is equal or smaller than the diameter), the particles stick and continue moving together. Aggregation continues until all the particles have formed one aggregate ($N_{AGG} = N_{col}$). The aggregation routine is performed with Matlab and the script is provided in the appendix.

Table 3.3 Conditions for the diffusion-limited aggregation simulations.

	N_{col}	D/d	ρd^2
III	1498	23.8	0.84
IV	2740	34.1	0.75
V	3013	36.0	0.74

3.3 Results

3.3.1 Particle synthesis

The colloidal particles that are used in this study are synthesized by the dispersion polymerization of styrene in ethanol/water,²³ which is a well-established technique for the formation of uniform, micrometer-sized particles. A uniform distribution is important for this work, because the particle size is the sole parameter that is varied in the synthesis of the colloidal cages. pS particles with diameters ranging from 0.9 to 5.0 μm and high uniformity ($\Delta = d_v/d_N < 1.1$) are successfully synthesized. The choice for this polymerization technique is also motivated by the requirement of an attractive potential between the particles at the o/w interface. During the polymerization the pS particles are sterically stabilized with pVP in ethanol/water. However, pVP is insoluble in hydrocarbons, such as heptane, and therefore can no longer sterically stabilize the pS particles once it is assembled at the o/w interface. This guarantees the attractive potential between the particles.

Dispersion polymerization is distinctly different from other methods to synthesize polymer colloids, such as emulsion polymerization, with respect to the solubility of the monomer in the continuous phase. All constituents of the initial reaction mixture, such as the steric stabilizer, initiator and including the monomer(s), are soluble in the organic solvent. During the polymerization, the formed polymer eventually becomes insoluble in the reaction mixture and starts to precipitate. The presence of the steric stabilizer controls the precipitation and allows a controlled nucleation and subsequent growth of the particles. The nucleation of particles typically occurs within the first 5% conversion of monomer. From that moment on, the number of particles is fixed and these particles grow with increasing consumption of monomer. Most dispersion polymerizations are performed in organic solvents, for example ethanol or heptane, and therefore require steric stabilizers. Ionic stabilizing groups, which are commonly used in emulsion polymerization, cannot generate sufficient electrostatic repulsion, due to the low dielectric constant of organic solvents. The size of the final particles is determined by a complex interplay of many factors, such as the concentration steric stabilizer, initiator and monomer. However, the determining factor is the solubility of the formed polymer in the initial reaction mixture. Roughly, it can be stated that a poor solubility results in small particles and that an increased solubility results in bigger particles. In this work, the solubility of pS is lowered by replacing ethanol with water to reduce the particle size. A larger fraction of styrene in the initial reaction mixture results in larger particles. The dispersion polymerizations performed in this study resulted in the controlled formation of pS particle dispersions. No significant aggregation occurred

in any of the polymerizations. Figures 3.1 to 3.4 show the results of the particle synthesis. A typical conversion plot for the free-radical dispersion polymerization of styrene can be seen in figure 3.1. Almost complete conversion is obtained after 12 hours. The final particle diameters, as determined from SEM images, are shown in figures 3.2 and 3.3. Both the number-average d_N and the volume average d_V diameters are shown in the graph to illustrate the uniformity of the particles. This clearly shows that the particle diameter can be controlled by adjusting the solvency of the reaction mixture, which is consistent with previously reported studies.²³

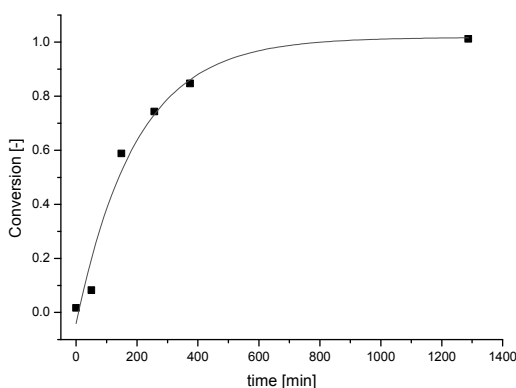


Figure 3.1 The conversion/time history of a typical dispersion polymerization of styrene. Results from dispersion polymerization VII is shown here. The conversion is determined gravimetrically.

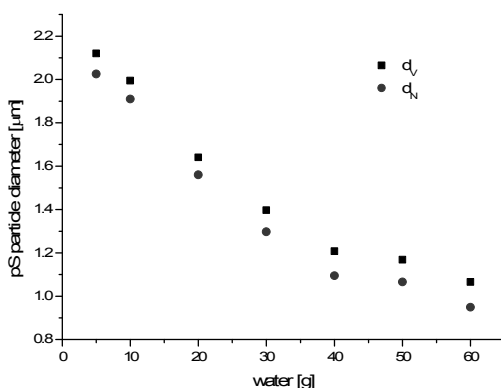


Figure 3.2 Particle diameters as a function of the amount water in the recipe. The results of dispersion polymerizations IV to X are shown. The particle diameter is determined from SEM images.

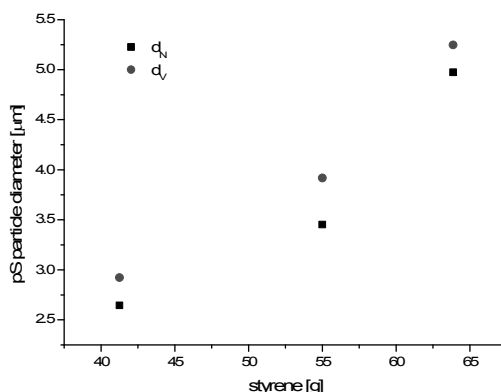


Figure 3.3 Particle diameters as a function of the styrene content in the recipe. The results of dispersion polymerizations I, II and III are shown here. The particle diameter is determined from SEM images.

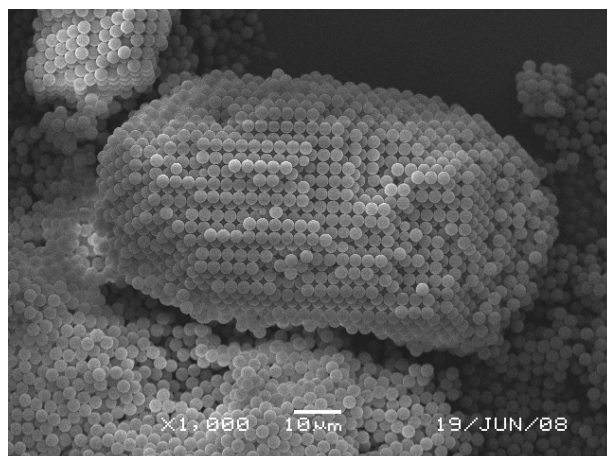


Figure 3.4 SEM image of 2.7 μm pS particles obtained from dispersion polymerization III.

The SEM image in figure 3.4 shows the typical results obtained from the dispersion polymerization of styrene, as performed in this study. The uniformity of the particles is demonstrated by the regular stacking of particles, which is displayed in the SEM image. Another SEM image of pS particles synthesized by dispersion polymerization I can be found in figure 2.7 of the previous chapter.

3.3.2 Colloidal cage formation

The procedure to synthesize the colloidal cages is actually quite straight-forward. The pS particles are dispersed in hydrocarbon oil (heptane). The pS particle dispersions in heptane are highly unstable and settle within seconds after shearing. The aggregation is expected, because the particles are no longer sterically stabilized in the heptane. This observation is quite relevant, because the attractive nature of the pS particles strongly influences the formation of the colloidosomes. Water is added instantaneously to the particle dispersion, while the mixture is being stirred. After the addition of water, the emulsion is additionally stirred for 10 seconds. Due to the shearing process, small water droplets are formed and the particles are simultaneously assembled at the oil/water (o/w) interface (fig. 3.5a). The number of particles with respect to the volume of water is chosen in such a way that in theory 50 μm droplets will form, assuming that all the particles adsorb to the w/o interface and densely pack in a hexagonal manner. Figure 3.5b shows a typical picture of such an emulsion. Individual water droplets covered with pS particles can clearly be seen. At this stage, the droplets are covered with individual particles, but collapse when one of the liquid phases, and herewith the interface, is removed. The particle layer needs to be reinforced to form a continuous shell around the droplet and actually form a capsule. Heating the mixture to 35 °C for 30 minutes proved sufficient to do so, although the glass transition temperature of pS is substantially higher (100 °C). The reduction of the glass transition temperature is caused by the plasticizing effect of the oil-phase, *i.e.* heptane. The pS particles are partly swollen with heptane and hereby softened. A drop of the colloidosome suspension is cast on a SEM sample holder and dried. The majority of the colloidosomes is mechanically stable and withstands evaporation of the liquid phases, which allows imaging and further characterization with SEM (fig. 3.5c and d).

The key parameter for the assembly of particles at soft interfaces is the wettability of the particles for the respective phases and the surface tension of the interface between the two liquids that constitute the emulsion.²⁴ The three-phase contact angle θ is normally used to express wettability and can be calculated by Young's equation (eq 1.1). It is commonly known that stable Pickering emulsion droplets are formed with intermediate contact angles ($\theta \approx 90^\circ$), where particles assemble near the middle of the interface between the two liquids. Additionally, θ determines the type of emulsion (w/o or o/w) that is preferred. Hydrophobic particles ($90^\circ < \theta < 180^\circ$) tend to form inverse w/o emulsions. An indication of θ for the used pS particles can be obtained from one of the SEM images (fig. 3.5d). The applied method is explained in chapter 2, but it exploits the deformation of the pS particles at the

o/w interface as a result of the sintering process. Upon heating, the particles apparently did not only coalesce to form stable capsules, but additionally flattened to minimize their contact area with water. The observed contact angle θ for the pS particles is roughly 130° .

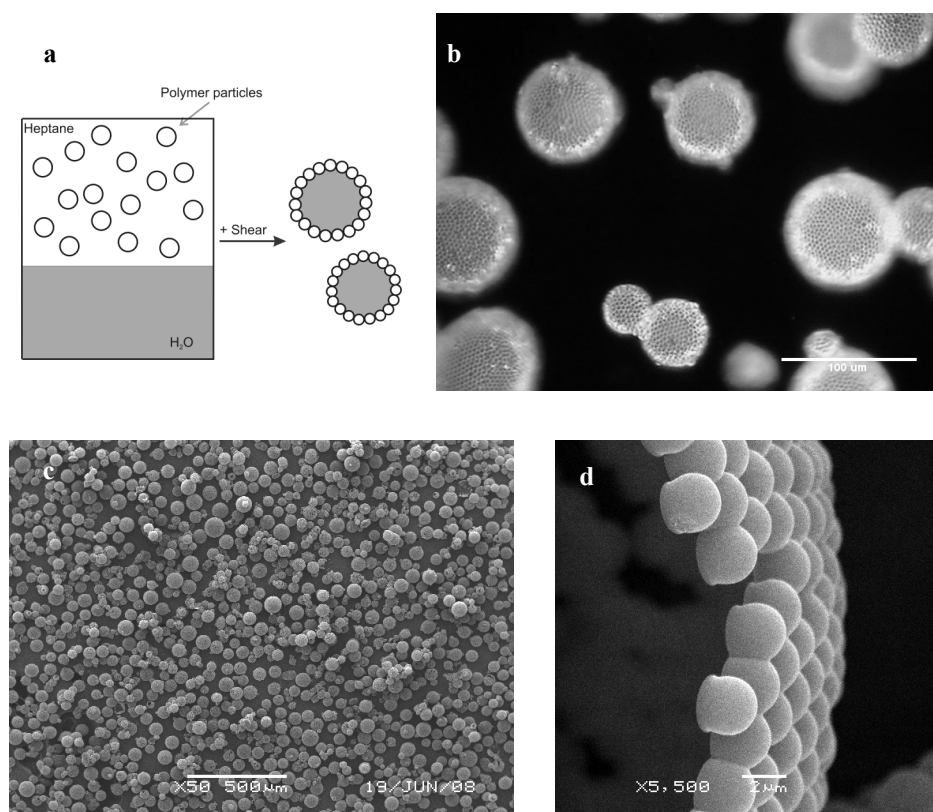


Figure 3.5 The formation of pS particle-stabilized emulsions and colloidal cages. **a**, Graphical representation of the formation of a particle-stabilized emulsion. **b**, Dark-field microscopy image of pS-particle covered water droplets in heptane. This particular emulsion is stabilized with $5.0\ \mu\text{m}$ pS particles. **c**, SEM image of pS colloidal cages, which remain intact even after evaporation of both heptane and water. **d**, A side-view of the colloidal cage wall. The SEM images are the capsules obtained from Pickering emulsion III.

The presence of functional groups on the particle surface is another important parameter, both to ensure a controlled synthesis of the particles²³ and to control the interparticle potential at the o/w interface. To achieve the desired attractive potential, ionic groups on the particle surface must be avoided, as this would lead to electrostatic repulsion. Even in oils

with low dielectric constants, ionic groups can be charged and result in repulsive potentials.¹³ Moreover, ionic groups dissociate and generate a repulsive potential in water at low ionic strengths. Therefore, a nonionic polymeric stabilizer (poly(vinyl pyrrolidone) (pVP)) is chosen that is soluble in ethanol/water, but is insoluble in the oil-phase. During the synthesis, pVP ensures the colloidal stability of the particles. However, after assembly on the o/w interface the particle is predominantly immersed in the oil-phase. As a result, the grafted pVP-chains collapse on the particle surface. They thus no longer sterically stabilize the particles, which effectively results in an attractive particle potential. During the synthesis of the particles, pVP can be both chemically grafted and physically adsorbed to the surface. The extent to which both effects occur is unclear, but given the hydrophobicity of the particle ($\theta \approx 130^\circ$) it is likely that the majority of pVP is physically adsorbed. The particle dispersions in heptane are unstable; our experiments showed that they settled within seconds after the stirring is stopped, a clear indication for the attractive nature of the interparticle potential.

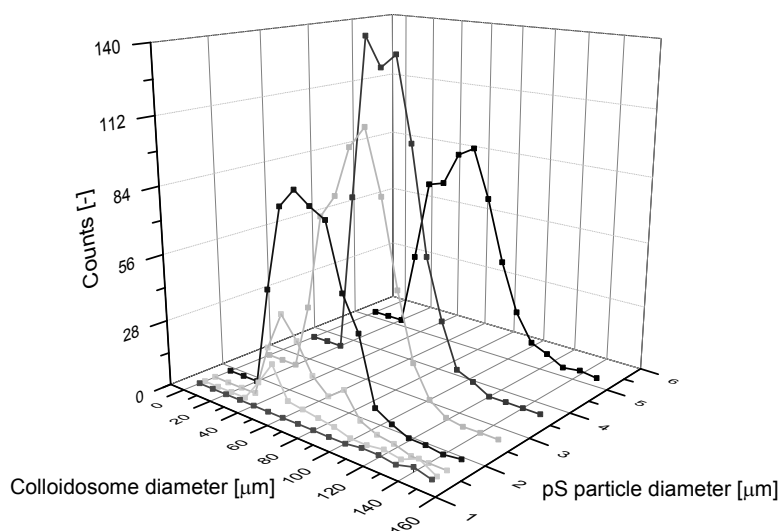


Figure 3.6 Colloidosome diameter distributions as derived from the SEM images at low magnifications (x 50).

The colloidosome diameter is determined from the SEM image in figure 3.5c, which provides more information on the extent of particle adsorption. SEM images are taken from

the other colloidosomes as well, at similar magnifications (x50). The number of colloidosomes in a particular size-range is counted and plot in a histogram (fig. 3.6). The distributions are fairly broad, but are remarkably similar for each set of colloidosomes. The colloidosome diameter ranges from 40 to 80 μm , which is consistent with the expected diameter of 50 μm . In principle, this indicates that all the available particles are in fact adsorbed to the o/w interface. However, a remarkable observation is that the number of colloidosomes decreases significantly below a particle diameter of approximately 2.0 μm . Figure 3.7 shows a SEM image of colloidosomes that are composed of 1.56 μm pS particles. Colloidosomes are clearly present, but the majority of the image shows broken colloidosome shells. It appears as if the colloidosomes were originally present, but collapsed during the sample preparation that is necessary for making the SEM images. Apparently, the capsules are mechanically unstable, which is caused by a thin particle layer and lower packing density (section 3.3.2a). The colloidosomes composed of particles in the range of 1.8 to 5.0 μm are further characterized as described in the following section.

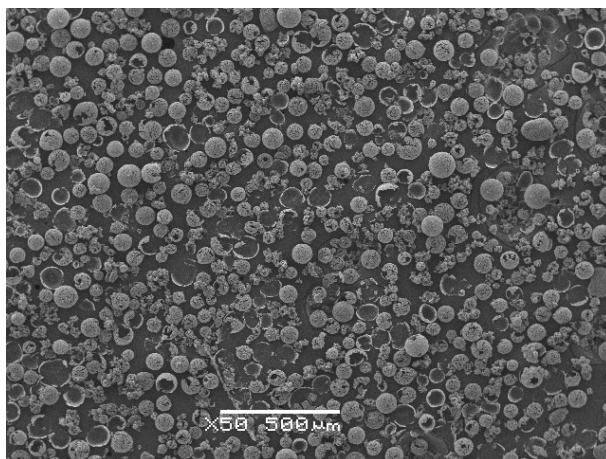


Figure 3.7 SEM images of colloidosomes obtained from Pickering emulsion VI.

3D structural characterization of particle packing

Close-ups of individual colloidosomes that are composed of particles of different sizes (1.8 - 5.0 μm) are shown in figure 3.8. At first sight, it can clearly be seen that the surface coverage decreases with decreasing particle diameter. The colloidosomes that are composed

of the largest particles (5.0 μm) exhibit the highest packing density and demonstrate a particle configuration similar to those found in previous studies.^{1, 15} The majority of the particles are packed in a triangular lattice and as a result of the curved interface we also observe grain-boundary scars (fig. 2.4b). The length of these scars is consistent with theoretical predictions of the dependence on the system size¹⁵. Although a high packing density is obtained in the colloidosomes shown in figure 3.8c, additional defects are clearly present. This already indicates that the particle configuration is jammed. If smaller particles are used, a more disordered particle configuration is observed with seemingly lower packing densities. Figure 3.8b exhibits a glass-like particle configuration, while figure 3.8a shows a liquid-like configuration. The particle configuration is quantified, as explained in the chapter 2, to identify the relation with the particle diameter. At least 5 images of colloidosomes composed of each particle size are analyzed to obtain a statistically significant comparison.

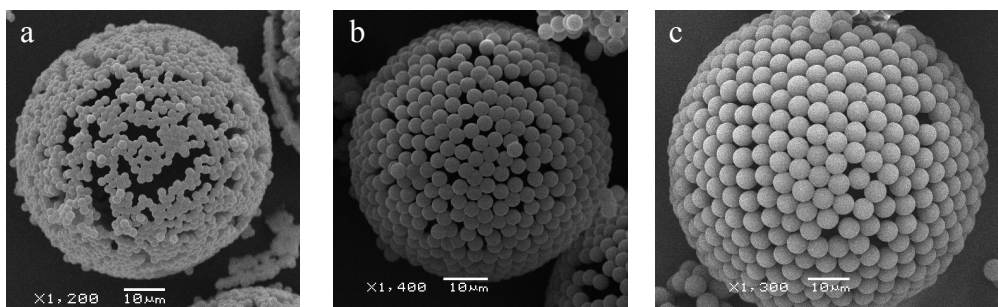


Figure 3.8 Colloidal cages that are composed of pS particles with different particle sizes show different particle configurations. a - c, SEM images of colloidal cages that are composed of 1.8, 3.3 and 5.0 μm pS particles, respectively.

The average colloidosome diameter is also determined from these SEM images as $D = 69.1 \pm 5.7 \mu\text{m}$, which is consistent with the previous observations. The colloidosome diameter is surprisingly constant throughout the different experiments (fig. 3.6, 3.9 and 3.12e). Normally, at low emulsifier concentrations, which is obviously the case considering the colloidosome structures, emulsification occurs through a limited-coalescence process.²⁵ Droplets with incomplete coverage continue to coalesce until full coverage with stabilizing particles is achieved. Full coverage can be obtained, because the total surface area of the

droplets decreases upon coalescence and the number of particles that are adsorbed to the o/w interface is fixed. In this regime the droplet diameter is determined purely by the volume of the dispersed phase and the amount of emulsifier that is present at the interface. In the present situation, this should result in different droplet diameters with an equally dense particle packing. However, our results show that the droplet diameter is independent of the number of particles at the interface and the packing density changes, as shown in fig. 3.9. Instead, our results indicate that the droplet diameter is determined purely by the shear that is applied during emulsification, which is kept constant throughout the experiment. The attractive particle potential ensures that the droplets are able to withstand coalescence, even at low fractional surface coverage.

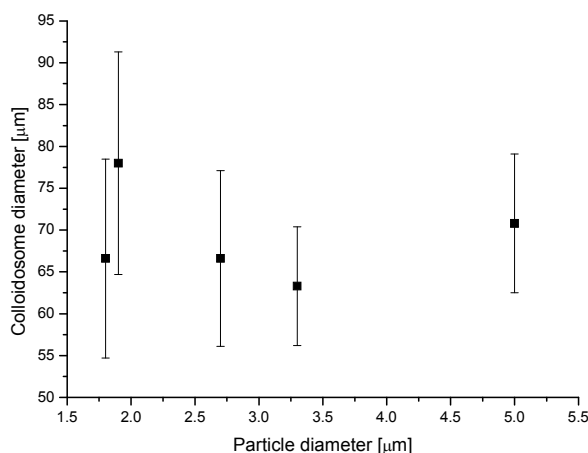


Figure 3.9 Colloidosome sizes. The average colloidosome diameter and standard deviation as a function of the particle diameter.

The particle configuration of each set of colloidosomes is quantified to identify the exact relation with the particle diameter. The positional data in 3 dimensions (3D) of the particles from each colloidosome is extracted from the SEM images, as explained in chapter 2. From the 3D positional data, several structural parameters can in principle be determined. A Delaunay triangulation is commonly used to determine the coordination number of each particle.¹⁵ Another structural parameter is the distribution of inter-particle distances, from which the radial distribution function $g(r)$ can be determined, as shown in figure 3.12. Results from the Monte-Carlo (MC) simulations are compared with the experimental data

based on the $g(r)$. The normalized particle density $\rho \cdot d_n^2$ is used here to characterize the colloidosome structure and obtain a relation with the particle diameter d_n . The density ρ is defined as the number of particles per unit area, which is obviously different for each particle size. Therefore, it has to be normalized by multiplying with the square of the diameter in order to make a fair comparison among the different particle sizes. The normalized packing density is different from the fractional surface coverage and ranges from 0 to 1.15 for a perfect hexagonal close packing.

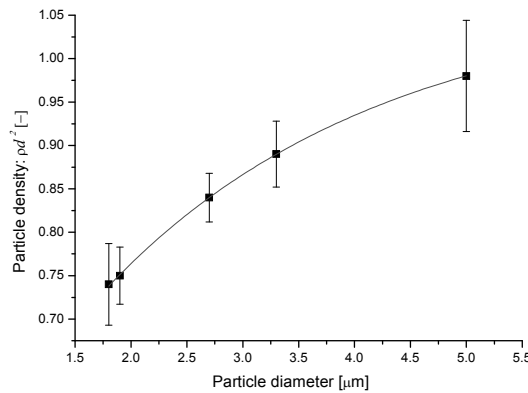


Figure 3.10 The packing densities of colloidosomes composed with pS particles of varying size. The red line is a fit with a power law dependence, $R^2 = 0.99$. The density $\rho \cdot d_n^2$ scales with $d_n^{0.28}$.

The packing densities of the colloidosomes for each particle size are shown in figure 3.10. Initially, we assumed that all the particles assemble at the interface and pack in a hexagonal manner. However, our data shows that the packing densities are substantially lower than those expected for hexagonal close-packing ($\rho \cdot d_n^2 = 1.15$). The density is 0.98 for the largest particles (5.0 μm) and gradually decreases with the particle diameter to 0.74 for the smallest particles (1.8 μm). From figure 3.10 it can be concluded that there is a power-law dependence of the packing density on the particle diameter. An excellent fit ($R^2 = 0.99$) was obtained, which showed that $\rho \cdot d_n^2 \sim d_n^{0.28}$. Extrapolation of this trend reveals a maximum packing density for even larger particle sizes of $\rho \cdot d_n^2 = 1.09$. It is expected that the maximum packing density on a spherical surface is lower, due to obligatory deviations from a hexagonal close-packing on a spherical surface.¹⁵ However, the observed differences are

too large to be accounted for by this effect. Instead, our results indicate that due to the attractive interactions the particles on the surface form a jammed network at densities significantly below the dense packing limit. This is analogous to attractive glasses and gels in 3D, where jamming takes place at volume fractions below the close packing limit.²⁶

Convection-limited particle adsorption

A possible explanation for the observed behavior is that the formation of the colloidosomes is kinetically determined. In other words, the time of the experiment is not sufficient to enable all particles to assemble at the droplet surface. It can be observed in the SEM images, in particular those with low packing densities, pores are formed that are larger than the particle diameter. As more particles are available in the continuous phase that could fill these pores, the observation of these large pores is in agreement with our assumption that the colloidosome formation is kinetically determined. Based on this picture of the particle assembly we would assume that continued stirring should lead to higher packing densities. To illustrate this, the particle adsorption is modeled for each particle size.

A single droplet with a diameter $D = 50 \text{ }\mu\text{m}$ is considered. The maximum number of particles N that can cover the droplet is calculated by equation 3.4. It is assumed that the particle can densely pack in a hexagonal manner and that curvature effects are negligible, in a similar manner as the experimental set-up. The concentration of particles in the bulk clearly depends on the particle size. At $t = 0$, the number of particles in the bulk N_B equals N . With time, particles adsorb onto the droplet with particle flux J . The particles irreversibly bind to the droplet surface. Therefore, the number of adsorbed particles N_A gradually increases, while N_B decreases. The total number of particles remains constant at all times (eq. 3.5). The particle flux is given by equation 3.6. In turbulent flow, which is the case during emulsification, particle transport is dominated by convection instead of diffusion.²⁵ The particle flux scales linearly with the number of particles in the bulk N_B . The particle flux also scales with the available surface area for particle adsorption, which obviously decreases in time. The maximum packing density ρ_{max} is obtained from extrapolation of the graph in figure 3.10. In principle, J is also dependent on the shear rate, but has been kept constant during the experiments and is therefore not accounted for. k is the rate constant for particle adsorption and is used to fit the model to experimentally observed packing densities.

$$N = \frac{\pi D^2}{2\sqrt{3}R^2} \quad 3.4$$

$$N = N_A + N_B \quad 3.5$$

$$J = \frac{dN_A}{dt} = kN_B \frac{\rho_{max} - \rho}{\rho_{max}} \quad 3.6$$

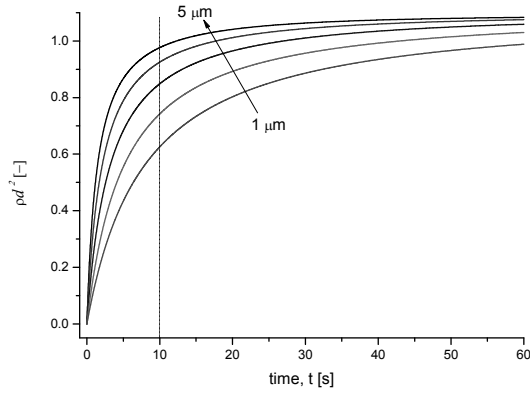


Figure 3.11 Adsorption profiles for particles of different size. The values for the initial particle flux are obtained by fitting the adsorption profile with the experimentally observed packing densities.

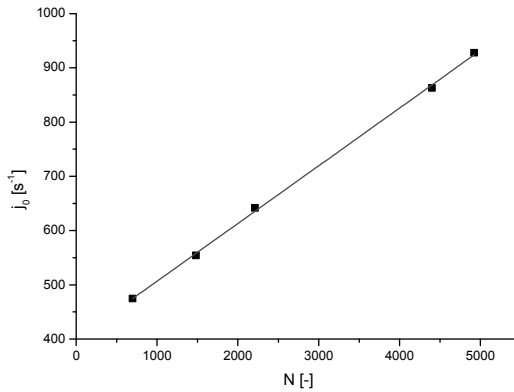


Figure 3.12 The initial ($t = 0$ s) particle flux from the bulk to the droplet surface as derived from the diffusion-limited adsorption model. The values for the initial particle flux are obtained by fitting the adsorption profile with the experimentally observed packing densities.

The adsorption profiles for 5 different particle sizes are shown in figure 3.11. The rate constant k is systematically varied for each particle size to fit the experimentally observed packing density at $t = 10$ s (dotted line), which was the shearing time used to synthesize the colloidosomes. The packing densities where the dotted line intersects the adsorption profiles are consistent with figure 3.10. The initial particle flux $J_0 = kN$ at $t = 0$ is compared with the initial concentration of particles in the bulk. For convective as well as diffusive particle transport, J_0 should scale linearly with N and this is actually the case (fig. 3.12). The model shows that although the particle flux for the ‘small’ particles is higher, the particle density develops much slower relative to the ‘large’ particles. In conclusion, the convection-limited particle adsorption model is consistent with previously reported studies²⁵ and, in principle, explains the observed dependence of the packing density on the particle diameter.

To further test the validity of our physical picture of the particle adsorption, and the above-described adsorption model, we test the dependence on the time scale of convection-driven adsorption directly in an experiment. Colloidosomes are formed with pS particles of intermediate size ($d_n = 2.7 \mu\text{m}$), which exhibit a packing density of approximately $\rho \cdot d_n^2 = 0.84$. The duration of emulsification is systematically varied from 2, 5, 10 and 15 s. According to the adsorption model, the packing density should systematically change as this time scale is varied. We measure both the colloidosome diameter and the packing density during emulsification, as shown in figure 3.13.

The results shown in figure 3.13 are consistent with a conventional emulsification process in which the water phase is gradually broken up into small droplets. It must be noted that droplet formation and particle assembly is extremely fast. Already after 10 seconds, the final droplet size of $D = 68.3 \mu\text{m}$ is obtained, which is consistent with the droplet diameters that are found in the SEM images (fig. 3.6). Initially, large droplets are observed and with time these droplets are broken up into smaller ones. Simultaneously, particles are assembled at the o/w interface. At shorter times (2 and 5 s) the particle assembly is therefore still incomplete, which is indicated by the presence of particle aggregates alongside the colloidal cages (fig. 3.13a). The SEM images from the colloidal cages are analyzed; surprisingly, as shown in fig. 3.13f, they indicate that the particle density remains approximately unchanged. While some variation is observed, within experimental error the values remain constant. Thus, this experiment indicates that the proposed adsorption model is not valid. The packing density does not significantly depend on the time of emulsification and instead appears to be an inherent property of the particle size. The structural organization of the

particles on the droplet surface is theoretically modeled in the following section to gain more insight in the studied system.

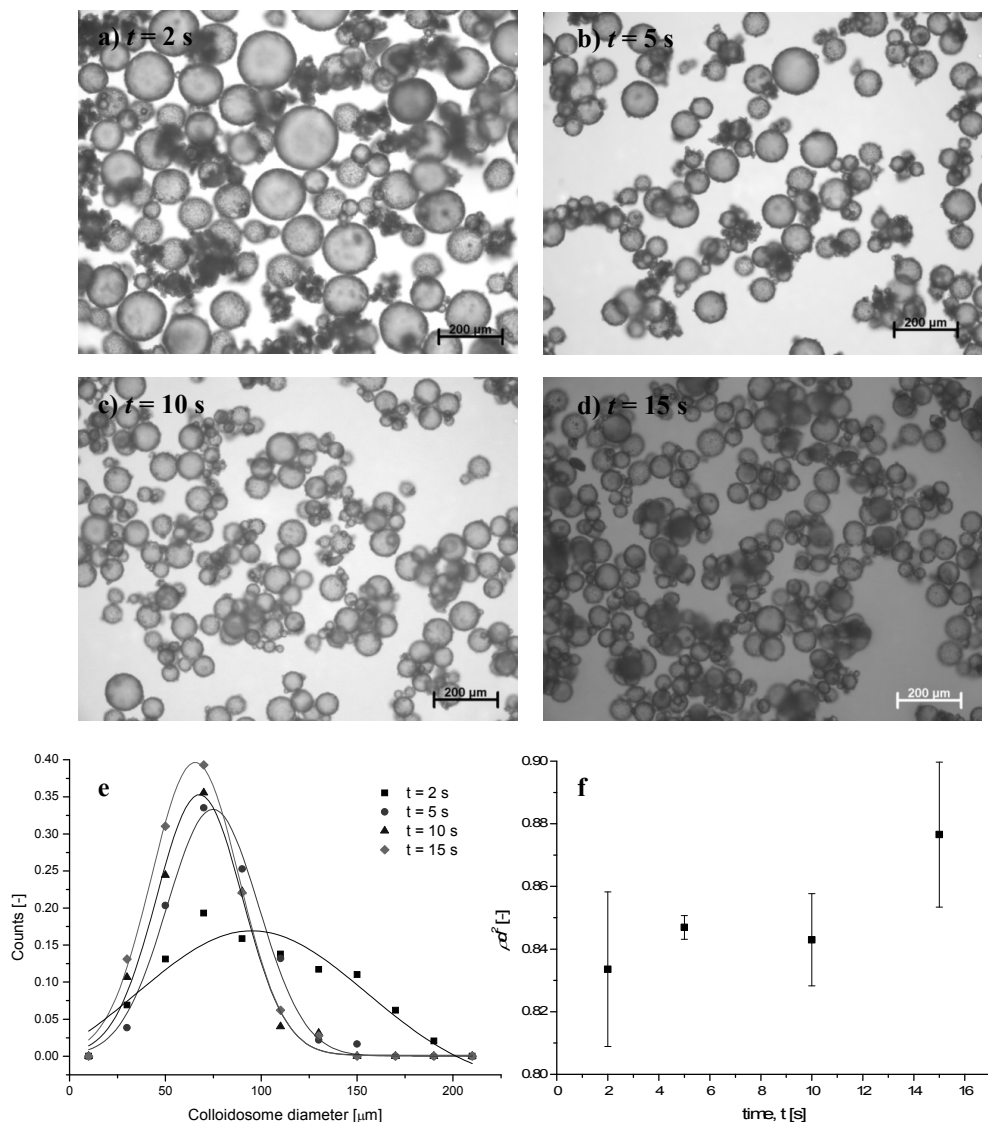


Figure 3.13 Colloidal cage formation followed in time. a – d) Light microscopy images of dispersions of colloidal cages at 2, 5, 10 and 15 s shearing time. Note the presence of aggregates alongside the colloidal cages at short shearing times. e) The droplet diameter distributions as a function of time. f) The particle packing density as a function of time.

3.3.3 Theoretical modeling of particle packing

In the following part, the particle configuration on the colloidosome surface is modeled by Monte-Carlo simulation and diffusion-limited aggregation on a sphere. The theoretical and experimental results are compared based on the radial distribution function $g(r)$ (fig. 3.14 and 3.15). The experimental $g(r)$ (red lines) of the different states shows distinct differences in the particle configuration. The colloidosome with the lowest packing density and smallest particle size exhibit a $g(r)$ typical of liquid-like structures. On the other hand, the colloidosomes with the highest packing density and the largest particle size show a more regular $g(r)$ and start to resemble a regular, triangular lattice. However, in all cases, the structural order of the particle configurations is relatively short-ranged (< 5 particle diameters), in contrast to what is commonly found for crystalline colloidosomes that are composed of repulsive particles.^{1, 13, 15} Particles with soft (repulsive) interactions are able to rearrange and equilibrate, which results in highly crystalline particle configurations. The attractive potential does not allow for rearrangements and thus jams the particle configuration. Based on the packing densities and the corresponding $g(r)$ it is concluded that the particle configurations are different to what has previously been reported, which is caused by the attractive particle potential.

Monte-Carlo simulation: equilibrium structures

MC-simulations are performed to investigate whether the attractive potential is reflected in the particle configuration. The procedure for the MC simulation is quite straightforward. A certain number of particles and particle diameters, corresponding to the experiments (table 3.2), are randomly placed on a sphere and are allowed to equilibrate. Two types of interactions are used, a purely hard sphere (HS) and a polarizable hard sphere (PHS) potential. The latter interacts attractively through van der Waals-forces. It is found that excellent agreement is obtained in all cases between simulation and experiment with the HS potential (fig. 3.14). When the attractive potential is used, more crystalline particle configurations are obtained. Interestingly, the experimental observations lead to believe that the attractive potential plays an important role, but the attractive potential is not reflected in the particle configuration. The pS particles thus appear to act as purely hard spheres and the particle configurations appear to be determined purely by the excluded volume. However, the visualizations of the colloidosome structures obtained from the hard sphere simulations, shown in fig. 3.14, clearly reveal that the particles do not form a jammed network on the surface of the colloidosome. While the $g(r)$ is in very good agreement with the experiment, these structures are clearly qualitatively different from those observed experimentally.

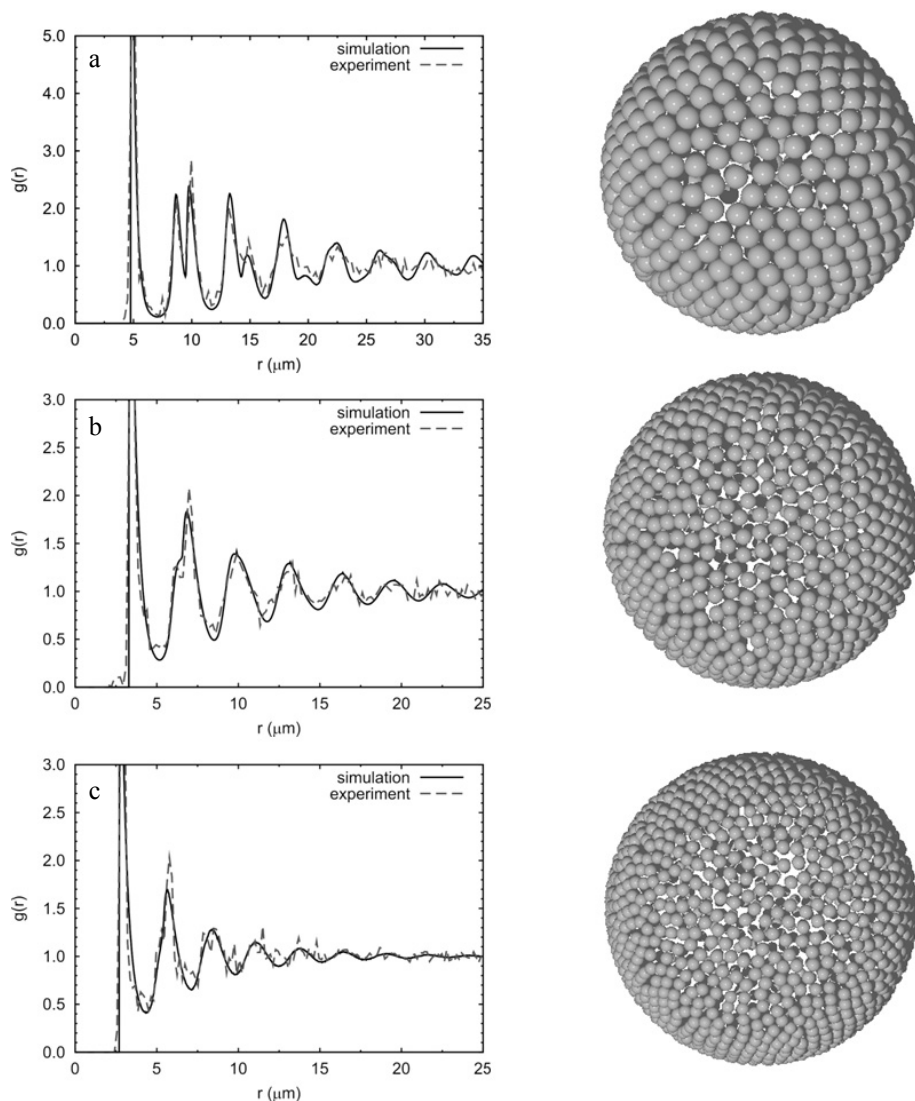


Figure 3.14 MC simulations of the particle configurations. **a - c**, The experimental (dashed red line) and simulated (solid black line) radial distribution functions of colloidosomes with a particle density of respectively 0.98, 0.89 and 0.84. Note that the x,y -scale in the graph **a** is different from the **b - c**.

A likely possibility to explain this discrepancy is that the particles are jammed once they are assembled on the droplet surface and hence cannot attain their equilibrium configuration. This notion is confirmed by observations with the light microscope, which did not reveal

lateral displacement on the droplet surface. Jamming occurs at lower packing densities due to the particle attraction and is more commonly found in colloidal gels and glasses. Nonetheless, equilibration of hard spheres requires rearrangement of the particles. Particle movement is not observed once the Pickering emulsion droplets are formed. However, particles can rearrange during emulsification and the application of shear. During the application of shear the particles will thus arrange as hard spheres, as the interactions between particles are small compared with the shear forces; once the shear is stopped the interparticle forces become dominant. We thus assume that the particles jam as a result of the attractive potential, as soon as the shear is no longer applied.

Diffusion-limited aggregation: non-equilibrium structures

To test this idea we develop a simple model that takes into account both steps in the formation of the colloidosomes, the hard sphere like assembly during shear, and the network formation that we assume occurs after the cessation of shear. To account for the second step in this picture of colloidosome formation, an aggregation routine is developed that resembles diffusion limited aggregation. A number of particles, corresponding to the experimental packing densities (table 3.3), are randomly placed on the surface of the sphere. All the particles are simultaneously and randomly moved over the surface of the sphere. When two particles touch, that is when their distance is equal to or smaller than the diameter, the particles stick and continue moving together. The aggregates move slower than the individual particles. The length of each random movement is inversely proportional to the square root of the aggregate size. Aggregation continues until all the particles form one aggregate.

The insets in figure 3.15 show the resulting structures of the aggregation routine, which show great resemblance to the SEM images of the individual colloidosomes (fig. 3.8) and actually represent colloidal cages. The $g(r)$ is also determined from the aggregated structures and is roughly similar to the experimental and MC-simulated $g(r)$. A critical note must be mentioned. Here the $g(r)$ of the aggregated structures is only determined from one sample, which explains the low resolution. This can be improved by performing the aggregation routine multiple times with several initial, random particle positions. Aggregation is also performed on the highest density states, but is not shown here. The final structures did not show a large difference with the MC-simulated structures. The low-density states did show a significantly different particle configuration, shown in figure 3.15. Both the MC-simulation, as well as the aggregated structure of the colloidosome with

intermediate density, *i.e.* $\rho \cdot d_n^2 = 0.84$, is shown, to make a fair comparison to the final structure.

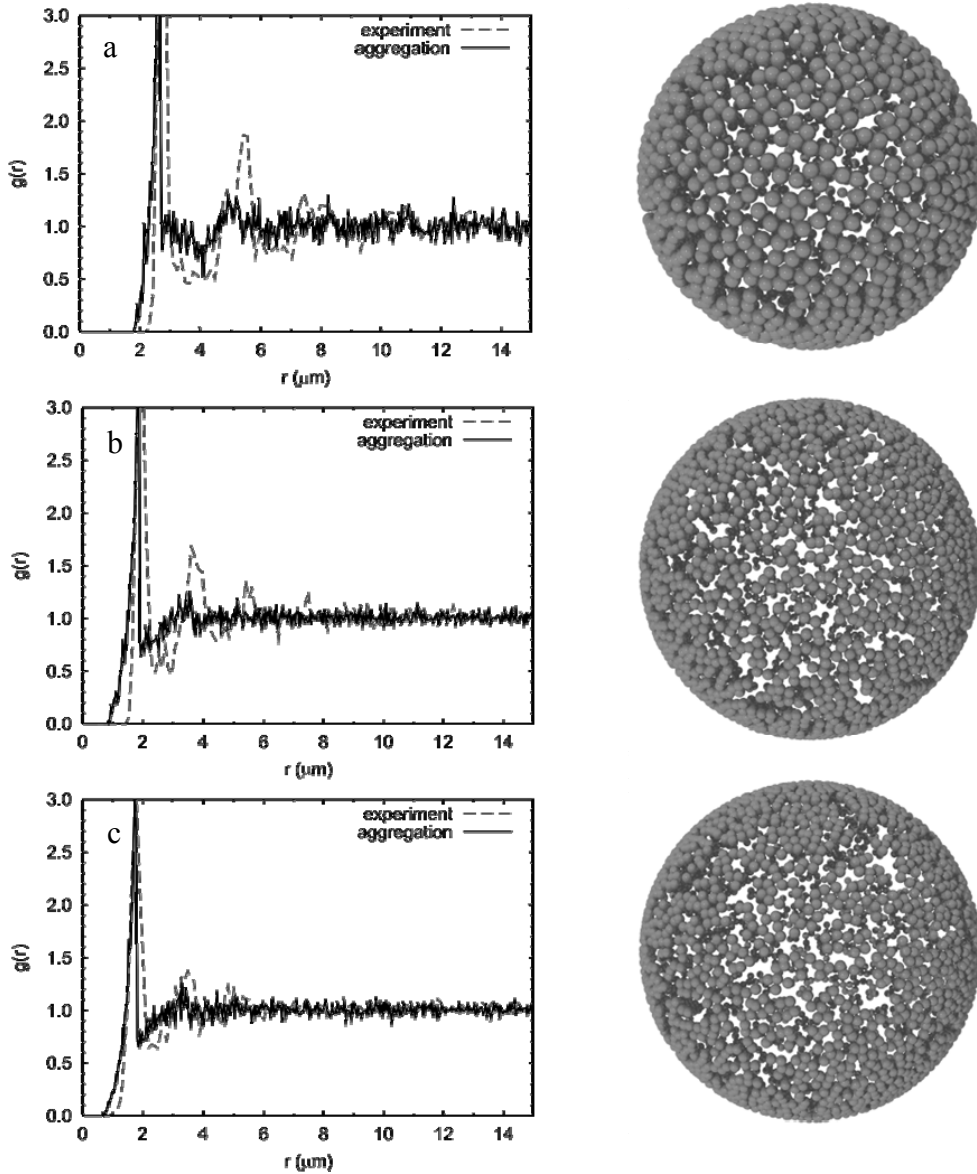


Figure 3.15 Results from the diffusion-limited aggregation. a-c) The experimental (dashed red line) and simulated (solid black line) radial distribution functions of colloidosomes with a particle density of 0.84, 0.75 and 0.74, respectively.

The graphical representations of the colloidosome show great resemblance with the SEM images, although, the aggregated $g(r)$ only roughly matches with the experimental $g(r)$. During aggregation, the particles are allowed to overlap. In fact, this is the criteria for sticking. The extent of overlap can be set and is chosen to be relatively large (overlap criteria when $r < 0.95 d_n$) in our simple simulation. In principle, the onset for the $g(r)$ is discrete and should occur at exactly d_n . This can be seen in the MC-simulated results. We reasoned that during the sintering process to make stable colloidosomes, the particles partly overlap. It is, therefore, incorporated in the aggregation routine, to more closely resemble the experimental situation. In conclusion, a larger data set and optimization of the aggregation procedure is needed to ‘fit’ the experimental results with the theoretical results. Nevertheless, the great resemblance of the graphical representations with the SEM images is very convincing. It can be concluded that the attractive potential plays a role in the aggregation and jamming of particles on the droplet surface, in direct analogy to the role of attractive interactions in the gelation of particle suspensions.

3.4 Discussion

The structural organization of particles on the droplet surface can best be understood as jamming of attractive particles on the droplet surface. There is no additional structuring due to an attractive interaction. In general, jamming of colloids is affected by the extent of attraction, the volume fraction and the shear that is applied to the system. Trappe *et al* proposed a “jamming phase diagram” for attractive colloids that included these three parameters. Shear is applied during emulsification and is required for the formation of small droplets and the adsorption of pS particles to the w/o interface. Moreover, it is concluded from the MC-simulations that the shear allowed the particles to rearrange on the droplet surface. Once the shear is no longer applied, the particles jam on the droplet surface. Visual observation of the particle-stabilized emulsion droplets confirms this. No lateral movement of particles on the droplet surface is observed. The attraction among the particles allows jamming to occur at surface coverages significantly below the close packing limit. This is further illustrated by the remarkable coalescence stability of these systems. For non-attractive particles, coalescence continues until full surface coverage of the droplets is achieved.

The question that still remains is: “How are the different packing densities obtained?” Although the attractive potential does not play a role in the organization at the w/o

interface, it does determine the dispersion and aggregation of the particles in the bulk of the continuous phase. In contrast to what is normally assumed for these systems, the particles are not ideally dispersed as individual units. During emulsification, the particles aggregate and these aggregates are continuously broken up due to the applied shear. An equilibrium aggregate size is attained, which is different for each particle size. The aggregate size in turn directly influences the structure of the formed colloidal cages. The larger particles are more easily dispersed and exhibit an aggregate size that is close to the particle size, which allows these aggregates to assemble at the surface with a high packing density. The smaller particles exhibit an aggregate size that is significantly larger than their particle size and the aggregate structure is by definition more irregular, which prevents the aggregates from packing densely. The aggregation routine supports such an assembly model. Although, the aggregates are formed on the droplet surface and not in the bulk, this does show that the irregular aggregates prevent the formation of an ordered and dense particle configuration. Figure 3.16 schematically demonstrates the assembly into either a dense, hexagonal close-packing or an irregular structure.

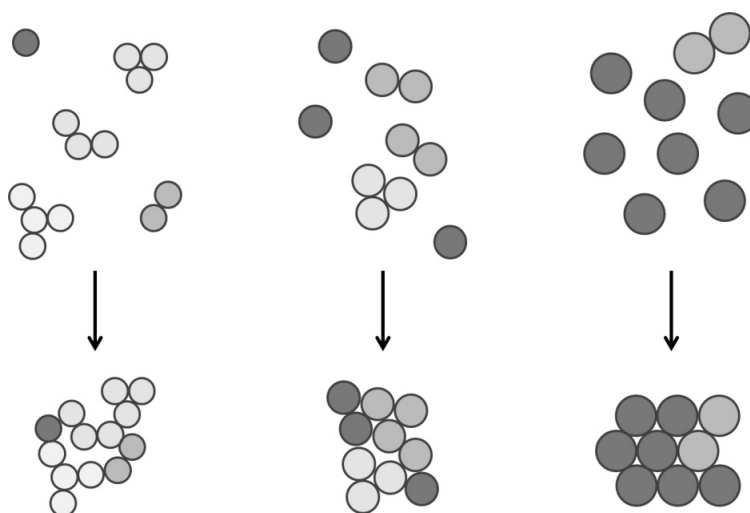


Figure 3.16 Schematic representation of the particle assembly. The particles are initially dispersed in the bulk and are aggregated (above). The extent of aggregation is determined by the particle size and influences the particle configuration of the colloidal cage (below). The different colors blue represent the different aggregate sizes.

3.5 Conclusion

It is demonstrated in this work that the use of attractive particles for the assembly of colloidosomes leads to new types of structures, referred to here as *colloidal cages*. The attractive nature of the interparticle forces proves to be the most important factor in the formation of such colloidal cages. In a first step, our results indicate that this attraction results in the formation of irregular-shaped aggregates that prevent the formation of a dense packing. And, secondly, they are also responsible for the formation of jammed particle networks on the droplet surface which are capable of resisting coalescence even at low packing densities. Using this strategy, colloidosomes with various particle configurations and well-defined porosities can be formed, ranging from network-like to dense, almost crystalline structures. We envisage that besides being useful model systems for the study of gelation phenomena, such structures could find useful applications for instance for the trapping of living cells in systematic biological studies or for the controlled release/dosage in drug delivery systems.

References

1. Dinsmore, A. D.; Hsu, M. F.; Nikolaides, M. G.; Marquez, M.; Bausch, A. R.; Weitz, D. A., *Science* **2002**, 298, (5595), 1006-1009.
2. Lee, R. F., *Spill Science & Technology Bulletin* **1999**, 5, (2), 117-126.
3. Dickinson, E., *Current Opinion in Colloid & Interface Science* **2010**, 15, (1-2), 40-49.
4. Rousseau, D.; Ghosh, S.; Park, H., *Journal of Food Science* **2009**, 74, (1), E1-E7.
5. Lu, S.; Pugh, R. J.; Forssberg, E., *Interfacial separation of particles*. Elsevier: Amsterdam, 2005; Vol. 20.
6. Frelichowska, J.; Bolzinger, M. A.; Pelletier, J.; Valour, J. P.; Chevalier, Y., *International Journal of Pharmaceutics* **2009**, 371, (1-2), 56-63.
7. Binks, P.; Horozov, T. S., *Colloidal particles at liquid interfaces*. Cambridge University Press: New York, 2006.
8. Bon, S. A. F.; Chen, T., *Langmuir* **2007**, 23, (19), 9527-9530.
9. Colver, P. J.; Bon, S. A. F., *Chemistry of Materials* **2007**, 19, (7), 1537-1539.
10. Hsu, M. F.; Nikolaides, M. G.; Dinsmore, A. D.; Bausch, A. R.; Gordon, V. D.; Chen, X.; Hutchinson, J. W.; Weitz, D. A., *Langmuir* **2005**, 21, (7), 2963-2970.
11. Kim, J. W.; Fernandez-Nieves, A.; Dan, N.; Utada, A. S.; Marquez, M.; Weitz, D. A., *Nano Letters* **2007**, 7, (9), 2876-2880.
12. Lee, D.; Weitz, D. A., *Advanced Materials* **2008**, 20, (18), 3498-+.
13. Leunissen, M. E.; van Blaaderen, A.; Hollingsworth, A. D.; Sullivan, M. T.; Chaikin, P. M., *Proceedings of the National Academy of Sciences of the United States of America* **2007**, 104, (8), 2585-2590.
14. Bowick, M.; Cacciuto, A.; Nelson, D. R.; Travesset, A., *Physical Review Letters* **2002**, 89, (18).
15. Bausch, A. R.; Bowick, M. J.; Cacciuto, A.; Dinsmore, A. D.; Hsu, M. F.; Nelson, D. R.; Nikolaides, M. G.; Travesset, A.; Weitz, D. A., *Science* **2003**, 299, (5613), 1716-1718.
16. Lipowsky, P.; Bowick, M. J.; Meinke, J. H.; Nelson, D. R.; Bausch, A. R., *Nature Materials* **2005**, 4, (5), 407-411.
17. Bowick, M. J.; Giomi, L., *Advances in Physics* **2009**, 58, (5), 449-563.
18. Zaccarelli, E., *Journal of Physics-Condensed Matter* **2007**, 19, (32).
19. Gazzillo, D.; Giacometti, A.; Fantoni, R.; Sollich, P., *Physical Review E* **2006**, 74, (5).
20. Hamaker, H. C., *Physica IV* **1937**, 4, 1058-1070.
21. Allen, M. P.; Tildesley, D. J., *Computer simulation of liquids*. Clarendon Press: Oxford, 1987.
22. Frenkel, D.; Smit, B., *Understanding molecular simulation*. Academic Press: San Diego, 1996.
23. Paine, A. J.; Luymes, W.; McNulty, J., *Macromolecules* **1990**, 23, (12), 3104-3109.
24. Binks, B. P.; Lumsdon, S. O., *Langmuir* **2000**, 16, (23), 8622-8631.
25. Tcholakova, S.; Denkov, N. D.; Lips, A., *Physical Chemistry Chemical Physics* **2008**, 10, (12), 1608-1627.
26. Kumar, A.; Wu, J. Z., *Applied Physics Letters* **2004**, 84, (22), 4565-4567.

The background of the entire page is a grayscale scanning electron micrograph (SEM) showing a dense field of spherical polymeric microcapsules. Many of the capsules exhibit a characteristic 'lemon' or 'orange' morphology, with a wrinkled or dimpled surface. The capsules vary in size and are distributed across the entire frame.

4

Steric stabilization

**of Pickering emulsions for the efficient synthesis of
polymeric microcapsules**

www.elsevier.com
X50-5000um

Abstract: Pickering emulsions are widely praised for their extreme stability against coalescence and are, therefore, potentially interesting for the synthesis of new materials, such as colloidosomes, microcapsules, composite particles, foams etcetera. However, for the *efficient* synthesis of such materials, one also has to consider the colloidal stability, as is argued in the introductory chapter. In this study it is demonstrated that steric stabilization is provided to Pickering emulsion droplets by the adsorption of poly(styrene-block-ethylene-co-propylene) (pS-b-EP) and that it is a requirement for the efficient synthesis of polymeric microcapsules. Highly uniform polystyrene (pS) particles of 0.65 μm large are synthesized by soap-free emulsion polymerization. A model Pickering emulsion is then formed by the addition of sodium chloride at a critical concentration of 325 mM and mixing it with either heptane or decane. Subsequently, pS-b-EP is added to the Pickering emulsion. Size exclusion chromatography is used to prove and quantify the adsorption of pS-b-EP onto the Pickering emulsion droplets. A maximum surface coverage of 1.3 mg/m^2 is obtained after 2 hours, which is approximately $1/3^{\text{rd}}$ of the adsorption on a pure pS surface. We believe that the presence of polar sulfate groups on the particle, which initially stabilized the particle in water, reduces the adsorption of pS-b-EP. Microcapsules are formed by heating the Pickering emulsion above the glass-transition temperature of the pS particles. Significant aggregation is observed, if no pS-b-EP is used. The adsorption of pS-b-EP provided steric stabilization to the Pickering emulsion droplets, reduces aggregation significantly and ultimately leads to the successful and efficient synthesis of pS microcapsules.

This chapter is published in *Langmuir*, 2010, **26** (18), pp 14929–14936

4.1 Introduction

The efficient micro-encapsulation is an increasingly important technology for a vast variety of applications, such as food, drugs, phase-change materials and biomedical applications.¹⁻⁵ A promising encapsulation technique is the formation of so-called Pickering or solid-stabilized emulsions and their subsequent processing to form stable capsules.^{6, 7} Pickering emulsions are stabilized by solid particles that are attached to the oil-water interface.⁸ The driving force for solid particles to self-assemble at an water-oil (w/o) interface is the reduction of the total interfacial energy, which is mainly realized by a reduction of the surface area between the dispersed and continuous phase.⁹ By definition, a particle is able to adsorb to the o/w interface if the three-phase contact angle (θ) is between 0° and 180° . θ is defined by Young's equation¹⁰ (eq. 1.1, see also fig. 1.2).

After the formation of a Pickering emulsion, stabilization of the particle layer around the droplets is required to obtain mechanically stable capsules, which can be achieved in a variety of ways. For example, a polymer can be adsorbed to physically cross-link the particles^{6, 12-14} or the particle layer can be chemically cross-linked.¹⁴⁻¹⁷ In the case of polymer particles, heating above the glass-transition temperature (sintering) allows the particles to partially or completely fuse and form a solid polymer shell.^{7, 18-20} A more recent development is the formation of an interpenetrating polymer network throughout the particles that reinforces the particle layer.²¹ The above-mentioned methods provide the material scientist with an extensive toolbox to synthesize novel materials. However, the experiments are performed on a small scale and are generally inefficient. For example, the physical or chemical cross-linking can take place between particles located at different emulsion droplets. Similarly, during the coalescence of particles to form a uniform shell, sintering can also lead to the aggregation of emulsion droplets. These disadvantages can be circumvented by working with low solid contents or specially designed set-ups. For example, Cayre used a light microscope to image a single colloidosome and study the sintering process.¹⁸ Laib on the other hand performed the sintering process on a larger scale in a stirred reactor, but the sintering is not selective to the emulsion droplets and significant aggregation occurred.¹⁹

The reason for aggregation of the emulsion droplets can be easily understood if one considers the colloidal stability of the particles that are used to form the Pickering emulsion. Various particles can be used as a solid-stabilizer, such as silica particles, clay and latex particles. Most of these particles are charge-stabilized and can be easily dispersed

in water. The charged groups on the surface strongly hydrate the particle and generate electrostatic repulsion when another particle approaches. However, the charge not only ensures colloidal stability it also prevents particles from approaching and adsorbing to the w/o interface²², because the interface is usually charged.²³ In practice, particles are accommodated at the w/o interface by screening of the electrostatic repulsion with electrolytes at high concentrations.^{24, 25} The ‘rule of thumb’ is that Pickering emulsions are obtained under conditions that correspond to weakly flocculating particles. S. Tcholakova *et al.* described the role of the electrostatic barrier to particle adsorption more elaborately in a review on solid-stabilized emulsions²². The need to screen electrostatic interactions in order to obtain a Pickering emulsion, results in flocculating emulsion droplets. This consequence is illustrated in a paper by Bon, in which he reported about the synthesis clay armored polymeric particles.²⁶ Salt is added to force the clay particles to the w/o interface and stabilize the monomer droplets. The polymerization was successful due to coalescence stability. However the final latex was unstable and settled in time. Dialysis of the final latex and the removal of salt resulted in a stable latex.

The previous paragraph describes the formation and stability of normal (o/w) Pickering emulsions. The same accounts for inverse (w/o) Pickering emulsions, however the origin of colloidal instability is different. The oil-phase of inverse emulsions does not allow sufficient electrostatic stabilization to obtain colloidal stability. Due to the low dielectric constant ($\epsilon \sim 2$) of most oils, ions cannot dissociate to generate the required surface charge.²⁷ Although, Laib and Routh successfully demonstrated the formation of microcapsules under mild conditions, the scanning electron microscopy (SEM) images that are presented in their paper show significant aggregation.¹⁹ The colloidal instability of inverse Pickering emulsion by charged particles is also demonstrated in the present chapter. Pickering emulsion droplets, either normal or inverse, need to be additionally stabilized in order to prevent aggregation and to allow the efficient synthesis of robust capsules. Others already realized this and published several methods in the scientific literature. Velez *et al.* adsorbed casein to lock the particles together and provide steric stabilization to the droplets.^{14, 28} Silica particles modified with long alkyl chains have been used to synthesize Pickering emulsions and to improve their dispersion.²⁹ Weitz⁶ and Van Blaaderen³⁰ and coworkers used sterically stabilized poly(methyl methacrylate) (pMMA) particles to form sterically stabilized Pickering emulsion droplets. In the present chapter we demonstrate a different approach to synthesize sterically stabilized Pickering emulsion droplets, in which a block copolymer is adsorbed onto the droplets to improve the dispersion of the droplets. It

is demonstrated in this paper that the additional steric stabilization of Pickering emulsion droplets by the adsorption of poly(styrene-block-ethylene-co-propylene) (pS-b-EP) is an absolute requirement for the efficient synthesis of novel materials.

In this chapter, a water-in-alkane Pickering emulsion that is stabilized by polystyrene (pS) particles is described, where the alkane is either heptane or decane. The emulsion droplets are then sterically stabilized by the addition and adsorption of pS-b-EP onto the particles. It is known that pS-b-EP can adsorb onto polymeric particles in hydrocarbon solvents.³¹ Awan *et al.* used this type of block copolymers as a polymeric stabilizer for anionic dispersion polymerization of styrene in hexane.³² Holderle *et al.* even used pS-b-EP to stabilize a pMMA dispersion in hydrocarbon solvents.³³ Therefore, pS-b-EP seemed suitable for the steric stabilization of pS particle-covered droplets. It is shown in this chapter that the Pickering emulsion droplets with the adsorbed pS-b-EP are stable against coalescence as well as aggregation with other droplets and can, therefore, be efficiently processed into microcapsules. This principle is demonstrated by sintering the droplets to form pS microcapsules both with and without the adsorbed block copolymer (fig 4.1).

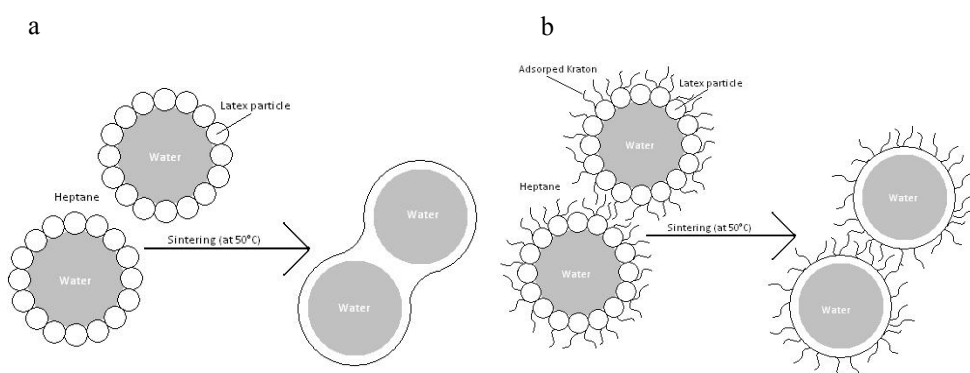


Figure 4.1 Illustration of the studied system. *a)* normal and *b)* sterically stabilized Pickering emulsion droplets and their subsequent processing.

The chapter is divided into the following parts. First, the synthesis of pS particles by soap-free emulsion polymerization (SF-EP)³⁴ is described. Second, the optimization of the conditions under which these particles form Pickering emulsions is reported. Third, the adsorption of pS-b-EP onto Pickering emulsion droplets is demonstrated and quantified by size exclusion chromatography (SEC). Finally it is shown that the adsorbed pS-b-EP

provides steric stabilization against aggregation, which has a beneficial effect on the processing of these Pickering emulsions.

4.2 Experimental

Materials Water is double de-ionized with a purification system. Styrene (99%, Merck) is passed over a column with aluminum-oxide (activated basic, Sigma Aldrich) prior to use to remove inhibitor. The inhibitor-free styrene is refrigerated for later use. Potassium persulfate (KPS) (Sigma Aldrich) is recrystallized twice from distilled water. Sodium chloride (NaCl) (99%, Sigma Aldrich). n-Heptane (>96% Biosolve) and n-decane (>97%, Sigma Aldrich). pS-b-EP (Kraton G1702H) is used as received. Kraton G1702H is a linear diblock copolymer of 155,000 g/mol and low polydispersity (1.09). The styrene content is 28 weight percent.

Particle synthesis SF-EP is performed in a 250 mL reactor equipped with four baffles and a four-blade pitched impeller. 214.75 g water and 25.00 g styrene are charged in the reactor. The reactor is purged with nitrogen for 45 minutes to remove oxygen from the mixture and finally heated to 70 °C. The polymerization is started by the addition of 0.25 g KPS dissolved in 10 g of water. The mixture is stirred at an impeller speed of 300 rotations per minute (rpm). The polymerization is carried out for at least 24 hours to assure almost complete conversion. The solid-content of the final dispersion is measured by gravimetric analysis. The particles are imaged with a desktop SEM (Phenom, FEI company). The sample holder is covered with double-sided conducting carbon tape and a droplet of the latex is cast on the sticker. The sample is dried under air and sputter-coated with a thin layer of gold before imaging with SEM. The particle size distribution is determined from the SEM image with image processing software (ImageJ).

The colloidal stability of the final latex is studied by measuring the particle size as a function of the NaCl concentration. The concentrations ranged between 10 and 750 mM. The particle size distribution of the latex at various NaCl-concentrations is measured with Dynamic Light Scattering (DLS) on a Malvern Zetasizer Nano-ZS at 20 °C. The samples are prepared by adding 5 microliter (μl) of latex to 10 mL NaCl-solution. During 10 minutes every 5 seconds a measurement is performed from which an average particle size is calculated.

Pickering emulsion The NaCl-concentrations that are used to study the formation of Pickering emulsions range between 100 and 1500 mM. 5 mL of NaCl-solution is added to 7.64 g of the latex. 100 mL of heptane is added to form the emulsion. The mixture is homogenized at 10,000 rpm for 15 seconds with a rotor-stator mixer (IKA Ultra-Turrax T25 basic). The amount of latex, and herewith the number of particles, and the volume of the dispersed phase is chosen such that the droplets have a predicted diameter of 50 μm . For the calculation of the droplet size it is assumed that all the latex particles are accommodated at the w/o interface, the particles are hexagonally packed and curvature effects are neglected (eq. 2.2). The Pickering emulsions are analyzed by light microscopy (LM). The droplet diameter is determined from the images to study the formation of the Pickering emulsion.

Adsorption of pS-b-EP A solution of pS-b-EP is added to the Pickering emulsion to allow the adsorption on the pS particles, which are now exposed to the oil-phase. The adsorption is followed in time by measuring the concentration of unadsorbed pS-b-EP in the continuous phase. The concentration of pS-b-EP in decane is determined with SEC. The SEC set-up consisted of a Waters Alliance 2695, a two-column set (Polymer Labs Mixed C), detectors in series: Dual Wavelength UV Detector (Waters, model 2487); and Differential Refractive-Index Detector (DRI) (Waters, model 2414). The eluent is THF at a flow rate of 1.0 $\text{mL}\cdot\text{min}^{-1}$. Data acquisition and processing are performed with Waters Breeze software. The calculated molar masses are based on a calibration curve for pS standards (molar mass range: 650 - 1.5×10^6 $\text{g}\cdot\text{mol}^{-1}$) of low polydispersity (Polymer Laboratories). Initially, a calibration curve is made to relate the integrated signal intensity to the solution concentration of pS-b-EP in decane. For this purpose a single pS-b-EP solution is prepared and, instead of using different solutions with known concentrations, different injection volumes (100 - 20 μL , table 4.1) of a single pS-b-EP solution are used. Each chromatogram is then integrated to obtain the signal intensity and related to the amount of pS-b-EP in solution to obtain the final calibration curve.

Table 4.1. Injection volumes that are used for the calibration curve.

Injection volume [μL]	100	80	60	40	20
pS-b-EP concentration [mg/mL]	1.05	0.84	0.63	0.42	0.21

67 mg of pS-b-EP is added to 100 mL of decane and is heated to 40 °C until complete dissolution is assured. The Pickering emulsion is made with the pS-b-EP solution in decane under the optimized conditions, as described above. The obtained Pickering emulsion is then transferred to a batch reactor equipped with four baffles and a four-blade pitched impeller and stirred for 3 hours at 30 °C. At timed intervals samples are taken for SEC analysis to determine the kinetics of adsorption. After a sample is taken and no further stirring is applied, the droplets settled. The supernatant pS-b-EP solution is then filtered to remove any particles or dust that is present. Finally, 100 μ L of this solution is injected for SEC measurement.

A reference experiment is performed to determine the maximum amount of pS-b-EP that can be adsorbed onto the pS particles. In this case, a Pickering emulsion is not formed, but only the pS particles are dispersed in decane. 7.64 g latex is freeze-dried to remove the water and the particles are subsequently redispersed in 100 mL of a 0.67 mg/mL solution of pS-b-EP in decane. Ultra-sonication (90% amplitude for 2 minutes) is used to disperse the pS particles in decane. After sonication the mixture is stirred at 200 rpm at 30 °C. The conditions under which this experiment is performed are similar to the previous conditions, with respect to pS-b-EP concentration and number of particles. At timed intervals samples are taken for SEC analysis to determine the adsorption kinetics.

Sintering The Pickering emulsion, both with and without the adsorbed pS-b-EP, is heated to 50 °C while it is stirred at 200 rpm for 90 minutes. The resulting pS microcapsules are imaged by SEM (Jeol, JSM-500) and light microscopy. For SEM measurements, the sample holder is covered with double-sided conducting carbon tape and a droplet containing the polymer microcapsules is cast on the holder. The sample is dried under air and finally sputter-coated a thin layer of gold before it is imaged with SEM.

4.3 Results

Before any Pickering emulsion can be made, one first has to obtain the stabilizing particles. For this study SF-EP of styrene is performed. SF-EP is a relatively straight-forward technique to produce charged particles³⁴ and the latex particles are known to form inverse Pickering emulsions.²⁵ No work-up of the final latex is required and the particles can be driven towards the interface by the addition of salt.

4.3.1 Particle synthesis

The SF-EP of styrene, as performed in this work yields stable latexes consisting of highly uniform pS particles. The uniformity of the particles is demonstrated by the regular, hexagonal packing that can be observed in the SEM image of figure 4.2. The SEM picture is analyzed with ImageJ to obtain the particle size distribution, which is shown in figure 4.2. The number average particle diameter is $0.65\ \mu\text{m}$ and the polydispersity index is 1.005 -. Gravimetric analysis of a sample of the final latex yields a solid-content of 0.08 g/g. The size of the pS particles is confirmed with DLS, which can be found in figure 4.3 at 0 mM NaCl-concentration. The particle diameter ($0.72\ \mu\text{m}$) is slightly larger than what is calculated from the SEM image. The difference in diameter could be ascribed to the hydrodynamic volume of the double-layer surrounding the particle and is taken into account with DLS and not with SEM. Minor flocculation can also result in somewhat larger particles than what is observed with SEM.

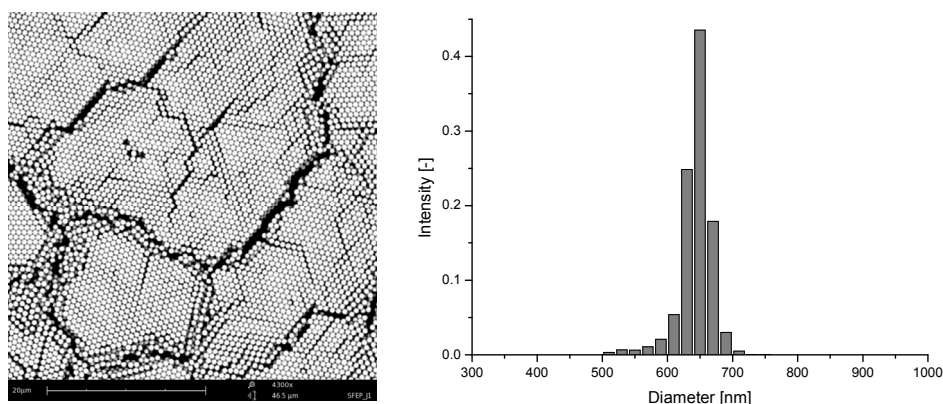


Figure 4.2 pS particles Left: SEM image of the pS particles obtained with SF-EP. Right: Particle size distribution obtained from analyzing the SEM image. Average particle diameter: $0.65\ \mu\text{m}$ and polydispersity: 1.005 -.

Colloidal stability

The addition of NaCl screens the electrostatic repulsion between the particles and promotes aggregation of particles. DLS will recognize aggregates as an increase of the particle size and can therefore easily be used to assess the colloidal stability. The critical salt concentration for aggregation can therefore be found by measuring the particle size as a

function of the NaCl-concentration. Figure 4.3 shows the average particle diameter as a function of the NaCl-concentration. Up to 250 mM, the latex is stable and has a constant particle size of 723 nm. From approximately 500 mM, the latex becomes unstable and the particle size increases strongly with the NaCl-concentration. These results are consistent with results from other published work that deal with sulfate-functionalized particles, which have a critical coagulation concentration around 300 mM.²⁵ Below 250 mM the particles do not adsorb to the w/o interface and above 500 mM not only are the particles accommodated at the interface, but aggregate in the aqueous phase. Ideally, a concentration between 250 and 500 mM NaCl is chosen to form a Pickering emulsion.

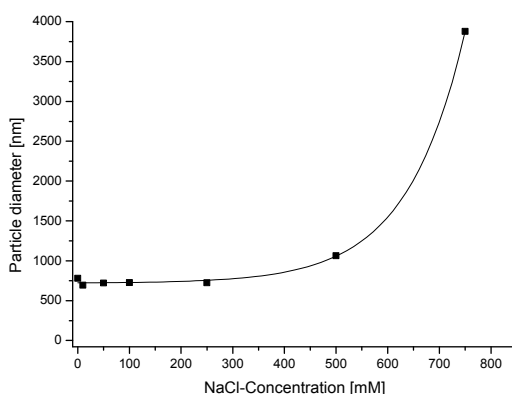


Figure 4.3 Average particle diameter of the pS latex as a function of NaCl-concentration. The particle diameter is measured by DLS.

4.3.2 Pickering emulsion

To further investigate the optimal conditions for the formation of a Pickering emulsion, several NaCl-concentrations are used. The general procedure is as follows: First, a 7.64 g of latex is added to a 5 mL of NaCl-solution. The reported concentrations are the final concentrations of the latex and NaCl-solution together. Second, 100 mL heptane is added to form the continuous phase. In all cases, two separate phases are still visible. A turbid latex phase that settled to the bottom of the flask and a clear oil-phase is found on top. Only after homogenizing the mixture at 10,000 rpm, the inverse Pickering emulsions are formed. If no salt is added, macroscopic phase separation occurred almost instantaneously and no emulsion droplets are formed. In the other cases, stable emulsion droplets are formed (fig.

4.4). However, the emulsion droplets settled immediately when no stirring is applied, which is caused by the large density difference between the dispersed- (water) and continuous-phase (oil) and the inherent colloidal instability of the Pickering emulsion.

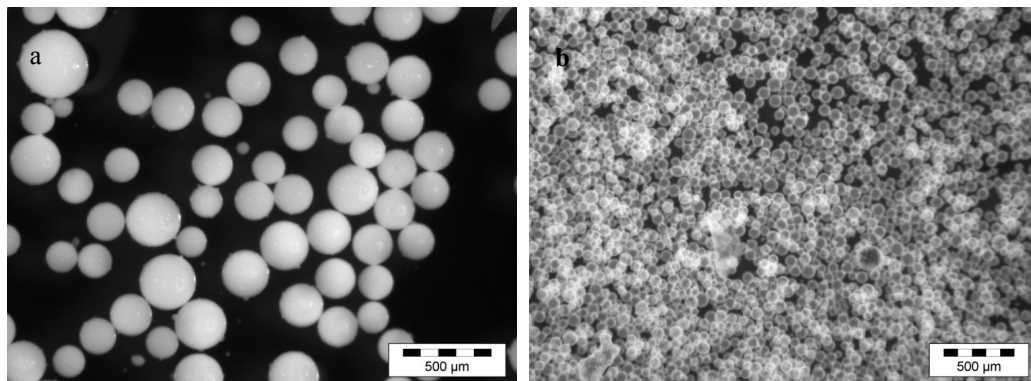


Figure 4.4 Light microscopy images of inverse Pickering emulsion droplets. **a)** Pickering emulsion is made with a NaCl-concentration of 250 mM and **b)** with a NaCl-concentration of 625 mM.

The amount of latex is chosen in such a way that, in the case that all the particles are accommodated to the interface and are densely packed, the average droplet diameter should be 50 μm. However, it is found that at low NaCl-concentrations relatively large droplets are formed, which can be ascribed to incomplete particle accommodation, *i.e.* not all the pS particles move to the w/o interface. This is confirmed by the LM image at 250 mM NaCl that shows stable, but turbid emulsion droplets. Here, most of the particles are still located in the interior of the droplet. In the LM image at 650 mM NaCl smaller droplets are formed, which are opaque, but clearly most of the particles are accommodated at the w/o-interface. Figure 4.5 shows the average droplet diameter and the distributions within the droplet diameter at various NaCl-concentrations. It can be concluded from this graph that the critical NaCl-concentration for particle accommodation is 325 mM. Above this value, the droplet diameter has a constant value of 89 μm and further increasing the salt concentration has no significant effect. The droplet diameter, below the critical value, is strongly increasing with a decreasing NaCl-concentration, which means that the number of particles that is accommodated at the interface decreases accordingly. The final droplet diameter is

larger than the expected value of 50 μm , which can be ascribed to incomplete particle accommodation (eq. 2.2) In this system, both particle aggregation and particle accommodation at the interface take place simultaneously, because their critical NaCl concentrations are similar. In fact, aggregates of particles are adsorbed to the w/o-interface and, therefore, less surface area is covered by the particles leading to a larger droplet diameter than expected. Based on the experimental droplet diameters, the available surface onto which pS-b-EP can adsorb is, therefore, around half of the maximum value.

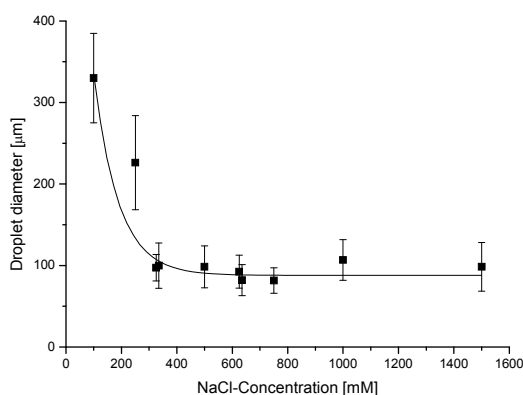


Figure 4.5 The droplet diameter as a function of the NaCl-concentration that is used to form the Pickering emulsion. The droplet size is determined from light microscopy images.

At this point, a model Pickering emulsion can be created that consists of water droplets, covered with pS particles that are exposed to the oil-phase. The most important parameter in forming this Pickering emulsion is the NaCl-concentration. 325 mM $\text{NaCl}_{(\text{aq})}$ proved sufficient to destabilize the latex and optimally form the inverse Pickering emulsion. The other parameters that could influence the formation of the Pickering emulsion, such as stirring speed, time, the amount of latex and oil-phase, are kept constant and will be the same as described above. Now, from the oil-phase pS-b-EP can be adsorbed to the surface of the pS particles and provide additional steric stabilization to the emulsion droplets.

4.3.3 Adsorption pS-b-EP

In a paper of Awan *et al.* pS-b-EP has been used as a polymeric stabilizer in the dispersion polymerization of styrene in aliphatic hydrocarbons.³² In that case, steric stabilization of the particles is achieved by the absorption of the pS-block onto the particle, while the poly(ethylene-co-propylene) block remains soluble in the solvent. The adsorption of pS-b-EP onto pS surfaces is measured by ellipsometry and yielded a maximum surface coverage of 4 mg/m². The adsorption of pS-b-EP, onto the pS particle covered emulsion droplets, is proven and quantified by SEC, to be sure that any beneficial effect is caused by the presence of pS-b-EP. The adsorption is determined by measuring the concentration of free, un-adsorbed polymer in the continuous phase. SEC is used for this purpose, because it is renowned for the quantitative analysis of the molecular weight of polymers. Additionally, the integration of a chromatogram yields direct information on the amount of polymer and is used here to measure concentrations of polymer solutions³⁵.

Calibration GPC

Initially, a calibration curve had to be constructed to relate the integrated signal intensity of the chromatogram with the solution concentration. A single pS-b-EP solution is prepared and 5 different volumes are injected in order to simulate different concentrations. It is made sure that the concentrations are in the same order of magnitude as the concentrations that are used by Awan *et al.*. The chromatograms are collected in figure 4.6, which clearly show that the signal intensity regularly decreases with the concentration. Another observation is, however, that the retention time shifts to lower values with decreasing injection volumes. Apparently, the molecular weight of pS-b-EP is changing, which cannot be the case since the same solution used. In fact, this is an artifact that is caused by using different injection volumes. In hydrocarbon solvents pS-b-EP forms micelles and when injected into the SEC setup the micelles slowly dissolve in the THF. Dissolution is generally slower than the chromatographic process. In the case of larger injection volumes more material has to dissolve and therefore tends to elute later. Similar effects are found in a study performed by Phillipsen *et al.*³⁶ Fortunately, it does not affect the calibration itself. A linear calibration curve with an excellent fit is obtained, when each chromatogram is integrated and plotted against the concentration (fig. 4.7).

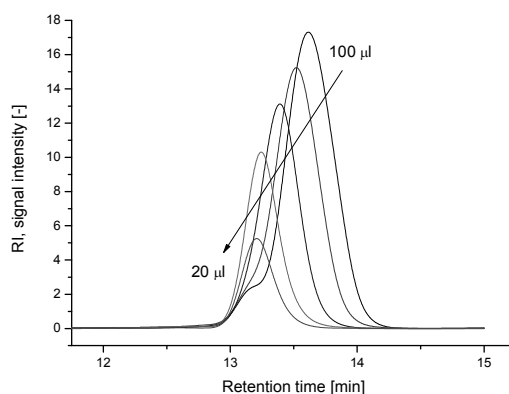


Figure 4.6 SEC-traces of a 1.05 mg/mL pS-b-EP solution in decane measured with different injection volumes ranging from 100 to 20 μL , with a step size of 20 μL , which correspond to different concentrations (Table 4.1).

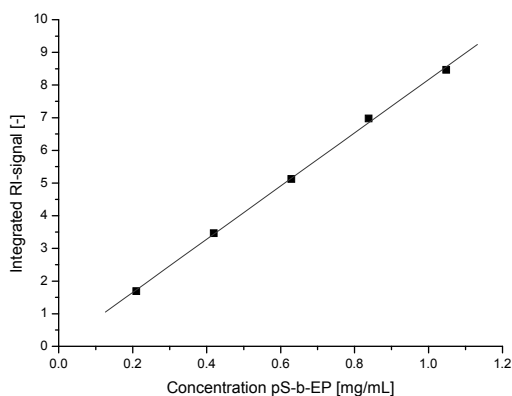


Figure 4.7 Calibration curve of the pS-b-EP concentration and the integrated RI signals from the chromatograms taken at different injection volumes. The red line is a linear fit of the data points.

Adsorption measurement

The Pickering emulsion is formed in a pS-b-EP/decane solution, under the optimized conditions as described above. Decane is used as the continuous phase instead of heptane, because heptane proved too volatile and evaporated easily during sample preparation and, therefore, gave a false representation of the adsorption. It is found that a change of the oil-

phase did not affect formation of the Pickering emulsion. When the pS particles are accommodated at the w/o interface, a pS surface is exposed to the oil phase, which allows pS-b-EP to be adsorbed. The adsorption profile of pS-b-EP is determined as described hereafter, see figure 4.8 to 4.10. Figure 4.8 shows the chromatograms of the samples taken at different times. The differences are small, but a clear and consistent decrease in signal intensity is observed. Each chromatogram is integrated and the concentration of unadsorbed pS-b-EP in decane is calculated from the calibration curve (fig. 4.7). The results are collected in figure 4.9. The adsorption profile is finally calculated from the change in concentration with respect to the initial concentration and the available pS surface that is exposed to the oil-phase (fig. 4.10). The pS surface that is available for adsorption is calculated from the average droplet diameter of the Pickering emulsion and the number of particles that is present in the system. As mentioned earlier, the droplet diameter is larger than expected, which means that the number of pS particles that is exposed to the oil-phase is actually 1/2 of the total number of particles. Moreover, the particles that are attached to the interface are partly immersed in the oil phase and in the water phase. The three-phase contact angle (θ) determines the extent of immersion and is assumed at a typical value of 120° . $3/4^{\text{th}}$ of the particle surface is then exposed to the oil-phase. A wide range of values for θ of sulfate functionalized pS particles at alkane/water interfaces have been reported ($101^\circ < \theta < 130^\circ$).^{37, 38}

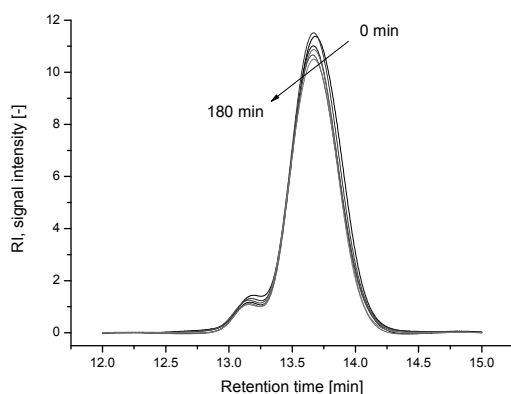


Figure 4.8 Chromatograms of the samples taken in time, which show a decrease in concentration of unadsorbed pS-b-EP in the continuous phase.

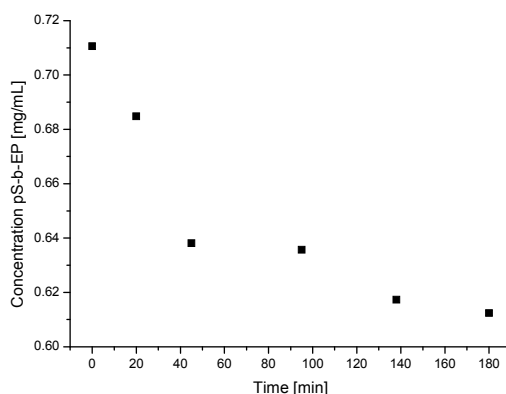


Figure 4.9 The adsorption profile of pS-b-EP onto Pickering emulsion droplets.

The adsorption profile initially shows a fast increase in the amount pS-b-EP on the droplet surface and stabilizes after approximately 2 hours at a surface coverage of 1.28 mg/m^2 . The adsorption profile is qualitatively similar to what is found by Awan *et al.*³² However, the final surface coverage is approximately $1/3^{\text{rd}}$ of their maximum adsorption, which gave a final surface coverage of 4 mg/m^2 . The significant difference in adsorption can partly be explained by different experimental conditions. For example, a different solvent is used to dissolve pS-b-EP and the nature of the oil-soluble block is different. Awan *et al.* adsorbed poly(styrene-block-butadiene) from hexane onto pS surfaces. Another, more important explanation is found in the nature of the pS surface. The particle surface is not pure pS, but additionally consists of sulfate groups that initially stabilized the particles in water. Sulfate groups are highly polar, which is unfavorable for the adsorption of pS-b-EP since it preferably adsorbs onto apolar surfaces, such as pS and pMMA.^{31, 32}

Another experiment is performed to gain more insight in the adsorption of pS-b-EP on sulfate-functionalized pS particles. The particles are separated from water by freeze-drying and redispersed in decane in the presence of pS-b-EP. The same measurements are performed as described above. The final adsorption profile is included in figure 4.10. Qualitatively similar behavior is observed as with the adsorption on the Pickering emulsion droplets. However, adsorption is significantly faster than the Pickering emulsion. Adsorption already stabilizes after approximately one hour at a surface coverage of 1.52 mg/m^2 . The reason for slower adsorption in the case of the Pickering emulsion could be due

to the presence of water. Particle adsorption at the w/o interface is a turbulent process, which can lead to a fraction of dissociated sulfate groups and a partially hydrated surface.³⁹⁻

⁴¹ Hydration of the particle surface that is in contact with the oil phase provides an additional barrier for pS-b-EP to adsorb. Moreover, the oil-phase is saturated with water and even the particle itself can contain water. Both effects enhance the polarity of the particle surface and slow down the adsorption of pS-b-EP.

The final surface coverage in both experiments seems similar, especially if one takes into consideration that the three-phase contact angle is not exactly known for these particles. The three-phase contact angle is assumed to be 120° . However, small differences can lead to different values for the available pS surface. If the contact angle is smaller, less pS surface is exposed to the oil and leads to higher surface coverages. In this case, a contact angle of 105° would yield a similar final surface coverage in both experiments. It is likely that in both cases the same amount of pS-b-EP is adsorbed, because there is no reason to believe that the adsorption should be different. The final surface coverage is still $1/3^{\text{rd}}$ in comparison with the work of Awan *et al.* We strongly believe that this is due to the nature of the pS surface, *i.e.* the presence of polar sulfate groups.

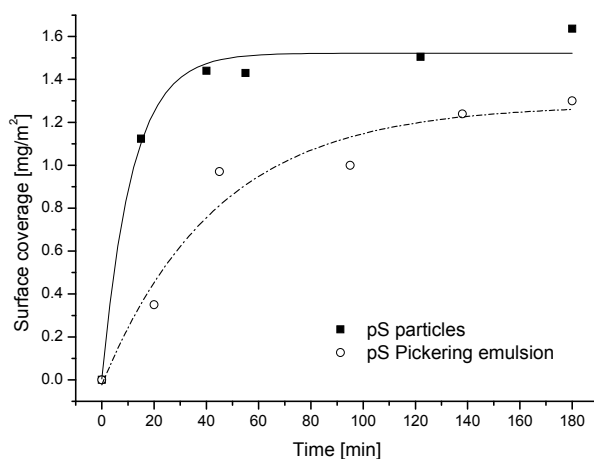


Figure 4.10 Adsorption profiles of pS-b-EP on the pS Pickering emulsion and the pS particles redispersed in decane.

In conclusion, we have shown that pS-b-EP is adsorbed onto the pS particles that cover the Pickering emulsion droplets, although to a smaller extent as measured on pure pS surfaces. The Pickering emulsion droplets are now both stabilized against coalescence, due to the presence of the particles, and the emulsion droplets are sterically stabilized against aggregation by pS-b-EP.

4.3.4 Microcapsule formation

A simple experiment is performed to study the effect of pS-b-EP on the synthesis of pS microcapsules. Two Pickering emulsions, with and without adsorbed pS-b-EP, are sintered in order to fuse the particles together and form a solid shell around the droplet. The two emulsions are stirred at 400 rpm and heated to 50 °C. Although, the T_g of pS is 100 °C, heating to 50 °C proved sufficient to fuse the individual particles, because decane has a plasticizing effect on pS. The result of sintering the two Pickering emulsions can be seen in the light microscopy images of figure 4.11. In both cases, the emulsion droplets are still visible and it is clear that a uniform pS layer has formed around the droplets. Before sintering, the Pickering emulsion droplets are opaque (fig. 4.4), due to the presence of individual particles. However, after sintering a transparent polymer layer has formed around the droplet, which indicates that the individual particles are no longer present. A distinct difference due to the presence of pS-b-EP is observed. The Pickering emulsion droplets aggregate dramatically when no pS-b-EP is used. In this case, the droplets are not sterically stabilized, meaning that particles from different droplets fused together. On the other hand, if pS-b-EP is added, practically no aggregation between different droplets is observed and fusion only occurs between particles of the same droplet. It can be concluded that the adsorption of pS-b-EP, indeed, provides sufficient steric stabilization against aggregation and improves the efficiency to produce novel materials from Pickering emulsions, such as polymeric microcapsules.

Figure 4.12 shows a SEM micrograph of pS microcapsules that are made by sintering a pS-b-EP stabilized Pickering emulsion. Figure 4.12 clearly demonstrates that the particles have been completely fused to form a uniform film and that aggregation is minimal. The indentations and fractures are an artifact due to drying, which is necessary for sample preparation in SEM.

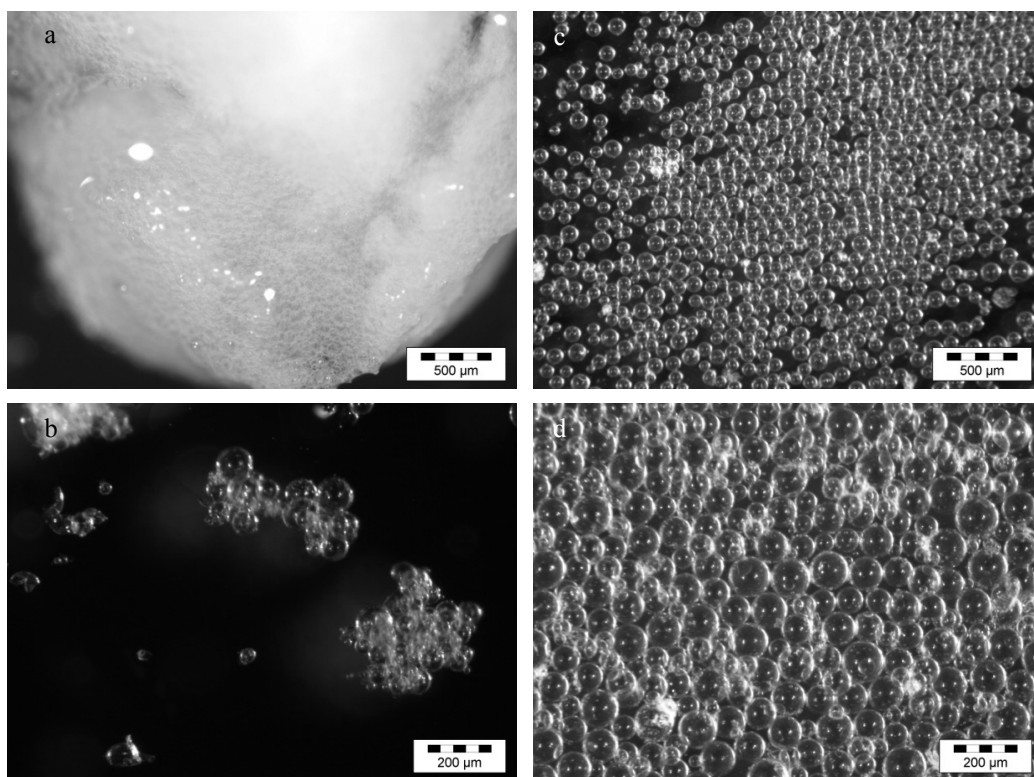


Figure 4.11 Light microscopy images of two Pickering emulsions that are heated to 50 °C for 60 minutes. **a, b)** left column: no pS-b-EP is used. **c, d)** right column: pS-b-EP is adsorbed on the droplets.

4.4 Discussion

The results clearly demonstrate the flocculating nature of Pickering emulsions. In this particular case, the reason is quite clear. The pS particles produced in a surfactant free emulsion polymerization are stabilized by ionic sulfate groups and are initially dispersed in water. After the interfacial adsorption, the particles and, therefore also, the Pickering emulsion droplets are exposed to the oil phase and are no longer colloidally stabilized. The low dielectric constant of the oil-phase, does not allow dissociation and ionization of the surface functional sulfate groups. As a result, the particle-stabilized emulsion droplets flocculate and irreversibly aggregate when the temperature is raised above the T_g . Flocculation cannot be avoided, because the critical salt concentration for coagulation and

particle adsorption are practically the same. The adsorbed pS-b-EP can prevent the aggregation of the pS particle-stabilized emulsion droplets.

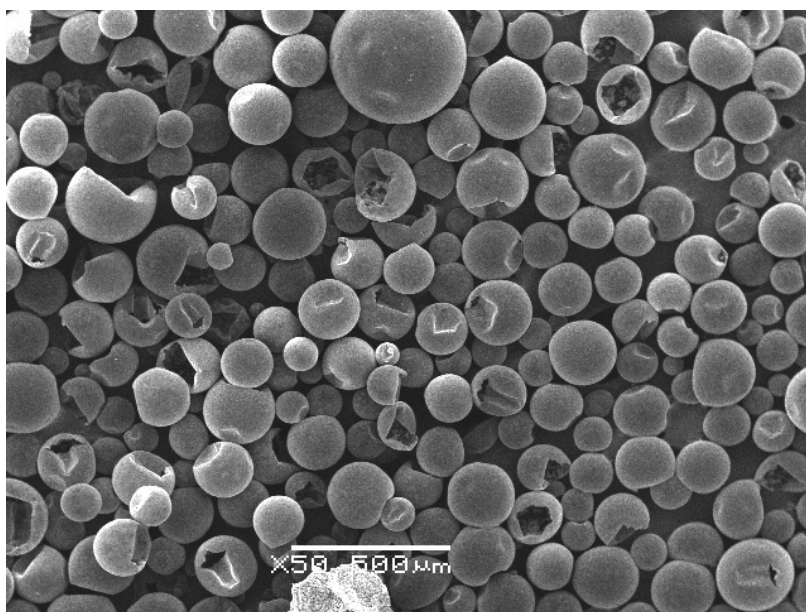


Figure 4.12 SEM image of hollow pS microcapsules.

However, besides additional steric stabilization, the adsorption of pS-b-EP affects the wetting properties of the particles and herewith the equilibrium position at the w/o interface. Chapter 5 reports a theoretical study on the effect of the polymeric stabilizer on the wetting properties of colloids. The results clearly show that there is a strong effect of the polymeric stabilizer and the possibility arises that the particles are completely desorbed from the w/o interface, which inevitably leads to coalescence. This is not desirable for the efficient production of microcapsules. Interestingly, this effect has not been observed in for the system studied in the present chapter. A possible reason can be found in the structure of the particle layer that surrounds the droplet. In this case, a multilayer of attracting particles is formed at the w/o interface, which is strong enough to resist desorption. Another reason is that the heptane or decane softens the pS particles, which additionally reinforced the interactions among the particles and allowed the formation of a rigid stabilizing particle layer around the droplets.

4.5 Conclusion

Monodisperse polystyrene particles of 0.65 μm are synthesized by soap-free emulsion polymerization. The latex is sufficiently de-stabilized, by the addition of sodium chloride at a critical concentration of 325 mM, to form an inverse Pickering emulsion. Subsequently, pS-b-EP is added to the Pickering emulsion droplets. Size exclusion chromatography proved and quantified the adsorption of pS-b-EP onto the Pickering emulsion droplets. A maximum surface coverage of 1.28 mg/m^2 is obtained after 2 hours, which is approximately $1/3^{\text{rd}}$ in comparison to a pure pS surface. We believe that the presence of polar sulfate groups on the particle's surface, which initially stabilized the particle in water, reduces the adsorption of pS-b-EP. The Pickering emulsion is heated above the T_g of the pS particles in order to form pS microcapsules. A significant effect of the presence of pS-b-EP copolymer is observed. Severe aggregation is observed, if no pS-b-EP is used. On the other hand, the adsorbed pS-b-EP provided additional steric stabilization to the Pickering emulsion droplets and ultimately leads to the efficient synthesis of pS microcapsules.

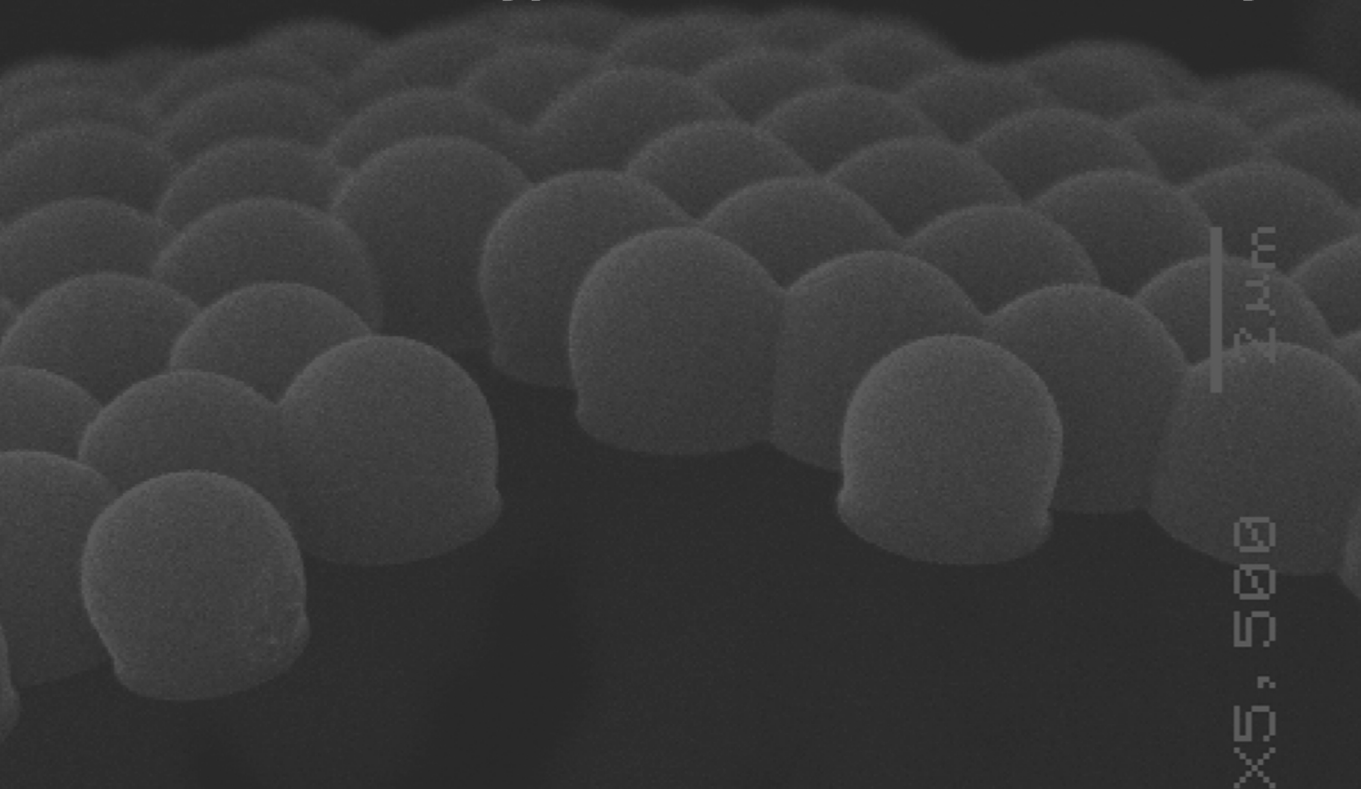
References

1. Augustin, M. A.; Hemar, Y., *Chemical Society Reviews* **2009**, 38, (4), 902-912.
2. Carturan, G.; Dal Toso, R.; Boninsegna, S.; Dal Monte, R., *Journal of Materials Chemistry* **2004**, 14, (14), 2087-2098.
3. Chaikof, E. L., *Annual Review of Biomedical Engineering* **1999**, 1, 103-127.
4. Madene, A.; Jacquot, M.; Scher, J.; Desobry, S., *International Journal of Food Science and Technology* **2006**, 41, (1), 1-21.
5. Sharma, A.; Tyagi, V. V.; Chen, C. R.; Buddhi, D., *Renewable & Sustainable Energy Reviews* **2009**, 13, (2), 318-345.
6. Dinsmore, A. D.; Hsu, M. F.; Nikolaidis, M. G.; Marquez, M.; Bausch, A. R.; Weitz, D. A., *Science* **2002**, 298, (5595), 1006-1009.
7. Hsu, M. F.; Nikolaidis, M. G.; Dinsmore, A. D.; Bausch, A. R.; Gordon, V. D.; Chen, X.; Hutchinson, J. W.; Weitz, D. A., *Langmuir* **2005**, 21, (7), 2963-2970.
8. Pickering, S. U., *J. Chem. Soc.* **1907**, 91, 2001-2021.
9. Pieranski, P., *Physical Review Letters* **1980**, 45, (7), 569-572.
10. Young, T., *Phil. Trans.* **1805**, 95, 65-87.
11. Binks, B. P.; Horozov, T. S., *Colloidal particles at liquid interfaces*. Cambridge University Press: 2006

12. Gordon, V. D.; Xi, C.; Hutchinson, J. W.; Bausch, A. R.; Marquez, M.; Weitz, D. A., *Journal of the American Chemical Society* **2004**, 126, (43), 14117-14122.
13. Lawrence, D. B.; Cai, T.; Hu, Z.; Marquez, M.; Dinsmore, A. D., *Langmuir* **2007**, 23, (2), 395-398.
14. Velez, O. D.; Furusawa, K.; Nagayama, K., *Langmuir* **1996**, 12, (10), 2374-2384.
15. Croll, L. M.; Stover, H. D. H., *Langmuir* **2003**, 19, (14), 5918-5922.
16. Lin, Y.; Skaff, H.; Boker, A.; Dinsmore, A. D.; Emrick, T.; Russell, T. P., *Journal of the American Chemical Society* **2003**, 125, (42), 12690-12691.
17. Skaff, H.; Lin, Y.; Tangirala, R.; Breitenkamp, K.; Boker, A.; Russell, T. P.; Emrick, T., *Advanced Materials* **2005**, 17, (17), 2082-2086.
18. Cayre, O. J.; Noble, P. F.; Paunov, V. N., *Journal of Materials Chemistry* **2004**, 14, (22), 3351-3355.
19. Laib, S.; Routh, A. F., *Journal of Colloid and Interface Science* **2008**, 317, (1), 121-129.
20. Yow, H. N.; Routh, A. F., *Langmuir* **2009**, 25, (1), 159-166.
21. Bon, S. A. F.; Cauvin, S.; Colver, P. J., *Soft Matter* **2007**, 3, (2), 194-199.
22. Tcholakova, S.; Denkov, N. D.; Lips, A., *Physical Chemistry Chemical Physics* **2008**, 10, (12), 1608-1627.
23. Marinova, K. G.; Alargova, R. G.; Denkov, N. D.; Velez, O. D.; Petsev, D. N.; Ivanov, I. B.; Borwankar, R. P., *Langmuir* **1996**, 12, (8), 2045-2051.
24. Binks, B. P.; Rodrigues, J. A., *Langmuir* **2007**, 23, (14), 7436-7439.
25. Golemanov, K.; Tcholakova, S.; Kralchevsky, P. A.; Ananthapadmanabhan, K. P.; Lips, A., *Langmuir* **2006**, 22, (11), 4968-4977.
26. Bon, S. A. F.; Colver, P. J., *Langmuir* **2007**, 23, (16), 8316-8322.
27. Hsu, M. F.; Dufresne, E. R.; Weitz, D. A., *Langmuir* **2005**, 21, (11), 4881-4887.
28. Velez, O. D.; Furusawa, K.; Nagayama, K., *Langmuir* **1996**, 12, (10), 2385-2391.
29. Brandriss, S.; Margel, S., *Langmuir* **1993**, 9, (5), 1232-1240.
30. Leunissen, M. E.; van Blaaderen, A.; Hollingsworth, A. D.; Sullivan, M. T.; Chaikin, P. M., *Proceedings of the National Academy of Sciences of the United States of America* **2007**, 104, (8), 2585-2590.
31. Riess, G.; Labbe, C., *Macromolecular Rapid Communications* **2004**, 25, (2), 401-435.
32. Awan, M. A.; Dimonie, V. L.; ElAasser, M. S., *Journal of Polymer Science Part A-Polymer Chemistry* **1996**, 34, (13), 2651-2664.
33. Holderle, M.; Mulhaupt, R., *Acta Polymerica* **1995**, 46, (3), 226-232.
34. Goodall, A. R.; Wilkinson, M. C.; Hearn, J., *Journal of Polymer Science Part A-Polymer Chemistry* **1977**, 15, (9), 2193-2218.
35. Goto, A.; Sato, K.; Tsujii, Y.; Fukuda, T.; Moad, G.; Rizzardo, E.; Thang, S. H., *Macromolecules* **2001**, 34, (3), 402-408.
36. Philipsen, H. J. A.; Oestreich, M.; Klumperman, B.; German, A. L., *Journal of Chromatography A* **1997**, 775, (1-2), 157-177.
37. Stancik, E. J.; Fuller, G. G., *Langmuir* **2004**, 20, (12), 4805-4808.
38. Paunov, V. N., *Langmuir* **2003**, 19, (19), 7970-7976.
39. Aveyard, R.; Clint, J. H.; Nees, D.; Paunov, V. N., *Langmuir* **2000**, 16, (4), 1969-1979.
40. Robinson, D. J.; Earnshaw, J. C., *Langmuir* **1993**, 9, (5), 1436-1438.
41. Sun, J. Z.; Stirner, T., *Langmuir* **2001**, 17, (10), 3103-3108.

Wetting & Colloidal stability

of hairy particles: a Self-Consistent Field theory



Abstract: The assembly of sterically-stabilized colloids at liquid-liquid interfaces is studied with the Self Consistent Field (SCF) theory using the discretization scheme that was developed by Scheutjens, Fleer and co-workers. The model is based on a poly(methyl methacrylate) (pMMA) particle with poly(isobutylene) (pIB) grafted to the surface. The stabilizing groups on the particle surface have a significant effect on the interfacial assembly and, therefore, also on the formation and properties of Pickering emulsions. The wetting behavior of the particle is altered by the presence of the stabilizing groups, which affects the equilibrium position of the particles at the interface. The stabilizing groups can also lead to an activation barrier before interfacial adsorption, analogous to the steric repulsion between two particles. These effects are numerically solved with the SCF theory. It is commonly known that flocculating conditions enhance the interfacial adsorption and yield stable Pickering emulsions, which is confirmed in this work. Additionally, it is concluded that those conditions are not an absolute requirement. There is a window of stabilizer concentrations $\Gamma_{\text{pIB}} : 2.2 - 3.3 \text{ mg/m}^2 \text{ pIB}$, that shows both partial wetting and colloidal stability. The activation barrier for interfacial adsorption is $140 - 550 k_B T$ and is an order of magnitude higher than the colloidal stability. The difference can be attributed to the unfavorable interaction of pIB with water and a difference in geometry (plate-sphere vs sphere-sphere). This study demonstrates the interplay, and provides a quantitative comparison, between the wetting behavior and the colloidal stability and it gives a better understanding of the colloidal assembly at soft interfaces and the formation of Pickering emulsions, in general.

Part of this chapter is submitted for publication to **Langmuir**.

5.1 Introduction

This chapter provides a quantitative comparison between the wetting behavior and the colloidal stability of sterically stabilized particles that are suitable for the formation of Pickering emulsions. Solid-stabilized or Pickering emulsions are water/oil (w/o) mixtures that are solely stabilized by small solid particles. They are found in many applications and industrial processes, such as crude-oil processing¹, food^{2, 3}, mineral flotation⁴ and cosmetics⁵. Furthermore, they have recently led to the development of advanced materials⁶, such as selectively permeable capsules⁷, colloidal nano-composites⁸, porous solids and foams.⁹ The assembly of colloidal particles at soft interfaces is governed by the interfacial free energies γ of the particle and the two soft phases, respectively. Young's equation, relates the interfacial tensions with the equilibrium position of the particle at the interface, through the 3-phase contact angle (θ) (fig. 5.1).¹⁰

Colloids normally have stabilizing groups on their surface, which is required for a controlled synthesis of the particles and to keep the particles in dispersion. There are two types of colloidal stabilization mechanisms, namely electrostatic stabilization and steric stabilization. In the first case, Coulombic repulsion occurs between particles and, in the other case, adsorbed or grafted polymer chains prevent the particles from aggregating. The stabilizing groups also have a significant effect on the assembly to soft interfaces and, therefore, on the formation and properties of Pickering emulsions. In the first place, the surface tension of the particle is altered by the presence of the stabilizing groups, which affects the wetting properties and herewith the equilibrium position of the particles at the interface.¹³ This is illustrated by the various θ that are reported in literature of, for example, polystyrene latexes.^{14, 15} Moreover, various values for θ ranging from 90° to 180° have been reported for poly(methyl methacrylate) (pMMA) particles.¹⁶⁻¹⁸ In the second place, the stabilizing groups can also lead to an activation barrier when a particle approaches the interface,¹⁹ analogous to the steric repulsion that occurs between two particles. Tchokalova wrote an elaborate review and reported specifically on the role of the electrostatic barrier in particle adsorption.²⁰ A reduction of this barrier allows the particles to adsorb to the w/o interface. Charged colloids therefore are known to adsorb at interfaces under 'flocculating' conditions.²¹⁻²⁵ It can be stated that the wetting behavior and the colloidal stability are fundamentally related through their surface functional groups, which is the explanation that in practice these two effects are often linked. The colloidal stability is also relevant for the synthesis of advanced materials from Pickering emulsions, which is demonstrated in a previously published study by our group.²³ The particles surrounding the emulsion droplets

inevitably determine the interaction with other droplets. Ideally, the particles exhibit both partial wetting, such that they assemble at interfaces, but remain colloidal stable. This theoretical study can be considered a search for these optimal conditions between the wetting behavior and colloidal stability.

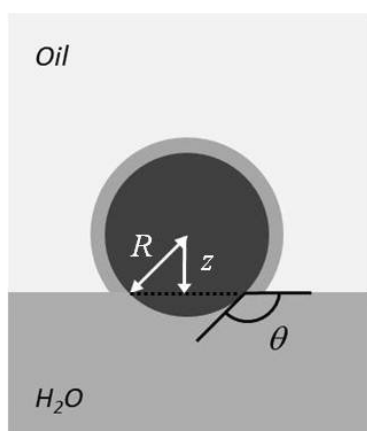


Figure 5.1 A solid particle that is assembled at an oil/water interface. R is the radius of the particle. θ is the three phase contact angle. z is the distance from the center of the particle to the interface. The dark grey circle represents the solid particle. The light grey area that surrounds the particle is the polymer stabilizer, which is attached to the particle and is soluble in the oil. The light grey area is insoluble in water and is therefore less extended and therefore not shown in this image.

Various aspects relevant to Pickering emulsions are studied in literature. For example, the contribution of capillarity in the stabilization of Pickering emulsions,²⁶ aggregation of colloids at planar liquid interfaces²⁷ and the adsorption and repulsion of particles at the w/o interface are studied.¹⁹ This chapter demonstrates the interplay and provides a quantitative comparison between the wetting behavior and colloidal stability of hairy particles and gives a better understanding of the interfacial adsorption and the formation of Pickering emulsions. These aspects are theoretically investigated within the framework of the Self Consistent Field theory, by consideration of a ‘single’ pMMA particle that adsorbs to a w/o interface. The three-phase contact angle, activation barrier for interfacial adsorption and colloidal stability are determined for the systems that show partial wetting.

5.2 Self-Consistent Field theory

The system is studied with the Self Consistent Field theory, for polymers at interfaces, using the discretization scheme that was developed by Scheutjens, Fleer and co-workers. The theory has been extensively discussed in literature,²⁸⁻³¹ but will be explained shortly here. The system, which is considered, is 1-gradient, in the sense that density gradients in just one direction, normal to the surface, are accounted for. Hence, the solution is divided in M lattice layers. Each layer l contains a volume fraction $\varphi(l)$ of one or several components, that is, concentration fluctuations in a layer are averaged over. At the basis of the SCF theory is the mean-field free energy density $f[\{\varphi\},\{u\}](l)$. This notation implies that the free energy is a function of two conjugated quantities, namely the density $\varphi(l)$ and the corresponding potential $u(l)$. Both quantities are dependent on the coordinate in the system $l = 1, 2, \dots, M$. The curly brackets indicate that for each segment type in the system the (φ, u) profiles are present. Each molecular component i in the system consists of a sequence of segments. The segment types are referred to by the letter A . The mean free energy is written as $F[\{\varphi\},\{u\}] = \sum_r L(l) f[\{\varphi\},\{u\}](l)$, where $L(l)$ is the dimensionless volume of the lattice layer l . All lengths are reduced by the size of the lattice sites. The free energy is formally given by:

$$F[\{\varphi\},\{u\}]/k_B T = -\ln Q(\{u\}) - \sum_r L(l) \sum_A u_A(l) \varphi_A(l) + F^{int}(\{\varphi\}) + \sum_r u'(l) (L(l) \sum_A \varphi_A(l) - 1) \quad 5.1$$

The 1st term of eq. 5.1 above features the partition function $Q(\{u\}, V, T)$, which can be computed from the segment potentials. The 2nd term is a Legendre transformation and together with 1st term essentially gives the dimensionless entropy in the classical $(\{n\}, V, T)$ ensemble. The 3rd term is the contribution that specifies all possible interactions between the different entities in the system. The 4th term decouples the volume fractions of the components, where the Lagrange parameter $u'(l)$ is linked to the incompressibility constraint $\sum_A \varphi_A(l) = 1$, which is a sum over all segment types, and is implemented locally for each coordinate r . In the model only the short-range nearest-neighbor interactions are accounted for, which is done by the Bragg-Williams approximation to estimate the number of neighboring contacts. For each contact between different segments A and B a Flory-

Huggins (FH) interaction parameter χ_{AB} is defined. The optimization of the free energy leads to the self-consistent field conditions:

$$\frac{\partial F}{\partial \varphi_A(l)} = -u_A(l) + u'(l) + \chi_{AB} \langle \varphi_A(l) - \varphi_{A,bulk} \rangle = 0 \quad 5.2$$

$$\frac{\partial F}{\partial u_A(l)} = -\frac{\partial \ln Q}{\partial u_A(l)} - L(l)\varphi_A(l) = 0 \quad 5.3$$

$$\frac{\partial F}{\partial u'(l)} = \sum_A \varphi_A(l) - 1 = 0 \quad 5.4$$

Eq. 5.2 details how in the Bragg-Williams approximation the segment potentials depend on the volume fractions. Eq. 5.3 gives the rule to compute the volume fractions from the potentials. The partition function Q is, by construction of the mean-field approximation, related to the single-chain partition functions $q_i(\{u\})$ for each molecule (including monomers) type i , $Q = \prod_i \frac{(q_i)^{n_i}}{(n_i)!}$, where n_i is the number of molecules of type i . The efficiency by which the partition function and thus the volume fractions can be computed heavily depends on the chain model. Following Scheutjens and Fleer we have implemented a freely-jointed chain model for which an efficient propagator method exists to evaluate both the single-chain partition function and the volume fraction distribution. The propagator equation is a discrete form of the Edwards diffusion equation³² and the details can easily be found in the literature.³³ Eq. 5.4 specifies the compressibility relation. Here we opt for the situation that the system is incompressible, i.e. the volume fractions add up to unity. The equations above are solved numerically and the result is known as the SCF solution. Numerically accurate SCF solutions are found iteratively. Routinely seven significant digits are obtained. As a result, detailed information on the volume fraction profiles of all molecular species in the system and exact numerical values for the mean-field free energy of the system are obtained.

5.2.1 The model

The model is based on a poly(methyl methacrylate) (pMMA) particle sterically stabilized by poly(isobutylene) (pIB), which is initially dispersed in the oil-phase and assembles at a w/o interface. Several examples are known in which a similar system is used.¹⁶⁻¹⁸ Various values for θ have been reported ranging from 90° to 180°, suggesting a strong effect of the

stabilizer. This system can be considered as a model for the assembly of sterically stabilized colloids to soft interfaces in general.

The different components in the system are modeled on a united-atom level. There are 3 components in the system, which are water, oil and a homopolymer of isobutylene that is grafted to the surface. Water (H_2O) is modeled as a collection of small clusters that each occupies 5 lattice sites. A central water segment is surrounded by 4 neighboring segments arranged in a star-like configuration. The reason is to mimic the formation of clusters of water molecules due to hydrogen bonding. It must be noted that this is a fairly simple model for water, but it has been successfully applied in other aqueous systems.^{34, 35} The segment type for water is denoted by W . The oil and polymer (pIB) consist of the same segment C , but have a different structure. The model for oil is based on a common hydrocarbon oil, namely heptane, and is therefore a chain of 7 C -segments (C_7). The polymer is modeled according to poly(isobutylene) (pIB) and has a degree of polymerization of 100. The repeating unit of pIB has 4 C -segments, of which 2 segments are part of the linear polymer backbone and the other two segments are side groups. pIB is oil-soluble and uncharged, therefore Coulombic interactions do not play a role. The amount of pIB that is grafted to the surface is varied from $\Gamma_{pIB} = 0$ to 1.0, which corresponds to a surface coverage of 0 to 5.5 mg/m^2 , where the upper limit is close to the overlap value upon which a polymer brush is formed. The surface that is considered is located at the boundary of the system. It, therefore, does not consist of segments, but it does interact with the molecules inside the system. In the model, the surface is denoted as S . The Flory-Huggins interaction parameters (χ) between the various segments are as follows: $\chi_{CW} = 1.1$, $\chi_{SW} = 0$. The latter value does have a consequence for the absolute values of γ (in particular when the solid is involved) but it will have no consequence for the evaluation of the system, for example θ and the repulsion. The relative change in free energy is considered, which is independent of the absolute values. Initially, χ_{SC} is systematically varied between 0 and -2.0 to simulate different materials and to demonstrate its effect on θ . Agreement between experimental data and SCF theory for pMMA surfaces is found for $\chi_{SC} = -0.5$. The positive sign for the interaction between C - W χ_{CW} indicates that there is a repulsion between the oil/pIB and water. The negative sign for χ_{SC} indicates an attraction of the oil and the surface.

5.2.2 Parameters

The relevant parameters to study the wetting behavior are the excess amount of a component that wets the surface and the interfacial energies. The total amount of a particular component in the system, for example C_7 , is $\Gamma_{C_7} = \sum_r \varphi_{C_7}(l)$. The excess amount is then $\Gamma_{C_7}^\# = \Gamma_{C_7} - M\varphi_{C_7,\text{bulk}}$, in which $\varphi_{C_7,\text{bulk}}$ is the volume fraction of C_7 in the bulk. The excess amount represents the adsorption of a particular compound from the bulk to a surface. The interfacial free energy is obtained from $\gamma = F - \sum_i \mu_i n_i$ in which μ_i is the chemical potential and n_i the number of all molecules of type i in the system. The summation includes all mobile components in the system, that is, C_7 and H_2O , but not the grafted polymer. All energies obtained from the SCF calculation are reduced by $k_B T$ and are therefore dimension-less. To obtain real values, γ must be multiplied with $k_B T/a^2$, in which a is the dimension of a lattice site. The three interfacial free energies of the various interfaces allow calculating the three-phase contact angle by Young's equation (eq. 1.1). The calculations also give access to the excess mean free energy $\Delta F(x)$ per unit area for a film of finite thickness (x) of one liquid (C_7) between the surface and the bulk of the other liquid (H_2O), which is used to simulate the repulsion that occurs when a particle approaches the interface. For a large value of the film thickness $x \rightarrow \infty$, this free energy converges to $\gamma(\infty) = (\gamma_{SO} + \gamma_{OW})$. The excess free energy is given by $\Delta F(x) = \gamma(x) - \gamma(\infty)$.

5.3 Results

The following section is organized as follows. In the first place, a simple binary mixture of oil and water is analyzed. The interfacial tension γ_{OW} and the concentration profile are determined, which are required later for the calculation of θ . Secondly, a surface is added to the system and the wetting of a binary mixture of oil and water on that surface is studied. χ_{SC} is systematically varied between 0 and -2.0 to simulate various materials. The interfacial tensions γ_{SW} and γ_{SO} are calculated for each χ_{SC} and θ is subsequently calculated by Young's equation. Thirdly, various amounts of pIB are grafted to the surface. A similar analysis is performed as described above, except that the θ will be given as a function of Γ_{pIB} . Additionally, for the conditions that show a partial wetting regime or in other words demonstrate $0^\circ < \theta < 180^\circ$, the change of excess free energy ΔF with a decreasing film thickness of C_7 is analyzed. This simulates the interaction, repulsion and attraction, of a particle with the w/o interface. Fourthly, the colloidal stability (kinetic barrier for particle aggregation) of the same systems is studied. In this case, no separate water phase is present,

but an identical surface with grafted pIB is gradually brought closer to each other. ΔF with decreasing separation distance simulates now the repulsion between two approaching particles. SCF theory, as performed here, yields the interaction between planar geometries. Therefore, a Derjaguin approximation is, finally, performed to convert the interactions to a plate-sphere and sphere-sphere geometry, respectively for the assembly of a particle at an w/o interface and for the colloidal stability against the aggregation of two spheres. The attractive energy that is involved is, in one case, the reduction of the interfacial energy and, in the other case, the Van der Waals interaction. The net energy profiles are obtained by a simple addition of the repulsive and attractive contributions.

5.3.1 w/o interface

To study the wetting behavior of various surfaces, both with and without grafted polymer attached to it, one has to know the interfacial tension between oil and water. A system consisting of 200 layers is filled with oil $\Gamma_{C_7} = 100$ and water $\Gamma_{H_2O} = 100$ and is allowed to equilibrate. The two components separate and a sharp interface, between the otherwise homogeneous phases, is formed. Moreover, it is found that both phases partition in the other. The water phase is saturated with C_7 and the concentration is $\varphi_{C_7, \text{bulk}} = 6.796 \cdot 10^{-4}$. This value will be referred to as the oil-in-water binodal or simply the binodal value. Once the SCF solution is found, the interfacial tension $\gamma_{ow} = F - \mu_{C_7} n_{C_7} - \mu_{H_2O} n_{H_2O} = 0.4968 \text{ } k_B T / \text{lattice site}$ is calculated. Considering the discretization of the molecular dimensions (e.g. heptane is taken to occupy 7 sites), the relevant area of a lattice site is estimated at 0.09 nm^2 . Therefore, in more common units $\gamma_{ow} = 0.068 \text{ J/m}^2$, which is in agreement to experimental surface tensions for heptane-water interfaces and indicates that the model is reliable.³⁶

5.3.2 s/w/o interface

A surface is now added to the system. To study the wetting behavior of this surface the adsorption isotherm of C_7 is recorded. A system with 100 layers is defined and, initially, only the surface and water ($\Gamma_{H_2O} = 100$) are present. C_7 is titrated to the system in steps of 0.1 to a maximum of $\Gamma_{C_7} = 20$, replacing the water. χ_{sw} is 0 and the χ_{sc} is systematically varied between 0 and -2.0 to simulate different materials and to demonstrate the effect on the wetting behavior. The adsorption isotherms of C_7 for each χ_{sc} are obtained by plotting $\varphi_{C_7, \text{bulk}}$ against $\Gamma_{C_7}^\#$ (fig. 5.2). The various adsorption isotherms demonstrate different wetting regimes, but ultimately merge at high values of Γ_{C_7} at the oil-in-water binodal value

(vertical dashed line). The surface with $\chi_{SC} = -2.0$ is in the complete wetting regime, which can be seen by the jump in the isotherm (see fig. 5.3) occurring below the binodal value. The isotherms for the other interaction parameters demonstrate partial wetting, which can be seen in the regime where the equal area construction fails (fig. 5.3).

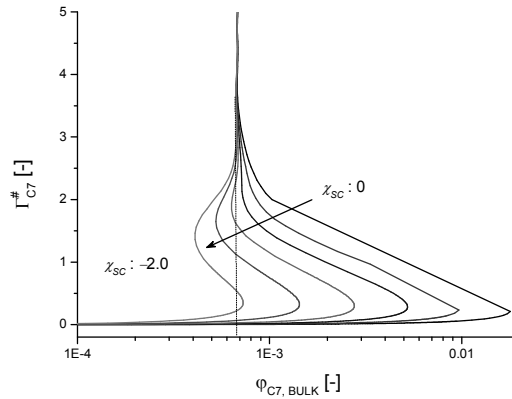


Figure 5.2 Adsorption isotherms of C_7 on surfaces with various FH interaction parameters $0 \leq \chi_{SC} \leq -2.0$, with a step size of 0.4. The dotted line is at the oil-in-water binodal value.

The three phase contact angle θ of the particular surface, C_7 and water can be determined from the interfacial free energies found for relevant systems at the binodal value. The interfacial tension γ is a function of the amount of C_7 at the surface and the result is plotted as a function of $\phi_{C7, bulk}$ in figure 5.3. Depending on $\phi_{C7, bulk}$ different surface tensions are found and cusp-like graphs emerge that correspond to the van der Waals loops of figure 5.2. From classical thermodynamics it is known that for a given value of the chemical potential, the system chooses the lowest value of the surface tension, and thus the crossing of the lines for $\chi_{SC} = -2.0$ corresponds to a surface phase transition from gas to a thin film (prewetting step, equivalent to the well-known equal area construction). All other curves do not have such a crossing point and thus have no surface phase transition. Instead, typical for partial wetting, all curves end at the bulk binodal (indicated by the dotted vertical line) and it turns out that all curves representing partial wetting states have two values for the interfacial tension at the binodal conditions. These two interfacial tensions are needed to compute the contact angle.

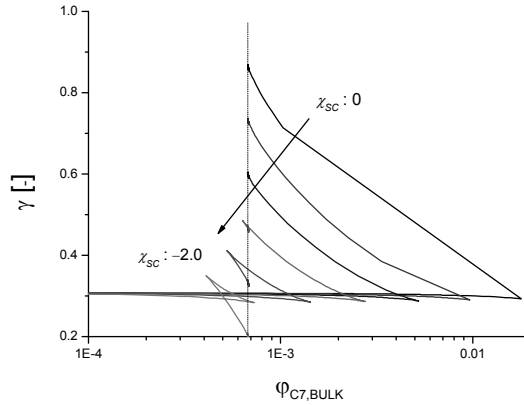


Figure 5.3 The interfacial free energy of the system as a function of $\phi_{C7,bulk}$ for surfaces with various FH interaction parameters $0 \leq \chi_{SC} \leq -2.0$, with a step size of 0.4. The dotted line is at the oil-in-water binodal value.

To be more informative, one isotherm is considered, namely $\chi_{SC} = -1.0$, of which the concentration profiles are shown. As seen from figure 5.2 the bimodal is crossed at $\Gamma_{C7} = 0.09$ and merges to this value at $\Gamma_{C7}^{\#} > 4$. The third crossing represents an unstable state of the system. The profiles of the two stable states at coexistence of C_7 and H_2O are shown in figure 5.4 in combination with a schematic representation of the system. In the first graph ($\Gamma_{C7} = 0.09$) there is just a small amount of oil at the surface and the remainder of the system is filled with water. The oil at the surface is in the ‘gas’ state, because the amount of oil is very low. This is represented by the dashed gray line in the schematic representation. The interfacial tension for this state is interpreted as γ_{SW} , and the corresponding value can be extracted from figure 5.3. The second graph ($\Gamma_{C7} = 20.0$) is obtained for the case that there is a large oil phase between the surface and the bulk water phase. In the wetting literature such a thick film is said to be macroscopically thick, because it exists at bulk coexistence. Evaluation of the interfacial tension for this macroscopically thick film gives $\gamma_{SO} + \gamma_{OW}$. Again, this sum is extracted from the result of figure 5.3. Subsequent subtraction of γ_{OW} , which is known from the previous consideration of the water and oil only system, yields γ_{SO} . The three relevant interfacial tensions are shown in figure 5.5. γ_{OW} is of course independent on the surface and also γ_{SW} changes little. The greatest effect can be seen on γ_{SO} that scales linearly with χ_{SC} , which is not unexpected. A more favorable interaction obviously reduces the surface tension between the surface and

C_7 . It must be mentioned that in principle negative free surface energies are not possible, but this is related to the choice of the interaction parameters with the surface. The absolute values of γ that involve the surface are irrelevant. With respect to θ , for example, the difference between $\gamma_{SO} - \gamma_{OW}$ is used, and the reference value drops out. θ is calculated with the obtained interfacial tensions and Young's equation (fig. 5.6).

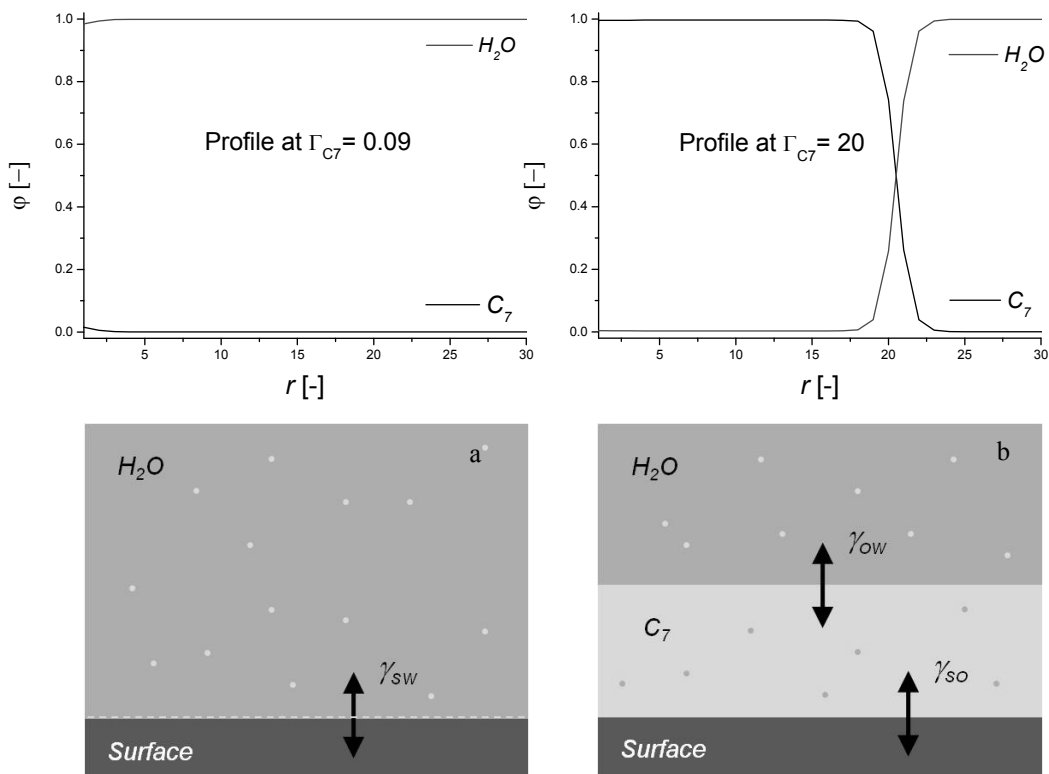


Figure 5.4 The concentration profiles and schematical representation of oil and water at a surface with $\chi_{SC} = -1.0$ at $\Gamma_{C7} = 0.09$ (a) and $\Gamma_{C7} = 20$ (b). The surface is located at $r = 0$. Please note that the small dots in the illustration are not droplets, but demonstrate the partitioning of one phase in the other. Note the thin C_7 that is adsorbed in the image.

θ , as calculated in this approach, is the angle that a water drop makes on a planar surface. Simultaneously, this is identical to the contact angle that a spherical particle of the same material exhibits at an oil/water interface. Therefore, with this approach, the equilibrium position of a particle at an oil/water interface is determined. Surprisingly, when the surface

has no preference for C_7 or water $\chi_{SC} = \chi_{SW} = 0$, $\theta < 90^\circ$. Arguing from an energetic point of view, one would expect that for this situation the contact angle is 90° . However, water and oil differ with respect to the molecular architecture and the two molecules experience different conformational entropy losses near the surface, which explains the observed effect. Otherwise, it is found that the contact angle θ increases approximately linearly with a decreasing χ_{SC} . From approximately $\chi_{SC} \sim -1.8$, a complete wetting regime with $\theta < 180^\circ$ is observed.

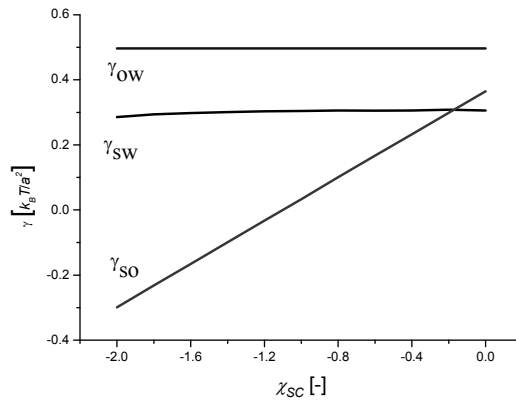


Figure 5.5 The interfacial tensions γ_{ow} , γ_{so} and γ_{sw} as a function of χ_{SC} .

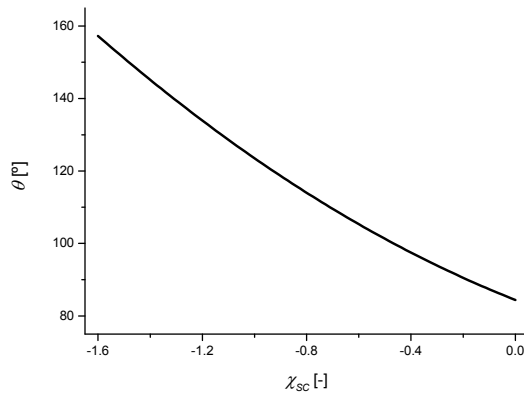


Figure 5.6 The 3-phase contact angles θ that were calculated with Young's equation are presented as a function of χ_{SC} .

5.3.3 s/pIB/w/o interface

The main aim of this work is to model sterically stabilized pMMA particles that assemble at w/o interfaces. Experimental data from pMMA surfaces is compared with the results from the SCF theory to find identical conditions. Some studies reported the use of pMMA particles for the assembly at soft interfaces. However, they reported a wide range of contact angles. This indicates a strong effect of the chemical groups attached to the particle surface, but therefore cannot be used to compare with the theoretical results. There is extensive experimental data on the surface tensions of pMMA.^{36, 37} Young's equation allowed the calculation of an experimental θ and resulted in a $\theta \approx 105^\circ$. This value suggests the use of $\chi_{SC} = -0.5$ and is used for the following part of this study. The other interaction parameters show more resemblance to for example polystyrene surfaces, which are more hydrophobic and show larger contact angles, or poly(methyl acrylate) that is more polar and exhibits a lower contact angle.

Wetting

In this part of the chapter, the effect of grafted polymer that is attached to the surface is investigated. This polymer, which is modeled after pIB, is oil-soluble and can act as a steric stabilizer in colloidal systems. The amount of pIB grafted on the surface is systematically varied from $\Gamma_{pIB} = 0$ to 1.0, which corresponds to a surface coverage of 0 to 5.5 mg/m². A similar analysis, as described above, is performed. In figure 5.7, a family of oil adsorption isotherms is shown for various pIB surface coverages. Qualitatively, an increase in pIB concentration is similar to the increase of the surface affinity for C_7 , as already shown in figure 5.2. A transition from partial to complete wetting is observed with increasing amount of grafted pIB. The increase of the contact angle with increasing grafting density is shown in figure 5.8. Here, the value of θ for $\Gamma_{pIB} = 0$ is obviously the same as for a clean (naked) pMMA surface. At $\Gamma_{pIB} = 0.6$ the contact angle is close to the transition value of 180° . In between $\Gamma_{pIB} = 0$ and 0.6 we find that the contact angle is approximately linear with grafting density. Larger Γ_{pIB} values demonstrate a complete wetting for C_7 . The effect of pIB on the contact angle is quite strong. There is only a small window of Γ_{pIB} values, which show partial wetting and for which the particles will assemble at w/o interfaces.

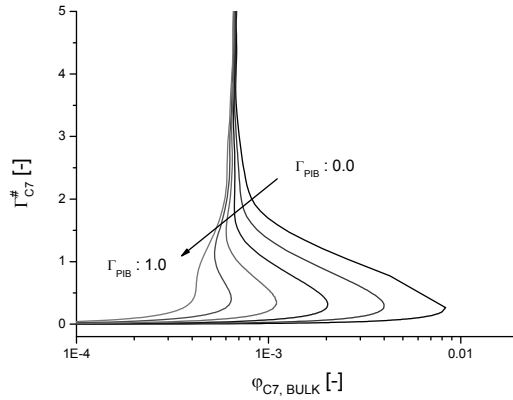


Figure 5.7 The adsorption isotherms of C_7 on surfaces with varying amounts of grafted pIB: $\Gamma_{\text{pIB}} = 0$ to 1.0, with a stepsize of 0.2, which corresponds to a surface coverage of 0 to 5.5 mg/m². $\chi_{\text{SC}} = -0.5$.

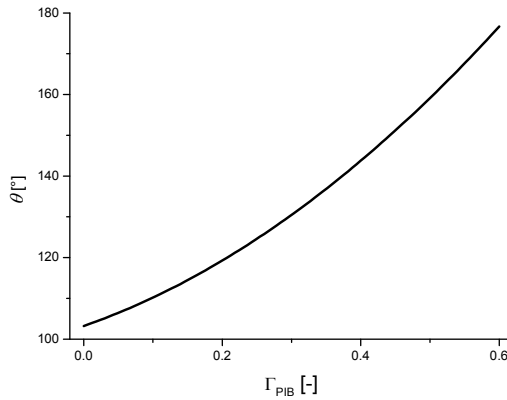


Figure 5.8 The 3-phase contact angles θ that were determined as a function of Γ_{pIB} . $\chi_{\text{SC}} = -0.5$.

Activation barrier

Not only is the equilibrium position of a particle at the interface affected by stabilizing groups at the surface. In analogy to steric stabilization in the bulk, a particle experiences also a repulsive force when it approaches an oil/water interface. This is investigated within the same framework as described above. The approach will be explained once more with slightly more detail to elucidate how the result was obtained. A surface with grafted

polymer is defined and immersed in water. Upon addition of C_7 it adsorbs to the surface and forms a separate oil film with a clearly defined thickness, as can be seen in figure 5.7. The adsorbed film thickness grows with the addition of oil C_7 . The interfacial free energy as a function of the film thickness is relevant. When the oil film is macroscopically thick, it can be imagined that the particle is somewhere in the oil phase. When the particle is near the oil-water interface, a finite film thickness of oil sits in between the surface and the water phase. A decreasing film thickness simulates the approach of the particle to the oil-water interface. For interfacial assembly, the free energy should exhibit at least a local minimum as a function of the separation. The presence of repulsion, which is seen as an increase of the free energy with decreasing distance, signals the presence of a kinetic barrier. When there is no local minimum in the interaction curve, then the particles cannot stick to the w/o interface. The latter happens for systems that show complete wetting.

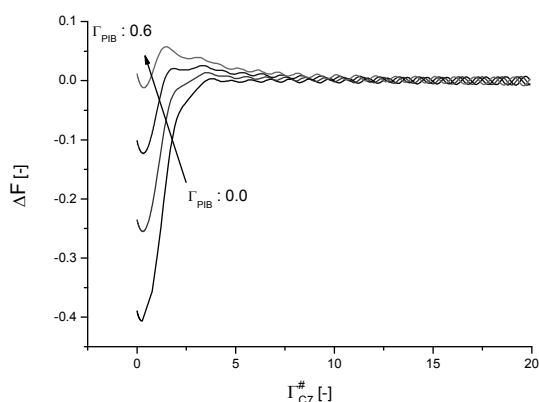


Figure 5.9 The excess free energy with decreasing film thickness C_7 . $\Gamma_{C7}^{\#}$ is a measure for the film thickness that is adsorbed to the pMMA surface. $\Gamma_{PIB} = 0$ to 0.6, with a stepsize of 0.2.

The disjoining forces, that is the free energy as a function of the film thickness is shown in figure 5.9 for various values of the grafting density of pIB polymers, focusing on the partial wetting cases. The first thing that can be seen is the oscillation of the free energy. It slightly distorts the image and is, unfortunately, inevitable. It is an artifact of the discretization scheme that is used in the SCF theory. Despite the oscillations it does show relevant data. At large $\Gamma_{C7}^{\#}$ the change in excess free energy ΔF is zero. The surface is completely immersed in the oil. Now typically, upon decreasing the film thickness a repulsive region

appears: the free energy increases. At shorter separations, the repulsion gives way to attraction and a local minimum is found for Γ_{C7} close to 0. This means that the oil film between the particle and the w/o interface becomes unstable and adsorption at the interface occurs. It is important to mention that the height of the local maximum (kinetic barrier) increases with increasing grafting density of pIB and appears absent when no polymers are on the surface.

5.3.4 Conversion to colloidal system: Derjaquin approximation

All the information that is obtained in the text above originates from planar geometries and all free energies are given per lattice site. It therefore needs to be converted to actually represent the assembly of a spherical particle to an w/o interface. The change of free energy (fig. 9) is converted from a planar to a sphere-plate geometry, which is done via a Derjaquin approximation.³⁸ The repulsive part in figure 5.9 is fitted with an exponential function to obtain $\Delta F(x)$, in which x is the distance between the surface and the w/o interface. This function is then integrated over half the surface A of the particle, according to equation 5.5, to obtain the total repulsion at each h . The results are shown in figure 5.10.

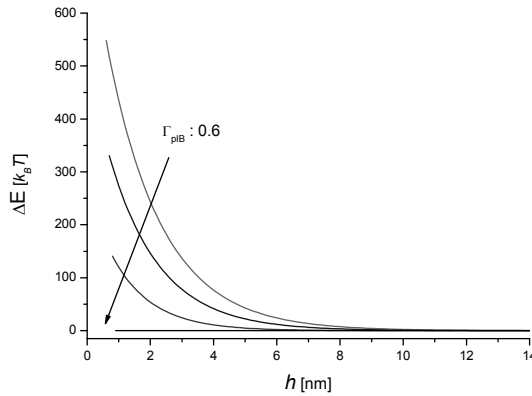


Figure 5.10 The free energy profile of a sterically stabilized particle that approaches an oil/water interface. The positive change in energy indicates repulsion of the particle from the interface. Γ_{pIB} ranges from 0 to 0.6, with a stepsize of 0.2.

$$\Delta E_{PI}(h) = \int_h^\infty \Delta F(x) \frac{dA}{dx} dx \quad 5.5$$

It can be seen that a particle experiences a repulsive force when it approaches an oil/water interface. The barrier for assembly at the interface is quite substantial. Thermal energy $k_B T$ is not enough to assemble the particle at the interface, although thermodynamically it prefers to be at the interface. This is consistent with experimental observations, because these systems generally require high-shear to form Pickering emulsions. Although the repulsion seems quite substantial, the free energy of adsorption is several orders of magnitude higher. At short separations, but still before the particle touches the interface ($h > 0$), the film between the particle and the interface becomes unstable (fig. 5.9). A strong attraction to the interface occurs and the particle adsorbs at the interface and moves to its equilibrium position.

The complete free energy profile of a spherical particle at an w/o interface is determined¹¹ (fig. 5.11) to illustrate this process. The particle position is given as z/R , in which z is the distance from the particle center to the interface and R is the particle radius (fig. 5.1). R is in this example 1 μm . To put it in perspective, $z/R = 1$ means that the particle is completely immersed in the water phase and for $z/R = -1$ the particle is completely immersed in the oil. It is assumed that the interface cannot deform upon particle adsorption. Now, for each particle position (z/R), the respective surface areas A_{wo} , A_{pw} and A_{po} are calculated. These surface areas are multiplied with the corresponding interfacial free energy to obtain the total energy (eq. 5.6). The Van der Waals interaction between the particle and the water droplet is not considered, because it is negligible with respect to the reduction of interfacial energy. For the chosen conditions, the particles experience a local minimum with respect to its position in relation to that of the oil-water interface, which means that the particles are bound to the w/o interface. As expected, the particle position and the adsorption strength depend on the grafting density of the pIB chains. Upon an increase of the amount of pIB the equilibrium particle position moves towards the oil phase. An illustration of this process is given in figure 5.12. Simultaneously, with increasing Γ_{pIB} , the free energy of detachment to the oil phase (E_B) decreases, while that of detachment into the water phase increases. For $\Gamma_{\text{pIB}} = 0.6$ the equilibrium particle position is $z/R = -0.999$ and E_B seems negligible, but is still $56 k_B T$. This is due to the choice of a relatively large particle size, because E_B scales with R^2 . For smaller particles, exhibiting a similar contact angle, the energy of detachment comes in the range of $k_B T$. Exchange of particles from the interface to the bulk is then

possible. This is unfavorable for the synthesis of new materials from Pickering emulsions, for which stable emulsion droplets are generally required.

$$\Delta E_{PI} \left(\frac{z}{R} \right) = \gamma_{wo} A_{wo} \left(\frac{z}{R} \right) + \gamma_{pw} A_{pw} \left(\frac{z}{R} \right) + \gamma_{po} A_{po} \left(\frac{z}{R} \right) \quad 5.6$$

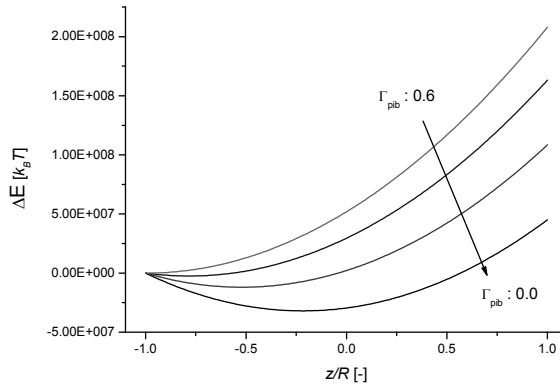


Figure 5.11 The free energy profiles of particles, which exhibit partial wetting, at the w/o interface. z is the distance of the particle center to the interface and R is the particle radius. At $z/R = -1$ the particle is completely immersed in the oil phase and at the $z/R = 1.0$ the particle is located in the water phase. The interface is located at position 0. Γ_{pIB} ranges from 0 to 0.6, with a stepsize of 0.2.

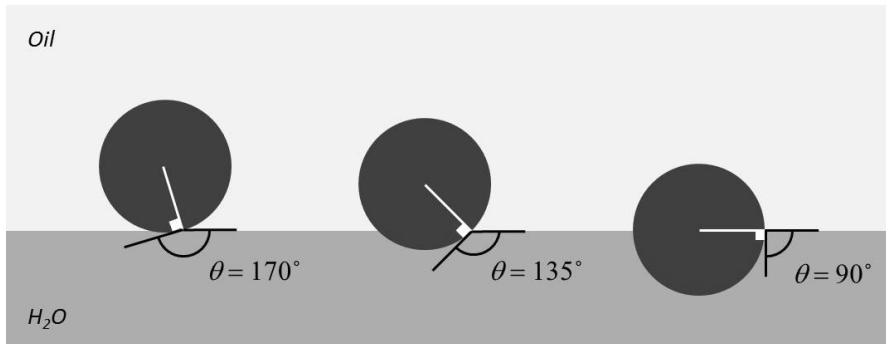


Figure 5.12. Illustration of the various 3-phase contact angles θ that were calculated with Young's equation.

5.3.5 Colloidal stability

A complementary analysis has been performed to calculate the colloidal stability. In this case two identical surfaces with grafted pIB are considered to simulate two particles that approach each other, instead of having just one surface. No separate water phase is present. Only a small amount of water is added that is dissolved in the oil to exactly match the previously defined (water-in-oil binodal) conditions. Initially, the two surfaces are separated such that the polymer chains, which are grafted to it, do not overlap. The two surfaces are then brought closer together, with steps of 1 lattice layer at a time. The excess free energy is calculated at each distance to calculate the repulsion. Due to the grafted chains we find a steric repulsion basically as soon as the surfaces are within a distance of the radius of gyration of the grafted chains. Again here the results are fitted with an exponential function and is integrated over x according to equation 5.7. This is the Derjaquin approximation to convert the interaction between two plates to a sphere-sphere geometry. The attractive contribution, in this case, is the Van der Waals-interaction (eq. 5.8), A_H is the Hamaker constant for pMMA in heptane.³⁹ The net interaction is obtained by adding the repulsive and attractive contribution (eq. 5.9, see fig. 5.13), which shows the different situations that are typically found in colloidal systems. The system with the highest amount of pIB is in fact colloidally stable, because there is a significant barrier ($70 k_B T$) for aggregation that under normal conditions ($k_B T$) cannot be overcome. For $\Gamma_{\text{pIB}} = 0.4$, a lower kinetic barrier is found ($8 k_B T$) and a secondary minimum is observed around 8 nm. The two systems with the lowest stabilizer concentration are unstable. There is no kinetic barrier for aggregation and the particles only experience an attractive potential.

$$V_R(h) = \pi R \int_h^\infty \Delta F(x) dx \quad 5.7$$

$$V_A(h) = -A_H R / 12h \quad 5.8$$

$$\Delta E_{PP}(h) = V_R + V_A \quad 5.9$$

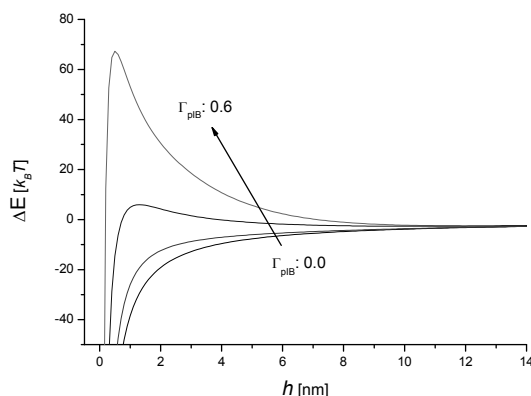


Figure 5.13 Colloidal stability The net free energy profiles of a sterically stabilized particle that approaches a similar particle with different pIB concentrations. The repulsive contribution is due to the interpenetration (overlap) of the pIB chains and the attractive contribution originates from the Van der Waals interaction. Γ_{pIB} ranges from 0 to 0.6, with a stepsize of 0.2.

5.4 Discussion

A critical note must be placed at the assumptions that have been made and the limitations of the SCF calculation. Firstly, the system that is considered is approximated on a mean-field level implementing one gradient direction and averaging is performed in the other two directions. Secondly, the molecular species are modeled on a united-atom level. In both cases, the incorporation of more detail in the model should yield more realistic results. The major drawback is, however, that it would require progressively more computing power. Nonetheless, the approximations that are applied within the framework of the SCF calculation are valid and have proven very useful in the field of physical and colloidal chemistry. Similar calculations have been performed to study polymer adsorption, micellization, colloidal stability and wetting phenomena.³¹ A major limitation of this study is the absence of curvature of the w/o interface. As already mentioned, several aspects relevant to Pickering emulsions are studied at the level of a ‘single’ particle that adsorbs at the w/o interface. It is assumed that the w/o interface is flat and does not deform, when the particle adsorbs. In reality, however, emulsion droplets are obviously curved, which could have an effect on the packing of particles and the interaction among particles at the w/o interface. In other cases, curvature could have a profound effect and is an interesting topic

of research. Unfortunately, this falls outside the scope of this chapter, since only a single particle is studied.

Taking into account the assumptions and limitations of the SCF calculation, we numerically solved the wetting behavior and the colloidal stability under exactly identical conditions and we can start to compare the various situations. It is generally accepted that for charged colloids, flocculating conditions enhance the particle adsorption to the interface and promote the formation of Pickering emulsions, which is partly confirmed in this work by the fig. 5.10 - 5.13. The conditions $\Gamma_{\text{pIB}}: 0.0 - 0.4$ are colloiddally unstable and show aggregating and flocculating conditions. At the same time these systems show appropriate contact angles for the assembly at liquid interfaces. However, it turns out that flocculating conditions are not an absolute requirement. The same figures show a window of stabilizer concentrations $\Gamma_{\text{pIB}}: 0.4 - 0.6$ that show both partial wetting and colloidal stability. Note that this is at a relatively low grafting density, well below the overlap condition, that is where the chains are in the mushroom regime. The results found in this study are remarkable and when these predictions are implemented may lead to the enhanced stability of Pickering emulsions. The particle covered emulsion droplets will not only be stable against coalescence, but also against aggregation. This is beneficial for the subsequent formation of colloidosomes or nano-composite particles or other materials synthesized from Pickering emulsions.

Another interesting observation is that under thermal conditions ($k_B T$), sterically stabilized systems do not assemble at liquid interfaces. Shear forces need to be applied to overcome the kinetic barrier for assembly and drive the particles to the interface. High-shear mixers, such as rotor-stator mixers or ultra-sonicators, have to be used to form the Pickering emulsions. In the formation of such emulsions shear is required to break up the dispersed phase and form small emulsion droplets. Simultaneously, particles are assembled at the interface. Interestingly, the kinetic barrier for assembly at an oil/water interface is an order of magnitude higher than the kinetic barrier for aggregation, which could be due to the following reasons. The interaction of pIB with water is more unfavorable than the interpenetration of pIB coils. Moreover, the attraction due to the Van der Waals-force is relatively long-ranged in comparison with a reduction of the interfacial energy, which only comes into play when a particle actually touches the interface. The Van der Waals-force

effectively lowers the kinetic barrier for aggregation. Finally, the difference in geometry (plate-sphere versus sphere-sphere) can play a role. In the case of a plate-sphere geometry more pIB coils interact with the w/o interface than is the case for a sphere-sphere geometry. Absolutely speaking, the barrier for assembly is quite high $140 - 550 k_B T$, although it must be noted that this value scales with R^2 . In this study a relatively large particle is used $R = 1 \mu\text{m}$. Nanoparticles, under the same conditions, would experience substantially less repulsion.

The above-discussed effects are studied as a function of the stabilizer concentration on the particle surface. Qualitatively, a similar effect is obtained when the polymer chain length is either increased or decreased. Longer polymer chains lead to more hydrophobic particles, higher activation barrier and enhanced colloidal stability. Vice versa, the opposite effect is observed for shorter polymer chains. However, if the grafting density is changed accordingly, such that the total amount of polymer is kept constant, then no effect on activation barrier and colloidal stability is observed. Therefore, the effect of the molecular weight is not reported.

An interesting question is now whether this principle applies to other systems, such as different core materials or charged colloids. The use of different core materials will definitely affect the ideal window of stabilizer concentrations, since the wetting properties are determined by both the surface (fig. 5.6) and the grafted polymer (fig. 5.8). For example, the use of polystyrene ($\chi_{SC} < -0.5$) would narrow the range of Γ_{pIB} that gives both partial wetting and colloidal stability and the use of silica, which is a hydrophilic surface ($\chi_{SC} > -0.5$), increases that range. Ideally, there is a large polarity difference between the particle and the oil-phase and, at the same time, the particles should have sufficient stabilizer to assure colloidal stability.

The presence of charged groups on the particle surface has an opposite effect, with respect to oil-soluble polymeric stabilizer. In principle, the same behavior is expected for charged colloids as for sterically stabilized systems. The charged groups alter the surface tension of the particle, although in the opposite way, and herewith change the equilibrium position at the interface. This is illustrated by the various θ ($90 - 130^\circ$) that are reported in literature of,

for example, sulfate- or carboxylic acid functional polystyrene latexes.^{14, 15} At the same time, these groups generate a repulsive force from the interface and from other colloids, as reported by Tcholakova.²⁰ The electrostatic barrier for particle adsorption is expected to be even higher, with respect to sterically stabilized colloids, because the w/o interface can be charged at low ionic strength aqueous phases.¹⁸ These experimental findings indicate that similar qualitative trends occur for charge-stabilized colloids. However, an additional SCF study is required to investigate whether a similar window of colloidal stability and partial wetting exists for charged colloids.

5.5 Conclusion

The assembly of sterically-stabilized colloids at w/o interfaces is studied with the SCF theory, using the discretization scheme that was developed by Scheutjens, Fleer and co-workers. A single pMMA particle with pIB grafted to the particle surface is considered, which is initially dispersed in the oil phase and assembles at a w/o interface. The effect of the stabilizing groups on the interfacial adsorption is investigated. The surface tension of the particle is altered by the presence of the stabilizing groups, which affects the wetting properties and herewith the equilibrium position of the particles at the interface. The stabilizing groups also lead to a kinetic barrier when a particle approaches the interface, analogous to the steric repulsion between two particles. These effects are numerically solved with the SCF theory. It is generally understood that dispersions under flocculating conditions form Pickering emulsions, which is in fact confirmed in this work. However, it is found here that flocculating conditions are not an absolute requirement. There is a small window of stabilizer concentrations $\Gamma_{\text{pIB}} : 0.4 - 0.6$, which corresponds to $2.2 - 3.3 \text{ mg/m}^2$, that shows both partial wetting and colloidal stability, which is ideal for the synthesis of new materials, such as Pickering emulsions, colloidosomes or colloidal nano-composites. In the other cases, the particles are either colloiddally unstable, or are completely wetting and, therefore, do not assemble at w/o interfaces. The activation barrier for particle adsorption at the w/o interface is relatively high $140 - 550 k_B T$ and is an order of magnitude higher than for colloidal stability. Possible reasons are the unfavorable interaction with water, the Van der Waals attraction among particles, which effectively lowers the kinetic barrier for aggregation, and the difference in geometry (plate-sphere versus sphere-sphere). This study demonstrates the interplay between the wetting behavior of the particles and their colloidal stability and gives a better understanding of the colloidal assembly at soft interfaces and the formation of Pickering emulsions in general.

References

1. Lee, R. F., *Spill Science & Technology Bulletin* **1999**, 5, (2), 117-126.
2. Dickinson, E., *Current Opinion in Colloid & Interface Science* **2010**, 15, (1-2), 40-49.
3. Rousseau, D.; Ghosh, S.; Park, H., *Journal of Food Science* **2009**, 74, (1), E1-E7.
4. Lu, S.; Pugh, R. J.; Forssberg, E., *Interfacial separation of particles*. Elsevier: Amsterdam, 2005; Vol. 20.
5. Frellichowska, J.; Bolzinger, M. A.; Pelletier, J.; Valour, J. P.; Chevalier, Y., *International Journal of Pharmaceutics* **2009**, 371, (1-2), 56-63.
6. Binks, P.; Horozov, T. S., *Colloidal particles at liquid interfaces*. Cambridge University Press: New York, 2006.
7. Dinsmore, A. D.; Hsu, M. F.; Nikolaidis, M. G.; Marquez, M.; Bausch, A. R.; Weitz, D. A., *Science* **2002**, 298, (5595), 1006-1009.
8. Bon, S. A. F.; Chen, T., *Langmuir* **2007**, 23, (19), 9527-9530.
9. Colver, P. J.; Bon, S. A. F., *Chemistry of Materials* **2007**, 19, (7), 1537-1539.
10. Young, T., *Phil. Trans.* **1805**, 95, 65-87.
11. Pieranski, P., *Physical Review Letters* **1980**, 45, (7), 569-572.
12. Levine, S.; Bowen, B. D.; Partridge, S. J., *Colloids and Surfaces* **1989**, 38, (4), 325-343.
13. Yan, N. X.; Gray, M. R.; Masliyah, J. H., *Colloids and Surfaces a-Physicochemical and Engineering Aspects* **2001**, 193, (1-3), 97-107.
14. Paunov, V. N., *Langmuir* **2003**, 19, (19), 7970-7976.
15. Stancik, E. J.; Fuller, G. G., *Langmuir* **2004**, 20, (12), 4805-4808.
16. Benkoski, J. J.; Hu, H.; Karim, A., *Macromolecular Rapid Communications* **2006**, 27, (15), 1212-1216.
17. Klein, S. M.; Manoharan, V. N.; Pine, D. J.; Lange, F. F., *Langmuir* **2005**, 21, (15), 6669-6674.
18. Leunissen, M. E.; van Blaaderen, A.; Hollingsworth, A. D.; Sullivan, M. T.; Chaikin, P. M., *Proceedings of the National Academy of Sciences of the United States of America* **2007**, 104, (8), 2585-2590.
19. Du, K.; Glogowski, E.; Emrick, T.; Russell, T. P.; Dinsmore, A. D., *Langmuir* **2010**, 26, (15), 12518-12522.
20. Tcholakova, S.; Denkov, N. D.; Lips, A., *Physical Chemistry Chemical Physics* **2008**, 10, (12), 1608-1627.
21. Binks, B. P.; Rodrigues, J. A., *Langmuir* **2007**, 23, (14), 7436-7439.
22. Golemanov, K.; Tcholakova, S.; Kralchevsky, P. A.; Ananthapadmanabhan, K. P.; Lips, A., *Langmuir* **2006**, 22, (11), 4968-4977.
23. Salari, J. W.; van Heck, J.; Klumperman, B., *Langmuir* **2010**, 26, (18), 14929-14936.
24. Simovic, S.; Prestidge, C. A., *Langmuir* **2003**, 19, (9), 3785-3792.
25. Binks, B. P., *Current Opinion in Colloid & Interface Science* **2002**, 7, (1-2), 21-41.
26. Denkov, N. D.; Ivanov, I. B.; Kralchevsky, P. A.; Wasan, D. T., *Journal of Colloid and Interface Science* **1992**, 150, (2), 589-593.
27. Reynaert, S.; Moldenaers, P.; Vermant, J., *Langmuir* **2006**, 22, (11), 4936-4945.
28. Scheutjens, J.; Fleer, G. J., *Journal of Physical Chemistry* **1979**, 83, (12), 1619-1635.
29. Scheutjens, J.; Fleer, G. J., *Journal of Physical Chemistry* **1980**, 84, (2), 178-190.
30. Schlangen, L.; Leermakers, F. A. M.; Koopal, L. K., *Journal of the Chemical Society-Faraday Transactions* **1996**, 92, (4), 579-587.
31. Fleer, G. J.; Cohen Stuart, M. A.; Scheutjens, J. M. H. M.; Cosgrove, T.; Vincent, B., *Polymers at interfaces*. Chapman & Hall: London, 1993.

- 32. Edwards, S. F., *Proceedings of the Physical Society of London* **1965**, 85, (546P), 613-&.
- 33. Evers, O. A.; Scheutjens, J.; Fleer, G. J., *Macromolecules* **1990**, 23, (25), 5221-5233.
- 34. Kik, R. A.; Leermakers, F. A. M.; Kleijn, J. M., *Physical Review E* **2010**, 81, (2).
- 35. Li, F.; Marcelis, A. T. M.; Sudholter, E. J. R.; Cohen Stuart, M. A.; Leermakers, F. A. M., *Soft Matter* **2009**, 5, (21), 4173-4184.
- 36. Weast, R. C.; Astle, M. J., *Handbook of chemistry and physics*. 61 ed.; CRC Press: Florida, 1980.
- 37. Wu, S., *Journal of Polymer Science Part C-Polymer Symposium* **1971**, (34), 19-&.
- 38. Derjaguin, B. V., *Theory of stability of colloids and thin liquid films*. Plenum Press: New York, 1989.
- 39. Hamaker, H. C., *Physica* **1937**, 4, (10), 1058-1072.

6

The relevance of drainage **during the w/o interfacial adsorption of hairy particles**

Abstract: The adsorption of sterically-stabilized colloids at water-oil (w/o) interfaces is studied experimentally by the formation of Pickering emulsions. Specifically, the effect of the steric stabilizer with respect to the kinetics of particle adsorption is investigated. The rate of particle adsorption is measured by the evolution of the droplet diameter during emulsification. Uniform, μm -sized poly(methyl methacrylate) (pMMA) particles that are stabilized with poly(isobutylene) (pIB) are used. The pIB concentration on the particle surface (Γ_{pIB}) is controlled by adjusting the steric stabilizer/monomer ratio during the synthesis of the particles. Pickering emulsions are formed by the addition of water to the non-aqueous pMMA dispersions and subsequent emulsification. A strong dependence of Γ_{pIB} on the kinetics of particle adsorption is found. It is known that the stabilizing layer around the particle leads to a repulsive barrier before interfacial adsorption, which decreases the probability for adsorption and hereby affects the rate of particle adsorption. The rate constant k for particle adsorption decays exponentially with Γ_{pIB} , which suggest the use of a Boltzmann factor to model the experimentally found k 's. The experimental results can be explained when the activation barrier E_A is of the same order as the average kinetic energy E_K of a particle colliding with an emulsion droplet, which is equivalent to $10^4 k_B T$. Interestingly, this makes E_A several orders of magnitude higher than the repulsive barrier for steric stabilization with another particle. A possible mechanism that can lead to such a repulsive force is the inhibited drainage of solvent from the layer of steric stabilizer upon interfacial adsorption. Deformation of the o/w interface occurs, when the solvent does not have time to drain, which results in a dramatic increase of the interfacial energy. This study identified the relevance of drainage in the formation of Pickering emulsions.

6.1 Introduction

The adsorption of colloidal particles at soft interfaces, such as o/w mixtures, is governed by the respective interfacial free energies γ of the particle and the two soft phases.¹ Young's equation, relates the interfacial tensions with the equilibrium position of the particle at the interface, through the 3-phase contact angle (θ) (eq. 1.1, see also fig. 6.1).² The stabilizing groups on the colloid surface strongly affect the interfacial adsorption, as is described extensively in chapter 5, and therefore also affects the formation of Pickering emulsions. The stabilizing groups lead, in the first place, to an activation barrier for adsorption, analogue to the colloidal repulsion between two particles. Secondly, the stabilizing groups lower the interfacial tension of the particle with the fluid in which it is originally dispersed, which alters the equilibrium position of the particle at the w/o interface.

The colloidal stability and the wetting behavior are fundamentally related through the surface functional groups. It is, therefore, not surprising that these two properties are often linked. For charge-stabilized colloids the rule of thumb is that 'flocculating' conditions enhance the interfacial adsorption and coalescence stability of the final Pickering emulsion.³⁻⁹ As a result, the Pickering emulsions are also flocculating. This is clearly demonstrated in the Pickering emulsions of chapter 3 and 4. Moreover, chapter 4 shows how the stability of a Pickering emulsion can be improved by the addition and adsorption of poly(styrene-block-ethylene-co-propylene) (pS-b-EP). The pS-block adsorbed onto the pS particle-stabilized emulsion. The EP-block remained soluble in the continuous phase and sterically stabilized the emulsion droplets. This prevents the aggregation of Pickering emulsion droplets and leads to the efficient synthesis of pS microcapsules.

A different approach to improve the stability of Pickering emulsions is described in this chapter. Sterically-stabilized or hairy particles are synthesized by dispersion polymerization and are used to form Pickering emulsions, which effectively results in sterically-stabilized Pickering emulsions (fig. 6.1). The previous chapter theoretically studied the wetting behavior and colloidal stability of poly(isobutylene) functionalized pMMA particles. It confirmed the wide-spread notion that flocculating conditions enhanced interfacial adsorption. Moreover, it demonstrated that there is a small window of stabilizer concentrations that exhibit both colloidal stability and partial wetting. These conditions are aimed for in the development of stable Pickering emulsions, which will be used in chapter 7 to synthesize pMMA microcapsules.

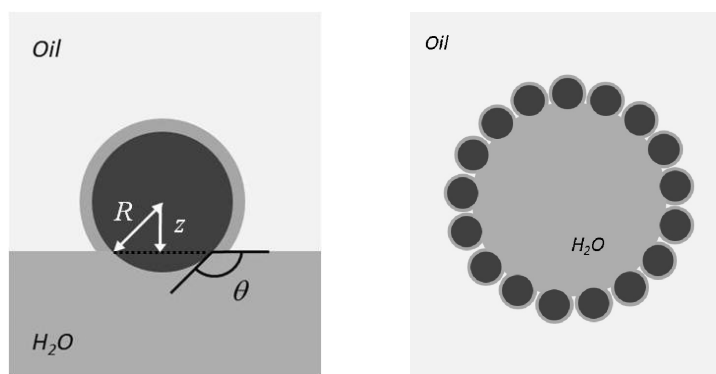


Figure 6.1 A hairy particle that is located at an w/o interface (left) and a Pickering emulsion droplet stabilized with same particles (right). R is the radius of the particle. θ is the three phase contact angle. z is the distance from the center of the particle to the interface. The dark grey circle represents the solid particle. The light gray area that surrounds the particle is the layer with polymer stabilizer, which is attached to the particle and is soluble in the oil. The light gray area is insoluble in water and is therefore less extended and therefore not shown in this image.

Tchokalova published a comprehensive review on Pickering stabilization, in comparison with conventional surfactants and proteins, and reported specifically on the role of the electrostatic barrier in particle adsorption.⁹ He concluded that the activation barrier for particle adsorption is relatively high, due to relatively large size of the stabilizing units. We theoretically studied the role of the steric stabilizer on the wetting properties and the activation barrier for particle adsorption in the chapter 5, which also demonstrated a significant activation barrier for particle adsorption. Recently, Teixeira and Bon suggested an additional contribution to the activation barrier, due to inhibited drainage of fluid and deformation of the w/o interface.¹⁰ Effectively, the energetic barrier decreases the chance of adsorption and hereby affects the kinetics of particle adsorption.⁹ The role and extent of the repulsive, activation barrier for particle adsorption is studied experimentally in this chapter. Various hairy pMMA dispersions are synthesized with different particle size and stabilizer concentrations. The rate of particle adsorption, to the w/o interface, is measured for each dispersion from which the activation barrier is derived.

This chapter is organized as follows. Hairy pMMA particles are synthesized by dispersion polymerization in heptane. The 1st part of the chapter describes the particle synthesis in detail. Two poly(isobutylene) steric stabilizers are used with different molecular weights of respectively 36000 g/mol and 42000 g/mol. Additionally, the stabilizer/monomer ratio is

adjusted to control the particle size and the surface concentration of poly(isobutylene). The obtained particle dispersions can be directly used to form Pickering emulsions by the addition of water and emulsification of the mixture. The 2nd part reports the formation and characterization of the Pickering emulsions. The rate of particle adsorption is determined from the evolution of the droplet size during emulsification. This is done with various pMMA dispersions that differ both in particle size and stabilizer concentration. The 3rd part of the chapter models the observed rate constants with a Boltzmann factor to derive the activation barrier for particle adsorption and discusses the implications for Pickering emulsions, in general.

6.2 Experimental

Materials Methyl methacrylate (MMA) (99%, Sigma Aldrich) is passed over a column with aluminum-oxide (activated basic, Sigma Aldrich) prior to use to remove inhibitor. The inhibitor-free MMA is refrigerated for later use. n-Heptane (> 96%, Biosolve). Azo-bis-isobutyronitrile (AIBN) (Sigma Aldrich) is recrystallized twice from methanol to remove any impurities. Methanol (99.8%, Biosolve) is used as received. Poly(isobutylene-co-isoprene) (pIB) (Kalene 800 and 1300, Royal Elastomers) are used as received. The molecular weights of Kalene 800 and 1300 are 36000 and 42000 g/mol, respectively. Both polymers contain 2.5 - 3.5 % unsaturated carbon-carbon bonds. Water is double de-ionized with a purification system.

pMMA particles are synthesized by dispersion polymerization in heptane. The synthesis is performed in a 250 mL double-walled reactor equipped with four baffles and a four-blade pitched impeller is used. The reactor is equipped with a water-cooled condenser. A thermostatic bath is used to control the reactor temperature. A typical dispersion polymerization initially contains 110.5 g heptane, 33.2 g MMA, 0.5 g AIBN and a particular amount of pIB. The amount of pIB is systematically varied (0.17 g to 5.51 g) throughout this work and is specified later. Initially, pIB and heptane are charged into the reactor and the mixture is stirred at 100 rotations per minute (rpm) until the pIB is completely dissolved. AIBN is dissolved in MMA and added to the heptane/pIB mixture. The reactor is purged with nitrogen to remove oxygen from the mixture. The thermostatic bath is heated to 80 °C and connected to the reactor, such that the reaction mixture is heated and the polymerization is started. The reaction mixture is stirred for at least 3 hours and is then cooled to room temperature. For one dispersion polymerization samples are taken to

determine the conversion gravimetrically. The solid-content is measured gravimetrically at the end of the polymerization for the other polymerizations (Table 6.1). The resulting dispersion is stored for later use, when the mixture has reached room temperature ($T = 20$ °C). The particles are imaged with a desktop scanning electron microscopy (SEM) (Phenom, FEI company). The sample holder is covered with double-sided conducting carbon tape and a droplet of the obtained dispersion is cast on the sticker. The sample is dried under air and sputter-coated with a thin layer of gold before imaging with SEM. The particle size distribution is determined from the SEM image with image processing software (ImageJ). Initially, static light scattering was also performed to determine the particle size and are similar than those obtained from the SEM images. Therefore, only data obtained from the SEM images are presented here (Table 6.1).

Table 6.1 Data concerning the synthetic conditions of the dispersion polymerizations and the formation of the Pickering emulsions.

Experiment	Mw pIB ^a [g/mol]	pIB/MMA ^a [g/g]	Particle diameter ^b [μm]	Solid content ^c [g/g]	Weight ^d dispersion [g]
1	36000	0.166	1.32	0.293	-
2	36000	0.083	1.54	0.237	-
3	36000	0.042	1.53	0.221	6.766
4	36000	0.033	1.68	0.221	7.532
5	36000	0.025	2.06	0.205	10.288
6	36000	0.016	2.16	0.224	10.304
7	42000	0.153	1.68	0.257	-
8	42000	0.040	2.29	0.289	-
9	42000	0.030	2.45	0.231	9.656
10	42000	0.025	2.49	0.215	10.740
11	42000	0.020	2.56	0.236	9.443
12	42000	0.015	2.74	0.255	9.625
13	42000	0.010	3.09	aggregated	-

^a synthetic conditions dispersion polymerization. ^b Final properties of the pMMA dispersions. ^c The amount of dispersion used to form the Pickering emulsion.

Pickering emulsions are produced by the addition of water to the particle dispersions and followed the application of high shear. The amount of dispersion with respect to water is chosen in such a way that a w/o emulsions with 50 μm droplets is expected. In this calculation it is assumed that all the particles are adsorbed at the w/o interface, densely packed in a hexagonal fashion and that curvature effects could be neglected. To form a Pickering emulsion, a certain amount of dispersion is weighed in a measuring cylinder and diluted with additional heptane to 100 mL. The amounts being used throughout the work described in this chapter depend on the particle size and solid content of the dispersion. The exact amounts are specified in the last column of Table 6.1. The diluted dispersion is charged to a 200 mL polyethylene bottle and 10 mL water is added. The whole mixture is sheared with a rotor-stator mixer (IKA Ultra Turrax T25 Basic) at 24000 rpm. The duration of shear applied to the mixture varied from 1 to 5 minutes and is specified at a later stage. The Pickering emulsions are characterized by optical microscopy. The droplet diameters are derived from the images with ImageJ.

6.3 Results

6.3.1 Particle synthesis: dispersion polymerization

Before the formation of any Pickering emulsion, a dispersion of particles has to be synthesized first. Then, a second, immiscible fluid can be added to form the actual emulsion. In this study, the particles are synthesized by dispersion polymerization of MMA in heptane. Dispersion polymerization is a common technique¹¹⁻¹³ to synthesize highly uniform colloids in the μm -range and has previously been used by Winnik and coworkers^{14, 15} to form model pMMA colloids. Contrary to heterogeneous polymerizations, the initial reaction mixture is homogeneous for dispersion polymerization. Initially, the monomer, stabilizer and initiator are completely dissolved in the medium. Upon polymerization, the formed polymer chains become insoluble and start to aggregate with other polymer chains to form a particle. The stabilizer controls the aggregation process, such that a colloiddally stable particle is formed. From that moment on, the number of particles remains approximately constant and the particles grow with increasing conversion of monomer. Since the polymerization is performed in a non-aqueous medium, a polymeric stabilizer is required. The stabilizers used in this study are commercially available poly(isobutylene) rubbers. These polymers contain 2.5 - 3.5 % unsaturated carbon-carbon bonds, which participate in the polymerization and subsequently graft to the formed pMMA particles. In

this way the particle formation is controlled and relatively stable dispersions are obtained. Figures 6.2 and 6.3 show a typical result of a dispersion polymerization.

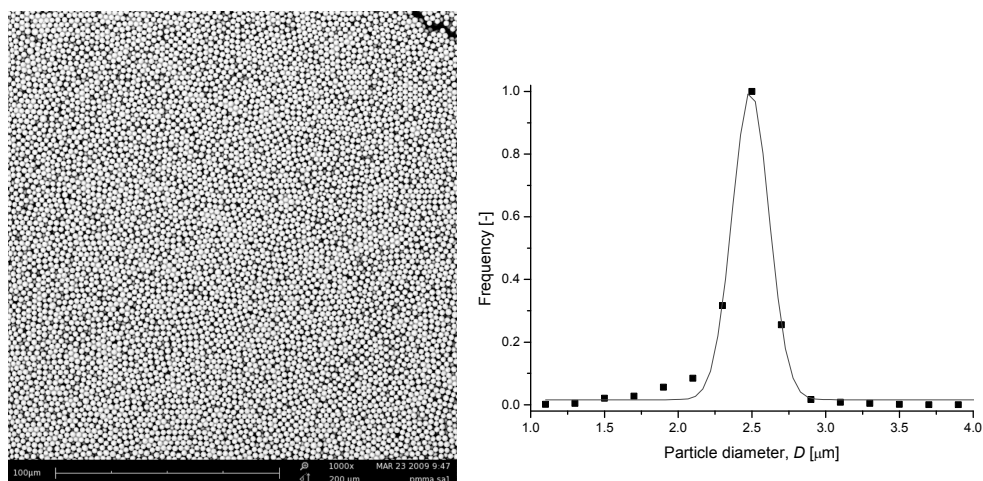


Figure 6.2 Typical results from dispersion polymerization of MMA in heptane. SEM image of pMMA particles from dispersion **10** (left) and the particle diameter distribution that is derived from the image (right). Synthetic conditions of dispersion polymerization: $M_{PIB} = 42000$ g/mol and $pIB/MMA = 0.025$ g/g.

The pMMA particles show a narrow particle size distribution. The particle formation occurred in a controlled manner. No significant secondary nucleation or aggregation is observed. The particle size is analyzed from the SEM image using image processing software (imageJ). The particle size distribution approximately obeys a Gaussian function and yields a mean particle diameter of 2.5 μm. The polydispersity index is $d_V/d_N = 1.02$, where d_V and d_N is the volume- and number-average particle diameter, respectively. The conversion curve in figure 6.3 shows that after approximately 3 hours, maximum conversion is achieved. From the other dispersion polymerizations, only a final sample is taken to measure the solid-content of the dispersion.

In the initial stages of our study, relatively high stabilizer concentrations were used, because these conditions assure controlled particle formation and colloidally stable dispersions. However, it was found that such conditions do not favor the formation of Pickering emulsions. Emulsions with a very broad water droplet size distribution were formed and the water droplets were unstable against coalescence. It is previously described that flocculating

conditions enhance the interfacial adsorption and the formation of Pickering emulsions. In aqueous dispersions, flocculation can be induced by the addition of salts, which suppresses the electrostatic repulsion. This cannot be done with sterically stabilized colloids in non-aqueous media, as is the case here. In the theoretical study (chapter 5) on the same system, it is demonstrated that the interfacial adsorption can be enhanced by a reduction of the stabilizer concentration at the particle surface. Using dispersion polymerization, this can be achieved by a reduction of the stabilizer/monomer ratio in the initial reaction mixture. Therefore, a series of dispersions are synthesized in which the stabilizer/monomer ratio is systematically varied, as can be seen in figure 6.4.

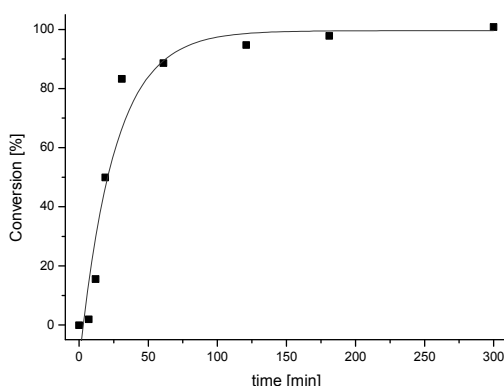


Figure 6.3 Conversion plot corresponding to dispersion polymerization 1. The conversion is determined gravimetrically.

Figure 6.4 shows that for both stabilizers the particle size increases strongly with decreasing stabilizer concentration, which is common for dispersion polymerization.¹¹⁻¹³ The same data can be presented in a double logarithmic plot, which is not shown here, but yields two linear relations with equal slopes. The particle diameter scales with stabilizer concentration, according to $d_n \sim [pIB]^{-0.21}$. Moreover, the results collected in figure 6.3 clearly demonstrate that the particle diameter depends on the molecular weight of the polymeric stabilizer. This can be explained by realizing that the weight ratios are kept the same in figure 6.3, so the molar concentration of pIB depends on the molecular weight. As a consequence, the particle diameter is larger for lower molar concentration of steric stabilizer, which is a common trend in dispersion polymerization. In all cases, a controlled

particle formation occurred and no secondary nucleation was observed. At low pIB concentrations ($\text{pIB/MMA} < 0.025 \text{ g/g}$), minor aggregation occurred, indicating that the limits of colloidal stability are reached. The dispersion with the lowest stabilizer concentration ($\text{pIB/MMA} = 0.01 \text{ g/g}$) was severely aggregated. Even in this case, particle nucleation occurred in a controlled manner, but the dispersion became unstable at a later stage of the polymerization when the particles grew to their final size. The solid content is measured by gravimetry (table 6.1) and is used later to determine the number of particles per unit volume of the continuous phase and the total surface area of the particle dispersion.

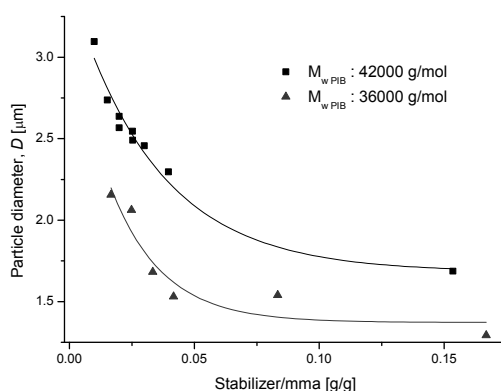


Figure 6.4 The particle diameter as a result of the pIB/MMA ratio in the initial reaction mixture. Two polymeric stabilizers are used with different molecular weights, respectively 36000 g/mol (red) and 42000 g/mol (black). The other synthetic conditions are kept constant.

As was already pointed out earlier, the pIB concentration on the particle surface (Γ_{PIB}) is the most relevant parameter with respect to the rate of particle adsorption to the w/o interface. Therefore, Γ_{PIB} is calculated as the ratio of the total amount of pIB and the total surface area of the final dispersion. It is assumed that all stabilizer is grafted to the surface. On forehand, it must be mentioned that is not the case. Only a fraction of the total amount pIB is actually grafted to the particle surface. The rest is still dissolved in the solvent. An effort was made to measure Γ_{PIB} , but it proved very difficult to determine the exact concentration on the particle surface. Therefore, for the rest of the work we assumed that in each dispersion polymerization, the same fraction of pIB, with respect to the total amount pIB present, is grafted to the particle surface and that the actual Γ_{PIB} scales with the calculated values.

Figure 6.5 shows Γ_{PIB} for the various dispersions and it is clearly demonstrated that Γ_{PIB} scales linearly with pIB/MMA ratio of the initial mixture. The lowest value $\Gamma_{\text{PIB}} = 0.006 \text{ g/m}^2$ showed severe aggregation and represents the lower limit of colloidal stability.

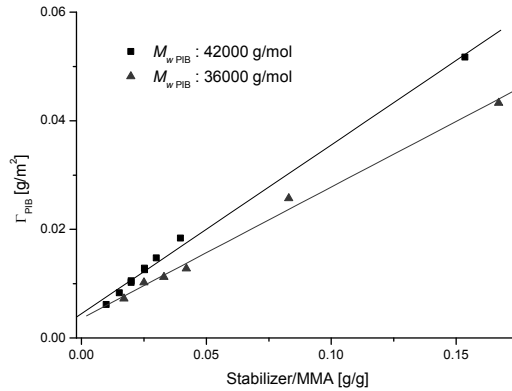


Figure 6.5 The surface concentration pIB Γ_{PIB} as a function pIB/MMA ratio in the initial reaction mixture. Two polymeric stabilizers are used with different molecular weights, respectively 36000 g/mol (red) and 42000 g/mol (black). The other synthetic conditions are kept constant.

6.3.2 Pickering emulsions

low M_w steric stabilizer

Pickering emulsions are prepared to study the effect of Γ_{PIB} on the rate of particle adsorption to the w/o interface, which is done by measuring the emulsion droplet diameter D . The number of particles N_A that are adsorbed to the w/o interface is related to D by equation 2.2. This calculation assumes a hexagonal close-packing on the droplet surface, which is confirmed by figure 6.6. A close-up of several typical Pickering emulsion droplets shows such a regular particle packing. The uniformity of the particles is also reflected by the regular packing of the particles.

The experiment is designed in such a way that the w/o interfacial area that can potentially be covered by the pMMA particles is kept constant and that 50 μm emulsion droplets are obtained when all the particles are adsorbed at the w/o interface. The volume of the dispersed phase (water) is in all cases $V_D = 10 \text{ mL}$ (*i.e.* 10% dispersed phase), but the particle diameter d_n is different for each dispersion. Therefore, the number of particles N is

adjusted for each Pickering emulsion, to obtain the same droplet diameter of 50 μm . The exact weight of the used dispersions to form the Pickering emulsions are collected in table 6.1 and range roughly between 6 and 11 g. The dispersions are diluted with additional heptane to a total volume of 100 mL, before water is added to form the actual emulsion.

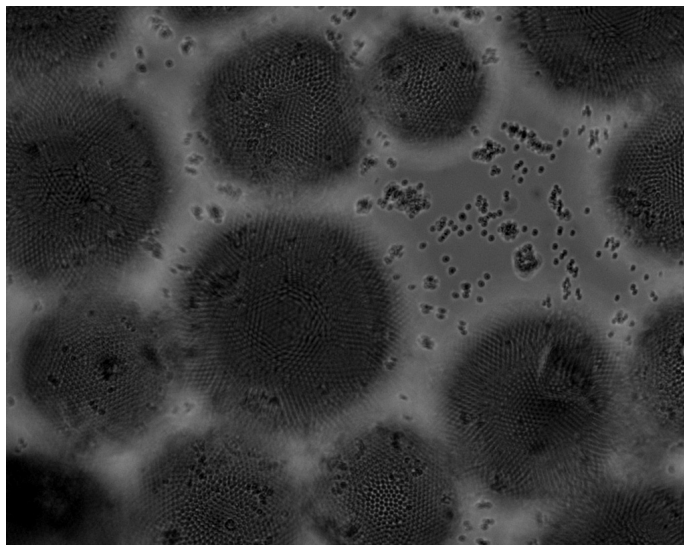


Figure 6.6 pMMA Pickering emulsion displaying the predominantly hexagonally close particle packing. LM image of Pickering emulsion 4.

In all four cases, stable Pickering emulsions are formed after shearing the mixtures for 1 minute at 24000 rpm. The emulsions did not show any coalescence while handling in the lab or imaging with the light microscope. The emulsions do sediment, because of the large density difference between the water and heptane phases. Figure 6.7 shows the final emulsions, which show clear differences in droplet size. Only emulsion 6 (fig. 6.7A) has the expected droplet diameter close to 50 μm , while the other 3 emulsions have much larger droplets. Apparently, only in emulsion 6, all the pMMA particles are adsorbed at the interface. For the other Pickering emulsions, particle adsorption is incomplete and decreases with an increasing Γ_{PIB} . The explanation for this behavior is the steric repulsion barrier that these particles experience when they approach the w/o interface, which scales with Γ_{PIB} . This means that colloiddally stable pMMA particles with high stabilizer concentrations (fig. 6.7D) are less likely to adsorb to the w/o interface. The colloids with low stabilizer concentrations adsorb much easier. This effect is more thoroughly investigated with another

set of pMMA dispersions that are synthesized with the high molecular weight (42000 g/mol) pIB stabilizer.

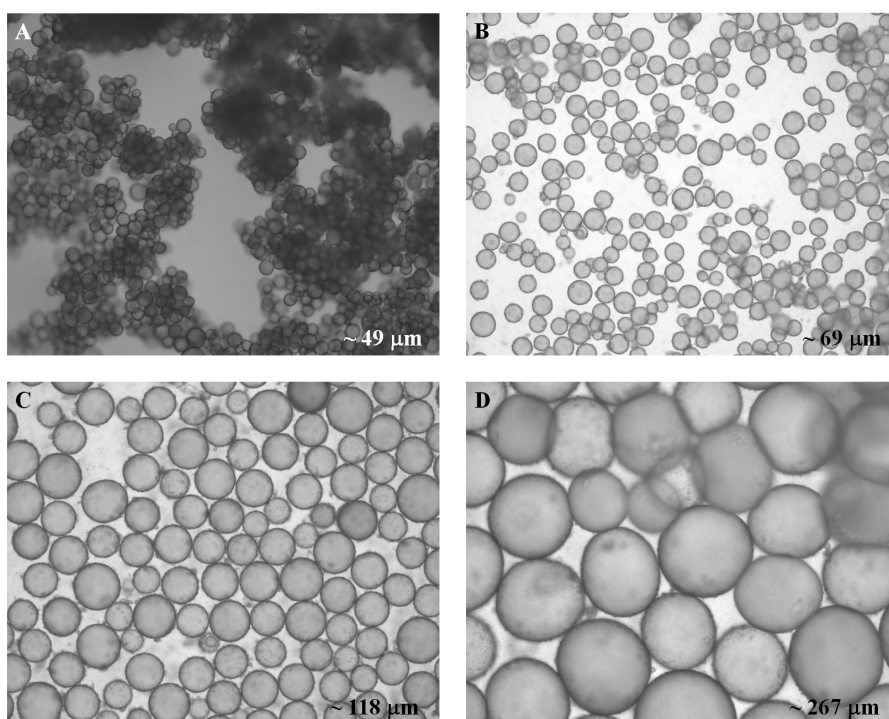


Figure 6.7 Light microscope images of pMMA Pickering emulsions. Water droplets in heptane are stabilized with different pMMA particles. A) Dispersion 6, pIB/MMA = 0.016 g/g. B) Dispersion 5, pIB/MMA = 0.025 g/g. C) Dispersion 4, pIB/MMA = 0.033 g/g. D) Dispersion 3, pIB/MMA = 0.042 g/g.

high M_w steric stabilizer

A different approach is used in the following part to quantify the rate of particle adsorption. The droplet diameter during emulsification is measured as a function of time, which gives information about the kinetics of particle adsorption. The Pickering emulsions are made in the same way as described above, except that the pMMA dispersions with high molecular weight pIB stabilizer are used (dispersions 9, 10, 11 and 12, see table 6.1). As an example, figure 6.8 shows the evolution of the droplet diameter during emulsification ($t = 1, 2$ and 3 min) for dispersion 12. A normal emulsification regime can be observed. The water phase is gradually broken up into smaller droplets and the size distribution becomes narrower, which demonstrates that in time, more particles are adsorbed to the w/o interface in order to

stabilize the droplets. The same experiment is performed with the other pMMA dispersions as well. At each moment, the number of particles N_A attached to the w/o interface is calculated. The calculation takes into account the complete distribution of droplet diameters. The results are shown in figure 6.9.

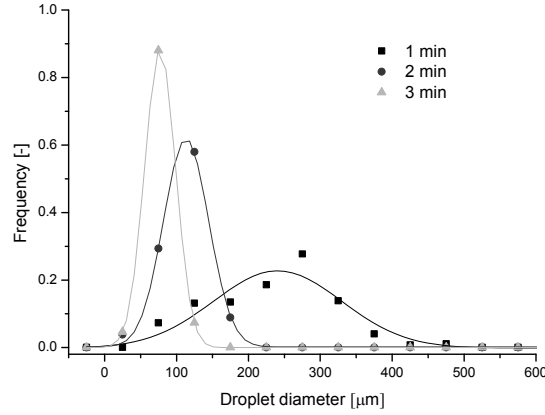


Figure 6.8 Evolution of the droplet diameter distribution during emulsification. The emulsion is stabilized with pMMA dispersion 12.

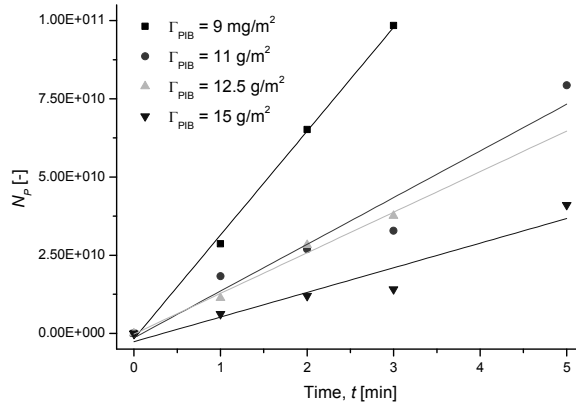


Figure 6.9 The number of pMMA particles accommodated at the w/o interface. Dispersion 12, $\Gamma_{\text{PIB}} = 9 \text{ mg/m}^2$. Dispersion 11, $\Gamma_{\text{PIB}} = 11 \text{ mg/m}^2$. Dispersion 10, $\Gamma_{\text{PIB}} = 12.5 \text{ mg/m}^2$. Dispersion 9, $\Gamma_{\text{PIB}} = 15 \text{ mg/m}^2$.

What already became clear in the previous experiment (fig. 6.7) is confirmed by the other dispersions, and their corresponding Pickering emulsions (fig. 6.9). The rate of particle adsorption is dependent on Γ_{PIB} . Particles with a high Γ_{PIB} show slower particle adsorption than the particles with a low Γ_{PIB} . All four dispersions qualitatively show the same behavior, which is that N_A increases linearly with time. In other words, there is a constant flux of particles that are being adsorbed at the w/o interface and consequently stabilize the droplets.

Rate constants k for particle adsorption

In the convective transport of particles, adsorption is a first order process with respect to particle concentration in the bulk.⁹ In other words, the rate of particle adsorption scales linearly with the number of particles in the bulk N_B (eq. 6.1). This means that upon prolonged emulsification, N_B decreases substantially and the rate of particle adsorption levels off. However, in the initial stages of emulsification the change in N_B is small compared with the total number of particles (table 6.2). Therefore, N_A can be assumed to increase linearly with time, as is the case in figure 6.9. The rate constants k can be simply derived from the slopes divided with N_B (eq. 6.1) and is presented as a function of Γ_{PIB} in figure 6.10.

$$\frac{dN_A}{dt} = kN_B \quad 6.1$$

$$N_A + N_B = N \quad 6.2$$

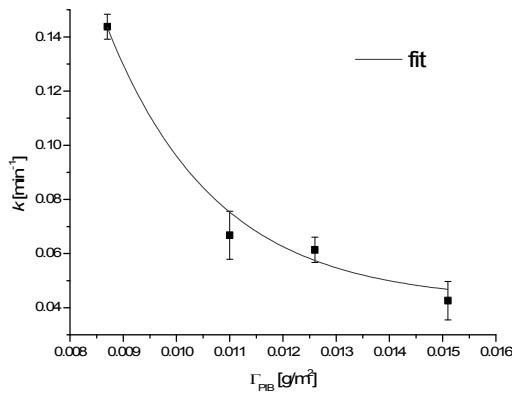


Figure 6.10 The rate constants k for particle adsorption at the w/o interface. The data is presented as a function of the surface concentration pIB, Γ_{PIB} .

6.4 Discussion

Throughout this chapter it is argued that the kinetics of particle adsorption is dominated by activation barrier of the particle with the w/o interface. In principle, other effects could play a role. For example, the available surface area for adsorption or the viscosity of the medium is known to affect the rate of adsorption. The available surface area during the formation of the Pickering emulsions is determined by the shear that is applied. In the experiment the shear is kept constant and, therefore, the available surface area is similar as well and is unlikely to play a role. The viscosity of the medium is affected by the concentration of dissolved polymer. Unreacted, freely dissolved pIB is still present after the polymerization and could play a role. However, the fraction of pIB in the heptane is small during the formation of the Pickering emulsion, because the dispersion is diluted with additional heptane. Therefore, the differences between the different particle dispersions are small and are unlikely to affect the particle adsorption. In conclusion, it is assumed that the activation barrier is the dominant parameter affecting the rate of particle adsorption.

Boltzmann factor

Figure 6.10 clearly shows that the rate of particle adsorption decreases with Γ_{PIB} , which is expected based on the increased repulsion of the particles with the w/o interface. Moreover, it is found that k decays exponentially with Γ_{PIB} (red line in fig. 6.10), which suggests the use of a Boltzmann factor.^{9, 16} Equation 6.3 is used to fit the experimental rate constants with Γ_{PIB} . C is the pre-exponential factor. For diffusive particle transport, thermal energy $k_B T$ is used for E . However, for convective transport to the w/o interface, E is a constant that is related to the kinetic energy (E_K) of a particle colliding with a droplet.

$$k = C \cdot e^{-\Gamma_{PIB}/E} \quad 6.3$$

$$\Gamma_{PIB} \sim E_A \quad 6.4$$

$$k \sim P_{ADS} = e^{-E_A/E_K} \quad 6.5$$

The presence of the steric stabilizer leads to an activation barrier E_A , which scales with Γ_{PIB} (eq. 6.4). Effectively, the activation barrier reduces the probability that a particle actually

adsorbs to the w/o interface. Equation 6.3 can therefore also be rewritten in terms of the activation barrier E_A and the kinetic energy E_K (eq. 6.5). The exponential fit of the experimentally observed rate constants, directly yields information on the probability for particle adsorption (P_{ADS}). Figure 6.11 shows P_{ADS} as a function of Γ_{PIB} values.

The squares give the experimentally observed values and the black line extrapolates P_{ADS} to lower Γ_{PIB} values. It is directly clear from figure 6.11 that the chance for particle adsorption is remarkably low for the four pMMA dispersions. Additionally, it shows that, if no stabilizer is present on the particle ($\Gamma_{PIB} = 0$), every collision results in particle adsorption to the w/o interface. Such a situation resembles the particle adsorption as is found in chapter 3. The pS particles did not experience any activation barrier. With increasing Γ_{PIB} the probability for adsorption decays exponentially and eventually becomes 0. The relation in figure 6.11 yields direct information on the ratio between the activation barrier E_A and the kinetic energy E_K of a particle. The previous chapter concluded that similar particles, which were suitable for Pickering stabilization, experienced an E_A of 225 to 450 $k_B T$ depending on Γ_{PIB} . This results in an average kinetic energy E_K of the particles colliding with the droplets equivalent to $E_K \approx 50 k_B T$.

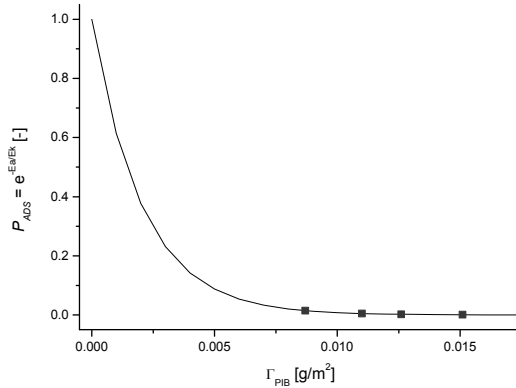


Figure 6.11 The probability for particle adsorption P_{ADS} to the w/o interface. The data is presented as a function of the surface concentration PIB, Γ_{PIB} .

Kinetic energy particles

E_K can also be calculated from the flow profile and the applied shear during emulsification. Emulsification of the mixture is performed with a lab scale rotor-stator mixer (Ultraturrax),

in which a rotating shaft is surrounded by a static cylinder. The narrow spacing (0.3 mm) between the rotor and the stator generates the shear. It is assumed that the pMMA particles are being adsorbed inside this narrow spacing between the rotor and the stator, because the shear is the highest at this position. The shear rate at 24000 rpm is $\tau = 53000 \text{ s}^{-1}$. Moreover, a laminar flow profile is assumed, where the fluid at the stator wall is stagnant ($v = 0$) and that the fluid at the rotor wall moves with the rotation velocity $v = v_{\text{ROTOR}}$ (fig. 6.12).

Depending on the relative positions of the particle and the droplet, they move with different speeds. When the centers of the particle and the droplet are aligned, both move at exactly the same speed and therefore will never collide. However, when the positions are different they exhibit different speeds and eventually collide. The average velocity difference $\langle \Delta v \rangle$ is given by shear rate τ divided by half the droplet radius $D/2 = 25 \text{ }\mu\text{m}$ (eq. 6.6). m_P is the mass of one pMMA particle.

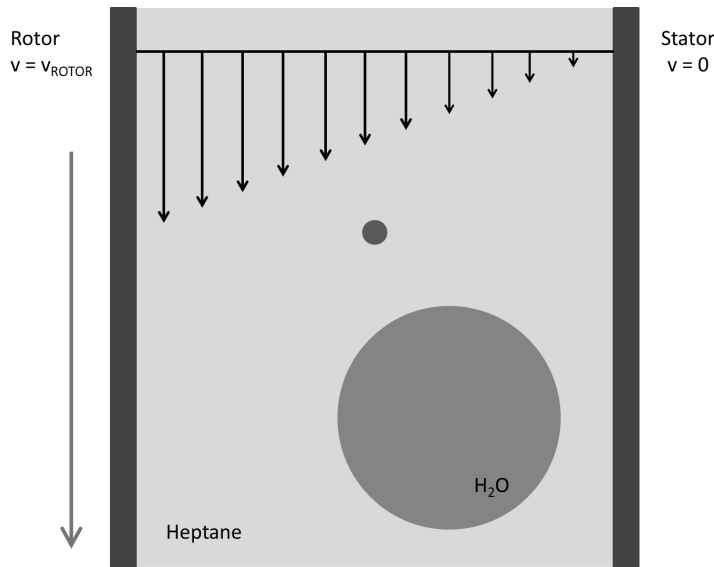


Figure 6.12 Schematic representation of the velocity profile inside the rotor-stator mixer. The stator is stagnant ($v = 0$) and the rotor moves with v_{ROTOR} . The black arrows demonstrate the gradient in the velocity between the rotor and the stator. The dimensions of the picture are exaggerated. The particle is indicated with the dark gray sphere.

$$\langle \Delta v \rangle = \frac{D}{4} \tau$$

6.6

$$E_K = \frac{1}{2} m_P \cdot \langle \Delta v \rangle^2 \quad 6.7$$

E_K of a particle colliding with a droplet is then in the order of $10^4 k_B T$, which is extremely high in comparison with the repulsive barrier that is calculated in the SCF-study ($E_A \approx 10^2 k_B T$) and the obtained experimental results ($E_K \approx 50 k_B T$). If E_A and E_K are calculated correctly, the Boltzmann factor would be close to 1 (eq. 6.8). This means that every collision results in particle adsorption and that particle adsorption is purely limited by convection. In other words, the rate of particle adsorption scales with the concentration of particles in the bulk (eq. 6.9). In the last experiment that would yield an opposite trend to what is actually found. Instead of an exponentially decaying relation, k should increase with Γ_{PIB} (table 6.2).

$$k \sim e^{-E_A/E_K} = 1 \quad 6.8$$

$$\frac{dN_A}{dt} \sim N_B \quad 6.9$$

Table 6.2 Properties of the pMMA particle dispersion that are used to stabilize the Pickering emulsions. Particle diameter D_P , the number of particles N used to form the Pickering emulsions, the surface concentration stabilizer Γ_{PIB} and the repulsive barrier for adsorption E_A as calculated with the SCF-theory.

Dispersion	D_P [μm]	N [-]	Γ_{PIB} [g/m^2]	E_A [$k_B T$]
9	2.45	$2.31 \cdot 10^{11}$	15	450
10	2.49	$2.24 \cdot 10^{11}$	12.5	340
11	2.56	$2.11 \cdot 10^{11}$	11	300
12	2.74	$1.85 \cdot 10^{11}$	9.0	225

Finally, it must be mentioned that the calculated average collision velocity should be considered as a minimum. A laminar flow profile is assumed in the calculation of $\langle \Delta v \rangle$. However, considering the shear and rotor speed, a turbulent flow profile is more likely to

occur. By definition, $\langle \Delta v \rangle$ is larger in a turbulent system than for laminar flow. Therefore, the calculated $\langle \Delta v \rangle$ is considered a minimal value and is in that sense still useful for comparison with E_A .

Drainage & deformation of the w/o interface

Based on the previous calculations, it can be concluded that E_A is seriously underestimated by the SCF calculation in the previous chapter, which should be of the same order of magnitude as E_K . In the SCF calculation E_A is calculated based on the assumption that the w/o interface does not deform. It takes only into account the enthalpic contributions of pIB with the water phase and entropic contributions due to compression of the pIB layer surrounding the particle. However, the w/o interface is soft and can easily deform, which leads to increased w/o interfacial area. Deformation of the w/o interface can occur, due to retarded drainage of solvent from the layer of stabilizing polymer. Drainage is a common effect, which is known to affect the stability of emulsion against coalescence (section 1.2.1). The liquid between two droplets needs time to drain to the bulk, when two droplets approach each other. If the liquid does not have time to drain, the droplets deform and cannot approach each other. In our system, this happens in a different manner. The layer of steric stabilizer that surrounds the particle is for the most part filled with solvent, which needs time to move to the bulk upon particle adsorption to the w/o interface. If the particle approaches and the solvent does not have time to drain, then the w/o interface deforms. Upon deformation of the w/o interfacial area, the energy increases and contributes repulsively. The magnitude of the interfacial energy that is involved is quite large, since relatively large micron-sized particles are used.

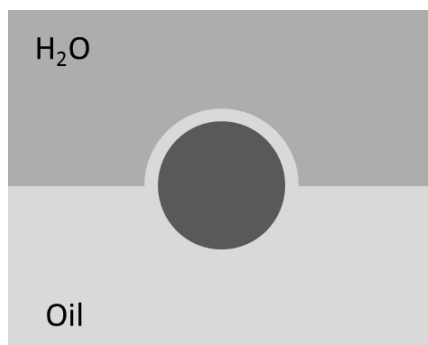


Figure 6.13 Deformation of the w/o interface due to inhibited drainage of the oil. Deformation of the w/o interface leads to an increased interfacial area and the corresponding interfacial energy. The particle is indicated with the dark gray sphere.

The increase of the interfacial free energy obviously depends on the extent of deformation. If half the particle deforms the interface, as depicted in figure 6.13, the w/o interfacial area increases with $\Delta A = 2\pi \cdot R^2$. The corresponding interfacial free energy is then $E_{def} = \Delta A \gamma_{ow}$. The energy of deformation is in the same order as the particle binding energy (eq. 1.2) and can reach $10^6 k_B T$ (fig. 5.11). This effect can account for the large discrepancy between the experimentally and theoretically determined activation barrier E_A .

Teixeira and Bon recently suggested the possibility of deformation of the w/o interface in the interfacial particle adsorption, which contributes to the activation barrier¹⁰ In conclusion, this kinetic study identified the relevance of drainage in the formation of Pickering emulsions. We studied sterically stabilized colloids, but in principle drainage, also plays a role in the formation of Pickering emulsions with charge-stabilized colloids. The electrical double layer surrounding the particle must also be compressed upon adsorption to the interface. If the water and ions present in the double layer do not have time to drain, then deformation occurs of the w/o interface in a similar manner as described above. The advantage of charge-stabilized colloids is that the double layer can be suppressed by the addition of salts, which allows the synthesis of the stabilizing particles in a colloidally stable regime and the resulting dispersion can be de-stabilized to form the Pickering emulsion. This cannot be done with sterically stabilized colloids.

An interesting comparison can be made between the dispersions synthesized with the high molecular weight ($M_w = 42\,000$ g/mol) and the low molecular weight ($M_w = 36\,000$ g/mol) stabilizer. Comparing the LM images in figure 6.7, with the rate of particle adsorption in figure 6.9 reveals that the low M_w dispersions adsorb much faster than the high M_w dispersions. Dispersion 6 shows after only 1 minute that all the particles are accommodated at the w/o interface, while the high M_w dispersions need several minutes to achieve only a fraction of that. The reason is not directly related to the M_w of the stabilizer or Γ_{PIB} , but to the particle size (fig. 6.4). The actual repulsive barrier E_A is not only related to Γ_{PIB} (eq. 6.4), but also to the particle radius (eq. 5.7).

$$E_A \sim R^2$$

6.9

Although Γ_{PIB} is similar for the various dispersions, the repulsive barrier E_A is significantly different. A larger particle has more surface area and therefore more steric stabilizer

interacting repulsively with the w/o interface. The use of such large particles in this work additionally explains the large values for E_A .

Colloidal stability

The previously described SCF study on this topic relates the colloidal stability with the wetting properties of Pickering stabilizers (chapter 5). For charge stabilized colloids it is known that ‘flocculating’ conditions enhance the interfacial adsorption. This is confirmed for sterically stabilized colloids in our previously published theoretical SCF study. Moreover, it demonstrated that there is a small window of Γ_{PIB} that shows both partial wetting and colloidal stability. These conditions are ideally used to form Pickering emulsions, because the surrounding particles inevitably determine the interaction with other droplets. These conditions are, in principle, aimed for. It is therefore an interesting question whether the experimental findings correspond with the SCF study. The systems that were suitable for Pickering stabilization in the SCF study had a PIB surface concentration of $0 \leq \Gamma_{PIB} \leq 5.5 \text{ mg/m}^2$. However, in this work Γ_{PIB} ranges from 9 to 15 mg/m^2 , which is a large difference. It must be mentioned that during the dispersion polymerization, not all the stabilizer grafts to surface of the particle, as is assumed in the calculation. An attempt has been made to measure Γ_{PIB} , but proved very difficult. It did show, however, that most of the stabilizer remains in solution. Γ_{PIB} is therefore overestimated in the calculation and is more likely to fall in the range that was found in the SCF-study. Dispersion 13 can be used as a reference to get an idea of the actual Γ_{PIB} , because it showed severe aggregation during the polymerization. According to the SCF study aggregating conditions correspond with a $\Gamma_{PIB} = 1.8 \text{ mg/m}^2$. Γ_{PIB} can be rescaled for the other dispersions 9, 10, 11 and 12 to respectively 4.5, 3.8, 3.3 and 2.6 mg/m^2 . Now, according to the SCF study dispersions 9 and 10 should be colloiddally stable and should therefore be ideal to form Pickering emulsions. To assess the colloidal stability, one can study the flocculation or aggregation behavior. Except for dispersion 13, all the polymerizations occurred in a controlled manner. Some minor aggregation is observed, but the majority remained in dispersion. The Pickering emulsions do not show severe flocculation or aggregation. However, all the Pickering emulsions sediment, because of the density difference between the water and oil phase. This makes it difficult to distinguish the differences in colloidal stability between the various emulsions. Further research is needed with respect to the colloidal stability to improve the stability of Pickering emulsions in general.

6.5 Conclusion

The adsorption of sterically-stabilized colloids at oil-water (w/o) interfaces is studied experimentally by the formation of Pickering emulsions. Especially, the effect of the steric stabilizer with respect to the rate of particle adsorption is investigated. The rate of particle adsorption is measured by the evolution of the droplet diameter during emulsification. Monodisperse, μm -sized poly(methyl methacrylate) (pMMA) particles that are stabilized with poly(isobutylene) (pIB) are used. The pIB concentration on the particle surface (Γ_{pIB}) is controlled by adjusting the stabilizer/monomer ratio during the synthesis of the particles. Pickering emulsions are formed by the addition of water to the non-aqueous pMMA dispersions and subsequent emulsification. A strong dependence of Γ_{pIB} on the kinetics of particle adsorption is found. The rate constant k for particle adsorption decays exponentially with Γ_{pIB} . The stabilizing layer around the particle leads to an activation barrier before interfacial adsorption, which decreases the probability for adsorption and hereby affects the rate of particle adsorption. An Arrhenius-type equation is used to model the experimentally found rate constants. An accurate fit is obtained when the repulsive barrier E_A is of the same order as the average kinetic energy E_K of a particle colliding with an emulsion droplet, which is equivalent to $10^4 k_B T$. Interestingly, this makes E_A several orders of magnitude higher than the repulsive barrier for steric stabilization in bulk. A possible mechanism that can lead to such a repulsive force is the drainage of solvent from the layer of steric stabilizer upon compression. Deformation of the w/o interface occurs, when the solvent does not have time to drain, which results in an increase of the interfacial energy.

References

1. Pieranski, P., *Physical Review Letters* **1980**, 45, (7), 569-572.
2. Young, T., *Phil. Trans.* **1805**, 95, 65-87.
3. Binks, B. P., *Current Opinion in Colloid & Interface Science* **2002**, 7, (1-2), 21-41.
4. Binks, B. P.; Rodrigues, J. A., *Langmuir* **2007**, 23, (14), 7436-7439.
5. Bon, S. A. F.; Colver, P. J., *Langmuir* **2007**, 23, (16), 8316-8322.
6. Golemanov, K.; Tcholakova, S.; Kralchevsky, P. A.; Ananthapadmanabhan, K. P.; Lips, A., *Langmuir* **2006**, 22, (11), 4968-4977.
7. Salari, J. W.; van Heck, J.; Klumperman, B., *Langmuir* **2010**, 26, (18), 14929-14936.
8. Simovic, S.; Prestidge, C. A., *Langmuir* **2003**, 19, (9), 3785-3792.
9. Tcholakova, S.; Denkov, N. D.; Lips, A., *Physical Chemistry Chemical Physics* **2008**, 10, (12), 1608-1627.
10. Teixeira, R. F. A.; Bon, S. A. F., Physical Methods for the Preparation of Hybrid Nanocomposite Polymer Latex Particles. In *Hybrid Latex Particles: Preparation With*, Springer-Verlag Berlin: Berlin, 2010; Vol. 233, pp 19-52.
11. Jayachandran, K. N. N.; Chatterji, P. R., *Journal of Macromolecular Science-Polymer Reviews* **2001**, C41, (1-2), 79-94.
12. Kawaguchi, S.; Ito, K., Dispersion polymerization. In *Polymer Particles*, Springer-Verlag Berlin: Berlin, 2005; Vol. 175, pp 299-328.
13. Barrett, K. E. J., *Dispersion polymerization in organic media*. Wiley-Interscience: London, 1975.
14. Lee, K. C.; Winnik, M. A.; Jao, T. C., *Journal of Polymer Science Part a-Polymer Chemistry* **1994**, 32, (12), 2333-2344.
15. Williamson, B.; Lukas, R.; Winnik, M. A.; Croucher, M. D., *Journal of Colloid and Interface Science* **1987**, 119, (2), 559-564.
16. Ivanov, I. B.; Ananthapadmanabhan, K. P.; Lips, A., *Advances in Colloid and Interface Science* **2006**, 123, 189-212.

Salt hydrate Pickering emulsions

& micro-encapsulation for heat storage applications

Abstract: Salt hydrates are promising materials for heat storage applications, because they can store large amounts of latent heat by undergoing a phase change. For that reason, salt hydrates are often referred to as phase change materials (PCMs). The development and use of salt hydrates as PCMs is hampered by the lack of an efficient micro-encapsulation technique. In this chapter we report, for the first time, the micro-encapsulation of calciumchloride hexahydrate ($\text{CaCl}_2 \cdot 6\text{H}_2\text{O}$). The procedure consists of two steps. First, the salt hydrate is emulsified in an oil with the aid of poly(methyl methacrylate) (pMMA) microparticles to form a so-called Pickering emulsion. The second step is the addition and *in situ* polymerization of MMA, which ultimately results in pMMA microcapsules. The procedure is inspired by the seeded dispersion polymerization technique, which is normally used to grow seed particles to a desired size. In this case, the seed particles are assembled to the droplet surface. The subsequent growth forces the particles to overlap, because the particles are restricted to the droplet surface area. The described micro-encapsulation procedure is versatile in terms of tuning the shell thickness and the microcapsule size. The shell thickness is tuned by adding and polymerizing different amounts of MMA. The microcapsule size is controlled by adjusting the number of particles adsorbed to the w/o interface with respect to the volume of dispersed phase. The Pickering emulsions and microcapsules are imaged by light- and scanning electron microscopy. The thermal properties are characterized by differential scanning calorimetry (DSC) and X-ray diffraction (XRD), which shows a clear effect of compartmentalization of $\text{CaCl}_2 \cdot 6\text{H}_2\text{O}$ on the crystallization behavior. Nucleation and crystallization is clearly restricted to the microcapsules, where otherwise a single nucleation results in the crystallization of the entire sample.

A part of this chapter has been filed as a Dutch patent application at the 31st March 2011. *‘Werkwijze voor het inkapselen van discrete kleine hoeveelheden materiaal en capsule verkregen onder toepassing van deze werkwijze.’*

7.1 Introduction

Salt hydrates have been suggested as suitable materials for thermal energy storage applications, due to their high latent heat of fusion and crystallization.¹⁻⁵ Therefore, salt hydrates are generally referred to as phase change materials (PCMs). Thermal energy storage is beneficial to reduce the mismatch between energy supply and demand, but it also conserves energy.¹⁻⁵ The great advantage of PCMs for this purpose is the high heat storage capacity in combination with a narrow temperature range in which the energy is stored. In principle, the phase change temperature (T_{PC}) is discrete, which means that energy is stored at exactly T_{PC} . In contrast to sensible thermal energy storage, which requires a wider temperature range to store the equivalent amount of heat. PCMs are suitable for many applications, such as integration in buildings⁶⁻⁸ and for efficient heat transport.⁹⁻¹¹ For example, PCMs can be incorporated in buildings as a heat buffer to dampen daily temperature fluctuations, which leads to a more comfortable indoor climate and energy/costs savings for heating and air conditioning. Moreover, PCMs can be dispersed in heat transfer fluids to efficiently transport heat from one location to another, which is particularly interesting for industrial applications or in combination with solar energy for domestic applications. The existing PCMs can be roughly divided in 2 classes; the *inorganic* PCMs, which comprise mostly salt hydrates, and *organic* PCMs that constitute paraffin or waxes and fatty acids. We believe that salt hydrates are the most promising class of materials for the application of PCM, because of their high heat density and low cost of production. A more thorough description of the (dis)advantages of both organic and inorganic PCMs is given in the introductory chapter.

Due to the solid-liquid phase transition, encapsulation is required for the application of any PCM. Moreover, PCMs need to be protected from the surrounding and vice versa. Salt hydrates, for example, are corrosive and sensitive towards water. The majority of commercially available PCMs are macro-encapsulated and only one example exists of a micro-encapsulated PCM. BASF commercialized micro-encapsulated paraffin under the trade name Micronal®.¹² The great benefit of this approach is that the microcapsules can be directly incorporated in commonly applied materials and technologies, such as concrete, plaster or insulation foams. A similar approach is envisioned for the micro-encapsulation of $\text{CaCl}_2 \cdot 6\text{H}_2\text{O}$.

Up to now the micro-encapsulation of salt hydrates has only been reported once by Capzo Int.,¹³ while similar techniques for organic PCMs are common practice, as illustrated by the

commercial production of Micronal®.¹² The encapsulation method developed by Capzo Int. starts from a polymer/salt hydrate composite, which is ground to form solid particles. The salt hydrate particles are subsequently encapsulated by deposition of styrene-maleic anhydride copolymers, which can be cross-linked to yield stable polymer shells. The method is limited in the particles size, due to the grinding process. Moreover, the present method requires modification of the core salt hydrate material. One can only speculate about the reasons for the large contrast between salt hydrates and organic PCMs, in terms of the micro-encapsulation. A possible reason could be that salt hydrates are not compatible with the traditional micro-encapsulation technologies, such as interfacial polymerization or (mini)emulsion polymerization.¹⁴⁻¹⁷ These methods generally require mixing with the core material, which is undesirable. For salt hydrates, the high salt content in the essentially aqueous solution negatively affects the solubility, reactivity and compatibility of the available monomers. If the monomer is soluble in the salt hydrate at all, which is often not the case, degradation occurs upon contact with the salt hydrates.

Ideally, the pure salt hydrate is emulsified and the shell forming material is applied from the continuous phase, as is the case for micro-encapsulation by *in situ* polymerization or (complex) coacervation.^{16, 18} These techniques encapsulate emulsion droplets by deposition of polymer purely from the continuous phase and require no mixing with dispersed phase. Also here, there is a large contrast between the number of publications that report the encapsulation of aqueous or lipophilic liquids. To the best of the author's knowledge, only one study reports the encapsulation of hydrophilic liquids using one of these methods.¹⁸ Landfester and coworkers precipitated poly(methyl methacrylate) (pMMA) onto aqueous mini-emulsion droplets by solvent evaporation. A mixture of a good and poor solvent is used, in which pMMA is dissolved. The good solvent is evaporated and pMMA precipitates and deposits onto the aqueous mini-emulsion droplets to yield the microcapsules. A similar, but novel method is described in this chapter. The difference is that the polymer is formed *in situ* and deposits onto pMMA particle-stabilized emulsion droplets. It is inspired by the seeded-dispersion polymerization technique, which is normally used to grow seed particles to a desired size.^{19, 20} The seed particles are assembled on the droplet surface and subsequent growth forces the particles to overlap, because they are restricted to the droplet surface area.

The micro-encapsulation procedure as described above is depicted in figure 7.1. The particles that are used in this study are synthesized by the dispersion polymerization of

MMA in n-heptane (chapter 6). The polymer particles can be grown to a desired size by the addition and subsequent seeded polymerization. The stability of the Pickering emulsion is paramount for the success and efficiency of the micro-encapsulation, as argued in chapter 1. The same is true for regular seeded dispersion polymerizations. The seed particles cannot be grown indefinitely. The colloidal stability limits the size of the particles, because upon growth, the fractional surface coverage of steric stabilizer on the particle surface (Γ_{ss}) decreases. Eventually, at a certain particle size, the dispersion becomes unstable. Aggregation occurs, when the polymerization continues and the system becomes unstable. In conclusion, the colloidal stability of the stabilizing particles and the Pickering emulsion droplets is a relevant parameter and has to be kept in mind for efficient micro-encapsulation.

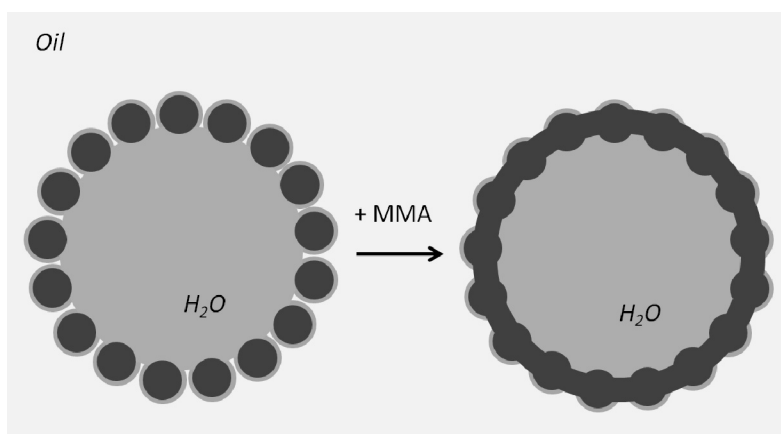


Figure 7.1 The micro-encapsulation procedure as described in this chapter. a Pickering emulsion droplet stabilized with hairy particles (left) that is used as a scaffold to synthesize a pMMA microcapsule (right).

In chapter 4 it is demonstrated that additional steric stabilization is required for the efficient synthesis of polymeric microcapsules. Sulfate-stabilized polystyrene (pS) particles were used to form a w/o Pickering emulsion. This Pickering emulsion was heated above the glass-transition temperature to form pS microcapsules. Dramatic aggregation occurred, when no additional stabilization was provided. The efficient synthesis of pS microcapsules

was achieved when a poly(styrene-*block*-(ethylene-*co*-proylene)) (pS-b-EP) was adsorbed to sterically stabilize the droplets. The same can, in principle, be performed with the pMMA particle-stabilized emulsion droplets, because pS-b-EP is known to adsorb onto pMMA surfaces.²¹ The experiment is not described in this thesis, but it was observed that the addition of pS-b-EP led to coalescence of the aqueous emulsion droplets. The adsorbed pS-b-EP lowered the interfacial tension of the particle with the oil-phase, altered θ and eventually the particles completely desorb from the w/o interface. This was not observed with the system in chapter 4, which is attributed to the formation of a rigid multilayer of attractive particles surrounding the droplet. The pMMA particles, used in this chapter, are sterically stabilized and are able to move over the surface of the droplet.

Chapters 5 and 6 reported a study on the stability of the stabilizing particles and Pickering emulsions both theoretical as well as experimentally. Chapter 5 demonstrated a small window of stabilizer concentrations Γ_{PIB} that exhibit both colloidal stability and partial wetting. These conditions are ideally used for the formation of Pickering emulsions. Chapter 6 focused on the effect of the steric stabilizer on the rate of particle adsorption, but demonstrated that relatively stable particles were able to form Pickering emulsions. It also gave a range of Γ_{PIB} that ensures colloidal stability and it is within these limitations that the pMMA microcapsules are synthesized in this work.

This chapter is divided into the following parts. The dispersion polymerization and formation of w/o Pickering emulsions is already described in chapter 6 and will only briefly be described in the 1st section of this chapter. Secondly, the formation of pMMA microcapsules is described. The Pickering emulsions and microcapsules are imaged with light microscopy (LM) and scanning electron microscopy (SEM). It is demonstrated how the shell thickness and the microcapsule size can be controlled. The 3rd and final part of the chapter characterizes the thermal properties of the micro-encapsulated $\text{CaCl}_2 \cdot 6\text{H}_2\text{O}$ with DSC and with XRD.

7.2 Experimental

Materials Methyl methacrylate (MMA)(99%, Sigma Aldrich) is passed over a column with aluminum-oxide (activated basic, Sigma Aldrich) prior to use to remove inhibitor. The inhibitor-free MMA is refrigerated for later use. n-Heptane (> 96%, Biosolve) is used as received. Azo-bis-isobutyronitrile (AIBN) (Sigma Aldrich) is recrystallized twice from methanol to remove any impurities. Methanol (99.8%, Biosolve) and poly(isobutylene-co-isoprene) (pIB) (Kalene800 and 1300, Royal Elastomers) are used as received. The molecular weights of Kalene800 and 1300 are, respectively, 36000 and 42000 g/mol. Both polymers contain 2.5 - 3.5 % unsaturated carbon-carbon bonds. Water is double de-ionized with a purification system. CaCl_2 prills are received as a gift from Nedmag BV.

pMMA particles are synthesized by dispersion polymerization in heptane as described in chapter 6. Briefly, the synthesis is performed in a 250 mL jacketed reactor. A typical dispersion polymerization initially contains 110.5 g heptane, 33.2 g MMA, 0.5 g AIBN and a particular amount of pIB. Dispersion 1 is synthesized with 1.09 g Kalene800, dispersion 2 is synthesized with 0.83 g Kalene1300 and dispersion 3 and 4 are synthesized with 0.66 g Kalene1300 (table 1). The mixture is stirred at 80 °C for at least 3 hours and is then cooled to room temperature. During the polymerization samples are taken to determine the conversion and solid content gravimetrically. The solid contents of dispersion 1 to 4 are, respectively, 0.22, 0.21, 0.24 and 0.27 g/g. The particles are imaged with a desktop scanning electron microscopy (SEM) (Phenom, FEI company). The sample holder is covered with double-sided conducting carbon tape and a droplet of the obtained dispersion is cast on the sticker. The sample is dried under air and sputter-coated with a thin layer of gold before imaging with SEM. The particle size distribution is determined from the SEM image with ImageJ.

Seeded dispersion polymerization is performed with dispersion 3 (table 1). 18.3 g pMMA dispersion is charged to the reactor and additional heptane is added to a volume of 200 mL. 0.24 g AIBN is dissolved in 4.83 g MMA. The AIBN/MMA solution is added to the reactor. At 100% conversion, the added MMA is equivalent to a particle growth of 0.7 μm . The pMMA dispersion is stirred at 400 rpm. The mixture is purged with nitrogen for at least 15 min, before the polymerization is initiated by heating the whole mixture to 80 °C. The final pMMA particles are analyzed with SEM in a similar way as is described for the particle dispersions. During the polymerization samples are taken at $t = 0, 30, 60$ and 90 minutes to determine the conversion with NMR. ^1H -NMR spectra were recorded from a

Varian VSR 400 MHz instrument. Deuterated chloroform (CDCl_3) is used to dissolve the sample of pMMA dispersion. All chemical shifts are reported in ppm downfield from tetramethylsilane used as an internal standard ($\delta = 0$ ppm).

$\text{CaCl}_2 \cdot 6\text{H}_2\text{O}$ is synthesized by the dissolution of CaCl_2 prills in an excess of water, with respect to the stoichiometric ratio. The mixture is heated to 80°C to assure complete dissolution of CaCl_2 . A brown flocculate was observed that did not dissolve. The solution is cooled to room temperature and filtered. The solution is stored in the fridge at 4°C to allow $\text{CaCl}_2 \cdot 6\text{H}_2\text{O}$ to crystallize. After at least 12 hours the remaining solution is decanted and the crystals are used to form the $\text{CaCl}_2 \cdot 6\text{H}_2\text{O}$ Pickering emulsions.

Pickering emulsions are formed by the addition of molten $\text{CaCl}_2 \cdot 6\text{H}_2\text{O}$ to the particle dispersions and emulsification of the entire mixture. The amount of dispersion, $\text{CaCl}_2 \cdot 6\text{H}_2\text{O}$ and the aimed droplet diameter are specified in table 1. In this calculation it is assumed that all the particles are adsorbed to the w/o interface, densely pack in a hexagonal fashion and that curvature effects were negligible. To form a Pickering emulsion, the specified amount of dispersion is weighed in a measuring cylinder and diluted with additional heptane to a total volume of 100 ml. The diluted dispersion is charged to a 200 ml polyethylene bottle. The whole mixture is sheared with an 'IKA Ultra Turrax T25 Basic' rotor-stator mixer at 24000 rpm. The mixture is sheared until all the particles are adsorbed to the w/o interface, which can be judged by the transparency of the continuous phase after sedimentation of the droplets. If the heptane phase is still opaque, then the mixture is additionally sheared. The Pickering emulsions are characterized by optical microscopy. The droplet diameters are derived from the images with ImageJ.

pMMA microcapsules are made by performing a subsequent polymerization of MMA in the presence of a pMMA Pickering emulsion. The Pickering emulsion is prepared as described above and charged to the same reactor as is used for the dispersion polymerization. Additionally, 100 ml heptane is added to fill the reactor to an appropriate volume. The specified amounts of dispersion and added MMA are specified in table 7.1. Pickering emulsion 1: 3.24 g MMA and 0.16 g AIBN are added, which is equivalent to a particle growth from $0.74\ \mu\text{m}$. Pickering emulsion 2: 1.39 g MMA and 0.069 g AIBN is added, which is equivalent to a particle growth from $0.42\ \mu\text{m}$. The emulsion is stirred at 400 rpm. The aimed particle growth for Pickering emulsion 3, 4 and 5 are $0.7\ \mu\text{m}$. The mixture is purged with nitrogen for at least 15 min, before the polymerization is initiated by

heating the whole mixture to 80 °C. The final pMMA microcapsules are analyzed with SEM in a similar way as is described for the particle dispersions.

Table 7.1 Data concerning the synthetic conditions of the (seeded) dispersion polymerizations, the Pickering emulsions and microcapsule formation.

Dispersion/ Emulsion	Droplet diameter [μm]	CaCl_2 $6\text{H}_2\text{O}$ [mL]	Particle diameter [μm]	Weight dispersion ^a [g]	Added ^b MMA [g]
1/1	50	10	1.68	7.532	3.24
2/2	50	10	2.49	10.740	1.39
3/3	50	20	2.56	19.6	4.60
4/4	100	20	2.70	9.14	2.43
4/5	150	30	2.70	9.14	2.43

The amount of dispersion used to form the Pickering emulsion.^a

Added monomer to form the pMMA microcapsules.^b

Thermal properties are characterized with X-ray diffraction and differential scanning calorimetry. The pMMA microcapsules are placed in a glass capillary, mounted and centred on a *Bruker SMART APEX* CCD area detector single crystal diffractometer. The temperature was controlled by an *Oxford Cryosystems Cryostream 700 Plus* cryostat with the nozzle directed onto the sample. X-ray diffraction photographs are collected over a period of 60 seconds whilst the sample was rotated through 360° around the goniometer φ -axis of the diffractometer. Successive rotation photographs were collected in this manner at 10 °C intervals from -50 °C to 30 °C. The two-dimensional data is converted to an abscissa/ordinate plot using the software *XRD2DScan*¹. The DSC measurement is performed on a TA instruments Q100 DSC system. It is calibrated according standard procedures using Indium. The heating and cooling rates are specified with the corresponding DSC curves (figs. 7.12 and 7.13). Several heating and cooling cycles are performed, in which the sample is cooled from 50 to -50 °C and vice versa.

7.3 Results

The Pickering particles are synthesized by the dispersion polymerization of MMA in heptane. Highly uniform pMMA particles are obtained in a controlled manner. The synthetic details of the dispersion polymerization and the subsequent formation of Pickering emulsions are described in chapter 6. A practical advantage of the procedure described in the previous chapter is that a non-aqueous pMMA dispersion is formed, to which the salt hydrate can be added directly to form a Pickering emulsion. Other methods often require a separate particle synthesis and re-dispersion in a suitable oil, which can be a laborious process. Optimization of the stabilizer concentration [pIB] was required to obtain particles that are suitable for Pickering stabilization. If a high [pIB] is used, the particles did not attach to the w/o interface ($\theta > 180^\circ$). On the other hand, if low stabilizer concentrations are used, the dispersion becomes unstable and severely aggregated. 4 pMMA dispersions, synthesized with intermediate pIB concentrations, are used for the micro-encapsulation of $\text{CaCl}_2 \cdot 6\text{H}_2\text{O}$ to demonstrate the flexibility of the approach presented.

7.3.1 Seeded dispersion polymerization

The micro-encapsulation procedure, as described in this chapter, is inspired by the seeded dispersion polymerization technique. Such a polymerization is performed as a reference experiment, to obtain information on the conversion/time history of MMA and the corresponding particle growth.

The conversion of MMA is determined by recording ^1H -NMR spectra in time. Figure 7.2 shows the methoxy-peaks ($\text{O}-\text{CH}_3$) in the ^1H -NMR spectra at 3.60 and 3.70 ppm. The first corresponds to the methoxy-group of MMA and the intensity decreases as the polymerization proceeds. The second peak corresponds to the same methoxy-group in the polymer and the intensity increases as fresh polymer is formed. The pMMA seed particles serve as an internal standard to calculate the conversion the ^1H -NMR spectra. Both peaks are integrated and normalized with respect to the total signal intensity, because that should remain constant throughout the polymerization. Figure 7.2 shows the peaks at different moments in time and it clearly shows a respective decrease and increase of signal, which indicates the conversion of monomer. The relative increase or decrease directly yields information on the conversion (fig. 7.3).

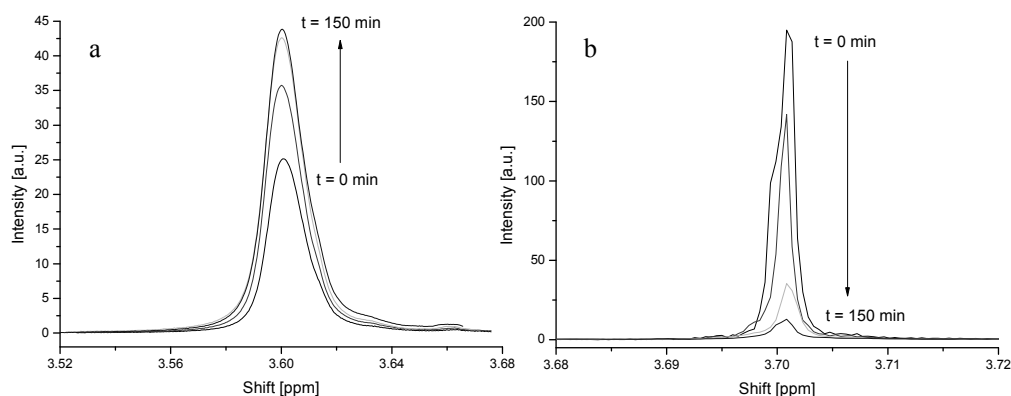


Figure 7.2 Conversion of MMA into pMMA. The methoxy-peaks ($\text{O}-\text{CH}_3$) in the ^1H -NMR spectra, corresponding to a) MMA ($\delta = 3.70$ ppm) and b) pMMA ($\delta = 3.60$ ppm), at different moments.

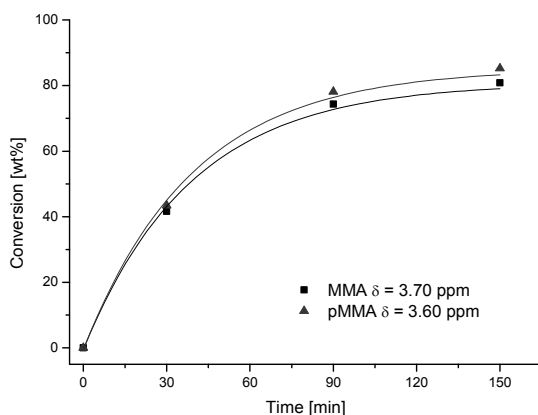


Figure 7.3 Conversion of MMA into pMMA.

The particle growth is the most important outcome of this experiment, because that will lead to the formation of a stable microcapsule. Figure 7.4 clearly shows the controlled growth of the pMMA seed particles. No secondary nucleation occurred nor is any significant aggregation visible in the SEM image. The particle diameter distribution is compared with the original particles (fig 7.4) and clearly shows the expected particle growth. Although, the particle growth is completely controlled, the final dispersion is unstable and aggregated severely. As is already argued in the introduction, the colloidal

stability limits the growth of the stabilizing particles. An indication of the lower limit of colloidal stability is provided in chapter 6. It is shown that dispersions with a $\Gamma_{\text{pIB}} = 6 \text{ mg/m}^2$ are colloiddally unstable and severely aggregated. The pMMA particles that are used have a $\Gamma_{\text{pIB}} = 11 \text{ mg/m}^2$. The expected particle growth during the microcapsule formation finally yields a $\Gamma_{\text{pIB}} < 6 \text{ mg/m}^2$.

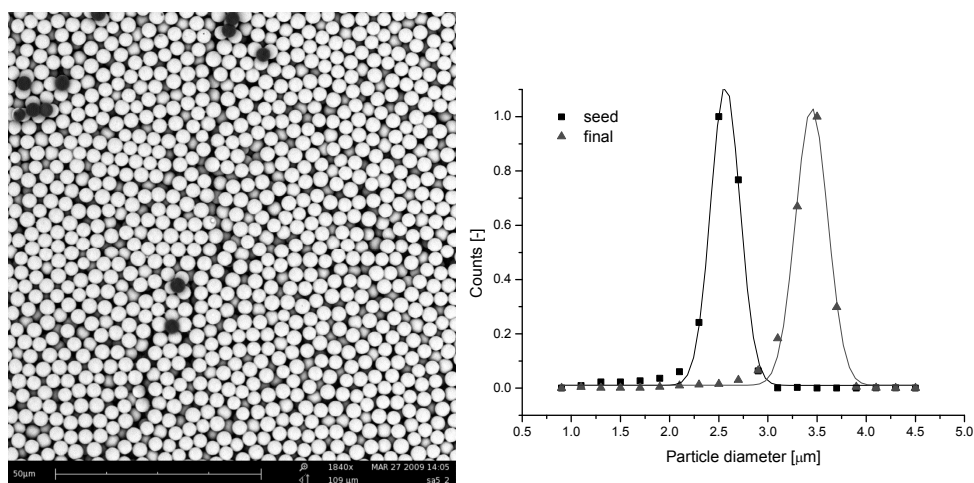


Figure 7.4 Particle growth in the seeded dispersion polymerization. SEM picture of the final pMMA particles and the particle diameter distributions of the seed and final particles.

7.3.2 $\text{CaCl}_2 \cdot 6\text{H}_2\text{O}$ Pickering emulsions

Pickering emulsions are produced by the addition of liquid $\text{CaCl}_2 \cdot 6\text{H}_2\text{O}$ to the particle dispersions. The amount of dispersion with respect to $\text{CaCl}_2 \cdot 6\text{H}_2\text{O}$ and the aimed droplet diameters are specified in table 7.1. The entire mixture is emulsified until all the particles are accommodated at the w/o interface, which can be judged by the transparency of the heptane phase after sedimentation of the droplets. Freely dispersed particles are still present when the heptane phase remains opaque. Figure 7.5 shows a typical LM image of Pickering emulsion 1. The average droplet diameter is close to the expected value of 50 μm, which demonstrates that most of the particles have been adsorbed to the w/o interface.

The Pickering emulsions are sufficiently stable against coalescence. The emulsions do sediment, because of the relatively large density difference between the heptane and

$\text{CaCl}_2 \cdot 6\text{H}_2\text{O}$. After sedimentation, the Pickering emulsion can be easily re-dispersed by manual shaking of the flask or gently stirring of the reactor content. Most droplets have adopted a spherical shape and, surprisingly, a few droplets show a more rectangular shape. In these cases, the $\text{CaCl}_2 \cdot 6\text{H}_2\text{O}$ has probably crystallized, because the image is taken at a temperature below the phase change temperature.

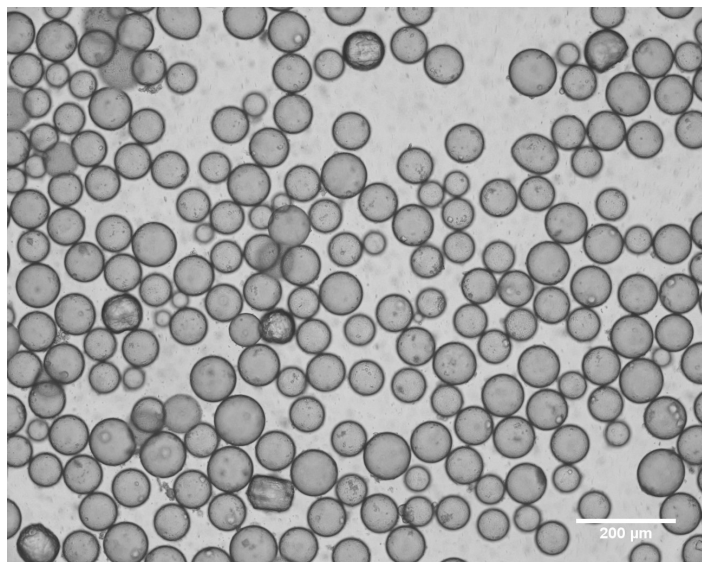


Figure 7.5 Light microscopy images of Pickering emulsion 1.

7.3.3 Microcapsules

Microcapsules are made by the *in situ* polymerization of MMA in the presence of pMMA particle-stabilized emulsions. The procedure is inspired by the seeded-dispersion polymerization technique, as is already described in the introduction and is schematically depicted in figure 7.1. MMA is added to the Pickering emulsion to swell the (primary) particles. A fraction of MMA is still present in the continuous phase, due to the high solubility of MMA in heptane. Therefore, the polymerization simultaneously takes place inside the particles as well as in the continuous phase. The extent of both mechanisms is unknown, but both lead to controlled particle growth as seen in the seeded dispersion polymerization and should therefore lead to the successful encapsulation of the $\text{CaCl}_2 \cdot 6\text{H}_2\text{O}$ Pickering emulsion droplets.

Tunable shell thickness

3.24 g MMA is added to Pickering emulsion 1. If all the monomer is consumed, this is equivalent to a particle growth from 1.68 to 2.42 μm . Within 90 minutes the conversion of MMA is 80 %, which corresponds to a particle diameter of 2.31 μm . Figure 7.6 and 7.7 show the formation of the pMMA microcapsules in time. Figure 7.6 shows 3 LM images of single Pickering emulsion droplets at different moments. At $t = 0$, the individual pMMA particles are still visible. In time, the individual particles gradually disappear. After 2 hours (fig. 7.7) the individual pMMA particles have completely disappeared and a stable capsule has formed. Imaging with SEM occurs in vacuum and requires dry samples. The fact that stable capsules are still present under these relatively harsh conditions indicates the mechanical stability. Otherwise, the structures would have completely collapsed.

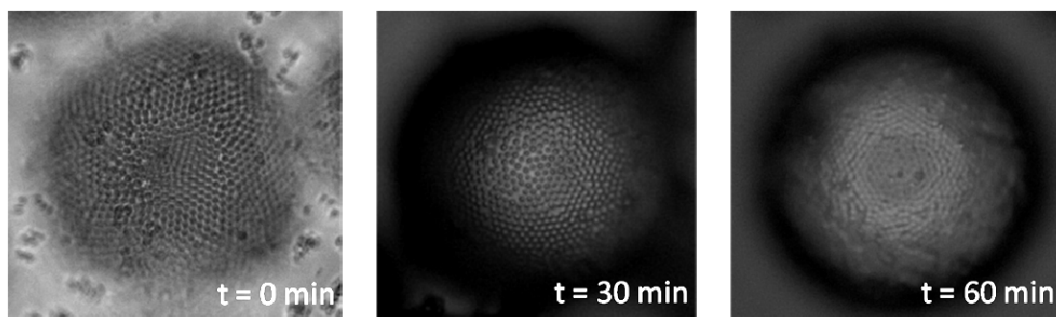


Figure 7.6 pMMA microcapsule formation. Pickering emulsions 1: LM images are taken at different moments of the polymerization.

Figure 7.7 clearly shows that the microcapsule formation by the second stage MMA polymerization is successful. However, the SEM image also shows some undesired effects, such as aggregation. As is already argued in the introduction, the colloidal stability limits the growth of the stabilizing particles and determines the aggregation of the microcapsules. The reference seeded dispersion polymerization also demonstrated this. The particle growth is controlled. However, the final dispersion is unstable and aggregates. It is therefore not unexpected that the capsules also aggregate. The shear rate during the polymerization breaks up the aggregates, prevents complete aggregation and allows for a relatively controlled capsule formation.

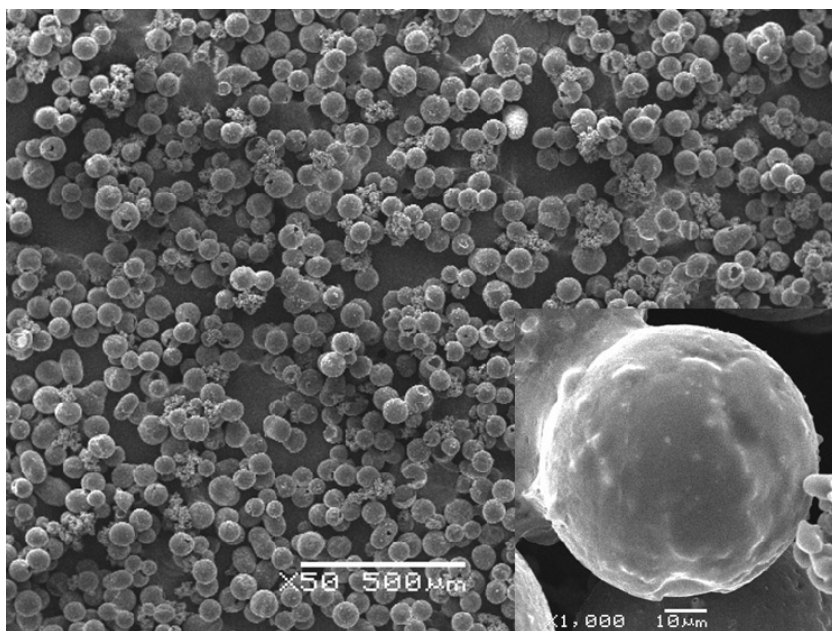


Figure 7.7 pMMA microcapsules synthesized from Pickering emulsion 1. The SEM images are taken after 120 minutes of polymerization and 80 % conversion.

Dispersion and Pickering emulsion 2 is also used to form pMMA microcapsules. The difference with Pickering emulsion 1 is that a significantly smaller amount of MMA is added, *i.e.* 1.39 g MMA is added instead of 3.24 g, which is equivalent to a particle growth from 2.49 to 2.85 μm . In this case, the colloidal stability is in principle maintained and the stabilizer concentration decreases only to $\Gamma_{\text{pIB}} = 9 \text{ mg/m}^2$. The result is shown in figure 7.8. Essentially, the same result is obtained as for Pickering emulsion 1, which is that stable pMMA microcapsules are obtained. The major difference is that the individual particles are still visible. Figure 7.8 clearly show the uniformity and the regular hexagonal packing as is expected for this kind of system. On forehand, a difference in aggregation is expected. However, it is difficult to distinguish the degree of aggregation based on the SEM images. Residual MMA is still present in the microcapsule dispersions that plasticizes pMMA and could lead to partial fusion of the microcapsules.

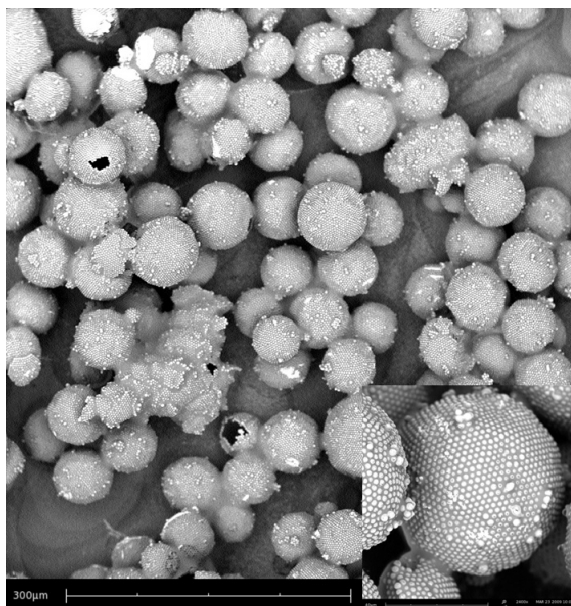


Figure 7.8 SEM images of pMMA microcapsules made from Pickering emulsion 2. The inset shows a close-up of one of the capsules.

Microcapsule size

To further demonstrate the flexibility of this approach, microcapsules with different size are synthesized. All other, previous experiments aimed at a capsule diameter of 50 μm. However, different sizes can be obtained by adjusting the number of stabilizing particles with respect to the core volume. The accurate $\text{CaCl}_2 \cdot 6\text{H}_2\text{O}$ volumes and the number of particles are specified in table 7.1. The procedure to form the Pickering emulsion is the same as described before. The added MMA is equivalent to an increase of the particle diameter of 0.7 μm. Figures 7.9 and 7.10 clearly show the differences in size.

Figure 7.9 shows the LM images of the final pMMA microcapsule dispersion. The polymerization occurred relatively clean. No aggregates are formed nor any secondary nucleation is observed. The difference in size is directly visible. Moreover, the LM images show buckled microcapsules, instead of spherical structures. Figure 7.10 shows the exact diameters and also shows that on average the capsules are slightly smaller than what is expected on forehand.

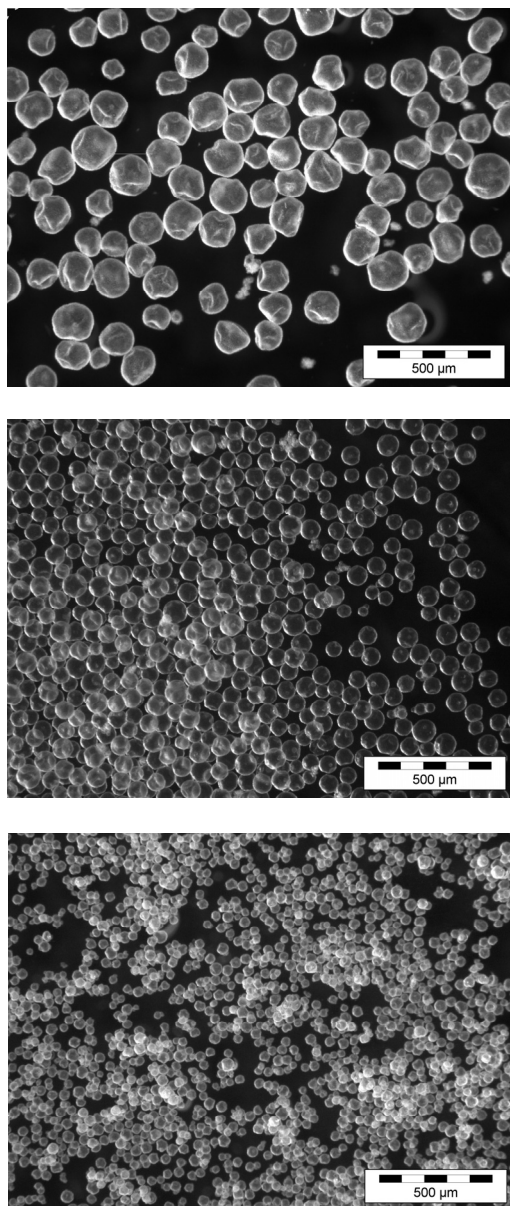


Figure 7.9 Light microscopy images of pMMA/CaCl₂·6H₂O microcapsules exhibiting different size. *Top*) Pickering emulsion 5 aimed diameter = 150 μm. *Middle*) Pickering emulsion 4 aimed diameter = 100 μm. *Bottom*) Pickering emulsion 3 aimed diameter = 50 μm.

A possible reason for the smaller microcapsule size is the evaporation of water from the emulsion droplets during the polymerization. The reaction takes place at 80 °C, at this

temperature water can easily evaporate. Condensation of evaporated water occurred on the lid of the reactor, which confirms this explanation. The different composition of CaCl_2 and water should be reflected in the thermal properties, which is investigated by DSC (fig. 7.13). It is unclear why Pickering emulsions 1 and 2 do not show the evaporation of water, while that clearly happens for Pickering emulsions 3, 4 and 5. A possible explanation could be that the $\text{CaCl}_2 \cdot 6\text{H}_2\text{O}$ Pickering emulsion 1 and 2 are stirred overnight, before the polymerization is initiated. During this time, $\text{CaCl}_2 \cdot 6\text{H}_2\text{O}$ could have absorbed water from the reaction mixture and the atmosphere. The absorbed water is later evaporated during the polymerization. Pickering emulsions 3/5 are polymerized directly after the formation of the emulsion and do not have an excess of water.

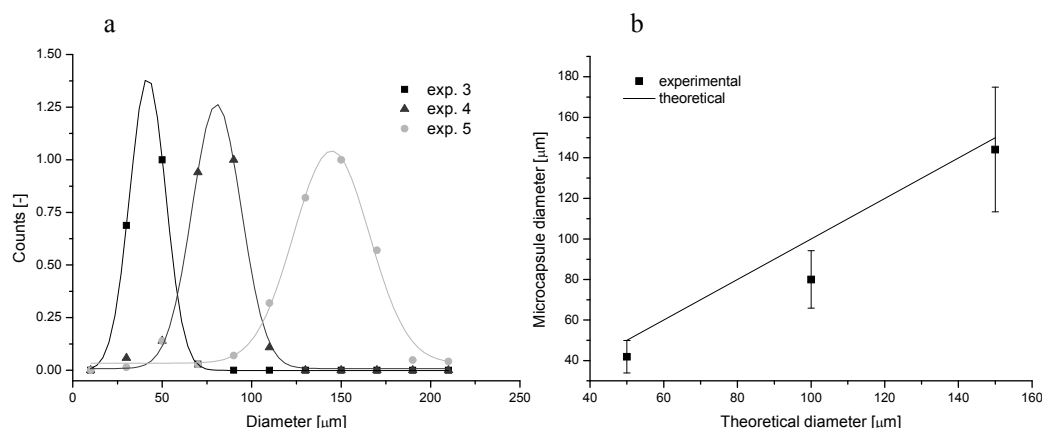


Figure 7.10 pMMA/ $\text{CaCl}_2 \cdot 6\text{H}_2\text{O}$ microcapsules diameters. *a)* Diameter distributions for Pickering emulsions 3, 4 and 5. *b)* Experimental average diameters in comparison with the calculated diameters.

In conclusion, the initial Pickering emulsion droplets are successfully encapsulated using this approach. The described method is flexible in terms of the shell thickness and microcapsule size. The microcapsule shell thickness can be controlled by the amount of MMA that is added relative to the quantity of stabilizing particles. However, some irregular structures (particle aggregates) are found. Some microcapsules have holes in their shell, which is an artefact of the sample preparation. The microcapsule size can be tuned by the number of particles with respect to the volume of the dispersed phase. The final part of this chapter characterizes the thermal properties of $\text{CaCl}_2 \cdot 6\text{H}_2\text{O}$, in an attempt to reveal the effect of compartmentalization.

7.3.4 Thermal properties

The thermal properties of the micro-encapsulated $\text{CaCl}_2 \cdot 6\text{H}_2\text{O}$ are characterized by XRD and DSC. A specialized powder diffraction setup is used that allows temperature 30 °C and -50 °C with intervals of 10 °C. First, a cooling and then a heating cycle is performed. The sample is initially in an amorphous, molten state at a temperature of -10 °C. A diffraction pattern appears at $T = -20$ °C indicating crystallization, see figure 7.11. There is no contribution of the pMMA shell, because the polymer is completely amorphous. The diffractogram is indexed based on the known X-ray diffraction pattern for $\text{CaCl}_2 \cdot 6\text{H}_2\text{O}$.^{22, 23} Heating from -50 to 30 °C shows solid $\text{CaCl}_2 \cdot 6\text{H}_2\text{O}$ up to a temperature $T = 0$ °C. The sample becomes amorphous from $T = 10$ °C.

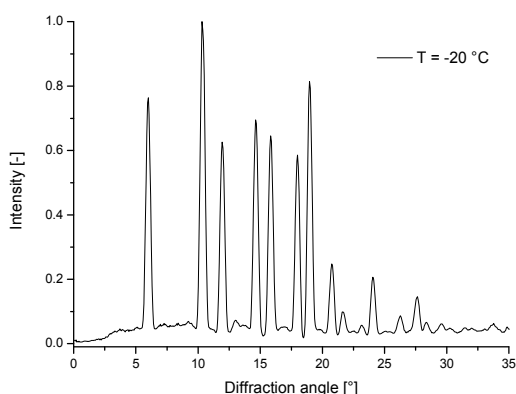


Figure 7.11 XRD diffraction pattern obtained from micro-encapsulated $\text{CaCl}_2 \cdot 6\text{H}_2\text{O}$. Microcapsules from Pickering emulsion 1 are measured.

The phase change temperature T_{PC} of pure $\text{CaCl}_2 \cdot 6\text{H}_2\text{O}$ is 28 °C.²⁴ It is commonly known that salt hydrates can be significantly undercooled. Also here, crystallization occurs at much lower temperatures than the T_{PC} . Melting also occurs at lower temperatures than T_{PC} , which can be an indication of an excess of water with respect to the stoichiometric ratio ($\text{CaCl}_2 : \text{H}_2\text{O} = 1 : 6$). A DSC measurement is performed on the same sample to obtain more detailed information on the melting and crystallization trajectories (fig. 7.12).

The DSC curve in figure 7.12 shows unusual crystallization behavior, which is caused by the segregated nature of $\text{CaCl}_2 \cdot 6\text{H}_2\text{O}$ due to the encapsulation. Instead of one crystallization peak, several smaller peaks are observed. Normally, nucleation leads to crystallization of

the entire sample, while here, nucleation and crystallization are restricted to each microcapsule. Each microcapsule has to nucleate and crystallize, which occurs at different temperatures. Nucleation is a stochastic process, which means that the crystallization temperature in bulk samples always shows a certain variation. This is exaggerated in the micro-encapsulated form of $\text{CaCl}_2 \cdot 6\text{H}_2\text{O}$.

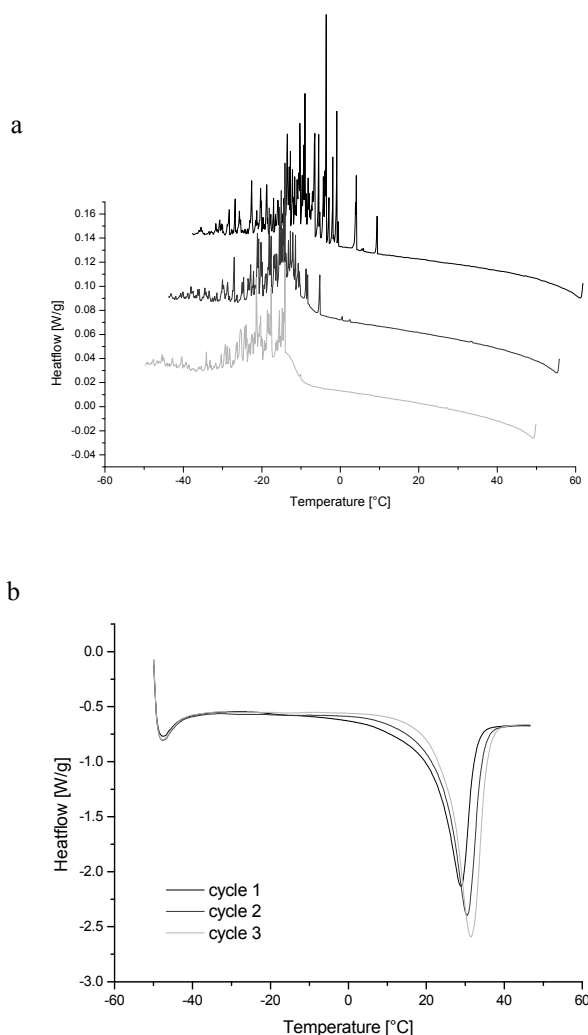


Figure 7.12 DSC cooling and heating traces of the micro-encapsulated $\text{CaCl}_2 \cdot 6\text{H}_2\text{O}$. pMMA microcapsules from Pickering emulsion 1 are measured at **a)** a cooling rate of 0.5 °C/min and **b)** heating rate of 10 °C/min.

The heating curve does show a single melting peak, but is relatively broad (fig. 7.12). This could be an indication for an excess of water, as is already conclude from the XRD measurement. For pure compounds a narrower peak is expected with a sharper offset for the melting temperature. Another observation is that the corresponding heat of fusion and crystallization (≈ 95 J/g) is lower than that of pure $\text{CaCl}_2 \cdot 6\text{H}_2\text{O}$ (170 J/g). Of course, the presence of pMMA reduces the heat capacity. The indicated excess of water also reduces heat of fusion and crystallization.

The melting and crystallization temperatures from the DSC measurements are consistent with those extracted from the XRD measurements. Crystallization starts at a temperature -10 °C and continues to $T = -50$ °C. Melting starts at approximately $T = 10$ °C, which was also observed in the XRD measurement. The deviating values for the melting and crystallization temperatures indicate an excess of water in comparison with the stoichiometric ratio.²⁴ It is commonly known that calciumchloride is a deliquescent salt, which is illustrated by its application as de-icer and dessicant. Calciumchloride can take up water from the atmosphere, which can even continue untill the entire sample is dissolved in the absorbed water. The samples are undeliberately exposed to moisture from the atmosphere, during the preparation of the samples and the measurement. Although $\text{CaCl}_2 \cdot 6\text{H}_2\text{O}$ is encapsulated in a shell of pMMA it still absorbs water from the air. Apparently, the pMMA shell is permeable for water and does not provide a sufficient barrier to stop the absorption of water. The uptake of water is measured by gravimetry and compared with pure $\text{CaCl}_2 \cdot 6\text{H}_2\text{O}$ crystals to shine more light on the deliquescent properties, which is discussed section 7.3.5.

The heating curve does show a single melting peak, but is relatively broad (fig. 7.12). This could be an indication for an excess of water, as is already conclude from the XRD measurement. For pure compounds a narrower peak is expected with a sharper offset for the melting temperature. Another observation is that the corresponding heat of fusion and crystallization (≈ 95 J/g) is lower than that of pure $\text{CaCl}_2 \cdot 6\text{H}_2\text{O}$ (170 J/g). Of course, the presence of pMMA reduces the heat capacity. The indicated excess of water also reduces heat of fusion and crystallization.

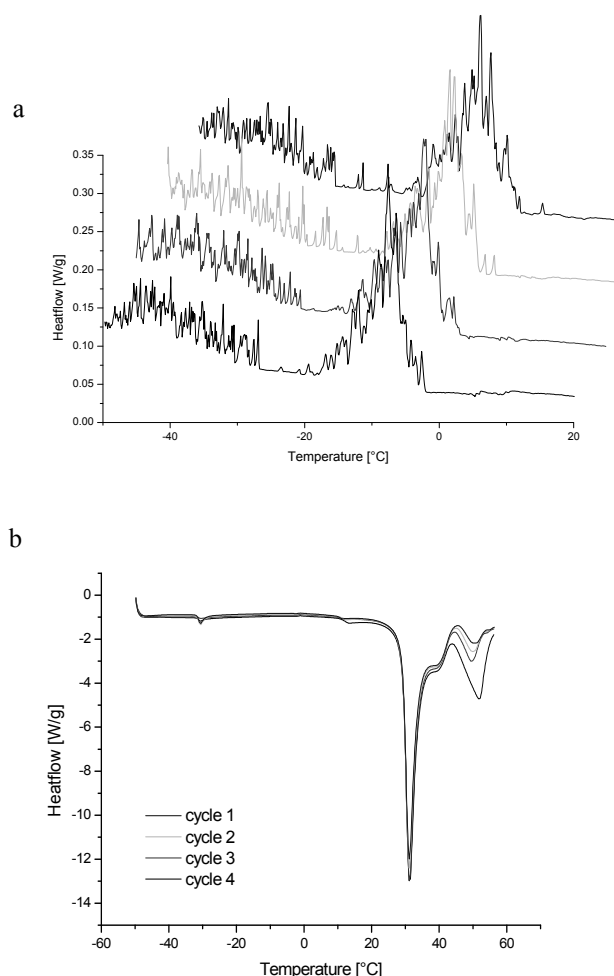


Figure 7.13 DSC heating and cooling traces of the micro-encapsulated $\text{CaCl}_2 \cdot 6\text{H}_2\text{O}$ that is made from Pickering emulsion 5. **a)** The cooling rate is $0.5\text{ }^\circ\text{C/min}$ and **b)** the heating rate is $10\text{ }^\circ\text{C/min}$.

The microcapsules made from Pickering emulsion 5 are also measured with DSC (fig 7.13). The LM images showed indentation of the microcapsules, which indicated the evaporation of water. This changes the composition and hereby affects the thermal properties, which can be seen in the DSC traces. It must be mentioned, that care has been taken to minimize the exposure of the microcapsules to the atmosphere. A drop of the microcapsule dispersion is directly put in the DSC cup and sealed. The previous samples were dried in air, to evaporate the heptane, and weighed in the DSC cup and sealed. This allowed the uptake of water from the atmosphere. The heating and cooling curves both show the formation of two

different hydrate forms. The evaporation of water decreases the solubility of CaCl_2 in its hydrate water, which allows the formation of $\text{CaCl}_2 \cdot 4\text{H}_2\text{O}$.²⁴ The phase transition temperature of $\text{CaCl}_2 \cdot 4\text{H}_2\text{O}$ is 45.5 °C. The heating and cooling traces show the melting and crystallization of $\text{CaCl}_2 \cdot 6\text{H}_2\text{O}$ as well as of $\text{CaCl}_2 \cdot 4\text{H}_2\text{O}$. Moreover, the compartmentalization effect on the crystallization, as demonstrated in figure 7.12, is observed here as well. This clearly demonstrates the success of the encapsulation procedure.

7.3.5 Deliquescence

The thermal properties of the micro-encapsulated $\text{CaCl}_2 \cdot 6\text{H}_2\text{O}$ are clearly affected by the ratio of CaCl_2 and water, as is demonstrated by the previous experiments. During sample preparation of the microcapsules synthesized from Pickering emulsion 1 (fig. 7.12), water is absorbed from the air. The excess of water leads to a lower phase transition temperature and increased under-cooling. On the other hand, during the polymerization of Pickering emulsion 3 to 5, water is evaporated. The changed composition led to the formation of $\text{CaCl}_2 \cdot 4\text{H}_2\text{O}$, instead of $\text{CaCl}_2 \cdot 6\text{H}_2\text{O}$. The uptake of water is measured over the course of two weeks, to illustrate the deliquescent properties of $\text{CaCl}_2 \cdot 6\text{H}_2\text{O}$. Both micro-encapsulated as well as pure $\text{CaCl}_2 \cdot 6\text{H}_2\text{O}$ crystals are measured.

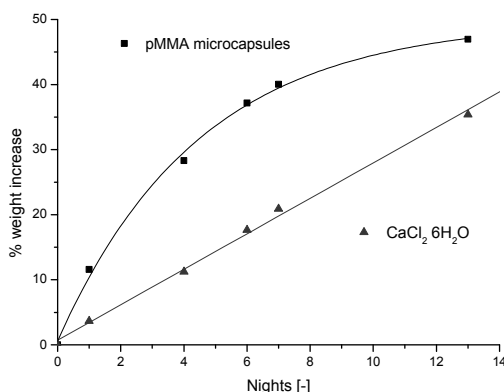


Figure 7.14 Deliquescence of pure and micro-encapsulated $\text{CaCl}_2 \cdot 6\text{H}_2\text{O}$. The water uptake is measured gravimetrically by the relative increase of weight.

Figure 7.14 shows that both the pure as well as the encapsulated $\text{CaCl}_2 \cdot 6\text{H}_2\text{O}$ are deliquescent. Over the course of 2 weeks, both samples absorb roughly 40% of water. Naively, one would think that the pMMA shell provides a barrier for the adsorption of water and adsorption would be slower. Surprisingly, the encapsulated $\text{CaCl}_2 \cdot 6\text{H}_2\text{O}$ takes up water much faster, which is caused by the larger surface to volume ratio of the microcapsules as compared to the pure $\text{CaCl}_2 \cdot 6\text{H}_2\text{O}$. By weight a similar amount of pure $\text{CaCl}_2 \cdot 6\text{H}_2\text{O}$ is taken for this experiment. The major difference is that this only comprises a few large (mm-sized) crystals, which exhibits a significantly smaller contact area with the atmosphere. The contact area limits the rate of water uptake from the atmosphere. The adsorption of water explains the deviating melting and crystallization temperatures as are found in the XRD and DSC measurements. In conclusion, $\text{CaCl}_2 \cdot 6\text{H}_2\text{O}$ is successfully encapsulated with a pMMA shell, but it does not provide a sufficient barrier for water absorption.

7.4 Discussion

The novel encapsulation procedure of $\text{CaCl}_2 \cdot 6\text{H}_2\text{O}$ is successful, but it does not have the desired effect in terms of the application as a PCM. The nucleation and crystallization is spread out over a wide temperature range due to the compartmentalization. For the application as a PCM, ideally, the melting and crystallization temperatures should be identical. However, the addition of nucleating agents and the optimization of the salt composition can overcome these negative effects. A much larger obstacle for the application as a PCM is the enhanced absorption of water by the microcapsules, which lowers the heat capacity of the material and alters the melting and crystallization temperature. $\text{CaCl}_2 \cdot 6\text{H}_2\text{O}$ is naturally deliquescent and its low vapor pressure causes the material to absorb water. The pMMA shell probably does provide some barrier for water. However, the large contact area of the microcapsules with the surrounding effectively enhances the rate of water adsorption significantly. Nonetheless, the enhanced water uptake and the compartmentalization effect on the crystallization confirm that the micro-encapsulation is successful.

The described approach for the micro-encapsulation of $\text{CaCl}_2 \cdot 6\text{H}_2\text{O}$ is flexible in terms of the microcapsule shell thickness and size. Moreover, the encapsulation procedure is not restricted to $\text{CaCl}_2 \cdot 6\text{H}_2\text{O}$ only. In principle, any other salt hydrate or aqueous solution can

be used, because the shell forming material (pMMA particles and monomer) is purely applied from the continuous phase and no modification or mixing is required with the dispersed phase.

7.5 Conclusion

In this chapter we presented a novel method to synthesize polymeric microcapsules that allow the encapsulation of $\text{CaCl}_2 \cdot 6\text{H}_2\text{O}$. The procedure consists of roughly two steps. First, the salt hydrate is emulsified in oil with the aid of poly(methyl methacrylate) (pMMA) microparticles to form a Pickering emulsion. The second step is the addition and *in situ* polymerization of MMA, which ultimately results in pMMA microcapsules. In this method, pMMA seed particles are adsorbed around a droplet and are subsequently grown. The growth forces the particles to overlap, because the particles are restricted to the droplet surface area, which results in the formation of a macroscopically closed shell. To the best of the authors knowledge, this is the first time that $\text{CaCl}_2 \cdot 6\text{H}_2\text{O}$ is micro-encapsulated. The thermal properties are characterized by DSC and XRD, which show a clear effect of the compartmentalization of $\text{CaCl}_2 \cdot 6\text{H}_2\text{O}$ on the crystallization behavior. Nucleation and crystallization are clearly restricted to the microcapsules, as opposed to the bulk salt hydrate, where a single nucleation normally results in the crystallization of the entire sample.

References

1. Farid, M. M.; Khudhair, A. M.; Razack, S. A. K.; Al-Hallaj, S., *Energy Conversion and Management* **2004**, 45, (9-10), 1597-1615.
2. Regin, A. F.; Solanki, S. C.; Saini, J. S., *Renewable & Sustainable Energy Reviews* **2008**, 12, (9), 2438-2458.
3. Sharma, A.; Tyagi, V. V.; Chen, C. R.; Buddhi, D., *Renewable & Sustainable Energy Reviews* **2009**, 13, (2), 318-345.
4. Zalba, B.; Marin, J. M.; Cabeza, L. F.; Mehling, H., *Applied Thermal Engineering* **2003**, 23, (3), 251-283.
5. Abhat, A., *Solar Energy* **1983**, 30, (4), 313-332.
6. Tyagi, V. V.; Buddhi, D., *Renewable & Sustainable Energy Reviews* **2007**, 11, (6), 1146-1166.
7. Zhu, N.; Ma, Z. J.; Wang, S. W., *Energy Conversion and Management* **2009**, 50, (12), 3169-3181.
8. Raj, V. A. A.; Velraj, R., *Renewable & Sustainable Energy Reviews* **2010**, 14, (9), 2819-2829.
9. Inaba, H., *International Journal of Thermal Sciences* **2000**, 39, (9-11), 991-1003.
10. Yang, R.; Xu, H.; Zhang, Y. P., *Solar Energy Materials and Solar Cells* **2003**, 80, (4), 405-416.
11. Zhang, P.; Ma, Z. W.; Wang, R. Z., *Renewable & Sustainable Energy Reviews* **2010**, 14, (2), 598-614.
12. http://www.micronal.de/portal/basf/ide/dt.jsp?setCursor=1_286688, **January 2011**.
13. Salari, J. W. O.; Reezigt, H.; Rouwers, B. W. M.; Glastra, H. COATED DISCRETE PARTICLE, METHOD FOR PREPARATION THEREOF, AND PRODUCT IN WHICH THIS PARTICLE IS APPLIED WO 2008/153378 A2
14. Jyothi, N. V. N.; Prasanna, P. M.; Sakarkar, S. N.; Prabha, K. S.; Ramaiah, P. S.; Srawan, G. Y., *Journal of Microencapsulation* **2010**, 27, (3), 187-197.
15. Yow, H. N.; Routh, A. F., *Soft Matter* **2006**, 2, (11), 940-949.
16. Ghosh, S. K., *Functional coatings : by polymer microencapsulation* Weinheim, 2006.
17. Chang, T. M. S., *Science* **1964**, 146, (364), 524-&.
18. Paiphansiri, U.; Tangboriboonrat, P.; Landfester, K., *Macromolecular Bioscience* **2006**, 6, (1), 33-40.
19. Barrett, K. E. J., *Dispersion polymerization in organic media*. Wiley-Interscience: London, 1975.
20. Lee, K. C.; Winnik, M. A.; Jao, T. C., *Journal of Polymer Science Part a-Polymer Chemistry* **1994**, 32, (12), 2333-2344.
21. Hirzinger, B.; Helmstedt, M.; Stejskal, J., *Polymer* **2000**, 41, (8), 2883-2891.
22. Rodriguez-Navarro, A. B., *Journal of Applied Crystallography* **2006**, 39, 905-909.
23. Leclair, A.; Borel, M. M., *Acta Cryst.* **1977**, B33, 2938 – 2940.
24. Carlsson, B.; Stymne, H.; Wettermark, G., *Solar Energy* **1979**, 23, (4), 343-350.

Epilogue

After 4 years of research and writing this thesis, this is the place to look back, dwell on the limitations and possibilities of the research that has been performed, discuss the new lines of research that have sparked up in my mind, but for which I did not have time to pursue, and look into the future. Several things come to mind that range from purely practical considerations to fundamentally novel concepts.

As a general reflection on Pickering emulsions and micro-encapsulation, I believe that the conventional micro-encapsulation methods could benefit from the stability against coalescence of Pickering emulsions. In the introduction of this thesis, a reference is made to the main encapsulation methods based on emulsions, *i.e.* interfacial polycondensation, (complex) coacervation and (mini-)emulsion polymerization. These methods use emulsion droplets as scaffolds for the formation of microcapsules and therefore suffer from continuous break-up and coalescence during the encapsulation process. As a consequence, the process conditions need to be optimized thoroughly to achieve efficient micro-encapsulation. Ideally the emulsion droplets are formed in the initial stages of the process and remain segregated during the encapsulation, as is the case for Pickering emulsions. Although it is argued in chapter 1 that there is no substantial experimental evidence to conclude that Pickering emulsions are more stable than conventional emulsions, it has been found that Pickering emulsions are sufficiently stable against coalescence. In the conventional stirred reactors that are used extensively in the work reported in this thesis, no coalescence is observed for most of the Pickering emulsions. Moreover, many of the Pickering emulsions described in this thesis did not show any coalescence upon prolonged storage. The widely accepted notion that Pickering emulsions are remarkably stable against coalescence is in principle beneficial for the above-mentioned encapsulation methods and could enhance their encapsulation efficiency.

As already mentioned in the very beginning, the research that is described in this thesis was originally motivated by the micro-encapsulation of salt hydrates for thermal energy applications. The micro-encapsulation of salt hydrates is finally achieved, as described in chapter 7, and is in that respect successful. However, chapter 7 also concludes that the properties of the pMMA microcapsules do not meet the criteria for their application as PCMs. The main limitation is the permeability of the pMMA shell for water. Apparently, the shell does not provide sufficient barrier properties for the diffusion of water. This makes the encapsulated salt hydrate susceptible for its surroundings, which negatively affects the

thermal properties. One of the aims of future research is therefore to use the same approach as described throughout this thesis and extend it to other materials that obey to the requirements for application as a PCM.

A good candidate that potentially meets the stringent requirements for application as PCM is silica or silicon dioxide (SiO_2). Various forms of silica exist, but all of them are generally considered impermeable. The great benefit of this material is that it is fully adaptable with the described encapsulation procedure. First of all, silica particles are known to form Pickering emulsions. Second, the surface of silica particles naturally contains chemically reactive groups (silanol-groups, Si-OH), which can be easily functionalized. The wettability of the silica particles can be adjusted by modification of the silica surface, which is paramount for Pickering stabilization. Third, several silica-precursors are available, such as tetraethoxy silane and sodium silicate, that can reinforce the particle layer that surrounds the droplet and ultimately lead to the formation of stable silica microcapsules.

Looking back, this thesis is not only a study towards the micro-encapsulation of salt hydrates, but it can better be seen as an investigation towards the efficient micro-encapsulation of aqueous liquids in general. The presented approach is robust and allows the encapsulation of other materials, besides salt hydrates, as long as aqueous/hydrophilic liquids are used. Other applications might benefit from the observed permeability of the microcapsule shell, *e.g.* drug-delivery systems or food. Another aim worth investigating is to find applications for which the reported pMMA microcapsules are more suitable.

The work that is described in this thesis is supported by the Capzo International BV (Capzo). For that reason, the research was focused on the success and *efficiency* of the developed encapsulation approach. Efficiency is less relevant in laboratory experiments, where the success factor is more important. However, for large scale production is the efficiency of the encapsulation process paramount. Material, energy and money is lost with every gram of material that is wasted. The continuous production of Pickering emulsions and microcapsules is worth investigating to further improve the encapsulation efficiency. At the moment, Capzo has focused on batch reactors/production. However, in the long term, Capzo could benefit from the research that is performed on the continuous (mini) emulsion polymerization, as performed by Smeets, Scholtens and Hoedemakers¹⁻³ and is continued by Tom Jansen. A similar approach could be adopted for the formation Pickering emulsion and the subsequent processing into microcapsules.

A novel encapsulation method could be obtained by the combination of Pickering emulsions and the encapsulation of inorganic particles, as reported by Syed Ali.^{4, 5} The encapsulation method uses block-copolymers obtained by controlled radical polymerization techniques, such as ATRP and RAFT, to functionalize inorganic particles. The block-copolymers are then extended, while adsorbed to the particles. The high degree of modification of the particles results in successful encapsulation to form composite (organic/inorganic) particles. Clay or silica particles have been used for this approach. At the same time, these particles can be assembled at water-oil interfaces to form a Pickering emulsion. Chain extension of the block-copolymers would then result in the encapsulation of the emulsion droplets. The advantages of this combination are in the first place that the block-copolymers can be used to adjust the wettability of the particles and herewith render it suitable for Pickering stabilization. Second, the adsorbed block-copolymer could reinforce the particle layer surrounding the emulsion droplet. Third, the use of controlled radical polymerization techniques restricts the polymerization to the water-oil interface, where the block-copolymer is adsorbed. Finally, a high degree of control over the molecular weight of the formed polymer is obtained with ATRP or RAFT, which controls the properties of the microcapsule shell.

Chapter 5 demonstrates the fundamental relationship between the wettability and colloidal stability for particles that are suitable for Pickering stabilization. The general notion is that ‘flocculating’ conditions enhance the interfacial adsorption of particles and improve the stability of the emulsion. This is confirmed by the SCF theory in chapter 5 for sterically stabilized particles. Moreover, it is found that there is a small window of steric stabilizer concentrations that show both partial wetting and colloidal stability. These two properties are ideally combined for the formation of Pickering emulsions and their processing into microcapsules or other advanced materials. It is interesting to further explore the fundamental relation between the wettability and colloidal stability for other systems, such as charge-stabilized particles. Not only the colloidal stability is of importance, there is also an inherent relation between the wettability and the particle interaction at the water-oil interface. Furthermore, it is interesting to experimentally verify the theoretical outcomes of chapter 5, in order to validate and optimize the used model.

Controlled radical polymerization techniques, such as ATRP or RAFT, could also play a role here. Hairy particles can be synthesized with great control over the chain length of the hairs. For example, silica particles can be functionalized with an ATRP initiator or chain transfer agents (RAFT) from which the polymerization proceeds. The conversion of

monomer determines the length of the hairs and herewith the wettability and colloidal stability. Another possibility is to use block-copolymers as steric stabilizers during emulsion polymerization, as described in the work of Hector Tello Manon⁶ and Alexandra Munoz-Bonilla.⁷ Adjusting the block-copolymer type and chain length and at the same time the particle size allows a high degree of control over the surface coverage of stabilizer. The careful control of the hair length and surface coverage allows an exact correlation between the interrelated phenomena of wettability and particle interactions.

A different topic that intrigued me while working with Pickering emulsions and colloidosomes is the particle ordering on the droplet surface. This is best expressed in chapter 3 that shows jammed, incomplete particle configurations on the droplet surfaces. Normally, denser particle configurations are observed that show a high degree of regularity. The majority of the particles are most commonly packed in a hexagonal close packing. Moreover, compulsory defects are formed on the droplet, due to the curvature of the surface. According to Euler's theorem, the total disclination charge on any sphere equals 12. Soccer balls and C₆₀ fullerenes are typical examples of this phenomenon. They have exactly 12 pentagonal patches and 20 hexagonal patches. As the number of particles on the sphere or droplet increases, additional dislocations are introduced, which consist of pairs of 5-7 defects. Chains of 5-7 dislocations, so-called grain-boundary scars, are formed when the system size exceeds the critical value of 5. Accordingly, the defects are organized in an icosahedral symmetry on the droplet surface (fig. E.1). Experimental observations of these phenomena opened up a new field of research that studies the effect of curvature and topology on the organization of matter. In my opinion, the highly symmetrical organization of defects on the droplet surface can be exploited to direct the assembly of a second type of particles. For example, 'smaller' particles could fit on the positions of the pentagonal-coordinated particles. Another possibility is to use 'larger' particles to fit on the positions of the heptagonal-coordinated particles. The directed assembly of secondary particles further reduces the elastic strain energy of the system. Under the right circumstances, the secondary particles organize themselves in the same symmetrical fashion as the defects of the primary particles. This allows tremendous control over the position of particles on the droplet surface.

The curvature-directed particle assembly becomes particularly interesting when the secondary particles have distinctly different properties to the primary particles, such as lower glass-transition temperature, lower- or upper- critical solution temperature or pH sensitivity. The secondary particles could serve as gates, which can be opened on demand,

to control transport across the shell when capsules are composed of two or even three different types of particles.

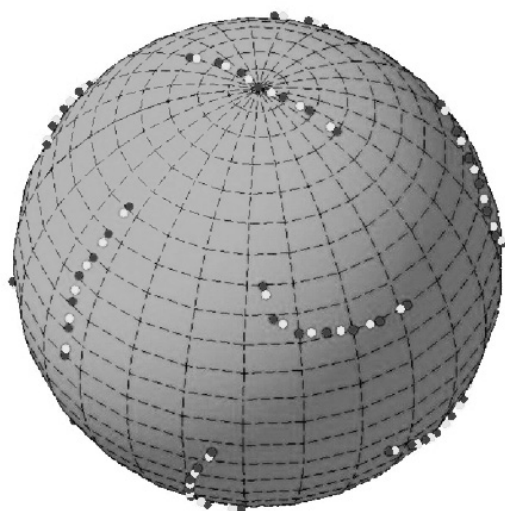


Figure E.1 Model grain-boundary scars on the surface of a colloidosome. The primary particles are omitted from the image. Only the pentagonal- (dark gray) and heptagonal-coordinated (light gray) particles are shown.⁸

In conclusion, Pickering stabilization offers great potential for micro-encapsulation in general. Existing encapsulation methods can be improved, due to the stability of Pickering emulsions, and novel advanced encapsulation concepts are envisioned.

References

1. Hoedemakers, G. F. M. Continuous emulsion polymerization in a pulsed packed column. Eindhoven University of Technology, Eindhoven, 1990.
2. Scholtens, C. A. Process development for continuous emulsion polymerization. Eindhoven University of Technology, Eindhoven, 2002.
3. Smeets, N. M. B. Molecular weight control in emulsion polymerization by Catalytic Chain Transfer. Eindhoven University of Technology, Eindhoven, 2009.
4. Ali, S. I. Colloidal templating: a route towards controlled synthesis of functional polymeric nanoparticles. Eindhoven University of Technology, Eindhoven, 2010.
5. Ali, S. I.; Heuts, J. P. A.; Hawket, B. S.; van Herk, A., *Langmuir* **2009**, *25*, 10523-10533.
6. Manon, H. T. Amphiphilic cationic block copolymers, from self-assembly to functional particles via emulsion polymerization. Eindhoven University of Technology, 2011.
7. Munoz-Bonilla, A.; Herk, A. M. v.; Heuts, J. P. A., *Macromolecules* **2010**, *43*, (6), 2721-2731.
8. Bausch, A. R.; Bowick, M. J.; Cacciuto, A.; Dinsmore, A. D.; Hsu, M. F.; Nelson, D. R.; Nikolaides, M. G.; Travesset, A.; Weitz, D. A., *Science* **2003**, *299*, (5613), 1716-1718.

Acknowledgements

It was not just me who did the research. There were many others who contributed to this thesis and for which I would like to thank them. I really believe that the realization of this thesis has been a team effort. The supervisors were obviously there, but also colleagues, collaborators, students, family and friends.

In the first place, I would like to acknowledge my two bosses: *Herman Reezigt* and *Bert Klumperman*. I could not decide who to acknowledge most. Although each of you contributed in a different manner it was of equal importance. I'm not only thankful for the scientific/technical support, but I am mostly thankful for giving me almost absolute freedom and trust to do my work and pursue my ideas. I really appreciated this attitude towards me and my work.

Jan Meuldijk thanks for your eternal optimism and thorough reading in the final stages of finishing my thesis. *Hans Wyss* thanks for being so involved in the project. I was lucky to have met you, since you worked in the group that basically invented the colloidosome. Your suggestions and view on the matter lifted the work to a higher level.

I would like to thank *Cor Koning* for allowing me, as a guest, to be a part of SPC and the secretaries *Pleunie Smits* and *Caroline van Os* for arranging whatever was necessary. I will never forget this! Also, many thanks to *Alex van Herk* for letting me participate in the emulsion meetings, SEP and conferences. A professor is supposed to supervise and train students. You took this task very seriously! I learned a lot (not always scientific ;-)) and I will never forget the times in Prague, Glasgow and Singapore.

During my PhD I had the chance to collaborate with many people, which I enjoyed a lot and who provided me with the new and necessary insights and perspectives. *Gorden Jemwa* thanks for being so patient and showing me the way through matlab. It was very useful. I even managed to perform simulations using matlab, which without your help would not have been possible. I would like to acknowledge *Len Barbour* and *Jan-Andre Gertenbach* for performing the temperature dependent XRD measurements. *Riccardo Fantoni*, it was a pleasure working with you and I really had a good time in Badajoz. I find it always a challenge discussing matters with theoretical physicists, who almost seem to speak a different language. However, in the end we managed to pull off some nice work together where theory and experiment come together. The way real science should be. *Frans Leermakers*, thanks for your help on the SCF theory, your extensive tutorials on

thermodynamics and of course for taking part in the opposition. The work on the relation of wetting and colloidal stability would not have been possible without your commitment.

I also enjoyed working with and supervising students. Not only because you have done a lot of the practical work in this thesis, but also for the company. A problem shared is a problem halved! *Elyounssi Abdelmohssin*, you were my first student. You were in Eindhoven for only three months, but you gave me a lot of results that took me the rest of my PhD to characterize, model and understand. Thanks for the hard work! *Bas Ravensteijn*, thanks for your hard work in Stellenbosch. You are a special guy and you're probably smarter than you realize. A great PhD and career lies ahead of you. *Jeroen van Heck*, your stay in Stellenbosch was short, but powerful. Thanks a lot for the nice piece of work! *Peter Albers*, I promised you a paper, but I didn't have time for it yet. I'm still planning to get it published. Thanks! And last, but not least I want to acknowledge *Guido Mutsaers*. Like a real PhD, you successfully managed to work independently during the second half of your project. Your work is the foundation of the last three chapters of this thesis. For that I owe you!

Special thanks for the Capzo/Salca team: *Gerard Oortmans*, *Bart Winters*, *Jolanda Reezigt*, *Hans Heupink*, *Henk Glastra*, *Bart Rouwers*. It's really unique to be (financially) supported in the way I was, especially, because the company is so young and was not making any profit yet. I'm really thankful for the trust and believe in me and my work. I'll work hard to make up for it. Although I spent most of my time in Eindhoven, the sun always shines on the other side of the Kuiperberg. It was always a pleasure to come to Ootmarsum.

Stefan Bon, thanks for taking part in the opposition of my defence. Your work was a source of inspiration, as you might have noticed. *Willem Kegel*, also many thanks for taking part in my opposition.

For some strange reason I always shared my office with women, which was always a pleasure. *Patricia* and *Marie-Claire*, thanks for teaching the BMF his way in the SPC world. *Pooja*, you are a crazy, funny girl. It was a pleasure sharing the office with you. I will definitely miss your care and curries :-). *Judith*, you have the challenging task to do what I couldn't, but I'm sure you'll manage. The future of Capzo is in your hands now! It was and still will be a pleasure to work with you.

Zusje, thanks a lot for designing the cover and 'tussenbladen' for each chapter. It looks really professional.

It is not possible to always work. Therefore it is good to have some distraction and for that I want to acknowledge Spartak SPC. I was never really a team player before I joined Spartak SPC, but with you guys it was always great fun to play soccer. So thank you all! *Hector, Eyygeni, Mark, Donglin, Tom, Marcos, Benjamin, Niels, Sjoerd, Michiel, Vladimir, Barish and Joost.*

SPC is a world on its own, with so many different people, cultures, nationalities and ideas. It therefore also has similar, but smaller, problems. Nevertheless, it was great to have spent the last 4 years with all of you. So thank you all! I will never forget it.

Bert Klumperman also gave me a chance to spend six months in his group in Stellenbosch. It didn't feel like working actually. It was more like a holiday. I especially want to acknowledge *Paul Reader*. You were an excellent host and a good friend. I really enjoyed our training sessions and bouldering trips. I hope I can ever be such a good host as you were. *Guusje*, it was great to have shared the time in Stellenbosch with you. I will never forget our coffee/cigarette breaks in the sun in front of the Neelsies. I really admire your open, child-like approach to the world. Baie Dankie!

Baby, I love you! I also want to acknowledge you. Although there was no 'significant' scientific contribution, without you I'm not sure this thesis would have seen the light. Especially during the last weeks before the deadline you made sure that my life kept on track, while I was focusing on writing. Now the thesis is finished, I will make sure that you'll get the attention you deserve so much. Now that my PhD and thesis is finished, it is time to move on to another project...

Sander, I had the right intention, but my planning was slightly too optimistic that you couldn't be my paranimf. So from this place I would like you to be my 'honorary' paranimf.

I can be short acknowledging my paranimfen. You know. Homies For Life, Respect!

Curriculum vitae

Joris W.O. Salari was born on 29th of May 1981 in Alkmaar, The Netherlands. After finishing the pre-university secondary education (VWO) in 1999 at the Jan Arentsz College in Alkmaar, he studied Chemical Engineering at the University of Twente in Enschede, The Netherlands. In 2006 he graduated in the groups of Supramolecular Chemistry and Technology and Inorganic Material Science on ‘Self-assembled Monolayers of Mono- and Di-Alkyl Phosphate on Ultra-smooth surfaces.’ From april 2006 until September 2007 he worked for Kobato Polytechnology BV on the micro-encapsulation of phase change materials for heat storage applications. In September 2007 he started a PhD project at the Eindhoven University of Technology at Eindhoven, The Netherlands, of which the results are presented in this dissertation. Since the start of his PhD project he has been employed at Capzo International BV.

Publications

Joris W.O. Salari, Jeroen van Heck, Bert Klumperman Steric stabilization of Pickering emulsions for the efficient synthesis of polymer microcapsules. *Langmuir*, 2010, **26** (18), pp 14929–14936

Joris W.O. Salari, Gordon T. Jemwa, Hans M. Wyss, Bert Klumperman Reconstruction of the 3D structure of colloidosomes from single SEM images. *Soft Matter*, 2011, **7**, pp 2033-2041

Joris W.O. Salari, Riccardo Fantoni, Hans M. Wyss, Jan Meuldijk, Bert Klumperman Colloidal cages: colloidosomes with tunable particle packing. The manuscript is in preparation.

Joris W.O. Salari, Frans A.M. Leermakers, Bert Klumperman Pickering emulsions: wettability and colloidal stability of hairy particles - a Self-Consistent Field theory. The manuscript is submitted for publication to *Langmuir*.

Patent

Dutch patent application has been filed at 31st March 2011. '*Werkwijze voor het inkapselen van discrete kleine hoeveelheden materiaal en capsule verkregen onder toepassing van deze werkwijze.*'

Presentations

Joris W.O. Salari, Elyounssi Abdelmohssin, Gorden T. Jemwa, Riccardo Fantoni, Hans M. Wyss, Bert Klumperman Colloidosomes with tunable particle packing: synthesis (Lunteren, 2009), characterization (Velthoven, 2010) and modeling (Velthoven, 2011) *Dutch Polymer Days*

Joris W.O. Salari, Elyounssi Abdelmohssin, Gorden T. Jemwa, Riccardo Fantoni, Hans M. Wyss, Bert Klumperman Colloidal cages: colloidosomes with tunable particle packing. *Macro2010, 43rd IUPAC World Polymer Congress*, Glasgow, Scotland, July 2010